UNIVERSITÀ DEGLI STUDI DI PAVIA
DOTTORATO DI RICERCA IN FISICA – XXXI CICLO

Silicon integrated devices for quantum photonics in the telecom band

Micol Previde Massara

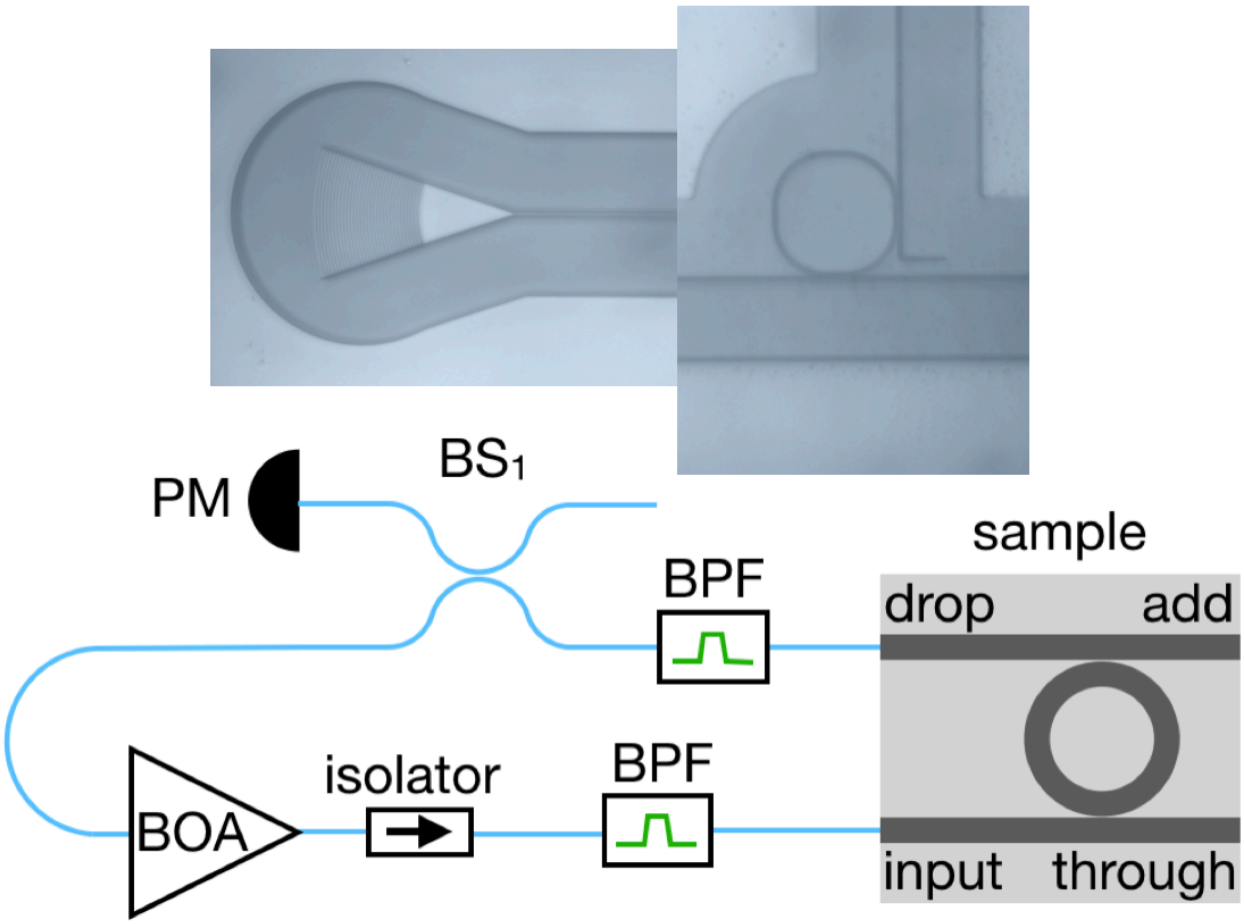

Tesi per il conseguimento del titolo

Università degli Studi di Pavia
Dipartimento di Fisica

DOTTORATO DI RICERCA IN FISICA – XXXI CICLO

Silicon integrated devices for quantum photonics in the telecom band

Micol Previde Massara

Submitted to the Graduate School of Physics in partial fulfilment of the requirements for the degree of

DOTTORE DI RICERCA IN FISICA

DOCTOR OF PHILOSOPHY IN PHYSICS

at the

University of Pavia

Supervisors: Prof. Daniele Bajoni, Prof. Matteo Galli

Cover: Top left: optical image of the INPHOTEC grating coupler.
Top right: optical image of the INPHOTEC add-drop resonator.
Bottom: experimental setup of the self-pumping cavity described in chapter 3.

Silicon integrated devices for quantum photonics in the telecom band
Micol Previde Massara
PhD thesis - University of Pavia
Pavia, Italy, December 2018

Contents

Chapter 0

Introduction

In the last years, a lot of research effort has been devoted to exploit the field of quantum information, for the many advantages that can be gained by applying the laws of quantum mechanics. This has led to a tremendous development of quantum technologies, that have moved from experiments on the foundation of quantum physics to being extensively studied in applied research.

Quantum technologies exploit quantum properties of physical systems, such as superposition and entanglement, in order to obtain unprecedented performances. In the last decade, a number of quantum technologies start-up companies were founded. Besides, even large companies, such as Google [1], IBM [2], Intel [3], Microsoft [4] and Toshiba [5], have started to consider quantum technologies an interesting field for investments. Moreover, very recently, even governments have started large funding programs in this attractive field, such as the Chinese program, in which a satellite has been recently launched for experiments on quantum communication [6], and the European flagship in quantum technologies, a long-term (10 years) and large-scale (about 1 billion of euros) program for taking Europe at the forefront of the research in quantum technolgies [7, 8].

The European flagship is divided in four major topics: quantum computation, which exploits the quantum nature of a system to perform fast calculations and tasks that are not possible to execute on current classical processors; quantum communication, where quantum properties, such as entanglement, are used to secure data transmission; quantum simulation, that employs quantum systems to perform quantum mechanical simulations; and quantum sensing and metrology, where an enhancement on the performance of measurements is achieved by exploiting quantum systems.

In quantum technologies, the fundamental unit of information is called quantum bit (or *qubit*), from the classical *bit* formalized by C. Shannon in 1948 [9]. A qubit is defined by a microscopic system, that could be a photon, an atom, a nuclear spin and so on. Conversely to a classical bit, that can

assume only two values (either 0 or 1), the qubit is defined by any linear combination of the states chosen as basis. This means that the qubit is in a *superposition* of the basis states [10]. Moreover, another property of quantum systems widely exploited in quantum technologies is that of *entanglement*, that happens when a quantum system made by more than one component cannot be separated in the single elements and has to be described as a whole [11]. From these considerations the first big difference between classical bits and qubits is that n entangled qubits are equivalent to 2^n bits [12], from which the advantage of quantum computation over classical processing comes.

In the last years, many systems have been used to implement the qubit, such as trapped atoms or ions [13], superconductors [14], quantum dots [15], nuclear spins [16] and photons [17]. In particular, even if superconducting circuits seem to overcome the other solutions when dealing with quantum computing applications, photons seem to be the best candidate for quantum communication [18] protocols. This is mainly due to their long coherence length, low noise and ease of implementation and manipulation with components that work at room temperature. A well-known application of quantum communication is made of quantum key distribution (QKD) protocols, that use a quantum-encrypted secret key to securely transmit data along a public channel. The first example of such protocols was developed by Bennett and Brassard in 1984 and it is called BB84 protocol [19]. So, the availability of the currently-employed telecommunication channel made of the fiber-optic network connecting cities all over the world, is another big advantage of photonics, for light is already employed in telecommunications.

In order to realize quantum applications in photonics, nonclassical states of light, that is radiation that cannot be described by the classical electromagnetic theory, have to be generated. Usually, the quantum states of interest are either single-photon states or entangled photon states.

Single-photon sources should emit on demand states where only one single photon is present. This is usually achieved through deterministic atomic-like sources, such as quantum dots, trapped ions etc. However, even the probabilistic emission of photon pairs can be used to produce single-photon states through the *heralding* method. Here, one photon is revealed, thus signaling the presence of the other photon that is then a single-photon state. In the last years, different devices have been exploited to prove the emission of heralded single photons, such as PPLN waveguides [20], silicon-based photonic crystals [21], silicon microring resonators [22] and hydex microring resonators [23].

Entangle-photon states, whose states cannot be described separately, are made of at least two photons among which nonlocal correlations exist and can be usually encoded in different degrees of freedom, such as polarization [24, 25], path [26] and phase [27, 28]. A variety of experiments showed the production of entangled-photon states,the first employing atomic radiative cascades [29] and BBO crystals [24]. After these first works, more practical sources able to emit photons with higher intensity and integration-compatible were proposed, for

example AlGaAs waveguides [30] and silicon integrated devices [31, 25, 32, 33].

In order to translate quantum technologies into real applications, the components has to be scalable, compact and compatible with the integration on an electronic chip. In the last decades, due to the growing interest in integration of photonic structures, the silicon platform has become one of the leading technologies. In fact, silicon structures are cheap and easy to fabricate and can be densely integrated on a chip, due to their compatibility to the CMOS fabrication process employed by the microelectronic industry. Moreover, the foundry services already utilized in microelectronics can be exploited for the fabrication of silicon photonic chips and multi-project wafers (MPW) shuttle runs are available to reduce the production costs. In the microelectronics environment this is well represented by the MOSIS service [34], whereas in silicon photonics this services are offered from organizations, such as the A*STAR Institute of Micorelectronics in Singapore and IMEC and CEA-LETI in Europe [35].

Another interesting property of the silicon platform is the availability of high-quality silicon-on-insulator (SOI) wafers, ideal for the creation of planar waveguide circuits. SOI wafers are usually made of a 220-nm-thick silicon guiding layer on top of a 2-μm-thick silicon oxide substrate. The photonic components are then realized through lithography and etching on the guiding layer. Moreover, due to the high index contrast between silicon and the cladding material (silicon oxide or air), strong optical confinement can be achieved in the SOI platform and, as a consequence, a high-integration level can be reached [36].

Many linear and nonlinear optical components can be created on the SOI basis, and all of them can be derived from a simple waveguide, that constitutes the building block of integrated photonic circuits. In SOI-based waveguides, light is confined through total internal reflection (TIR) in a very small (<1 μm^2) core region. An example of structure derived from the waveguide is the Bragg waveguide (BW), that is obtained by periodically shrinking the width of the waveguide in order to get an effective change of the refractive index. This is the silicon photonic integrated version of a distributed Bragg reflector (DBR) and it is mainly employed as integrated filter [37]. Moreover, due to the strong confinement in SOI-based waveguides, small bending radii can be designed without radiation losses. This, make the construction of very small ring resonators (about 10-μm radius) possible. Microring resonators are made of a channel waveguide looped-back onto itself to follow a circular path, coupled to a bus waveguide needed to couple light in and out of the resonator, and can have different applications, such as filters, sensors, modulators and photon sources [38].

In particular, in this thesis we will explore the capabilities of BWs and microring resonators to emit photon pairs. Since silicon is a centrosymmetric material, only the third-order nonlinearity can be used to generate pairs of photons and the process responsible for that is four-wave mixing (FWM) [39,

40, 41]. FWM can be seen as a four-photon elastic scattering in which two pump photons are converted into idler and signal photons. This effect has been observed in optical fibers [42] and waveguides [43], but it is in microring resonators that can achieve very high generation rates, up to $10^6 - 10^8$ Hz (see chapter 3) [44, 45, 46].

The aim of this work is to study silicon integrated nonlinear optical components and characterize their ability of emitting entangled photons. In particular, our research contributes to the final goal of designing a silicon integrated source of nonclassical states of light, where the source, filtering and multiplexing stages are all integrated on the same chip [37]. So, this work will be focused on assessing the efficacy of integrated filters on spectrally clean the generated photon pairs and studying a way to overcome the lack of laser emission in silicon. Beside the main theme of silicon integrated devices and their applications, we will also treat an aside interesting topic related to quantum computation, that is the emulation of quantum gates by using classical waves. This obviously comes at the price of losing the exponential advantage of true quantum computation.

In the first chapter, we will give a general introduction to the generation of nonclassical states of light in photonics. Starting from the comparison between bit and qubit, we will point out how the employment of quantum mechanics can take real advantage over classical systems. At this purpose we will describe the main areas of research in quantum technologies: quantum computing, quantum metrology and sensing and quantum communication. Then, since this work mainly deals with integrated silicon photonic devices, we will explain the important role played by the silicon platform in quantum photonics applications. After that, we will introduce the topic of nonlinear optics, focusing in particular on the FWM process and outline how it works on some devices, that will be used in the next chapters. Finally, we will report on the possible kinds of sources of quantum states of light.

In the second chapter, we will start addressing the first problem of silicon photonics, that is the possible pollution of the generated quantum states due to the on-chip filtering of the pump. In fact, even if different devices are employed for filtering light on a chip, such as microring resonators, Bragg waveguides and cascaded interferometers, they have all a common feature: they are made of hundreds of microns of silicon waveguide and can potentially generate photon pairs themselves. This generated photons have usually spectral and temporal correlations that differ form those of the photons emitted by the real source and, thus, in case of quantum applications, can pollute the quantum state at the output. At this purpose, we will perform a FWM experiment on an integrated Bragg waveguide in order to determine the generation rate and spectral correlations of the photons emitted by the filter. Our experiment will be also supported by a theoretical model of the studied integrated structure.

In the third chapter, we will address the more complex topic of the difficulty of achieving lasing in silicon, due to its indirect bandgap. This is of

fundamental importance in order to construct an integrated silicon photonic source and bring the employment of silicon devices towards the mass production. Even if, in the last years, different systems have been studied to find a way to achieve laser emission in silicon, such as stimulated Raman scattering, rare-earth doping and III-V compounds, a solution has not yet been found. We will then describe a way of overcoming this obstacle by building a fiber-loop cavity with the source of light (microring resonator) inside it. The choice of constructing a fiber-loop cavity is mainly due to the fact that fiber lasers are a well-known and widely employed technology in the field of telecommunication, whereas the decision of using a microring resonator comes form their excellent qualities as light sources and their design that, in the add-drop configuration, is well-suited for being closed in a loop. We will report on the two performed experiments on the built cavity. In the first measurement, we will employ a ring with a relatively low quality factor and carry out a stimulated FWM experiment, followed by the determination of the joint spectral density of the idler and signal photons. Then, we will insert in the cavity a microring resonator characterized by a higher quality factor and observe spontaneous FWM emission in the self-pumping geometry. We will conclude this experiment with a coincidence measurement on the emitted photons in the self-pumping regime.

The fourth chapter will be dedicated to a topic that goes beyond the central theme of the thesis. However, the found results could be of potential interest as testbeds and teaching purpose in the field of quantum computing. The starting point comes form the fact that the propagation of a single particle in a linear network is equivalent to the propagation of a classical wave in the same network, as long as probabilities at individual outputs are detected and no correlations are measured. So, after introducing the most common quantum computing algorithms, we will report on a method that can be used to implement quantum gate operations on a classical wave network. Obviously, this usually comes at the price of losing the exponential advantage of employing a true quantum machine. We will implement the Bernstein-Vazirani (BV) algorithm in a three-qubit configuration on an electronic circuit with discrete electronic components and show that the advantage over classical digital logic is still retained, even if in a fully classical implementation. Moreover, we will perform a second experiment aimed at showing that in the special case of the BV algorithm, where qubits are never entangled, the resources can scale linearly with the number of qubits.

Finally, in the fifth and last chapter, conclusions and perspectives will be presented.

Concluding, in this thesis, novel contributions have been brought to the field of integrated photonics and they have already been published by peer reviewed papers, of which the author of this thesis is the first author. The first main achievement has been obtained through the nonlinear characterization of a silicon integrated Bragg waveguide filter. Here, it has been proved that Bragg waveguides present better performance than other filter designs, having

low spontaneous FWM emission. This work, described in chapter 2, have been reported in a paper published by Optics Letters in 2018 [47]. The second main achievement of this work has been the observation of FWM emission in a self-pumping geometry. Here, the external tunable laser acting as optical pump in FWM experiments has been removed, thus eliminating the saturation of the generated idler intensity at high pump powers. Consequently, very high FWM generation rates can be reached. The stimulated FWM experiment performed in a self-pumping geometry and the relative joint spectral density measurement, that can be found in chapter 3 (Sec. 3.1), have been described in a paper published by Applied Physics Letters in 2018 [48].

Chapter 1

Nonclassical states of light in silicon photonics

Nowadays, much importance is given to the field of quantum information, since it could bring many advantages in different areas, from quantum computation, to quantum communication and quantum metrology. These are only few examples of quantum information applications and different systems have been studied for actual implementations. In our work we will be mainly interested in light-based applications, so we will treat the generation of nonclassical states of light, that are modes of the electromagnetic field that cannot be included within the classical electrodynamics formalism.

The first chapter wants to introduce the reader to the subject of nonclassical states of light, focusing in particular on integrated silicon photonics. So, we will start with a brief review on the main technologies developed in the quantum field, focusing in particular on the use of photons as carriers of information. Next, we will discuss the importance of silicon photonics. First, we will describe the nonlinear process responsible of photon pairs generation in silicon, that is four-wave mixing. Then, we will analyze the building blocks of photonic integrated circuits, in particular describing the structures we will consider in the next chapters, that are waveguides, the distributed Bragg reflector and microring resonators. Finally, we will explain how we can use photonic circuits as photon sources, and generate both entangled- and single-photon states.

1.1 From bits to qubits

In 1948, C. Shannon formalized how to quantify information in what he called *bits*, or binary digits [9]. The Shannon's bit became the fundamental unit of information and it was soon implemented in technological devices.

A classical bit is usually a macroscopic system (for example a memory element) and can be described by one or more continuous parameters (e.g. voltages). Within the range of these parameters, two well-separated regions

are chosen to represent 0 and 1. Then, a memory of n bits can have 2^n logical states: starting from a string of zeros of length n, all the combinations are spanned till a n-string made of ones. Classical computers not only store data, but they also manipulate them, and a sequence of boolean operations (e.g., NOT and AND) acting on the bits is sufficient to realize any deterministic transformation.

In contrast, the fundamental unit for quantum information is called *qubit*, or quantum bit. A qubit is defined by a microscopic system, such as an atom, a photon, a nuclear spin and so on. The $|0\rangle$ and $|1\rangle$ (in the Dirac notation) states are now represented by a fixed pair of distinguishable states of the qubit. For example, if the photon polarization is considered to implement the qubit, then $|0\rangle$ and $|1\rangle$ could be represented by the horizontal and vertical polarizations:

$$|0\rangle = \leftrightarrow \qquad \text{and} \qquad |1\rangle = \updownarrow .$$

A big difference compared to the classical bit is that a qubit can also assume all the intermediate states between $|0\rangle$ and $|1\rangle$, that is called *superposition* and is represented by a complex linear combination of the basis state [49]:

$$|\psi\rangle = \alpha|0\rangle + \beta|1\rangle, \tag{1.1}$$

where α and β are the complex amplitudes for $|0\rangle$ and $|1\rangle$, respectively. For photons, $|\psi\rangle$-like state are represented by other possible polarizations (such as circular or diagonal). Moreover, in classical computation it is possible to know if a bit is in the 0 or 1 state, but in quantum mechanics we can only speak about probabilities. So,the probabilities of measuring the state $|0\rangle$ or $|1\rangle$ is given by $|\alpha|^2$ and $|\beta|^2$, respectively, and

$$|\alpha|^2 + |\beta|^2 = 1. \tag{1.2}$$

Eq. (1.1) represents a qubit that can be associated to a two-level quantum system, such as the spin of an electron or the polarization of a photon, and described by a point on a sphere, that is called *Bloch sphere*. In fact, since Eq. (1.2) holds, the expression in Eq. (1.1) can be written as:

$$|\psi\rangle = e^{i\gamma}\left[\cos\left(\frac{\theta}{2}\right)|0\rangle + e^{i\varphi}\cos\left(\frac{\theta}{2}\right)|1\rangle\right], \tag{1.3}$$

where γ, ϕ and θ are real numbers. Since the factor $e^{i\gamma}$ has no observable effects, the state can be expressed as [10]:

$$|\psi\rangle = \cos\left(\frac{\theta}{2}\right)|0\rangle + e^{i\varphi}\cos\left(\frac{\theta}{2}\right)|1\rangle, \tag{1.4}$$

in which φ and θ describe a point on a three-dimensional sphere with unitary radius. This is represented in Fig. 1.1.

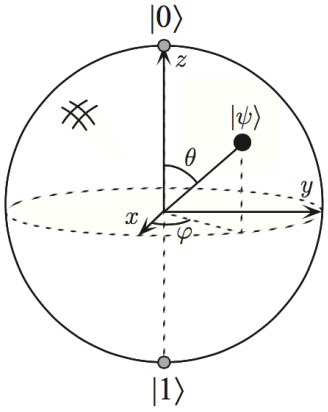

Figure 1.1: Bloch sphere [10].

Generally, a string of n classical bits can be combined in 2^n boolean states, whereas a string on n qubits can exists in any state of the form [12]:

$$|\psi\rangle = \sum_{x=00\ldots0}^{11\ldots1} c_x|x\rangle, \tag{1.5}$$

in which c_x are the complex amplitudes associated with the states $|x\rangle$ and $\sum_x |c_x|^2 = 1$. So, a quantum state made of n qubits is represented by a complex vector $|\psi\rangle$ of unit length in a 2^n-dimension Hilbert space. Thus, in the classical case, the number of parameters grows linearly with the size of the system, whereas the Hilbert space has an exponentially-large dimensionality.

The state represented in Eq. (1.1) can be described by a single vector in the Hilbert space and is then a *pure* state, i.e. a state that is exactly known. In general, for *mixed* state the density operator (or density matrix) has to be introduced:

$$\rho = \sum_i P_i|\psi_i\rangle\langle\psi_i|, \tag{1.6}$$

where $\sum_i P_i = 1$ and $Tr(\rho) < 1$. In the case of a pure state, the density matrix reduces to $\rho = |\psi\rangle\langle\psi|$ and $Tr(\rho) = 1$. More information about the principles lying at the basis of quantum information and computation can be found in [10] and are outside the scope of this thesis.

Another interesting property introduced when dealing with quantum mechanics is *entanglement*. For example, let us consider a system made of two states $|\psi_1\rangle$ and $|\psi_2\rangle$. Then, the Hilbert space describing the combined physical system is given by the tensor product of the Hilbert spaces of the single states:

$$\mathcal{H} = \mathcal{H}_1 \otimes \mathcal{H}_2. \tag{1.7}$$

Now, if the two states $|\psi_1\rangle$ and $|\psi_2\rangle$ are prepared independently and kept isolated, then each state form a closed system and the combined state can be written as [11]:

$$|\psi\rangle = |\psi_1\rangle \otimes |\psi_2\rangle = |\psi_1\rangle|\psi_2\rangle. \tag{1.8}$$

A state $|\psi\rangle$ of the form (1.8) is said to be a *separable* state, for the two states $|\psi_1\rangle$ and $|\psi_2\rangle$ can be treated independently. This case is similar to a classical system, that can be decomposed in each single state it is made of and each state can be described separately.

However, in general, a quantum state of the form (1.1) cannot be written as in Eq. (1.8). In fact, if the states $|\psi_1\rangle$ and $|\psi_2\rangle$ are allowed to interact, then the closed system consists in both $|\psi_1\rangle$ and $|\psi_2\rangle$ together. In the two-qubit system we are considering, this means that the composite state $|\psi\rangle$ is a vector in a four-dimensional Hilbert space given by Eq. (1.7), where $\mathcal{H}_1$ and $\mathcal{H}_2$ are two-dimensional Hilbert spaces, respectively. From these considerations, a first big difference between quantum and classical systems can be found: *n entangled* qubits are equivalent to 2^n classical bits. Hence, the "famous" exponential advantage gained by using a quantum machine instead of classical computers.

Furthermore, in electronics, Boolean functions are implemented in logic gates (e.g. NOT, AND, OR etc.) that perform operations on one or more binary inputs and generate a single binary output. In the same way, logic gates, which can perform operations on quantum states, are needed in quantum computation. Then, entanglement plays a role even in the case of quantum gates. In fact, in the same way a two-qubit state cannot be separated in the product of its single-qubit states, there are two.qubit gates that act nontrivially on both qubits and cannot be separated in the tensor product of single-qubit gates. Obviously, these considerations are still valid for higher-dimensionality Hilbert spaces. An important example of this kind of gates is given by the quantum controlled-not (CNOT) gate, that can be represented as [10]:

$$U_{\text{CNOT}} = \begin{bmatrix} 1 & 0 & 0 & 0 \\ 0 & 1 & 0 & 0 \\ 0 & 0 & 0 & 1 \\ 0 & 0 & 1 & 0 \end{bmatrix}. \tag{1.9}$$

The CNOT is a maximally entangling two-qubit gate and is the equivalent of the classical XOR (exclusive-OR) gate [10, 50]. The CNOT is a very interesting gate, since with single-qubit gates is the prototype for all the other possible gates [10]. Other common gates are the Hadamard (H), Pauli-X (σ_x), Pauli-Y (σ_y), Pauli-Z (σ_z) and phase gates.

It is important to notice, that there are three classes of quantum algorithms which provide an advantage over known classical algorithms [10, 50].
The first class consists of algorithms based upon quantum versions of the Fourier transform, such as the Shor's algorithms. To perform the fast Fourier transform through classical logic would require $n2^n$ steps to transform 2^n numbers, whereas on a quantum machine the same operation would require only about n^2 steps, having an exponential saving.
The second class is identified in quantum search algorithms, in which given N elements in a database and no prior knowledge about them, an element which satisfies a particular property wants to be found. Classically, about N operations are needed, whereas quantum search algorithms would solve the problem

in $\sqrt{N}$ steps, having a quadratic speedup over classical logic.
Finally, the third class consists in quantum simulation. Quantum computers are obvious candidates for the simulation of quantum mechanical systems, that is difficult to perform on classical computers. This because classical computers, to describe a general quantum system, would need a number of complex numbers that grows exponentially with the size of the system, rather then linearly as occurs for classical systems. So, if a quantum system is composed of n different elements, storing the information of such a state on a classical computer would require c^n bits of memory (c is a constant which depends on the properties of the system being simulated and on the accuracy of the simulation). However, on a quantum computer the simulation would require only kn qubits (k is again a constant depending on the properties of the simulated system). So, quantum machines would efficiently perform simulations of quantum mechanical systems that are believed not to be efficiently performed on a classical computer.

In this thesis, we do not intend to give an exhaustive description of the quantum algorithms, that can be found in [10] and [11]. However, in chapter 4, we will give an overview some of the most important quantum algorithms.

Another very important property that it is worth to be mentioned and derives from entanglement is that the unities of information carried by two entangled qubits cannot be separated. So, any perturbation on the first qubit, will influence the behavior of the second qubit, even at large distances [51, 52]. This is a very important feature for quantum information, as we will show in the next sections.

Concluding, in entanglement the strength of quantum information processing over its classical counterpart can be found.

1.1.1 Quantum technologies

Nowadays, many research areas, such as computation, metrology and communication, are experiencing big improvements because of the application of quantum laws, and in each field disparate quantum technologies are studied to look for the best solution. In the following, the most important applications will be presented.

Quantum computing

Quantum computing is that part of the field of quantum information that exploits quantum mechanical phenomena, such as superposition and entanglement, to perform operations on data and tasks that would not be possible by employing a classical machine. Before describing the different technologies employed for implementing quantum computers, it is useful to give the hardware requirement a quantum information processor should have [53]. First of all, the quantum system has to be initialized in a well-defined state. Second, arbitrary unitary operators have to be available and used to bring the initial

state into an arbitrary entangled state. Third, the measurement of qubits has to be performed with high quantum efficiency. Fourth, long decoherence time, larger than the gate operation time, are needed.

Unfortunately, these hardware requirements rule out most of the known physical systems, such as conventional solid-state devices already in use for classical information. Then, in order to find good candidates for quantum information processors, one has to look at the fields of atomic physics and quantum optics. Here, we will give an overview of the main strategies used for the physical implementation of a quantum information processors. An exhaustive treatment can be found in [10, 54] and lies beyond the scope of this thesis.

One of the possible way of implementing quantum information processing is by using *trapped atoms* or *ions* in which the angular momentum of the atom is used to create qubits. Atoms or atom ions are confined in free space with nanometer precision by using appropriate electric fields from nearby electrodes [55] and laser pulses are employed to implement quantum gate operations. Trapped atoms or ions show long coherence time for small systems and low noise level [56]. However, for larger system qubits can interact by phonon mediated coupling. This, along with current difficulty in preparing the atoms in the initial state are among the major drawbacks of this technology [57, 13].

A second option for quantum information applications consists in *quantum dots* and *dopants in solids*. Indeed, the difficulty of cooling and trapping single atoms in vacuum can be overcome if atoms are part of a solid-state matrix. So, impurities or semiconductor nanostructures behave as "artificial atoms" and can bind to one or more electrons (or holes) and form a localized potential with discrete energy levels. There are different ways for realizing quantum dots. Some exaples are: group III-V semiconductors [58], spin-free group-IV semiconductors [15], single impurities (such as phosphorus atom) [59] and nitrogen-vacancy centers in diamond [60, 61]. Even if the issue of the deterministic placement of the dots in the surrounding material has been overcome either by using deterministic fabrication techniques or by employing site-controlled quantum dots, the very low working temperature required from these systems still remains the biggest obstacle in the applications. Moreover, apart from nitrogen-vacancy centers that show long coherence times, usually the exchange interaction in these systems is short-range (being a spin-spin coupling) leading to decoherence on large scales [54].

Another possible implementation of a quantum information processor can be found in *superconductors*. Indeed, at low temperature, in superconductors electrons bind into Cooper pairs, forming a state with zero-resistance current and a well-defined phase. So, superconducting circuits would not suffer from decoherence coming from resistive losses. Moreover, in superconducting circuits, macroscopic quantities, such as inductances, capacitances and so on, can be controlled in order to change the potential for the quantum variables of the Cooper-pair condensate, thus allowing the creation of qubits. Usually,

superconducting circuits are made of an LC circuit with a Josephson junction, that is a thin insulating layer separating sections of a superconductor. In this technology, qubits can be implemented in three different ways: charge [14], flux [62] and phase [63]. The biggest advantage of this technology is that it resemble the classical high-speed integrated circuits and can thus be fabricated by using the existing technology, encoding qubits in ordinary electrical circuit design [64]. However, like for quantum dots, one big issue is that it requires cryogenic temperatures in order to operate, that results in a very expensive technology. Moreover, they have to overcome the big challenge given by the decoherence due to the macroscopic nature of the produced qubits, that involve the collective phenomena of a large number of conduction electrons [54].

Even *nuclear magnetic resonance* (NMR) has been considered for the implementation of a quantum information processor [16, 65]. Because of the rapid molecular motion, nuclei maintain their spin orientation for many seconds, a time comparable to the coherence time in trapped atoms. In NMR, nuclear spins are identified by their Larmor frequency and by using radio-frequency pulses it is possible to manipulate different nuclei, thus generating one-qubit gates. Then, two-qubit gates are created from the indirect coupling mediated through molecular electrons [66, 67]. However, to date, no NMR technique has overcome the difficulties in initializing and scaling up the system.

Finally, many other systems, all exhibiting quantum coherence, have been proposed. Some examples are: small polar molecules instead of single atoms or ions [68], carbon-based nanomaterials, such as fullerene [69], nanotubes [70] and graphene [71], low-decoherence environment on the surface of liquid helium [72], molecular magnets [73] and so on [54]. However, even if many options are available, the use of superconductors as quantum processors seems the best choice. In fact, very recently, some results have been obtained by big companies such as Intel, where a 49-qubit superconducting circuit has been realized [74], IBM, that fabricated a 50-qubit chip [75], and Google, that in 2018 has announced a 72-qubit superconducting circuit [76].

A very important sub-field of quantum computation is *quantum simulation*, that exploits quantum systems in order to mimic other quantum systems. In fact, big challenges are met by classical computers when quantum systems have to be simulated, for the number of parameters and operations needed for the simulation increase exponentially with the system size. Thus, approximation methods are currently employed. Nevertheless, approximations are not always available or they suffer from some limitations and implementing quantum simulations still remains a hard task [77]. Nowadays, different architectures are used to implement quantum simulators of a determined physical system, such as superconducting circuits [78], trapped ions [79, 80], NMR [81] and single photons [82, 83, 84, 85].

Even if no one of the mentioned systems seem to overcome the others, it is worth to mention the role of photonics, due to the low-noise and long coherence time and length of photons. Qubit states could be encoded naturally in the

polarization of the photon and a single-qubit gate could be realized with linear optical components. Moreover, photons are easy to manipulate and individually addressed and moved with high precision by working at room temperature. This are important features for the simulation of complex and nonlocal many-body interactions, even if they imply a challenge in the implementation of two-qubit gates, due to the low-interaction among photons.

Recently, different results have been obtained in the field. For example, photons have been employed to calculate the energy spectrum of the hydrogen molecule to a precision of twenty bits [86] and to simulate frustrated spin systems [87]. Moreover, a very important work by S. Aaronson and A. Arkhipov showed that the simulating the propagation af a photon in a linear network made of beam splitters is a computationally difficult task for classical computers even for few tens of photons [88], for it would occur in an exponential overhead in time and resources. This has been called the *boson-sampling* problem [89] and many experiments have then implemented to show that it can be efficiently treated on quantum simulators [90, 91, 92, 93, 94, 95]. However, the big problem of scalability remains and only few-photon systems have been experimented.

Quantum metrology

Quantum metrology is the field that studies measurements and discrimination procedures that gain some kind of advantage in precision, efficiency, ease of implementation, by introducing the laws of quantum mechanics [96]. In fact, a general measurement is affected by both systematic and statistical errors. While the former are repeatable errors due to either damaged or wrongly-used instruments or wrong experiment design and cannot be reduced, the latter can be either accidental or fundamental-limit-related errors. Statistic errors can be decreased by repeating the measurement and averaging the outcome result. These errors scales as $1/\sqrt{N}$ (Gaussian), where N is the number of resources (e.g. repetitions, particles etc.). This is usually referred to as standard quantum limit (SQL) and is related to measurement procedures which do not exploit the quantum nature of the investigated system. Quantum metrology explores exactly the SQL bound and the strategies that could be used to beat it, and it is currently exploited in different fields, the most important being the estimation of a quantum phase, the measurement of either a quantum state or a process and quantum imaging [97].

The measurement of an optical phase with an interferometer is the typical example of application of quantum metrology. In fact, in a classical experiment the precision on the measurement is given by $1/\sqrt{N}$, where now N stands for the number of detected photons, but in principle it is possible to reach the Heisemberg limit $1/N$ when employing quantum resources [98]. This can be achieved through the use of entangled photons [99], squeezed states (i.e. states having a standard deviation below that one of the ground state of the operators composing them) or NOON states (i.e. multiphoton entangled states) [96]. So,

in this area of quantum metrology, the field of photonics plays a crucial role.

Quantum states carry unity of quantum information and, in order to study a determined quantum process, quantum states need to be prepared, controlled and measured. So, it is important to find ways to precisely measure both the quantum state and the quantum process. Currently, the most used method for measuring a quantum state is the quantum state tomography (QST) of maximum likelihood estimation, which is based on the fact that a single qubit can be determined by taking four projection measurements [100]. Even in this case, QST can help enhancing the precision of the measurement to $1/N$, where N represents the number of measurement trials [97]. Conversely, in order to identify an unknown quantum dynamical process, quantum process tomography (QPT) is needed [97]. One possible way for QPT is to use the known quantum states to probe a quantum process and employ QST to understand how the process works [101, 102, 103]. The first approach used date back to 1996 (standard QPT) [101]. Here, an ensemble of quantum states is prepared and sent through the process. Then, the states at the output are identified through QST. However, this is an indirect technique, since it requires QST to reconstruct the quantum process. However, other direct methods, such as the direct characterization of quantum dynamics (DCQD), can be employed to provide a full characterization of quantum systems without the need of QST [103]. Now, the advances in quantum technologies allow to prepare states with a growing number of qubits and research is needed to reduce the measurement bases and time for data analysis processes [104, 105].

Quantum imaging is a very interesting sub-field of quantum metrology. It exploits quantum properties, such as entanglement, in order to image objects with much more resolution than what obtained through quantum optics. So, through quantum imaging the classical Rayleigh diffraction limit can be overcome. Quantum ghost imaging and quantum lithography are two possible applications of quantum imaging.

In ghost imaging entangled photons are generated through a nonlinear process. The two generated photons are then separated through a beam splitter. The signal photons, after passing the object to be imaged, are collected on a spatially non-resolving bucket detector, whereas the idler photons reach a spatially resolving detector, i.e. a CCD camera. Then the image is constructed by taking the coincidence between the signal on the bucket detector and the idler on the CCD. The term *ghost*, is due to the fact that the image is built without obtaining any spatially-resolved image information from the object [106, 107]. In the first implementation of ghost imaging, position-momentum entangled photons were employed [106, 108]. However, later on, it was demonstrated that ghost imaging can also be performed by considering classical light, because only spatial (i.e. classical) correlation between the beams was required [109, 110, 111]. Still, it was also proved that twin beams have stronger correlation than two coherent states [112], so twin entangled beams can detect a weaker absorption, thus improving the sensitivity of the measurement, even

beyond the SQL imposed by the shot noise [113, 114]. Finally, a recent experiment used the induced coherence between entangled photons generated from two independent sources in order to image an object with photons that do not interact with it [115].

Quantum lithography can help solving an issue encountered by classical optical lithography, that is used to transfer a geometric pattern from a mask to a photoresist (see Sec. 2.1 and 3.1.1), with a resolution of the order of the wavelength of the used light. Usually, in order to obtain a better resolution, the fringe separation has to be decreased, and light at shorter wavelength has to be employed. However, in this way, the photon energy is increased, till it reaches a value at which the object could be damaged. Then, the employment of entangled states can overcome this problem. For example, by introducing N-photon entangled states (NOON states) the resolution can go down to $\lambda/2N$, that is a factor of N below the classical Rayleigh diffraction limit [116]. However, until now only quantum lithography with $N = 2$ has been realized due to current technology limitations [117]. So, even in quantum imaging, photonics seems the best candidate for real applications.

Quantum sensing is another possible subfield of quantum metrology. Here, quantum mechanical systems are employed as sensors for different physical quantities, such as time, frequency, electric and magnetic fields, temperature and so on. Many different systems have been studied to implement quantum sensors depending on which external parameter the sensor responds to. For example, spin-based systems are mainly employed as sensors for magnetic fields [118], whereas trapped ions are used when dealing with electrical fields [119]. Usually, a quantum sensor has to respond when a wanted signal is triggered, but it also has not to be affected by unwanted noise. These requirements define a very important feature of quantum sensors, that is their intrinsic sensitivity. Different strategies have been employed to make this value the lowest possible [120].

Quantum communication

Quantum communication refers to the art of transferring a quantum state from one place to another by using quantum mechanics to guarantee secure communication (*quantum cryptography*). The basis of quantum cryptography lies in quantum mechanics rules that can be summarized by the *no-cloning* theorem, that states that it is impossible to create an identical copy of a quantum state [121]. Usually, in quantum communication a sender, called Alice, and a receiver, named Bob, want to share secrete information through a public channel. Then, they have to face the problem of a possible eavesdropper, called Eve, that could intercept their message without being noticed. Let us now restrict to the example of quantum key distribution (QKD), that is one possible application of the broad quantum information field. In QKD, Alice and Bob produce a shared random secret key, that is used to encrypt and decrypt messages. The quantum properties of the qubit are exploited for

the key transmission, whereas the message can be sent by the usual classical channel.

The first QKD protocol date back to 1984 and is due to C.H. Bennet and G. Brassard, hence the name BB84 [19]. The protocol was implemented by using photon polarization, but other properties of any quantum objects, such as the spin of an electron, can be used. In BB84 Alice and Bob have two possible basis to choose: either horizontal and vertical polarization ($|0°\rangle, |90°\rangle$) or diagonal polarization ($|-45°\rangle, |+45°\rangle$). Alice will pick up one of the two basis and send the message and Bob will randomly choose one of the two basis to read it. Every time Alice and Bob will select different basis, they will obtained uncorrelated measurements. At this point, both Alice and Bob declare through a public channel which basis they took for each qubit of a fraction of the original message. They can thus discard the qubits for which they used different basis. The remaining bits will then form the *sifted key*, that has an error of about 50% since they will choose half of the times the same basis. Let us now consider the case where an eavesdropper intercept the message coming from Alice and resend it to Bob after having measured the polarization through one of the two possible basis (intercept-resend strategy). Eve will use the same basis of Alice about 50% of the times and Bob will choose half of the times Eve's basis. So, finally, the error on the sifted key will decrease to 25% and Alice and Bob will be able to detect the presence of Eve. They will thus discard the process before the key is established.

Another version of the BB84 protocol based on entangled photons was proposed in 1991 by A.K. Ekert [122]. In the past years (and till now) many new protocols based the BB84 and Ekert ideas were proposed in order to optimize their implementation and we refer the interested reader to [123, 18].

As we have seen, many different technologies have been explored for implementing quantum information technologies. However, in the last ten/fifteen years, great attention has been given to *photonics* [98, 123, 17]. Indeed, realizing qubits by using photons characteristics, such as polarization, is very interesting due to their long coherence times. Moreover, photons seem to be the natural choice for quantum communication, as they can travel long distances through either atmosphere or optical fibers with very low environmental noise level. However, one major drawback of this technology is given by the need of interactions between photons for universal multi-qubit control. Indeed, these interactions require optical nonlinearities stronger than those available in conventional nonlinear media and cavity quantum electrodynamics (QED) was employed to increase the atom-photon interaction [124]. However, in 2001, Knill, Laflamme and Milburn proved that scalable quantum computing is possible by using only single-photon sources and detectors, and linear optical circuits (KLM scheme) [125]. Their scheme is based on quantum interference with the use of auxiliary photons at beam splitters and single-photon detection to induce interactions non-deterministically.

In the last years, the advances made in the nonlinear optics field have made

possible to generate both single- and entangled-photon states through nonlinear parametric processes. In fact, when a strong pump laser field is injected into a nonlinear medium, a photon pair could be generated by the nonlinear process, and the two photons could be either in an entangled or in a single photon state. Another big advantage of photonics is that the components of the system used in the laboratory, such as beam splitters, mirrors, phase shifters and so on, can be easily integrated on a chip, that is a key property for moving a technology into the industry world [126, 127]. Ideally, all the steps needed for quantum experiments would be integrated on a single chip [128], even if the major issues of integrating both single-photon detectors and a laser source have to be solved. For sure, the ability of integrating the source of nonclassical states of light and the needed filters is already a big step forward over the use of bulk optical setups [37]. Regardless of the technology used for building photonic chips and the approaches used for photons sources and detectors, losses remain a significant challenge for this kind of technology and are comparable to the decoherence issue in solid-state qubits. Usually, integrated waveguides have losses of about 0.1 dB cm^{-1} and current photonic circuits use about 1 cm per logic gate [129, 130].

Because of the development of photonic technologies and due to the need of transferring quantum states over long distances, different experiments have been performed in the field of quantum communication and distributed quantum networks. In this framework, great importance is given to the distribution of entangled particles over large distances. The obtained results are essential not only for quantum communication protocols [122], but also for quantum teleportation [131, 132] and quantum networks [133]. However, usually, this kind of experiments is limited by the noise of the single-photon detectors and the absorption along the quantum channel, that is usually an optical fiber [134].

Different ways have been studied to overcome this problem, for example by dividing a long distance in small parts and employing quantum repeaters. Nevertheless, the realization of such a technology is experimentally challenging [135, 136]. Another option is given by connecting a Earth-orbit satellite to a ground station, thus employing free space as linking channel [137, 138]. Global QKD is then obtained by exchanging quantum keys between the satellite and various ground stations, thus enabling the use of secret keys between two random ground stations [139]. In this way, in principle, it would be possible to transfer quantum states among very distant location on the Earth, even if they are separated by thousands of kilometers. In fact, the traveling photons would experiment turbulence and losses in the 10 km of the atmosphere closest to the Earth. Then the transmission is almost in vacuum with zero absorption and decoherence. At this purpose, many experiments have been carried out. Free-space distribution of entangled photons was first demonstrated over a distance of 600 m [140] and 13 km [141]. Triggered single photons were transmitted over a one-link free-space channel of 144 km [142] and quantum

teleportation over 16 km in free space was achieved in 2010 [143]. Then, in 2012 the group of J.-W. Pan experimentally proved the quantum teleportation of independent qubits over a one-link free-space channel of 97 km [144]. In the same experiment, the distribution of entangled photons over a two-link channel was achieved with an almost 102-km-long separation of the two photons. Few months later, this record was broken by the Austrian group of A. Zeilinger [145]. In this experiment, quantum states were successfully transmitted over a distance of 143 km, between the two Canary Islands of La Palma and Tenerife. Finally, very recently, the satellite Micius was launched from Jiuquan in China to an altitude of about 500 km. This satellite is dedicated to quantum science experiments [6]. Three ground stations located in Delingha, Nanshan and Lijiang (Gaomeigu Observatory) were chosen for the experiment. The physical distances of the ground stations are 1203 km (Delingha-Lijiang) and 1120 km (Delingha-Nanshan), whereas the separation between the satellite and each ground station goes from 500 km to 2000 km. In the experiment, a periodically poled $KTiOPO_4$ crystal, inside a Sagnac interferometer, was pumped by a CW laser diode with a central wavelength of 405 nm and linewidth of about 160 MHz. The pump is split by a polarizing beam splitter in order to pass through the crystal both in clockwise and anticlockwise directions, simultaneously. In turn, down-converted photon pairs in polarization-entangled states are generated at a wavelength of about 810 nm. In the experiment, the group of J.-W. Pan proved entanglement through a Bell test, between two photons at a distance of 1203 km [6]. This experiment has been a real breakthrough for QKD and quantum teleportation and paves the way to new quantum communication and quantum optics experiment at distances that were, until now, inaccessible on the ground.

In this thesis we will focus in particular on integrated sources of entangled photons for quantum applications. Since we will mainly deal with photonics, our results can be framed in the context of quantum communication and metrology. Many different platforms are currently used for producing chips employed for quantum photonics applications.

For example, gallium arsenide (GaAs) allows for the fabrication of low-loss waveguides. Light can be confined in tight regions due to the high refractive index of this material, allowing for the production of compact circuits and devices. Due to its large electro-optic effect, GaAs is a very promising platform for single photons fast routing and manipulation. Moreover, two ways can be used to emit single photons in this material. First, taking advantage of its high $\chi^{(2)}$ nonlinearity, spontneous parametric down conversion in waveguides can be exploited [146]. Second, on-demand nonclassical light sources, that are single quantum dots (QDs), can be directly integrated in nanophotonic structures [147, 148]. Finally, even single-photon detectors on GaAs waveguides have been demonstrated [149], making GaAs waveguides circuits very promising

for the construction of quantum photonic integrated circuits. For a complete review on GaAs integrated quantum photonics we refer the reader to [150].

Another possible platform for building integrated photonic circuits is silicon nitride (Si_3N_4). Here, circuits based on Si_3N_4 waveguides can directly incorporate GaAs nanophotonic devices containing self-assembled QDs. Then, the passive Si_3N_4 waveguide-based circuit can be used for distribution, low-loss routing and interference of light across the chip [151]. Moreover, even Si_3N_4 microring resonators can be directly used as on-chip sources of light [152].

Another appealing platform for quantum photonics is diamond. In fact, diamond is host to different color centers [153] that can be individually integrated through ion implantation. In particular, the negatively charged NV centers are very interesting for implementing the qubit in quantum applications due to their spin readout, ease of manipulation and long coherence time. Usually, NV centers require the use of cavity quantum electrodynamics (CQED), where the single-photon spontaneous emission rate can be controlled through a photonic cavity that enhances the interaction strength between the NV center and the single optical mode. Particularly, among the employed photonic cavities, it is important to mention photonic crystal cavities, which provide very strong enhancement because of their small volumes. Moreover, they have already been widely studied in the context of light-matter interaction with QDs [154].

Finally, even silicon-based photonic circuits play a crucial role in the construction of integrated sources of quantum states of light. The main advantage of the silicon platform is the production of systems that are easily reproducible by industrial processes. This is the reason why in this work we will focus on silicon-based photonic systems, as it will be described in detail in the next section.

1.2 Silicon photonics

As already explained in Sec. 1.1.1, photonics is a very promising field for the production of nonclassical states of light needed for many quantum applications. However, in order to translate quantum technologies into real applications, the features of compactness, scalability and compatibility with the integration on an electronic chip are required. For this reason, in the last decades the necessity of integrating photonic structures on a chip has become of pivotal importance.

Silicon photonics has then turned into one of the leading technological solutions for the production of integrated-photonic circuits not only for the development of quantum applications. Indeed, the interest in silicon photonics has grown for solving some technological problems such as high performance computing, optical communications (telecom/datacom), optical sensors, and on-chip optical interconnects.

The reasons why silicon has overcome other platforms are that chips made

of this material are cheap, easy to fabricate and can be densely integrated. This is mainly due to the compatibility to the traditional complementary metal-oxide-semiconductor (CMOS) fabrication process that dominated the microelectronic industry in the last 40 over years. Indeed, the field of silicon photonics has benefited from the billions of dollars invested in the CMOS fabrication, allowing for a high level of integration. With this technology, devices that modulate, detect, route and filter light can all be co-located on the same wafer and built using the same tools.

In order to lower the fabrication costs and making them available even at the small scale, the foundry services already in use for the development of microelectronic circuits plays a crucial role. In the fabs, once a silicon photonic model is in place, multi-project wafers (MPW) shuttle runs can be organized to reduce overheads associated with chip fabrication through the sharing of photomask and wafer processing costs. In the electronics industry, this is well illustrated by MOSIS [34], an organization that provides MPW services from various commercial semiconductor foundries for electronic circuit design and innovation. Indeed, even for silicon photonics, a number of institute around the world are offering foundry services in order to lower the fabrication costs. These services are offered, for example, by the A*STAR Institute of Microelectronics (IME) in Singapore, AIM Photonics [155] in the USA and, in Europe, by IMEC and CEA-LETI [35].

Another motivation on the choice of silicon for the production of photonic circuits, is the availability of high-quality silicon-on-insulator (SOI) wafers, that is an ideal platform for creating planar waveguide circuits. SOI wafers usually consist of about either 220-nm-thick or 300-nm-thick silicon guiding layer on top of a silicon oxide substrate of about 2 μm of thickness. All the components of the photonic circuit are realized on the top of the guiding layer through lithography and etching processes, as it will be described in detail in the next chapters for each sample used.

The strong optical confinement offered by the high index contrast between silicon ($n_{Si} = 3.48$ at 1550 nm) and its oxide (usually, $n_{SiO_2} = 1.44$ at 1550 nm) or air ($n = 1$), that constitute the cladding, makes it possible to scale photonic devices to the hundreds of nanometer level, allowing for a high-integration level. Indeed, in the case of a silicon core embedded in silica, the high refractive index contrast, which we define as $\Delta n \equiv n_{core} - n_{clad} \approx 2$, allows a total internal reflection with a very large incident angle of 60° [36].

Besides the above arguments in favor of silicon photonics, it is also worth to mention that silicon has also excellent material properties that are important in photonic devices. Indeed, silicon has high thermal conductivity, high optical damage threshold and high third-order optical nonlinearities. However, it is also important to mention that the main limiting factor in silicon devices when high powers applications are needed is the onset of the TPA process. Moreover, silicon is an excellent material in the midwave IR spectrum (1.3 to 1.55 μm), having a low-loss window extending from 1.1 μm to nearly 7 μm, as shown in

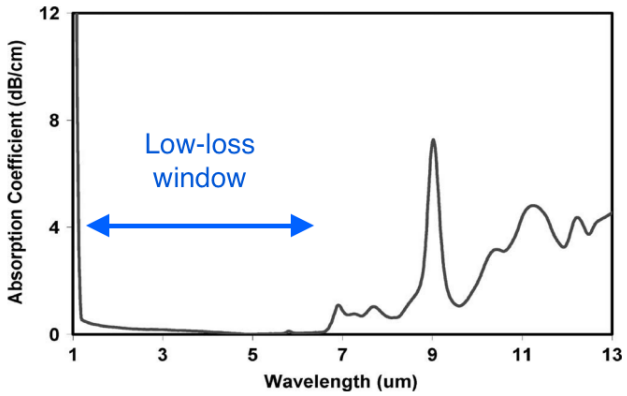

Figure 1.2: Linear absorption in silicon. Silicon has a low-loss window extending from 1.1 μm to nearly 7 μm, making it an excellent material in the midwave IR spectrum.

Fig. 1.2 [156].

In this section we will first describe the nonlinear process through which it is possible to generate photons in silicon, that is the four-wave mixing process. Then, we will describe in details the main photonic structures that can be integrated on a chip. We will focus on waveguides, distributed Bragg reflectors (or Bragg waveguides) and microring resonators, since they will be the leading subject of this thesis.

1.2.1 Nonlinear optics

Nonlinear susceptibility

The field of *nonlinear optics* studies phenomena that occur as a consequence of the modification of the optical properties of a material system by the presence of sufficiently intense light (laser light). The word *nonlinear* means that the optical phenomena occur when the response of a material system to an applied optical field depends in a nonlinear manner on the strength of the optical field.

In order to describe optical nonlinearities it is necessary to consider the dependence of the polarization vector $\mathbf{P}(\omega)$ of a material system on the strength $\mathbf{E}(\omega)$ of an applied optical field that propagates in the medium.
In usual *linear* optics, the induced polarization $\mathbf{P}(\omega)$ depends linearly on the electric field strength $\mathbf{E}(\omega)$ and we can write:

$$\mathbf{P}(\omega) = \epsilon_0 \chi(\omega) \mathbf{E}(\omega), \tag{1.10}$$

where ϵ_0 is the permittivity of vacuum and χ is the linear susceptibility.

However, in any real atomic system, the electric field propagating in the medium induces a polarization that is not exactly proportional to the field strength. So, in *nonlinear* optics, if the electric field $\mathbf{E}(\omega)$ is sufficiently small

and assuming that the medium response is instantaneous, Eq. (1.10) can be generalized to the following expression:

$$P_i = \epsilon_0 \left(\sum_j \chi_{ij}^{(1)} E_j + \sum_{jk} \chi_{ijk}^{(2)} E_j E_k + \sum_{jkl} \chi_{ijkl}^{(3)} E_j E_k E_l + \dots \right), \tag{1.11}$$

where ϵ_0 is always the vacuum dielectric constant as for Eq. (1.10), and $\chi_{ij}^{(1)}$, $\chi_{ijk}^{(2)}$ and $\chi_{ijkl}^{(3)}$ are the first-, second- and third-order nonlinear susceptibilities of the medium, respectively. $\chi_{ij}^{(1)}$, $\chi_{ijk}^{(2)}$ and $\chi_{ijkl}^{(3)}$ are tensors of second, third and fourth rank and the indexes i, j, k, l represent the components along a generic axis. The nonlinear optical susceptibilities observe the following symmetry relations:

$$\chi_{ijk} = \chi_{ikj}, \qquad \chi_{ijkl} = \chi_{i[kjl]}, \tag{1.12}$$

where $[kjl]$ indicates any permutation of the indexes k, j, l.
The nonlinear components in Eq. (1.11) decrease quickly, and higher-order terms can be neglected. Indeed, we can write [39]:

$$\left| \frac{P_i^{(n+1)}}{P_i^{(n)}} \right| \approx \left| \frac{E}{E_{at}} \right|, \tag{1.13}$$

where E_{at} is the characteristic atomic field strength, that is usually of the order of 10^{10} Vm^{-1}. Now, considering a field $E \sim 10^5$ Vm^{-1}, it can be seen that the high-order terms in Eq. (1.11) are very weak, since each term is roughly five orders of magnitudes smaller that the previous one [40].

In Eq. (1.11), the term $\chi^{(1)}$ gives the linear response of the dielectric medium and is the linear susceptibility of Eq. (1.10): the model can be reduced to that of the harmonic oscillator and the polarization is proportional to the intensity of the electric field.
The following terms in Eq. (1.11) are important when the intensity of the incident beam is such that the electrons in the medium start to feel the anharmonicity of the potential. In particular, in $\chi^{(2)}$, the polarization is proportional to the square of the electric field. The second-order nonlinearity is responsible for many effects. For example, second-harmonic generation (SHG), in which two photons at the same frequency interact with the nonlinear medium and generate a photon with twice the energy of the initial pair. Parametric down-conversion (PDC), where one photon is converted into two photons of lower energy. Optical parametric amplification (OPA), in which two photons enter the the nonlinear medium and one of them is amplified at the output through the creation of a second photon. Sum- and difference-frequency generation (SFG and DFG), where two pump photons generate another photon with the sum or difference of the energies of the pump beams. The second-order nonlinearity is different from zero only in noncentrosymmetric crystals (i.e. crystals with no inversion symmetry). In fact, for symmetry reasons, in centrosymmetric media, a change in the sign of the electric field would produce a change in

the sign of the polarization. So, from Eq. (1.11), it should be:

$$\chi^{(2)}_{ijk} E_j E_k = -\chi^{(2)}_{ijk} \left(-E_j\right) \left(-E_k\right), \tag{1.14}$$

that can be satisfied only when $\chi^{(2)}_{ijk} = 0$. This is the case of silicon, that crystallizes in a centrosymmetric diamond cubic structure and thus not producing second-order nonlinear optical interactions.
The $\chi^{(3)}$ term becomes then the first useful nonlinear component in centrosymmetric crystals and is responsible for many phenomena. Few examples are: third-harmonic generation (THG), in which three photons are destroyed, creating a single photon at three times the frequency of the input laser beam, optical Kerr effect, that can be described as a modification of the refractive index of the nonlinear medium due to a high-intensity light beam propagating in the system, four-wave mixing (FWM), in which two pump photons are annihilated in the medium and two other photons are created following the energy-conservation law.
For a more detailed description of the nonlinear properties of a medium we refer to [39, 40, 41].

General third-order nonlinear optical process

In the experiments described throughout this work, we will deal only with processes related to $\chi^{(3)}$. So, following the arguments in [40], let us now focus on a generic third-order nonlinear process.
Consider the simple case in which the applied field is monochromatic and is given by the following expression:

$$\mathbf{E}\left(t\right) = E_\omega \cos\left(\omega t\right). \tag{1.15}$$

From Eq. (1.11), the third-order contribution to the polarization is given by:

$$\mathbf{P}^{(3)}\left(t\right) = \epsilon_0 \chi^{(3)} \mathbf{E}^3\left(t\right). \tag{1.16}$$

Since $\cos^3\left(\omega t\right) = \frac{1}{4}\cos\left(3\omega t\right) + \frac{3}{4}\cos\left(\omega t\right)$, Eq. (1.16) can be written as:

$$\mathbf{P}^{(3)}\left(t\right) = \frac{1}{4}\epsilon_0 \chi^{(3)} E^3_\omega \cos\left(3\omega t\right) + \frac{3}{4}\epsilon_0 \chi^{(3)} E^3_\omega \cos\left(\omega t\right). \tag{1.17}$$

The first term in Eq. (1.17) describe the THG process, in which three photons at a frequency ω are annihilated to create a photon at frequency 3ω. Instead, the second part of the equation describes a nonlinear contribution to the polarization at the frequency of the incident radiation ω. This term leads to a nonlinear contribution to the refractive index experienced by a wave at frequency ω and we can write:

$$n = n_0 + n_2 I, \tag{1.18}$$

where $I = \frac{1}{2} n_0 \epsilon_0 c E_\omega^2$ is the intensity of the incident field, n_0 is the linear (or low-intensity) refractive index and n_2 is an optical constant that characterizes the strength of the nonlinearity and is given by:

$$n_2 = \frac{3}{2 n_0^2 \epsilon_0 c} \chi^{(3)}. \tag{1.19}$$

The constant n_2 is usually referred to as *Kerr coefficient* and is due to the *optical Kerr effect*.

As explained above, silicon has a diamond cubic crystal structure and does not have the second-order nonlinearity. However, it has a large third-order nonlinearity with respect to other materials. Indeed, silicon exhibits a Kerr coefficient that is 10^2 bigger than silica glass at the telecommunication wavelengths, being $n_{2,Si} = 4.5 \times 10^{-14}$ cm^2 W^{-1} [157] and $n_{2,SiO_2} = 2.2 \times 10^{-16}$ cm^2 W^{-1} [158] at 1.55 μm, allowing efficient nonlinear interaction at relatively low power. For this reason, few-centimeters-long SOI-based waveguides are extensively studied for processes based on the third-order nonlinear susceptibility, among which THG [159, 160] and FWM [161, 162, 44, 46] can be found.

However, there are two major drawbacks for silicon waveguides. First, even if larger than in other materials, the Kerr coefficient for systems that exhibit the third-order nonlinearity is still quite low and of the order of $n_2 \sim 10^{-14}$ cm^{2}W^{-1}, requiring the adoption of smart strategies in order to confine the field and thus enhancing the light-matter interaction [157]. Second, silicon nonlinear processes suffer from the presence of the undesired TPA effect [163], consisting in the creation of a free electron-hole couple due to the absorption of two photons exceeding half of the band-gap energy $E_g = 1.2$ eV, that in silicon corresponds to a wavelength of about 1.1 μm.
The two-photon transition in an indirect gap material, such as silicon, is phonon mediated. The TPA effect leads to changes in the refractive index and susceptibility of the material, due to free-carriers absorption by the electrons promoted in the conduction band, and represents the nonlinear losses. Thus, if we write the complex dielectric function as $\epsilon(\omega) = \alpha + i\beta$, the TPA process represents the imaginary part of $\epsilon(\omega)$, whereas the Kerr effect (and thus n_2) is described by the real dispersive part of $\epsilon(\omega)$ [164].

Four-wave mixing

We will now focus on one of the possible third-order nonlinear effects observed in silicon, that is FWM. This process will be the main theme of this thesis.
So, let us now consider again Eq. (1.11). This expression can couple fields with different amplitudes and frequencies. For the case of interest, we can consider only the third term of the Taylor expansion (1.11) that we report here for convenience:

$$P_i^{(3)} = \epsilon_0 \sum_{jkl} \chi_{ijkl}^{(3)} E_j E_k E_l. \tag{1.20}$$

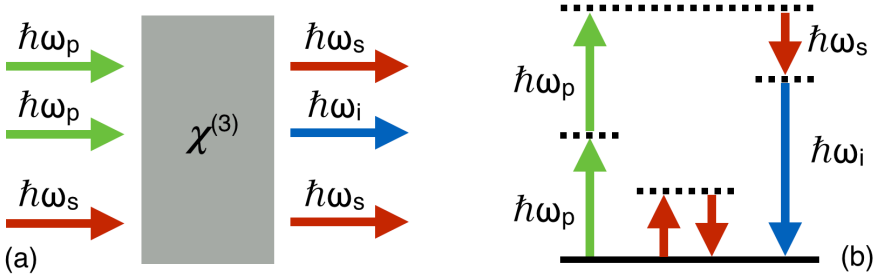

Figure 1.3: Stimulated four-wave mixing (FWM) process. Two pump photons and a signal photon at energies $\hbar\omega_p$ and $\hbar\omega_s$, respectively, enter the nonlinear medium. The signal photon is not directly involved in the transition and is found again at the output, whereas the two pump photons are converted in an idler ($\hbar\omega_i$) and signal ($\hbar\omega_s$) photon pair. (a) Schematic view of the stimulated FWM process. (b) Energy diagram of the stimulated FWM process.

From Eq. (1.20), we can observe that four fields with different frequencies can interact each other. One particular case, the degenerate FWM (DFWM), consists in the situation where two of the incoming fields have the same frequency. So, the polarization oscillates at a frequency $2\omega_2 - \omega_3$ and we can write:

$$P\left(2\omega_2 - \omega_3\right) \propto \chi^{(3)} E_{\omega_2}^2 E_{\omega_3}. \tag{1.21}$$

In Fig. 1.3, a representation of the DFWM, called *stimulated* FWM in this case, is given. Here, three incoming fields, two of them called *pump* and at a frequency ω_p and the other one called *signal* at a frequency ω_s propagate in the nonlinear medium. These waves couple to the $\chi^{(3)}$ term in the susceptibility and generate a new wave, called *idler* at a frequency ω_i. So, Eq. (1.21) can be written as:

$$P\left(\omega_i\right) \propto \chi^{(3)} E_{\omega_p}^2 E_{\omega_s}. \tag{1.22}$$

In the FWM process energy and momentum are conserved:

$$2\omega_p = \omega_i + \omega_s, \tag{1.23}$$

$$2\mathbf{k}_p = \mathbf{k}_i + \mathbf{k}_s. \tag{1.24}$$

The DFWM, as defined above, will be considered from now on in this work.

As shown in Fig. 1.4, the FWM process can also be seen as a four-photon nonlinear scattering initiated by vacuum fluctuations. In the interaction, two incoming fields (*pump*) at a frequency ω_p are converted in a photon pair (*idler* and *signal*) at a frequency ω_i and ω_s, respectively. In this case we talk about *spontaneous* FWM (SFWM), since the incoming field at ω_s is no longer present. As in a general quantum system (e.g. an atom or a molecule) stimulated emission is the classical counterpart of spontaneous emission [165], the same happens for FWM. Indeed, while the stimulated FWM process can be described in a classical way, SFWM requires a fully quantum theory in order to be understood.

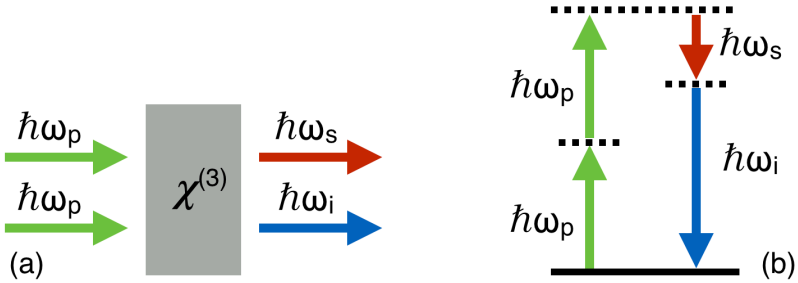

Figure 1.4: Spontaneous four-wave mixing (SFWM) process. It can be seen as a four-particle scattering, where two pump photons at energy $\hbar\omega_p$ are converted in an idler ($\hbar\omega_i$) and signal ($\hbar\omega_s$) photons. (a) Schematic view of the SFWM process. (b) Energy diagram of the SFWM process.

DFWM is part of a class of processes defined as *parametric* processes, in which the initial and final quantum-mechanical states of the system are identical. This means that, in a parametric process population can be removed from the ground state only for those brief intervals of time when it resides in a virtual level ($\delta t \sim \hbar\delta E$, where δE is the energy difference between the virtual level and the nearest real level). Conversely, processes that do involve the transfer of population from one real level to another are known as *nonparametric* processes.
Parametric processes can always be described by a real susceptibility and the photon energy is always conserved, whereas nonparametric processes are described by a complex susceptibility and energy need not be conserved because it can be transferred to or from the medium.

As a simple example to discriminate between parametric and nonparametric processes, we can consider the case of the linear index of refraction. Its real part describes a response that occurs as a consequence of parametric processes. The imaginary part, instead, occurs as a consequence of nonparametric processes, since it describes the absorption of radiation, which results from the transfer of population from the atomic ground state to an excited state.

1.2.2 Silicon photonic devices

In this section we will describe the main photonic structures we will use for the experiments of this work, that are silicon waveguides, distributed Bragg reflectors (DBRs) or Bragg waveguides (BWs) and microring resonators. We will also describe the FWM process for each structure.

Waveguides

The first structure is worth describing is the silicon waveguide. This is the building block of integrated photonic circuits, since many structures can be derived from a simple waveguide.

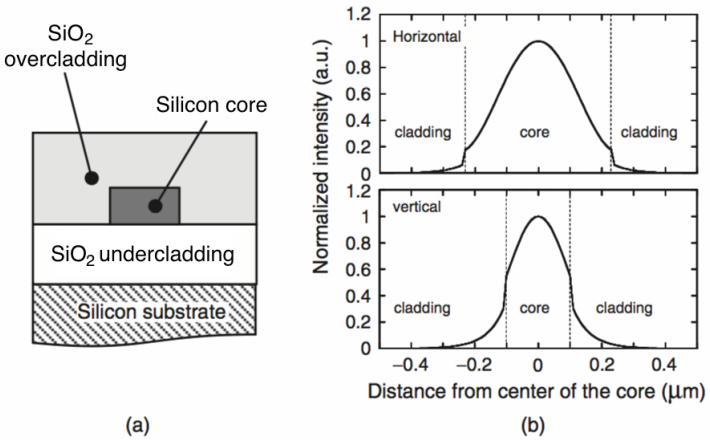

Figure 1.5: (a) Cross-sectional view of a silicon wire waveguide. (b) Optical intensity distribution along the horizontal and vertical directions of a typical silicon wire waveguide.

So far, two main types of silicon waveguides have been considered in integrated photonic circuits: rib waveguides, which have core dimensions of a few micrometers [166, 167] and wire (or ridge) waveguides, with core dimensions of several hundreds of nanometers [168, 169, 170, 171]. Silicon wire waveguides are especially promising because their ultra-small core dimensions and micrometer bending sections match the dimensions of electronic circuits, being very suited for electronic-photonic convergence.

In SOI-based waveguides, light is channeled through transverse and lateral confinement in a silicon core ($n_{Si} = 3.48$ at 1550 nm) surrounded by a silicon oxide (usually silica) bottom cladding ($n_{SiO_2} = 1.44$ at 1550 nm) and a low index top cladding (usually, silica or air). A scheme of a silicon photonic wire waveguide is shown in Fig. 1.5, with its optical intensity distribution along the horizontal and vertical directions [36].

The core dimension should be determined so that a single-mode condition (for one polarization at a wavelength of 1550 nm) is fulfilled. Moreover, the high index contrast between the core and the cladding gives rise to very strong confinement which enables light-guiding in bends with very small radii without radiation losses. In order to accomplish the single-mode condition with a high refractive index contrast, the waveguide's cross section must be reduced, to the submicrometer scale. In particular, the waveguide's dimensions have to be of the order of $(\lambda/n_{core})^2$, where λ is the wavelength of light in vacuum and n_{core} is the refractive index of the waveguide core. With the current SOI technology it possible to fabricate wire waveguides in which light is confined in a region of area below 1 μm^2. The common dimensions for a silicon wire waveguide, for very high index contrasts (e.g. silicon to air or silicon to silica), is between 400 nm and 500 nm in width and with an height between 200 nm and 250 nm when operating at telecom wavelengths (between 1.3 μm and 1.6 μm) [169, 172, 173, 174].

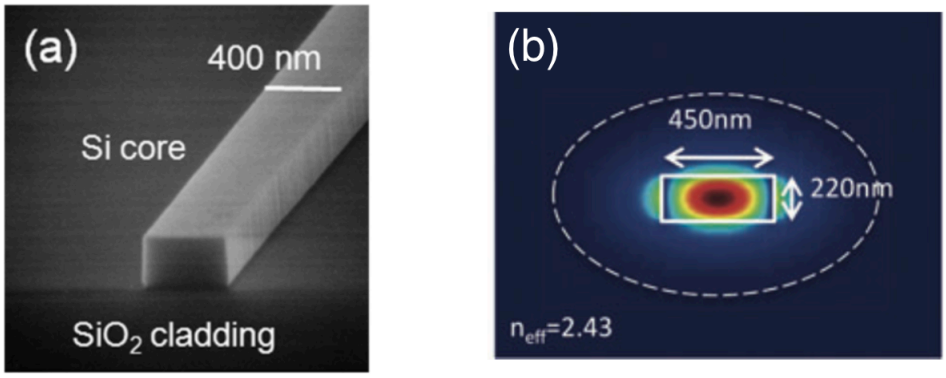

Figure 1.6: (a) SEM image of a typical silicon wire waveguide 400-nm wide [36]. (b) Cross-sectional view of the TE-mode profile propagating in a 450-nm wide and 220-nm tall silicon wire waveguide embedded in silica. The effective index determined the simulation is $n_{eff} = 2.43$ [38].

A SEM image of a typical silicon wire waveguide is presented in Fig. 1.6 (a) [36], along with the cross-sectional view of the transverse electric (TE) mode profile propagating in a 450-nm wide and 220-nm tall silicon wire waveguide embedded in silica (b) [38].

In order to analyze the guided modes of a silicon wire waveguide, different numerical methods can be used, such as the finite difference method (FDM) [175], finite element method (FEM) [176] and film mode matching method (FMM) [177]. In Fig. 1.7, the calculated (FMM) effective indexes n_{eff} of guided modes for IR light at a wavelength of 1550 nm as a function of the core width are shown for two different core thicknesses (200 nm in (a) and 300 nm in (b)). E^x and E^y represent the TE-like and transverse magnetic (TM)-like modes, respectively. As can be promptly seen from Fig. 1.7, in the case of a 200-nm-thick waveguide, the single-mode condtion is fulfilled for a core width less then 460 nm for TE-like propagating mode. This explain the common dimensions of silicon wire waveguide as mentioned above.

In silicon wire waveguides the large index contrast causes the waveguide dispersion to dominate over intrinsic material dispersion. So, the effective index of the propagating mode will depend on the wavelength, that means that pulses of light at distinct wavelengths will travel at different velocities along the wire waveguide. In particular, in crystalline silicon at the telecom wavelengths ($\sim$1.55 μm) the index of refraction increases for decreasing wavelength ($\frac{\partial n_{eff}}{\partial \lambda} < 0$) and one can speak about *normal* dispersion. However, due to high modal confinement in SOI waveguides, the waveguide dispersion can counteract the effect of the normal material dispersion and allow the waveguide to operate in an *anomalous* regime [178].

For photon energies below the band gap ($\sim$1.1 eV), the intrinsic loss in silicon is very low. Then, the propagation loss of silicon wire waveguides are mainly due to scattering caused by the surface roughness of the core [179] and

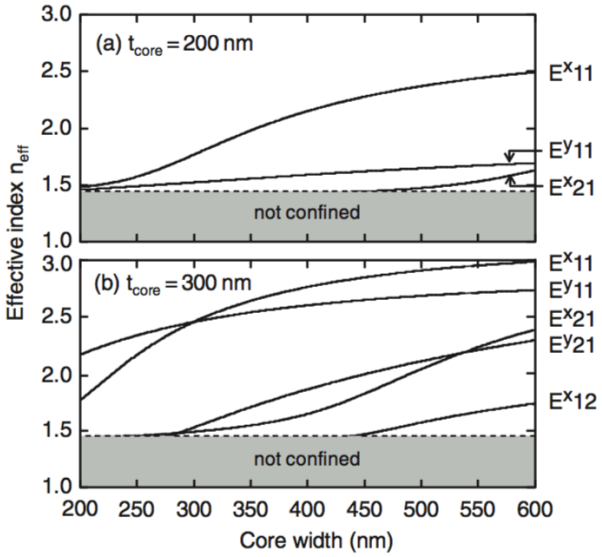

Figure 1.7: Dependence of the effective indexes of a silicon wire waveguide on the core width for a core thickness of (a) 200 nm and (b) 300 nm, at 1550 nm. E^x and E^y stand for the TE-like and TM-like modes, respectively.

can go down to 2-3 dB cm^{-1} for air cladding and less then 2 dB cm^{-1} when the cladding is made of silicon oxide [38]. Propagation losses of 0.4 dB cm^{-1} in the C-band has been demonstrated in [171] by using high-resolution lithography technology to fabricate the waveguide. The strongest effect of scattering losses is considered to be due to the sidewall roughness and it is unavoidable because of the lithography fabrication process [38].
Another source of loss can be the substrate leakage, that is light can be coupled to radiative modes in the substrate. These leakages decrease exponentially with the thickness of the bottom cladding and, for a usual 2-μm-thick bottom cladding layer, they are negligible for the TE-like mode and of the order of 0.001 dB cm^{-1} for the TM-like mode [38].
Because of the high refractive index contrast in SOI-based wire waveguides, it is possible to make very sharp bends, up to a radius of 3 μm, with still low radiations. However, the waveguide bending could influence both substrate leakage and scattering losses. In a 500-nm-wide SOI waveguide, bending losses are measured to be 0.01 dB/90° for a 4.5-μm bend, up to 0.071 dB/90° for a radius of 1 μm [180]. Moreover, it is worth to mention that at high bending radii (< 5 μm) the dominant contribution to the losses is due to the mismatch losses at the straight-bend transition. This is particular important when dealing with recetrack resonators. Indeed, transition losses are responsible for higher round-trip losses in racetrack resonators compared to microring resonators.
Finally, for high powers, the contribution of TPA and free-carrier absorption can add to the nonlinear absorption [38].

Different devices can be realized starting from a simple silicon wire waveg-

uides, such as Y-branches, directional couplers, distributed Bragg reflectors, devices to couple light in and out of a waveguide, microring resonators and so on. We will give here an overview of the main elements we will use in the next chapters.

One of the major problems of silicon photonic integrate circuits is to couple light between a single-mode optical fiber and a sub-micron waveguide on a chip. In this sense it is very important to reduce the coupling losses as much as possible in order to perform measurements that involve small signals. Because of the strong confinement of the guided mode in the waveguide core, that is few-nanometers thick, there is a large mismatch between the mode of the waveguide and the mode of the single-mode fiber. As it will be detailed in Sec. 2.1 and Sec. 3.1.1, when the sample we used in the experiments will be thoroughly described, there are two main strategies to solve the problem of coupling light in and out of a chip: edge couplers and grating couplers.
In order to obtain edge coupling the highly confined mode (mode diameter < 1 μm) of the waveguide has to be broadened, so it can be supported by an external optical fiber (mode diameter of about 10 μm) and, vice versa, the optical fiber mode has to be shrunk to fit the waveguide mode. On the fiber side this can be done by using lensed optical fibers, whereas on the waveguide edge an adiabatic taper can be used. With this coupling method the fiber-to-waveguide insertion loss can reach 1 dB at the telecom wavelengths [181]. Unfortunately, this method is very sensitive to alignment and forces to couple light at the chip edges only.

Grating couplers are made by expanding the width of one side of the wire waveguide and etching a grating that diffracts light out of the plane into a fiber placed in the vertical direction, almost orthogonal to the chip. The losses of the grating couplers we will use are around 3 dB each grating, even if lower insertion loss values have been measured [182, 183]. The advantage of grating couplers is that they can be placed anywhere on the chip, they do not require the polishing of the facets and they facilitate the alignment process. However, the main drawback that can be meet in some applications is the limited bandwidth (few tens of nanometers) of grating couplers.

Even distributed Bragg reflectors and microring resonators can be obtained starting from a wire waveguide, and will be described in detail later in this section.

Let us now outline the FWM process in a SOI wire waveguide. Consider again Fig. 1.3, where two pump photons at a frequency ω_p and a signal photon at a frequency ω_s propagate in the waveguide. Because of the $\chi^{(3)}$ nonlinearity, an idler photon at a frequency $\omega_i = 2\omega_p - \omega_s$ is generated. The energy and momentum are conserved and Eqs. (1.23), (1.24) still hold. Since part of the optical power injected into the waveguide is found at the output at the idler frequency, DFWM is in general considered as a frequency-conversion experiment. This implies that the pump is much more intense than the signal and

idler fields:

$$|E_p| \gg |E_s| \gg |E_i|, \tag{1.25}$$

where $E_j = A_j \exp\left[i\left(k_j z - \omega_j t\right)\right]$, with $j = p,\ s,\ i$, are field propagating in the z direction with polarization orthogonal to the propagation direction. Then, induced effects as the depletion of the pump and self-phase modulation and cross-phase modulation of the generated idler and signal beams can be neglected. By ignoring phonon-induced nonlinearities due to Raman scattering effects, the fields E_p, E_s and E_i satisfy the following equations [39, 164]:

$$\frac{\partial A_p\left(z\right)}{\partial z} = \left(j\beta_p - \frac{\alpha_p}{2}\right) A_p\left(z\right), \tag{1.26}$$

$$\frac{\partial A_s\left(z\right)}{\partial z} = \left(j\beta_s - \frac{\alpha_s}{2}\right) A_s\left(z\right) + \gamma A_p^2\left(z\right) A_i^*\left(z\right), \tag{1.27}$$

$$\frac{\partial A_i\left(z\right)}{\partial z} = \left(j\beta_i - \frac{\alpha_i}{2}\right) A_i\left(z\right) + i\gamma A_p^2\left(z\right) A_s^*\left(z\right), \tag{1.28}$$

where $A_p\left(z\right)$, $A_s\left(z\right)$ and $A_i\left(z\right)$ are the complex amplitudes for the pump, signal and idler propagating fields, respectively; β_p, β_s and β_i are the longitudinal propagation constants of the waveguide mode at each frequency; α_p, α_s and α_i are the propagation loss coefficients and γ is the waveguide nonlinear coefficient, which gives the strength of the interaction between the pump and signal fields in order to generate the idler and is a linear function of the real part of the third-order nonlinear susceptibility. In deriving Eqs. (1.26)-(1.28), we have disregarded all the terms related to the imaginary part of the third-order nonlinear susceptibility. We also assumed to be in the CW or quasi-CW regime and to have a sufficiently low pump power so effects of TPA-generated free carriers will not affect the FWM generation efficiency [164]. The last term in Eqs.(1.27) and (1.28) describe the FWM interaction: both the idler and signal fields depend quadratically on the pump amplitude and linearly on the signal and idler fields, respectively. Finally, $P_p = |A_p|^2$, thus it is proportional to the intensity of the pump beam.

From Eqs. (1.26), (1.27) and (1.28), the phase mismatch of the interacting waves can be written as:

$$\Delta k = 2k_p - k_s - k_i. \tag{1.29}$$

Let us finally remark that the energy-conservation law given in Eqs. (1.23), (1.24), requires that two pump photons annihilate in order to create an idler-signal pair. So, as depicted in Fig. 1.3, the signal field in only needed for stimulating the interaction, but it is not directly involved in the transition. A measurement of FWM in a silicon wire waveguide can be found in [184].

Distributed Bragg Reflectors

The distributed Bragg reflector (DBR) or Bragg mirror is a structure made of multilayer-stack of alternating materials with different refractive index (high

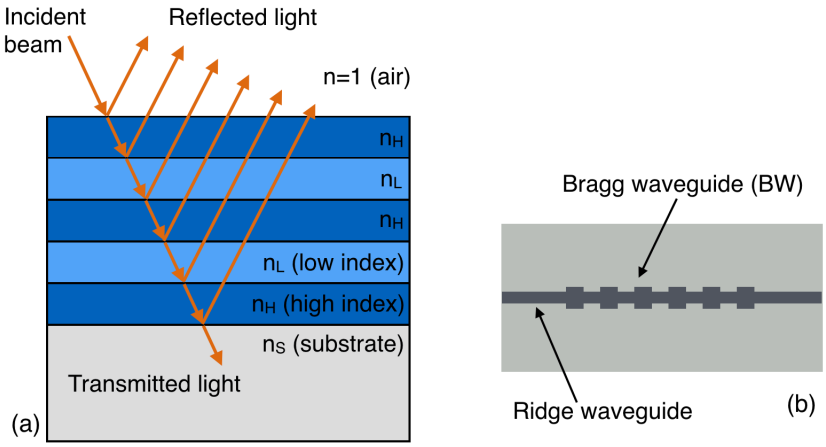

Figure 1.8: (a) Distributed Bragg reflector (DBR). It is a structure formed from multiple layers of alternating materials with varying refractive index. If the incident light has a wavelength close to four times the optical thickness of the layers, constructive interference occurs on the reflected light and the structure acts like a high-quality reflector. The range of wavelengths that are reflected are called photonic *stopband*. (b) Bragg waveguide (BW). It is a DBR integrated on a silicon chip. It is made by periodically varying the width of a ridge waveguide, that results in a periodic variation of the effective refractive index of the waveguide.

and low), as shown in Fig. 1.8 (a). As can be seen from the figure, on each layer interface, a part of the incident light is reflected. The reflected light gets a phase of 180° only when it passes from the low-index (n_L) medium to the high-index (n_H) one. Then, the relative phase difference of all reflected beams is either zero or a multiple of 360° and constructive interference occurs. So, the intensity of the transmitted light decreases during its travel through the DBR structure, whereas the reflected light intensity increases at each layer (considering the absorption of each layer negligible).

If the refractive indexes and geometrical thicknesses of the layers are chosen so that the optical thicknesses of each layer are $\lambda/4$, where λ is the center wavelength of the DBR, we can then write:

$$t_H = \frac{\lambda}{4n_H} \quad \text{and} \quad t_L = \frac{\lambda}{4n_L}, \tag{1.30}$$

where t_H and t_L indicates, respectively, the geometrical thicknesses of the high- and low-index films.

If we have an odd number of layers, i.e. N layers with a high refractive index n_H and $(N-1)$ low-index (n_L) films (as shown in Fig. 1.8 (a)), then the reflectance R_{2N-1} of the quarter-wave stack at the DBR central wavelength is given by:

$$R = \frac{1-Y}{1+Y}, \tag{1.31}$$

where Y is the admittance of the $(2N-1)$-quarter-wave stack, and is defined as:

$$Y = \left(\frac{n_L}{n_H}\right)^{2N} \frac{n_S}{n_H^2}, \tag{1.32}$$

in which n_H and n_L are the refractive indexes of the high- and low-index films, respectively, n_S is the refractive index of the substrate and $(2N+1)$ is the number of layers in the structure.
If the number $(2N+1)$ of films is large enough and the absorption can be neglected, the expression of the reflectance given in Eq. (1.31) can be approximated as:

$$R \approx 1 - 4Y = 1 - 4\left(\frac{n_L}{n_H}\right)^{2N} \frac{n_S}{n_H^2}. \tag{1.33}$$

Moreover, since the transmittance is $T = 1 - R$, we can write:

$$T \approx 4Y = 4\left(\frac{n_L}{n_H}\right)^{2N} \frac{n_S}{n_H^2}. \tag{1.34}$$

If we now take the the natural logarithm of both members of Eq. (1.34), we have:

$$\ln(T) = \ln\left(\frac{4n_S}{n_H^2}\right) - 2N\ln\left(\frac{n_H}{n_L}\right). \tag{1.35}$$

The refractive index contrast of the layers is $\Delta n = n_H - n_L$, then Eq. (1.35) becomes:

$$\ln(T) - \ln\left(\frac{4n_S}{n_H^2}\right) = -2N\ln\left(1 + \frac{\Delta n}{n_L}\right). \tag{1.36}$$

By using the series expansion

$$\ln(1+x) = \left(1 + x + \frac{x^2}{2} + \dots\right), \tag{1.37}$$

Eq. (1.36) simplifies to:

$$\ln\left(\frac{T}{\frac{4n_S}{n_H^2}}\right) \approx -2N\frac{\Delta n}{n_L}. \tag{1.38}$$

For most practical case, n_L can be approximated to $\bar{n} = \frac{n_H + n_L}{2}$ and we have that:

$$T = \frac{4n_S}{n_H^2} e^{-2N\frac{\Delta n}{\bar{n}}}. \tag{1.39}$$

So, the transmittance results to be:

$$T \propto e^{-2N\frac{\Delta n}{\bar{n}}}. \tag{1.40}$$

Form Eq. (1.40), we see that the transmittance decrease exponentially with N, where $(2N+1)$ is the number of layers in the DBR structure. So, not many

layers are required to have very low transmission of light through the DBR. For instance, if we take $\Delta n/\bar{n} \sim 10^{-3}$, it is:

$$T \propto e^{-2N10^{-3}}, \tag{1.41}$$

and we get a ∼3 dB attenuation when $2N10^{-3} = 1$, that means $N = 500$. Since we chose the $\lambda/4$ condition, we have that the period of the DBR structure is $\Lambda = \frac{\lambda}{2\bar{n}}$. If we consider for the central wavelength of the DBR IR light at $\lambda = 1550$ nm and $\bar{n} = 1.5$, then we get a 3 dB attenuation for a DBR length of 250 μm. So, with a structure long few millimeters we can get almost total rejection of light at the chosen wavelength.

It is also worth to calculate the bandwidth of the rejected frequencies in a DBR. It can be shown [185, 186] that:

$$\Delta\nu = \nu_0 \frac{4}{\pi} \arcsin \left| \frac{n_H - n_L}{n_H + n_L} \right|. \tag{1.42}$$

by using the series expansion

$$\arcsin(x) = x + \frac{x^3}{6} + \ldots, \tag{1.43}$$

Eq. (1.42) can be written as:

$$\Delta\nu = \nu_0 \frac{4}{\pi} \left| \frac{n_H - n_L}{n_H + n_L} \right| = \nu_0 \frac{4}{\pi} \left| \frac{\Delta n}{\bar{n}} \right|. \tag{1.44}$$

So, for a central frequency $\nu_0 = 2 \times 10^{14}$ Hz (corresponding to a wavelength $\lambda_0 = 1.5$ μm) and $\Delta n/\bar{n} = 10^{-3}$ we get $\Delta\nu \simeq 250$ Ghz, that is a typical bandwidth value for integrated filters. Moreover, it is worth to notice that in the presence of chromatic dispersion, in Eq. (1.44) the average effective index $\bar{n}$ should be changed with the group index n_g.

The DBR structure described above can be integrated on a photonic chip. This can be done by periodically shrinking the width of a silicon wire waveguide, that results in an effective change of the refractive index. This new structure can also be called Bragg waveguide (BW). A schematic of this structure is shown in Fig. 1.8 (b). An example of this structure, used for the FWM experiment on a DBR, will be described in Sec. 2.1.

Since the BW is derived from a silicon wire waveguide, we can extend the discussion about FWM in integrated silicon wire waveguides to BWs.

Microring resonators

A cavity which forces light to circulate along the same predetermined path is usually defined as *ring resonator*. In free space, it is possible to obtain a ring

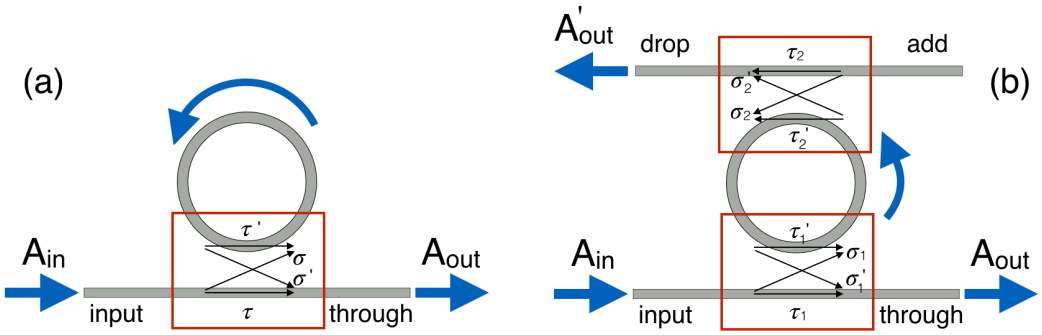

Figure 1.9: Schematic representation of a microring resonator in a (a) usual configuration, coupled to a single wire waveguide, and (b) in the add-drop configuration, in which two wire waveguides are coupled to the cavity. The scheme is not in scale and the gap between the ring and the waveguide was made big in order to show the coupling coefficients. τ and τ' are the coefficients that take into account the transmission along the waveguide and ring resonator, respectively. σ and σ' are the cross-coupling coefficients and represent the light transmission from the waveguide to the ring and vice versa. A_{in} represents the amplitude of the incoming field and A_{out}, A'_{out} are the amplitudes of the output fields in the through and drop port, respectively.

resonator by using three mirrors oriented in such a way that a beam of light can circulate along the triangle defined by the mirrors. In integrated optics a ring resonator consists of a wire waveguide looped back on itself to form a circular path (as schematically depicted in Fig. 1.9 (a)). As for waveguides, light is confined in the ring resonator through total internal reflection (TIR). Moreover, light traveling in the loop builds up in intensity at each round-trip because of constructive interference. Usually, for building an integrated ring resonator, small bend radii (around 10 μm) are required. This is only possible by using waveguides with a high refractive index contrast, which allows for strong confinement. For this reason SOI-based waveguides are the most promising and diffuse starting point for building *microring resonators*. Indeed, silicon wire waveguides can reach bend radii of about 5 μm, that allows the production of very compact microring resonators, in contrast with other materials where ring have to be much larger [38]. Usually, the term *ring resonator* refers to a circular resonator, whereas the term *recetrack resonator* is employed when the shape is elongated with a straight section along one direction (usually the coupling direction).

When the optical path length of the ring resonator is an integer multiple of the wavelength of the guided mode, constructive interference arises in the cavity and a resonance occurs. This can be expressed as [41]:

$$m\lambda_0 = 2\pi R n_{eff} \quad \text{with} \quad m \in \mathbb{N}, \tag{1.45}$$

where λ_0 is the wavelength of the guided mode, R is the ring radius and n_{eff} is the effective refractive index of the mode propagating in the waveguide.

Thus, as shown in Fig. 1.10, ring resonators support evenly spaced multiple resonances, whose separation is defined as free spectral range (FSR):

$$\mathrm{FSR} = \frac{\lambda_0^2}{n_g L}, \tag{1.46}$$

where $L = 2\pi R$ is the round-trip length and n_g is the group index that takes into account the dispersion of the waveguide and is defined as:

$$n_g = n_{eff} - \lambda_0 \frac{\partial n_{eff}}{\partial \lambda}. \tag{1.47}$$

The group index and the corresponding group velocity $v_g = c/n_g$ describe the velocity of the envelope of the pulse propagating in the waveguide. The above equations show that the photonic properties of a ring resonators depend only on its circumference L and on the effective index n_{eff} of the traveling mode. In particular, the separation of the resonances depends on the inverse of the ring radius, since $\mathrm{FSR} \propto 1/R$.

A ring resonator as a standalone device only becomes useful when a coupling mechanism is used to access the loop, in order to input/output light from the cavity. The most used coupling mechanism is the codirectional evanescent coupling to a straight wire waveguide, as shown in Fig. 1.9 (a). In this configuration, the evanescent tails of the waveguide and ring resonator guided modes overlap and light can be coupled from the waveguide to the ring and vice versa. The amplitudes of the output field A_{out} and of the input field A_{in} are related through the following expression:

$$A_{out} = \left\{ \tau + \sigma\sigma' e^{-i\delta} \left[1 + \tau' e^{-i\delta} + \left(\tau' e^{-i\delta} \right)^2 + \ldots \right] \right\} A_{in}, \tag{1.48}$$

where τ and τ' are the coupling coefficients that describe the transmission along the waveguide and the ring, respectively, σ and σ' are the cross-coupling coefficients that represent the transmission of light from the waveguide to the ring and from the ring to the waveguide, respectively, and

$$\delta = \frac{2\pi n_{eff} L}{\lambda_0} = kL \tag{1.49}$$

is the phase shift acquired by light after one round-trip. In Eq. (1.48), the first term in the curly brackets describes the transmission along the waveguide only, whereas the other terms represent the interaction between the ring and the waveguide. Now, since the ring and the waveguide have same cross-section and refractive index, we can write:

$$\sigma' = \sigma^* \quad \text{and} \quad \tau' = -\tau^*. \tag{1.50}$$

If we assume the losses are negligible in the coupling region, then we can write:

$$|\sigma|^2 + |\tau|^2 = 1. \tag{1.51}$$

So, by using the above expressions and by summing all the terms in Eq. (1.48), we obtain the ratio of the transmitted field to the incident field [41, 187]:

$$\frac{A_{out}}{A_{in}} = \frac{\tau - ae^{-i\delta}}{1 - a\tau^* e^{-i\delta}}, \tag{1.52}$$

where $a = \exp(-\alpha L/2)$ is a term taking into account the attenuation of the amplitude of the guided mode due to bending or scattering losses in the ring described by the coefficient α.
If we now take the absolute square of Eq. (1.52) we obtain the transmission of the ring resonator:

$$T = \left|\frac{A_{out}}{A_{in}}\right|^2 = \frac{a^2 + \tau^2 - 2a\tau\cos(\delta)}{1 + a^2\tau^2 - 2a\tau\cos(\delta)}. \tag{1.53}$$

From the above expression we can see that for ideal cavities with no losses ($a \approx 1$), the transmission is $T = 1$ for each phase shift δ. Moreover, when the phase shift acquired by light after one round-trip is an integer multiple of 2π ($\delta = 2\pi m$ with $m \in \mathbb{N}$), that is at the resonance condition, Eq. (1.53) reduces to:

$$T = \frac{(a-\tau)^2}{(1-a\tau)^2}. \tag{1.54}$$

Eq. (1.54) shows that in the case $\tau = a$, that is called the *critical coupling* condition, the transmission goes down to zero. This happens when the cross-coupling coefficient equals the the propagation losses inside the cavity and $|\sigma|^2 = 1 - |a|^2$. Thus, at the critical coupling condition all the power coupled into the ring resonator is dissipated inside the ring and light-matter interaction is maximized [41, 38]. When $\tau < a$ the ring resonator is said to be in *overcoupling*, whereas when $\tau > a$ the system is *undercoupled*. In real systems, all these different coupling situations can be controlled by changing the distance between the ring resonator and the coupled waveguide. Since in critical coupling light-matter interaction in the ring resonator is maximized, when performing FWM experiments it is preferred to be in this condition in order to obtain the maximum generation efficiency inside the ring.

An example of ring resonator spectrum is given in Fig. 1.10. As already mentioned, the spectrum is characterized by evenly spaced dips, called resonances, from which the main features of the cavity can be obtained.
The full width at half maximum (FWHM) of a resonance is given by [38]:

$$\text{FWHM} = \frac{(1-a\tau)\,\lambda_0^2}{\pi n_g L\sqrt{a\tau}}, \tag{1.55}$$

and is basically given by the resonance bandwidth in the frequency domain $\Delta\omega$. From the FWHM it possible to derive an important property of a ring resonator, that is the finesse $\mathcal{F}$, defined as:

$$\mathcal{F} = \frac{\text{FSR}}{\text{FWHM}}, \tag{1.56}$$

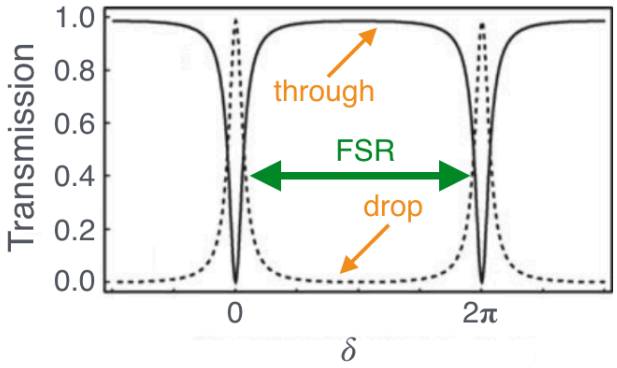

Figure 1.10: Transmission spectrum of a ring resonator (solid line) as a function of the phase shift δ. In the case of the add-drop configuration the solid line represents the transmission at the through port, whereas the dashed line is the transmission at the drop port. The resonances occurs when $\delta = 2\pi m$, with $m \in \mathbb{N}$. FSR stands for free spectral range.

that is a measure of the sharpness of the resonances relative to their spacing. The finesse can be though as the number of round-trips made by light in the ring resonator before its energy is reduced to $1/e$ of the initial energy, within a factor of 2π.
Another important feature of a ring resonator is its quality factor, that helps us understanding how much the resonator is good in trapping light, thus determining the enhancing properties of a given resonator. For a general resonator, the quality factor Q of a resonance ω_0 is defined as the ratio of the energy stored to the the energy dissipated per optical cycle, that is:

$$Q = \omega_0 \frac{\text{energy stored}}{\text{power loss}}. \tag{1.57}$$

Both finesse and quality factor are related to the number of round-trips light can made in the resonator before escaping it through internal loss and the coupled waveguide. The finesse and quality factor can also be written as a function of the physical parameters of a ring resonator as [38]:

$$\mathcal{F} = \frac{\pi\sqrt{a\tau}}{1 - a\tau}, \tag{1.58}$$

$$Q = \frac{\pi n_g L\sqrt{a\tau}}{\lambda_0 (1 - a\tau)}. \tag{1.59}$$

As it can be seen from the above expressions, the finesse and Q-factor of a ring resonator are determined by the resonator losses only and are independent on the resonator length.

Since the transmission spectrum of ring resonators represents resonances that can be fitted by a Lorentzian curve, we can write:

$$T(\omega) \propto \frac{\Gamma}{(\omega - \omega_0)^2 + \Gamma^2}, \tag{1.60}$$

where Γ is the FWHM of the Lorentzian shape and represents the coefficient describing the energy-loss rate due to all losses. If E_0 is the initial energy, on the one hand, we can write the stored energy at a certain time t as:

$$E_{stored} = E_0 \exp(-\Gamma t). \tag{1.61}$$

On the other hand, the energy that is lost is :

$$E_{lost} = E_0 [1 - \exp(-\Gamma t)]. \tag{1.62}$$

The power lost is then given by:

$$P_{lost} = \Gamma E_0 \exp(-\Gamma t), \tag{1.63}$$

being the derivative of the energy lost per optical cycle. Then, the Q-factor can be written as:

$$Q = \frac{\omega_0}{\Gamma}, \tag{1.64}$$

and is proportional to the inverse of the resonance bandwidth $\Delta\omega$. By converting Eq. (1.64) in the wavelength domain, we notice that the Q-factor can be directly derived from the experiment through the following expression:

$$Q = \frac{\lambda_0}{\Delta\lambda}. \tag{1.65}$$

Indeed, a simple Lorentzian fit to the resonance is required in order to extrapolate both the central wavelength λ_0 and the resonance linewidth $\Delta\omega$.
From Eq. (1.64), it is possible to obtain another expression for the Q-factor, that is:

$$Q = 2\pi\Delta t_p \nu_0, \tag{1.66}$$

where $\nu_0 = 2\pi\omega_0$ is the central frequency of the given resonance and Δt_p is the photon dwelling time in the cavity.

Finally, we would like to distinguish between the terms *unloaded* and *loaded* Q-factor. The first term refers to a ring resonator not coupled to a waveguide. Once the resonator is coupled to a waveguide, additional losses are introduced to the cavity and the Q factor will decrease. This is called the loaded Q-factor. The definition of loaded Q-factor is given by [41]:

$$Q_{unloaded} = \frac{2\pi n_{eff}}{\lambda_0 \alpha}, \tag{1.67}$$

where we have assumed that for small values of σ, the energy-loss coefficient can be written as $\Gamma = \alpha c/n_{eff}$ since the losses are mainly due to photon scattering from impurities and bending losses.

As seen from the above expression, the quality factor of a ring resonator can be maximized by decreasing the propagation loss α. This is a crucial step in practical realizations of ring resonators. Moreover, from Eq. (1.59) it seems that high Q-factors can be obtained by increasing the ring radius. However,

this is strongly related to propagation loss, since a longer circumference implies higher losses. For example, considering propagation losses of 2.7 dB cm^{-1}, that correspond to silicon wire waveguides produced through the standard *imec* fabrication process, the highest reachable Q-factor is about $1.42 \cdot 10^5$ for a ring resonator with $L \approx 10$ mm [38]. However, since the finesse is proportional to the FSR and the is inversely proportional to L, large lengths would decrease in turn the finesse. So, having a ring resonator with low losses and high quality factor requires an accurate balance of all the effects above described.

Let us now briefly describe another possible configuration for a microring resonator, that is called *add-drop ring resonator*. In this case the ring is coupled to two waveguides, as shown in Fig. 1.9 (b). The first report of this configuration is given in [188]. Usually, the port named *input* is used to enter light in the system and the *add* port is needed in case one wants to add an additional pulse to the system. On the *through* and *drop* ports light is collected. As in the case of an all-pass ring resonator, constructive interference arises when the optical path length of the add-drop resonator is an integer multiple of the guided mode wavelength, so Eq. (1.45) still holds. Then, the spectra at the through and drop ports still presents evenly spaced multiple resonances with a Lorentzian shape and their separation is given from the FSR as expressed in Eq. (1.46). Usually, the light out of resonance is transmitted to the through port, whereas the light corresponding to the resonances is transmitted to the drop port. Then the spectrum looks like the one shown in Fig. 1.10, where the solid line represents the light collected at the through channel and the dashed line the spectrum found at the drop channel. So, at the through port, the spectrum is represented by equally spaced Lorentzian dips, whereas at the drop port the spectrum presents Lorentzian peaks when the resonance occurs.

The mechanism to couple light in and out of an add-drop resonator is still the codirectional evanescent coupling, but now the configuration is the one given in Fig. 1.9 (b), with two regions where the coupling occurs. The τ coefficients still represent the transmission either along the waveguide or the ring resonator, whereas the σ coefficients still stands for the cross-coupling coefficients between the waveguide and the ring and vice versa. The amplitudes of the input field A_{in} and of the output fields A_{out} and A'_{out} are still related and the transmission of the ring resonator is now given by [38]:

$$T = \left| \frac{A_{out}}{A_{in}} \right|^2 = \frac{a^2\tau_2^2 + \tau_1^2 - 2a\tau_1\tau_2\cos(\delta)}{1 + a^2\tau_1^2\tau_2^2 - 2a\tau_1\tau_2\cos(\delta)}, \tag{1.68}$$

in the case of the through port, and

$$T' = \left| \frac{A'_{out}}{A_{in}} \right|^2 = \frac{(1-\tau_1^2)(1-\tau_2^2)\,a}{1 + a^2\tau_1^2\tau_2^2 - 2a\tau_1\tau_2\cos(\delta)}, \tag{1.69}$$

for the drop port. At the resonance condition $\delta = 2\pi m$, the above expressions reduce to:

$$T = \frac{\left(a\tau_2 - \tau_1\right)^2}{\left(1 - a\tau_1\tau_2\right)^2}, \tag{1.70}$$

$$T' = \frac{\left(1 - \tau_1^2\right)\left(1 - \tau_2^2\right)a}{\left(\ -a\tau_1\tau_2\right)^2}. \tag{1.71}$$

From the above expressions it is clear that in case of negligible losses (i.e. $a \approx 1$), the critical coupling condition is found for $\tau_1 = \tau_2$, so the two coupling regions have to be symmetric. However, in the case the losses cannot be neglected, then the critical coupling occurs at $a = \tau_1/\tau_2$.

We can still define the same figures of merit of an all-pass ring resonator, but some changes are needed. The FWHM is now described by [38]:

$$\text{FWHM} = \frac{\left(1 - a\tau_1\tau_2\right)\lambda_0^2}{\pi n_g L\sqrt{a\tau_1\tau_2}}, \tag{1.72}$$

whereas the finesse and Q-factor can be now be expressed as [38]:

$$\mathcal{F} = \frac{\pi\sqrt{a\tau_1\tau_2}}{1 - a\tau_1\tau_2}, \tag{1.73}$$

$$Q = \frac{\pi n_g L\sqrt{a\tau_1\tau_2}}{\lambda_0\left(a\tau_1\tau_2\right)}. \tag{1.74}$$

The expressions (1.64)-(1.66) for the Q-factor are still valid in the add-drop configuration.

Usually, in order to define the Q factor of a ring, the resonator have to be excited till a certain level in order to consider the rate of power decay. So, in order to get high-Q resonances, coupling losses and round trip losses have to be small. For this reason, an all-pass resonator (Fig. 1.9 (a)) will always exhibit a higher Q-factor than an add-drop resonator (Fig. 1.9 (b)) with the same geometric parameters. Indeed, two coupling regions will always make coupling losses bigger than in an all-pass ring resonator.

As for all-pass ring resonators, in order to obtain a high-Q add-drop resonator, the round-trip length and the losses have to be carefully balanced. It has been found that the state-of-the art value of the Q-factor for a ring resonator in the add-drop configuration would be $1.36 \cdot 10^5$ for a round-trip length of about 13 mm [38].

Ring resonators, both in the all-pass and in the add-drop configurations, are suitable for a variety of applications. We will give just a brief overview of their utilization and a more accurate description can be found in [38].

Since only selected wavelengths are at resonance with the ring resonator, a first application is the one of a *spectral filter*. This is extremely useful for telecommunication and data communication purposes, in order to multiplex or

demultiplex wavelength division multiplexing (WDM) signals [174, 189, 190, 191]. The WDM technique is used to combine multiple optical signals onto a single optical fiber by using different wavelengths of the laser light, thus increasing the capacity of an optical transmission system. For example, cascaded add-drop ring resonators are very suitable for this purpose [192]. Moreover, an application of add-drop ring resonators as filters can be found in [37], where they have been used to divide and route to a second chip the signal and idler photons generated in an all-pass ring resonator.

Another useful application for ring resonators resides in *sensing*. Indeed, the position and shape of the resonances in the ring spectrum depend on the optical round-trip length of the ring and on the accumulated losses. So, ring resonators can be sensitive to a variety of effects, such as temperature variations and physical deformation or compositional changes of both the core and the cladding of the waveguide. Essentially, a shift in the resonance position is caused by a change of the effective index n_{eff} of the propagating mode.
The sensing application of ring resonators is particularly interesting in the *biosensing* field. Indeed, in medical diagnostic, drug development, environmental monitoring and food quality control there is an increasing demand for biosensors that can specifically detect selected compounds or molecules. However, the technological development of such biosensors is very challenging, for it requires to react to the presence of few-nanometers-large particles, that can have low concentrations and are found in fluids which contain many other molecules at a higher concentration. At the same time, SOI-based microring resonators can be good candidate for biosensing, for they are highly manufacturable resonators with transmission spectra depending on the ring's environment, they can be made with large Q-factors and low insertion loss and they are very compact, allowing to build a single sensor with many rings to perform simultaneous measurements on different molecules. Finally, since they are compatible with the CMOS fabrication process, they can be made cheap. A recent application for biosensing is the realization of microring resonators made of porous silicon [193].

Compact microring resonators are also very interesting to realize *optical delay lines* or *buffers* in photonic integrated circuits [194, 195, 196]. Indeed, ring resonator can store the optical signal before releasing it due to the fact that close to the resonance the dispersion is high and the traveling mode has a large group delay. While the group delays generated by a single resonator are too small for practical applications, many rings can be cascaded to increase the group delay in two main configurations: a SCISSOR made of all-pass filters and a coupled resonator optical waveguide (CROW) [194, 197].

Microring resonators can even be used in an active configuration, as an electrically actuated device, such as electro-optic modulators [38]. When the microring is employed as a modulator, the resonator is tuned to an operating wavelength chosen to be on the slope of the resonance peak. Then, a modulation on the optical length of the microring resonator would result in a

resonance shift and in a related change of the transmission/reflection of the cavity. Usually, microring resonators at the critical coupling condition are employed for this kind of applications. In fact, the strong deep in the microring spectrum allows for a large modulation depth with a relatively small shift of the microring's resonance. Moreover, the more the resonance is steep, the more the modulation is efficient. So, microrings with high Q-factor and finesse are needed. However, in high-Q microrings, light is trapped in the resonator for a long time, limiting the modulation speed of the microring. So, usually, microrings with a Q-factor of $5000 - 25000$ are used [38].

Another possible application for microring resonators is the one of wavelength routers or switches [198]. This is very important for setting up the signal path within a photonic network, that is exploited by using active or passive components. When active switches are employed, the state of the switch is reconfigurable, and the signal paths can be dynamically set. On the other hand, when passive components are employed, the signal path is set by the wavelength of the optical signal injected the input of the network according to resonances of the switches met along the path.

Finally, microring resonators are also very interesting for the production of optical frequency combs [199, 200, 201]. In microrings, combs are usually generated by injecting a CW laser in the resonator and using the nonlinear optical process of parametric frequency conversion, such as FWM. Being first used for the realization of optical clocks and precision spectroscopy, frequency combs are now widely used in many different areas, such as remote sensing, astronomical spectrograph calibration and precision distance measurement [199]. Moreover, recently, have been also considered for the generation of multiple states of nonclassical light [202].

Four-wave mixing in microring resonators

As already mentioned, the silicon Kerr coefficient is 10^2 bigger than the one of silica glass at the telecommunication wavelengths [157, 158]. So, silicon has a large third-order nonlinearity compared to other materials. Moreover, in silicon wire waveguides the propagating mode is confined in a small core region of the order of several hundreds of nanometers. For these reasons, FWM can be achieved in a few-centimeters-long silicon waveguide with a detectable idler flux.

Silicon microring resonators are resonant structures due to their looped shape and can thus further improve light-matter interaction in the structure, allowing very small footprints (radii of the order of 10 μm). The first experiment of enhanced stimulated FWM on semiconductors microring resonators was performed by Absil *et al.* in 2000 by using GaAs/AlGaAs structures [203]. The repetition of this experiment on SOI-based microring resonators has then been performed in 2008 in an experiment by Turner *et al.* [44]. So, let us now consider the stimulated FWM process in a silicon microring resonator as the one depicted in Fig. 1.9 (a). We assume the system to be at the critical cou-

pling condition ($\tau = a$). As shown in Fig. 1.3, in order to observe stimulated FWM in a ring resonator, a strong CW pump laser at a frequency ω_p and with a power P_p and a CW signal laser defined by a frequency ω_s and a power $P_s \ll P_p$ are injected into the system. Then an idler wave at a frequency ω_i and with a power P_i is stimulated by the presence of a signal laser in the ring resonator. We can now solve the coupled wave equations (1.26)-(1.28) and by considering the relation between the amplitudes of the output and input fields (A_{out} and A_{in}) given in Eq. (1.52), the FWM conversion efficiency η can be written as [203]:

$$\eta = \frac{P_i}{P_s} = (\gamma L P_p)^2 \left| F(k) \right|^8. \tag{1.75}$$

From the above expression, the power of the generated idler can be derived:

$$P_i = (\gamma L)^2 \left| F(k) \right|^8 P_s P_p^2, \tag{1.76}$$

where $\gamma = \frac{n_2 \omega_0}{c A_{eff}}$ is the wire waveguide nonlinear parameter, ω_0 is the central frequency of the resonance, c is the speed of light in vacuum, A_{eff} is the effective mode area and $F(k)$ is the *field enhancement*, that is assumed to have the same expression for pump, signal and idler:

$$F(k) = \left| \frac{\sigma}{1 - a\tau e^{(ikL)}} \right|. \tag{1.77}$$

The field enhancement depends on the coefficients τ and σ, that express the transmission along the waveguide and the cross-coupling between the waveguide and the ring, respectively, and on the propagation losses given by a. At the resonance frequency, $k = k_0$ and the field enhancement reaches its maximum value $F_0 = F(k_0)$. So, in order to observe FWM in a ring resonator the pump and signal frequencies have to be tuned to the microring resonances. Consequently, the energy-momentum conservation law expressed in Eqs. (1.23) and (1.24) is automatically verified since the idler photon will be generated at a resonance frequency given by $\omega_i = 2\omega_p - \omega_s$.

In order to understand the improvement in FWM efficiency obtained by using a resonant structure, such as a microring resonator, instead of a straight waveguide, we can compare Eq. (1.76) to the idler power generated in a wire waveguide:

$$\frac{P_{i,ring}}{P_{i,waveguide}} = \left(\frac{L_{ring}}{L_{waveguide}} \right)^2 F_0^8. \tag{1.78}$$

From the above expression, it is clear that the gain in FWM experiments that employ microring resonators instead of straight waveguides goes as the eighth power of the field enhancement. This turns in a powerful increase in the frequency conversion efficiency and in the power of the generated idler.

Now, consider the expression given in Eq. (1.59), that at the critical coupling condition gives:

$$Q = \frac{\pi n_g L \tau}{\lambda_0 (1 - \tau)^2}. \tag{1.79}$$

Considering that $|\sigma|^2 + |\tau|^2 = 1$ and $\lambda_0 = 2\pi/k_0$, the expression above can be written as:

$$Q = \frac{k_0 L n_g}{2} \frac{\sqrt{(1-\sigma^2)}}{\sigma^2}. \tag{1.80}$$

Assuming $\sigma \ll 1$, the quality factor results to be:

$$Q \simeq \frac{k_0 L n_g}{2\sigma^2}. \tag{1.81}$$

Thus, we can get a relation between the on-resonance field enhancement F_0 and the Q-factor at the critical coupling condition:

$$F_0 = \left| \frac{\sigma}{1-\tau^2} \right| = \frac{1}{\sigma} = \sqrt{\frac{2Q}{k_0 L n_g}}. \tag{1.82}$$

The above discussion refers to an ideal case, in which waveguide propagation losses are neglected, indeed choosing $\sigma \ll 1$ implies $a \approx 1$. However, in general, the experimental quality factor, determined by the resonance linewidth, have to be considered. So, by substituting Eq. (1.82) in Eq. (1.76) we get:

$$P_{i,ST} = (\gamma 2\pi R)^2 \left(\frac{Q v_g}{\omega_p \pi R} \right)^4 P_s P_p^2, \tag{1.83}$$

that allows to predict the generated idler power as a function of the pump and signal powers, in the limit of the undepleted pump approximation [44]. In finding Eq. (1.83) we have assumed the Q-factors of the pump, signal and idler resonances to be similar, and thus, $\omega_p \sim \omega_s \sim \omega_i$. From Eq. (1.83), it is clear that the the idler power P_i scales linearly with the signal power P_s and quadratically in the pump power P_p. Moreover, the conversion efficiency scales as Q^4/R^2. Finally, we would like to stress that the idler power given in Eq. (1.83), can be calculated from the microring parameters, for γ is the waveguide nonlinearity coefficient, Q is the resonances Q-factor, R is the radius of the ring, ω_p is the pump frequency and v_g the group velocity of the traveling mode.

As we have just discussed, in the stimulated FWM experiments, besides a pump laser, a signal laser is injected into the system in order to produce the idler field. However, as can be seen from Fig. 1.3, the signal photon does not contribute to the energy transfer in the process. Indeed, as already mentioned in the section dedicated to four-wave mixing, the third-order nonlinearity selection rules and the conservation of energy do not require the presence of the signal photon. Thus, the FWM, now called spontaneous four-wave mixing (SFWM), can be initiated by vacuum fluctuations and seen as a four-photon scattering in which two pump photons annihilate, producing a photon pair (idler and signal), as illustrated in Fig. 1.4. SFWM in a CW regime in a silicon waveguide and in a microring resonator was first exploited by Clemmen *et al.* in [45]. SFWM is particularly interesting for quantum technology

applications, for it can be employed to generate correlated photon-pairs. As already mentioned, SFWM does not have a classical explanation and a fully quantum description is required. A detailed description of the process can be found in [204] and [205] and lies outside the scope of this thesis. We report here only the main results in [204], in which, from the third-order Hamiltonian describing the waveguide, the ring and the coupling between them, the theory for SFWM is presented.

As in [204], let us now name the pump resonance order as N_p. Then, if one photon is generated through SFWM near a wavelength associated with a resonance order N on one side of the pump, the other photon will be generated at a wavelength associated with a resonance order $\bar{N} = 2N_p - N$ on the other side of the pump. From a classical calculation in the undepleted pump and signal approximation, the idler power, generated for a CW input pump power P_{N_p} near resonance N_p and CW input signal power P_N near resonance N, can be expressed as:

$$P_{\bar{N}} = \left(\gamma P_{N_p} L\right)^2 |F_N|^2 |F_{\bar{N}}|^2 |F_{N_p}|^4 P_N, \tag{1.84}$$

where F_N represents the field enhancement of the given resonance. The above expression agrees with Eq. (1.76) in the limit of no loss and weak coupling. Finally, by assuming that N and $\bar{N}$ are very close to N_p, thus having $\omega_{N_p} \approx \omega_N \approx \omega_{\bar{N}} \equiv \omega_0$, in the weak coupling ($\sigma \approx 1$) approximation and at the resonance condition, we can write [204]:

$$P_{\bar{N}} = \left(\gamma P_{N_p} L\right)^2 |F_0|^6 \frac{\hbar \omega_0 v}{2L}, \tag{1.85}$$

where F_0 in the on-resonance field enhancement, as defined in Eq. (1.82). If we compare the last expression we found with Eq. (1.84), we notice that the factor

$$\zeta = \frac{\hbar \omega_0 v}{2L|F_0|^2} \tag{1.86}$$

is the quantum analogous of the classical seed power typical of stimulated FWM in SFWM calculations.

By inserting Eq. (1.82) in Eq. (1.85), we get the generated idler power in the SFWM process [46]:

$$P_{i,SP} = (\gamma 2\pi R)^2 \left(\frac{Q v_g}{\omega_p \pi R}\right)^3 \frac{\hbar \omega_p v_g}{4\pi R} P_p^2. \tag{1.87}$$

So, we see that the generated idler power depends on the square of the injected pump power. As in the case of stimulated FWM, the idler power can be predicted from the ring resonator parameters, such as its radius R, the resonances quality factor Q, the waveguide nonlinear parameter γ, the group velocity of the traveling mode v_g, and from the pump frequency ω_p. Now, the conversion efficiency scales as Q^3/R^2.

We can now compare the generated idler powers for the stimulated and spontaneous FWM experiments as following [46]:

$$\frac{P_{i,SP}}{P_{i,ST}} = \frac{1}{4Q}\frac{\hbar\omega_p^2}{P_s}. \tag{1.88}$$

The above expression is independent from the ring size, but it is related uniquely to the resonances Q-factor, to the power of the signal injected in the stimulated FWM experiment and on a characteristic energy $\hbar\omega_p^2$, that is connected to the pump wavelength. For example, if we choose $\lambda_p = 1.5$ μm (i.e. in the telecom band), we get $\hbar\omega_p^2 \approx 1$ mW.

SFWM experiments on silicon microring resonators have shown that the generated photons are correlated [206] and that can be time-energy entangled [27]. More recently, it has also been proved that a microring resonator can be driven to produce either nearly-uncorrelated or time-energy entangled photon pairs depending on the spectral properties of the pump (either pulsed or CW, respectively) [207]. All these results are very important for quantum information processing, since applications require the employment both of entangled and single photons.

1.3 Sources of quantum states of light

As already explained at the beginning of this chapter, the generation of nonclassical states of light is of pivotal importance in many quantum technology applications. In particular, photonics has turned out to be a very interesting platform in the implementation of quantum experiments. In photonics, quantum states of light are generated through nonlinear parametric processes. In fact, if an intense pump laser is injected in a nonlinear medium, then a pair of photons can be generated with a certain probability. The two generated photons could be either in an entangled state or uncorrelated photons.

In nonlinear optics, the spontaneous nonlinear parametric processes responsible of generating photon pairs are either spontaneous parametric down-conversion (SPDC) or spontaneous four-wave mixing (SFWM), depending on the kind of nonlinearity of the generating material. In fact, on the one hand, in media which present second-order nonlinearities ($\chi^{(2)}$) one pump photon is annihilated to produce two photons, called idler and signal. On the other hand, materials which exhibit a third-order nonlinearity (such as silicon, as already explained in Sec. 1.2.1), will generate a photon pair from the injection of two pump photons. The two described nonlinear processes have a classical counterpart, namely difference-frequency generation (DFG) and stimulated FWM, respectively.

The main difference between SPDC and SFWM lies in the frequency of the generated idler and signal photons. Indeed, the energy-momentum conservation law requires that the two photons produced through SPDC are at

frequencies that are symmetrically spaced around half of the pump field frequency, whereas in SFWM they have to be symmetrically located with respect the pump frequency. So, in SFWM, the pump, idler and signal frequencies can be all very similar. This, even if useful for satisfying phase-matching conditions, creates some difficulties in filtering out the pump field in order to separate the idler and signal photons.

Since both SPDC and SFWM can generate either entangled or uncorrelated photons, that are the key states of interest for quantum applications, we will report on them below.
Finally we will conclude this section describing the joint spectral density (JSD) technique, a useful method that can be used to discriminate between entangled and uncorrelated photons.

1.3.1 Entangled photons sources

Both for SPDC and for SFWM, entanglement between the idler and signal photons comes from the combination of the energy-momentum conservation law with vacuum fluctuations. Different degrees of freedom can be chosen to generate entanglement, depending on the initial configuration of the conversion process. For example, many quantum algorithms rely on polarization, path, time and energy entanglement.

As explained in Sec. 1.1, in general, a quantum state, for example made of two particles, is said to be entangled if it cannot be separated in the states describing the single particles and implies nonlocal correlations between measurements performed when the particles are well-separated.
So, when dealing with nonlinear parametric processes, in order to have the production of entangled photons, the idler and signal have to be at least in a two-mode state. For example, if we consider the SPDC process, we can have that the two generated photons have always the same polarization (Type I SPDC) and the final state (1.8) can be written as:

$$|\psi\rangle = |H\rangle_s |H\rangle_i, \tag{1.89}$$

where the states $|\psi_1\rangle$ and $|\psi_2\rangle$ are now represented by the polarization states $|H\rangle_s$ and $|H\rangle_i$, respectively. This state is a separable state and, thus, it is not useful for the production of entangled photons. However, in type II SPDC the generated idler and signal would have orthogonal polarizations and the final state would be:

$$|\psi\rangle = |H\rangle_s |V\rangle_i + |V\rangle_s |H\rangle_i, \tag{1.90}$$

thus obtaining an entangled state, for the states $|H\rangle_s$ and $|H\rangle_i$ cannot be treated independently [208].

Usually, two main methods can be used to experimentally prove entanglement: the firs one is based on the violation of a Heisenberg-like inequality for the inferred variances, whereas the second one consists in verifying the violation of Bell's inequalities [209]. Since the majority of experimental works refer

to the second approach, we will focus on it, and we will refer the reader to [210, 211, 212, 213] for more information on the first method. However, we do not intend to give an exhaustive description of the theory behind Bell's inequalities, that can be found in [52] and we will report only few results. Bell's inequalities are a condition that has to be verified in order to prove entanglement and they also prove the nonlocal realism of quantum mechanics. Since SPDC and SFWM generate states that are typically maximally entangled, then the violation of Bell's inequalities is a proof of entanglement [214]. An operative definition of Bell's inequalities can be found in [215] and it consists in a coincidence measurement between the two arms A and B of a bipartite entangled state for different detectors settings. Let us consider the case of polarization entanglement (that will be described in the next paragraph). The expression to be violated for entangled states is [216]:

$$S \equiv |E(a,b) - E(a,b')| + |E(a',b) + E(a',b')| \leq 2, \tag{1.91}$$

where a and a' represent the possible settings for the arm A (e.g. the idler photon) and b and b' are the settings for the arm B (e.g. the signal photon). The above expression is called CHSH (Clauser-Horne-Shimony-Holt) inequality for polarization entangled states. Since we are dealing with polarization entanglement, the possible settings correspond to which angle the polarizers are positioned in front of the detectors, then Eq. (1.91) can be written as:

$$E(a,b) = \frac{\xi(a,b) + \xi(a+90°, b+90°) - \xi(a, b+90°) - \xi(a+90°, b)}{\xi(a,b) + \xi(a+90°, b+90°) + \xi(a, b+90°) + \xi(a+90°, b)}. \tag{1.92}$$

In the above expression, $\xi(a,b)$ represents the number of coincides measured when the idler polarizer is set to a and the signal polarizer is chosen to be in the b configuration. Then, the maximum violation of the CHSH inequality is found for $a = 0°$, $a' = 45°$, $b = 22.5°$ and $b' = 67.5°$ [208].

The example above was referred to the case of polarization entanglement. However, different Bell's inequalities can be exploited to prove other entanglement degrees of freedom. For example, in the case of time-energy entanglement a useful relation was found by Franson [217], as it will be described later in this section.

A great number of experiments have investigated the production of entangled states of photons. The first ones made use of atomic radiative cascades [29] and, later on, the entangled states were produced in nonlinear birifringent dielectric crystals, such as BBO (beta-barium borate) crystals [24]. All the experiments performed on those crystals exploited the second-order nonlinearity $\chi^{(2)}$, thus producing photon pairs through SPDC. After these pioneering experiments, more practical sources capable of producing photon pairs with higher intensity were investigated. For example, SPDC has been study in periodically-poled lithium niobate (PPLN) waveguides [218, 219] and SFWM has been investigated in dispersion shifted fibers (DSFs) [220].

Unfortunately, all the described sources present many disadvantages. For example, PPLN waveguides show group velocity mismatch [221], whereas DSFs produce noise photons through spontaneous Raman scattering, thus requiring a cooling apparatus [222]. Another major drawback of these sources is the big difficulty encountered in meeting applications requirement, since they are not suited for the integration on a chip.

So, a solution to the integration problem was found in integrated waveguides. For example, recently, polarization-entangled photons have been generated via SPCD in AlGaAs waveguides [30]. Moreover, as already discussed in Sec. 1.1.1, silicon is a very interesting material for the generation of entangled photons in few-centimeters-long waveguides that are compatible with the CMOS fabrication process, and many experiments have been already been performed on this topic [31, 223, 25, 32, 33].

As extensively explained in Sec. 1.2.2, another way of generating photon pairs in silicon is by employing structures able to enhance light-matter interaction compared to straight waveguides, i.e. microring resonators. The first results of photon pairs production in a CW regime in a microring resonator were reported by Clemmen *et al.* in [45] and they were followed by other works, such as in [224]. The first step needed after having proved photon pairs emission from microring resonators, has been the verification of the concurrent emission of idler and signal. This has been studied by Azzini *et al.* in [206]. Finally, the emission of both time-energy [27] and time-bin [28] entangled photons from microring resonators have been shown.
More recently, even alternative silicon-compatible materials have been explored and the generation of entangled photon states has been proved both in hydex [202] and silicon nitride [225] ring resonators.

We will now analyze the different degrees of freedom used to generate a state made of entangled photons.

Polarization encoding

Polarization encoding is probably the simplest way of proving the violation of the Bell's inequality, as shown in Eq. (1.92). For this reason, polarization entanglement was the first to be used on the first sources based on atomic cascades [29].

In this kind of encoding, the computational basis is given by the two possible polarization states: horizontal $|H\rangle$ and vertical $|V\rangle$. So, the general entangled state (1.1) can be expressed as:

$$|\psi\rangle = \alpha|H\rangle + \beta|V\rangle. \tag{1.93}$$

Practically, the waveplate (WP), that is a birefringent device responsible of introducing a phase delay between two light beams orthogonally polarized passing through it, is the optical device employed to implement single-qubit gates. Two kinds of WPs are most used: the half waveplate (HWP) and the quarter waveplate (QWP). The former changes the polarization direction of

a linearly polarized photon, whereas the latter turns linear into circular polarization. Even polarizing beam splitters (PBS), which select two different paths for horizontal and vertical polarization, are useful devices for generating polarization encoded qubits. Many experiments have been carried out exploiting polarization entangled photons generated from different sources, from BBO crystals, to AlGaAs integrated waveguides and an integrated silicon chip [24, 30, 25].

Even if of easy implementation, polarization encoding suffers from decoherence in optical fibers over long distances (bigger than few kilometers). Nowadays, optical fibers have improved a lot than one or two decades ago. However, even if now birefringence is very small and does not affect the telecom industry, it is still a big problem for quantum communication, for the smallest birifringence possible would always affect the polarization-entangled state [123]. Indeed, states that are either parallel or orthogonal to the stress or asymmetry that causes birefringence, would propagate with different phase velocities, changing the overall polarization state of the light traveling in the fiber.

Phase encoding

As for polarization, even the *phase* of photons is a good choice for single-qubits encoding. Usually, the phase of photons can be measured through interferometric techniques. Indeed, in the case of a balanced interferometer, i.e. when the photon coherence time is much smaller than the optical path difference between the two arms of the interferometer, single photons act as coherent light. If we now label the two output ports of the interferometer as $|p_1\rangle$ and $|p_2\rangle$ we can write the general state (1.1) of a photon coming out the interferometer as:

$$|\psi\rangle = \frac{1}{\sqrt{2}}\left(c_1|p_1\rangle + e^{i\phi}c_2|p_2\rangle\right), \tag{1.94}$$

where we have used $|p_1\rangle$ and $|p_2\rangle$ as the computational basis and the two-level quantum system is represented by varying the phase difference ϕ between the two arms of the interferometer. c_1 and c_2 are constants that depend on the splitting ratio of the first beam splitter composing the interferometer. For example, both polarization and phase encoding can be used to implement the BB84 protocol [18]. In the case of polarization encoding Alice can send a qubit in the $(|H\rangle, |V\rangle)$ basis and Bob will randomly choose either $|H\rangle$ or $|V\rangle$ to perform the measurement, whereas if phase is chosen for the encoding, then Alice Has two possible basis for sendig qubits, that are $\phi_1 = \left(0, \frac{\pi}{2}\right)$ and $\phi_2 = \left(\pi, \frac{3}{2}\pi\right)$ and Bob will choose one of them to detect the arriving photons. Usually, phase encoding is implemented in two methods. The first one, proposed by Franson [217], consists in using two interferometers and a CW pump laser. This configuration is mostly used to reveal time-energy entangled photons [27]. The second method, proposed by Brendel [226], is a modification of the Franson technique and uses three interferometers and a pulsed pump laser. This design allows to detect time-bin entangled photons.

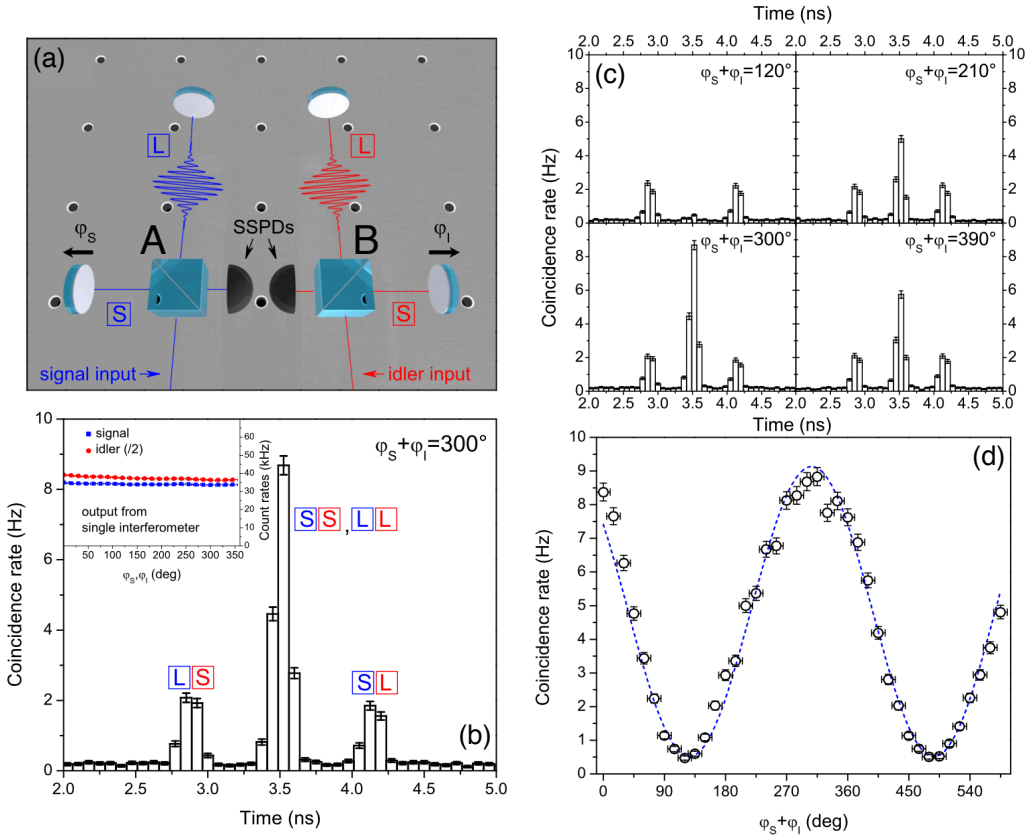

Figure 1.11: (a) Scheme of the Franson method, consisting in two unbalanced interferometers. The signal photon enters the A interferometer, whereas the idler photon the B apparatus. (b) Depending on which arm of the interferometer the photon will travel (short-short, long-long, long-short, short-long), three coincidences peaks will arise. (c) Due to the indistinguishability of the short-short and long-long cases, by varyingthe interferometer's relative phase, the central peak will exhibit an interference pattern. (d) The interference pattern of the central peak violates the Bell's inequality, proving the time-energy entanglement of the generated photons [27].

Let us focus now on the case of *energy-time entanglement* and consider the situation depicted in Fig. 1.11 (a), where a source emits photons at the same time. The kind of process responsible for the generation of photon pairs is not relevant at the moment (it could be SPDC, SFWM etc.), but it is important that energy is conserved in order to have correlation between the signal and idler emitted photons due to the long coherence time of the pump laser [227, 228, 229, 27]. Then, as shown in Fig. 1.11 (a), the two generated photons are separated and sent to two identical unbalanced interferometers, called A for "Alice" and B for "Bob". The output from the two interferometers is then sent to single photon detectors and detected in coincidence, i.e. recording the detection time at the end of B with respect to the arrival time at the end of A. There are four possible combinations of paths: both photons travel along either the long arm ($|l_A, l_B\rangle$) or the short arm ($|s_A, s_B\rangle$), the photon in A takes the long path and the photon in B the short path ($|l_A, s_B\rangle$) and, vice versa, in A the photon follows the short arm and in B the long one ($|s_A, l_B\rangle$). Since we are dealing with equally unbalanced interferometers, the short-short and long-long cases are indistinguishable and will result in a single coincidence peak. Thus, the resulting spectrum is made of three peaks, as shown in Fig. 1.11 (b), where the first one corresponds to the case where the photon has followed the long arm in A and the short arm in B, and vice versa for the last peak. The second peak corresponds to the short-short and long-long indistinguishable cases and can be expressed as:

$$|\psi\rangle = \frac{1}{\sqrt{2}} \left(|s_A, s_B\rangle + e^{i\varphi} |l_A, l_B\rangle \right), \tag{1.95}$$

where $\varphi = \phi_A + \phi_B$ is the phase difference given by the sum of the optical phase difference between the two paths of the A and B interferometers.

Since $|l_A, l_B\rangle$ and $|s_A, s_B\rangle$ are indistinguishable, from quantum mechanics rules we can find the probability of detecting such a state, that is given by the squared modulus of the sum of the individual amplitudes. Then, as it can be seen from Fig. 1.11 (c) and (d), by varying the relative phase between the short and long arms in the A interferometer ϕ_A and in the B interferometer ϕ_B, an interference in the coincidence rate of the central peak $R_{central}$ will be observed [217]:

$$R_{central} = \frac{1}{4} V \cos^2 \left(\phi_A + \phi_B \right), \tag{1.96}$$

where V is the visibility of the two-photon interference and a value $V > \frac{1}{\sqrt{2}}$ implies the violation of Bell's inequality and prove the energy-time entanglement of the measured state [230].

It is worth to say that time-energy entanglement is very interesting for quantum information processing applications, for it can be easily implemented on integrated devices ([27]) and suffers of less information loss over long distances.

If we now consider a Franson-like setup, as the one presented in Fig. 1.11 (a), and consider a pulsed pump laser as source of the photon pairs, we get

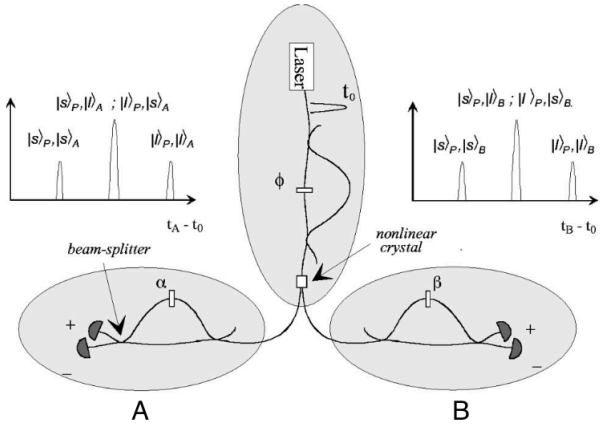

Figure 1.12: Schematic representation of the setup used to generate time-bin entangled photons [123].

time-bin entanglement [226]. Usually, the short pump laser is injected into an unbalanced interferometer. Now, the path length difference has to be bigger than the coherence length of the pulse. So, two time bins, or time intervals, are created at the output of the interferometer. The time intervals are large as the pump pulse and their time separation is given by the unbalance between the interferometer arms. Each pulse can then generate a photon pair in the first or second time slot. This is true if we assume the pump laser power to be low, thus having a low probability of pair-emission. In this way it possible neglecting the cases in which a pair is produced in both pulses or two pairs are produced in one pulse. At this point, as schematically shown in Fig. 1.12, the two generated photons are separated and sent to two interferometers, labeled as A and B. If the the A and B interferometers are matched to the first one within the coherence length of the pump pulse, both at the A and B outputs, three time intervals will be detected when looking at the arrival times of the photons. As depicted in the figure, the first time bin corresponds to the case in which the pump photon has traveled through the short arm of the first interferometer and the generated photon in the short arm of A. We can label this case as $|s\rangle_p|s\rangle_A$, where p and A stand for pump and A-interferometer photon. The third peak is due to when both the pump and generated photons go through the long path and the state will be labeled as $|l\rangle_p|l\rangle_A$. The central bin, as in the case of time-energy entanglement, is due to the two indistinguishable cases corresponding to the pump passing in the short arm of the first interferometer and the generated photon in the long arm of the A-interferometer ($|s\rangle_p|l\rangle_A$) and vice versa ($|l\rangle_p|s\rangle_A$). Obviously, the same discussion is valid for the B-interferometer, as reported in Fig. 1.12 [123].
In the degenerate case one of the two photons carry a phase acquired when traveling in the long arm of an interferometer. Then, the two states at the end

of the A and B interferometers can be written as:

$$|\psi\rangle_1 = |s\rangle_p + e^{i\phi_J}|l\rangle_J, \tag{1.97}$$

$$|\psi\rangle_2 = |s\rangle_J + e^{i\phi_p}|l\rangle_p, \tag{1.98}$$

where $J = A, B$. If we now define

$$|s\rangle_p + |s\rangle_J = |0\rangle, \tag{1.99}$$

$$|l\rangle_p + |l\rangle_J = |1\rangle, \tag{1.100}$$

the final state can be written as:

$$|\psi\rangle = \frac{1}{\sqrt{2}}\left(|0\rangle + e^{i\theta}|1\rangle\right), \tag{1.101}$$

where $\theta = \phi_p, \phi_J$.

Following [231], it can be useful to introduce the notation $|n_1, n_2, n_3\rangle_J$, where n_1 photons are in the first time bin, n_2 photons are in the second time bin and n_3 photons are in the last time bin and $J = A, B$. Now, if the difference in the arrival times at the A and B detectors are measured, the resulting spectrum will be something similar to the one depicted in Fig. 1.13, in which three different peaks are present. The two satellite peaks correspond to distinguishable events and can be neglected by choosing a sufficiently small window around the central peak. Three different events are related to the central peak and they are characterized by the fact that the photons take the same path in the A and B interferometers: $|1,0,0\rangle_A|1,0,0\rangle_B$, $|0,0,1\rangle_A|0,0,1\rangle_B$ and $|0,1,0\rangle_A|0,1,0\rangle_B$. On the one hand, the first two cases are again distinguishable, since they correspond to a photon created in the first (second) time bin that passes through the short (long) arm of A and B. On the other hand, in the third case two combinations are possible: the photon is created in the first time bin and passes then through the long arms of A and B, acquiring the relative phases ϕ_A and ϕ_B, respectively, or the photon is created in the second time bin, acquires a phase ϕ_p and then travels through A and B short arms. Since it is not possible to distinguish between these last two combinations, for it is impossible to distinguish which path the photon have chosen, interference is observed as in the case of the Franson experiment. Thus, time-bin entanglement can be proved.

Path encoding

A third way in which a single qubit could be encoded is by considering the path variable. *Path encoding* can be implemented by a beam splitter (BS), where the photon can take two different paths and the qubit is defined according to which one is chosen. This kind of encoding seems to be a good candidate for on-chip integration and will probably play an important role in future quantum technology applications.

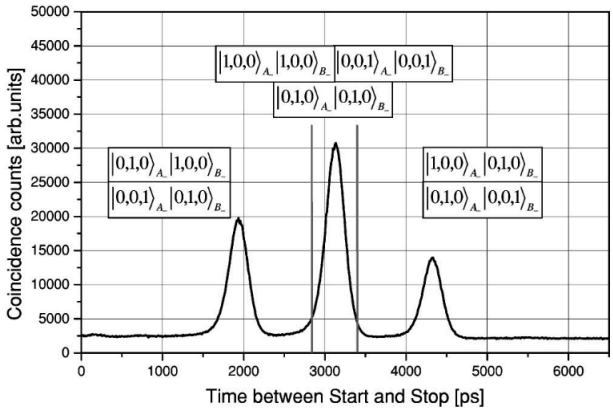

Figure 1.13: Time histogram of the difference in the arrival times at the A and B detectors [231]. As for the time-energy entanglement, three different peaks are present.

Usually, in an integrated chip, multiple photon paths can be represented by different on-chip waveguides, and two waveguides only are needed to generate path-entangled states So, in the simplest case of two input wire waveguides, the qubit could be assumed to be $|0\rangle$ if the photon is in the upper waveguide and $|1\rangle$ if it is in the lower waveguide, and the computational basis will be $(|0\rangle, |1\rangle)$. Then, the general qubit can be written as an arbitrary superposition of the two elements of the basis:

$$|\psi\rangle = \alpha|0\rangle + \beta|1\rangle. \tag{1.102}$$

This state can be obtained in integrated optics through the use of directional couplers, that are the analogous of BSs on an integrated photonic chip [26]. Phase shifter are then used to control the phase between the two optical paths and, thus, manipulate the state of the path-entangled qubit [130, 232].

Finally, it is worth to mention that the generation of path-entangled states in waveguides is very tolerant to significant losses. Indeed, in order to destroy entanglement one would need very strong losses, capable of preventing the coupling between the two waveguides [233]. Another advantage is that a polarization encoded qubit can be translated into a path encoded qubit by employing a polarizing BS and a HWP [234].
In the last chapter of this thesis we will use path encoding to show a way of implementing quantum logic through the use of classical waves on a simple electronic circuit.

1.3.2 Heralded single-photon sources

Many quantum information processing applications require the production of single-photon states, i.e. a state where one and only one photon is present. In general, in quantum optics, an ideal single-photon source should be efficient, have a high photon generation rate, emit indistinguishable photons in

a pure Fock state, emit photons on demand, the probability of emitting more than one photon per pulse should be zero and avoid loss of coherence and indistinguishability.

Single-photon sources are divided in two classes, depending on whether the photons can be produced on demand or at an unknown time. The former are called *deterministic* sources, the latter *probabilistic* sources [208].
In general, for quantum computation applications, deterministic sources are preferable and they are produced, for example, by trapped atoms, quantum dots or color centers. As concerning photonics, the easiest way to produce a single photon state one could think of is to use highly attenuated laser pulses. In fact, the photon distribution of a laser follows the Poissonian distribution and the amount of multi-photon generation probability scales linearly with the mean photon number. So, if the mean photon number is very small, then the multi-photon generation probability approaches a single-photon state. However, the efficiency of generating photons scales again linearly with the mean photon number, thus making this method very inefficient. Moreover, the probability of finding more than one photon per time interval cannot be neglected. So, a widely-used alternative is to consider probabilistic sources of single-photon states.

In spontaneous parametric processes, such as SPDC and SFWM, photons are always emitted in pairs and they are time correlated. In this scheme, the single-photon states are obtained through a process called *heralding*, where photon pairs are separated in order to get single photons. In the heralding process, one photon (the *herald*) is revealed, thus signaling the presence of the other photon (the *heralded*). However, this approach is limited by loss and multiple pair generation. In fact, when a photon in a pair is not detected, either no heralding occurs (thus the single photon state is no longer acceptable) or an empty state is revealed.

In the last year emission of heralded single photons has been proved in different devices: PPLN waveguides [20], silicon-based photonic crystals [21], silicon microresonators [22] and hydex microring resonators [23].
Usually, the state generated through either SPDC or SFWM can be expressed in the following way [165]:

$$|\psi\rangle = \sum_{n=0}^{\infty} c_n |n\rangle_s |n\rangle_i, \tag{1.103}$$

where $|n\rangle$ is an n-photon state, with $n \in \mathbb{I}$, i and s stand for idler and signal respectively and c_n are complex coefficients, with $|c_n|^2$ being the probability of finding exactly n photons in the idler and n photons in the signal. In order to get single photon states from Eq. (1.103), the pump intensity should be low. A typically used rule of thumb is to maintain an average below 0.1 signal/idler pairs either per pump pulse or per pump coherence time depending on one is working in either a pulsed or CW regime, respectively [208].

When dealing with heralded single photon sources, it is very important

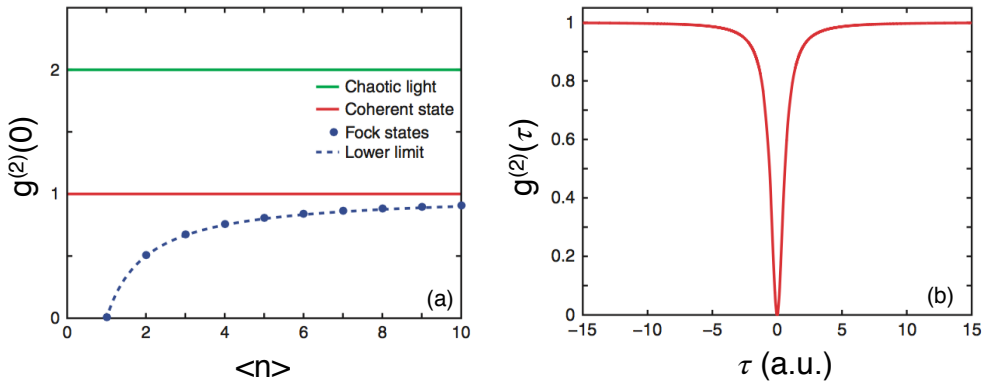

Figure 1.14: (a) $g^{(2)}(\tau)$ function at zero time delay as a function of the mean number of photons. For quantum states $g^{(2)}(0)$ can go below unity. (b) $g^{(2)}(\tau)$ as a function of the relative arrival time for a single-photon source.

to experimentally prove that the heralded photon is actually a single photon state, i.e. a Fock state with $n = 1$. Usually, this can be done by a triple coincidence measurement, where the photons of a pair are divided by sending one of them (the herald) to the detector and the other one (the heralded) to a Hanbury-Brown andTwiss (HBT) interferometer [235]. Then, the intensity correlations at the output ports of the interferometer are measured through the second-order coherence, called the $g^{(2)}(\tau)$ function, that describes the photon statistics of a field and can be expressed as [165, 236]:

$$g^{(2)}(\tau) = \frac{\langle I(t)\, I(t+\tau)\rangle}{I^2}, \tag{1.104}$$

where $I(t)$ is the field intensity at the time t. Classically, the $g^{(2)}(\tau)$ function at zero delay is:

$$g^{(2)}_{classical}(0) \geq 1, \tag{1.105}$$

where the equal sign holds for coherent states and the $>$ sign for thermal light. However, in a quantum description, the field is described by an operator and the function at zero delay can go below one. In particular, for number states (such as Fock states), the $g^{(2)}(\tau)$ function at zero delay can be expressed as:

$$g^{(2)}_{n}(0) = 1 - \frac{1}{n}, \tag{1.106}$$

where n is the number of photons in the state. The plot of $g^{(2)}(0)$ for different cases is shown in Fig. 1.14 (a). So, for a single photon source it must be:

$$g^{(2)}_{n=1}(0) = 0. \tag{1.107}$$

So, in the HBT experiment, when the herald is detected and if the heralded photon is in a single photon state, then the probability of measuring a coincidence event at the output ports of the interferometer should be zero. Thus,

the number of coincidences at the output ports of the interferometer as a function of the relative arrival time of the photons τ, will have a dip at $\tau = 0$, as depicted in Fig. 1.14 (b). In practical single photon sources $g^{(2)}(0)$ has to be less then 0.5 to confirm the presence of a single-photon state [208].

Many quantum information applications require the interference of one or more photons, thus needing the single photons to be in a *pure* state to get high visibility. In order to herald photons in a pure state unentangled photons are desired [237]. Different techniques are available to measure the purity of a single-photon state. For example, the density matrix of the state $\hat{\rho}$ can be used to assess the purity of the state ($Tr(\hat{\rho}^2) = 1$) [238, 239]. However, this is a complicated experiment, since for a D-dimensional quantum system made of n photons D^{2n} different projection measurements are needed to determine the trace [100]. Alternatively, in order to demonstrate the purity of the single-photon state, the source has to be proved to be single mode [208]. Usually, a measurement of the correlations of signal and idler for a specific variable gives the number of modes. An example of this measurement will be described in detail in the next section and consists in determining the joint spectral density (JSD) to show the signal-idler correlations in the frequency domain. If a source is single-mode, than the emitted photons will be uncorrelated (as shown in Fig. 1.15 (a)), whereas a multi-mode source will be characterized by by correlated photons (see Fig. 1.15 (b)).

Along with purity, single photon sources are also characterized by the *heralding probability* (or heralding fidelity). This parameter indicates the probability of detecting the heralded photon once the herald photon is revealed and is defined as [240, 241]:

$$\eta_{heralding} = \frac{C_C - C_A}{C_H \eta_{detector}}, \tag{1.108}$$

where C_C is the coincidence counts rate, C_A represents accidental rate, C_H stands for the single photon rate in the herald arm and $\eta_{detector}$ is the detection efficiency.

Finally, one last parameter should be considered to understand how well the source generates photon pairs. It is called the *coincidence-to-accidental ratio* (CAR) and can be used for both single and entangled photons sources. A formal definition of the CAR is given by [224]:

$$CAR = \frac{\int_{-\tau_{coh}/2}^{+\tau_{coh}/2} g_{si}^{(2)}(t)\, dt}{\int_{T_\infty-\tau_{coh}/2}^{T_\infty+\tau_{coh}/2} g_{si}^{(2)}(t)\, dt}, \tag{1.109}$$

which basically gives the ratio between the sum of all coincidences in the coincidence peak and the sum of the coincidences in a temporal window of the same size of the peak far away from the peak.
From an experimental point of view, the CAR is defined as the ratio between the coincidence counts rate C_C and the accidental rate C_A [45, 22]:

$$CAR = \frac{C_C}{C_A}. \tag{1.110}$$

Some processes, such as multiple-pair generation, noise in the detectors and losses can affect the CAR value [242]. However, if competing processes to the generation process can be neglected then the CAR can be directly related to the probability of emitting multiple pairs [243] and, consequently to the goodness of a source in generating single-photon states.

1.3.3 Deterministic sources of photons

As mentioned above, *deterministic* sources should in principle generate single and indistinguishable photons on demand and, usually, they are desired for quantum computing and quantum communication applications. Many systems have been studied to this purpose and most of them are "single emitters" quantum systems, i.e. systems made of two levels prepared in a excited state in which de-excitation occurs with the consequent emission of a single photon [244].

The main strategies used to emit single photons on demand are trapped ions (or molecules or atoms) [245, 246], quantum dots [247, 248] and color centers [249, 250, 251]. Even if all these methods are very promising, they still have some drawbacks. First of all they suffer from losses, that can degrade their deterministic nature and produce a probabilistic-like behavior [208, 244]. Moreover, it is very difficult to create identical emitters [208], even if many techniques are now available for erasing the frequency mismatch, like e-field tuning [252], strain tuning [253, 254] and temperature tuning [255].

Besides, in this work we are interested in the on-chip generation of photons, not only for the advantages gained in the actual realization of such devices, but also for the always growing need of cheap devices. Obviously, generation of photons through nonlinear processes is intrinsically random and is usually governed by a Poissonian statistic. So, the single-photon generation probability is limited to less than 25% [256]. Thus, the heralding process can increase this probability without degrading the quality of the source by using active multiplexing technique [208, 21, 257, 258, 259], showing high indistinguishability [260]. Photon multiplexing can be implemented both in space [21, 257, 258] and time [259, 260]. However, the path implementation requires many devices for each photon source and thus is of difficult scalability. Conversely, in the temporal implementation only one source is required, thus making it much more efficient. However, till now, low single-photon generation efficiency has been measured after multiplexing and the overall loss is a very important factor to be considered in order not to degrade the fidelity of the source [208].

1.3.4 Joint spectral density technique

A way of discriminating between the generation of entangled or uncorrelated photons is given by the joint spectral density (JSD) technique. As already mentioned in Sec. 1.2, SFWM can only be described in the framework of quantum mechanics, whereas stimulated FWM does have a classical explanation.

This is somehow the same situation of spontaneous and stimulated emission, that are linked through the Einstein's equations [165]. In general, performing measurements of spontaneous emission is much more complicated than using stimulated emission. Indeed, classical-generated fields are stronger than spontaneous-generated ones. The Einstein's relations are the starting point for the JSD technique. A full derivation of the analogous of the Einstein's equations in the case of stimulated and spontaneous FWM can be found in [261] and [262] and will not be reported in detail in this thesis.

Let us consider the state

$$|\omega_s, \omega_i\rangle = \hat{a}^\dagger(\omega_s)\,\hat{a}^\dagger(\omega_i)\,|0\rangle, \tag{1.111}$$

which is composed by two photons at the frequency ω_s and ω_i and where $\hat{a}^\dagger$ describes the creation operator. If we consider a parametric process as SPDC or SFWM and following [263], we can write the final state of the generated photon pairs as:

$$|\psi\rangle = \iint d\omega_s d\omega_i\, f(\omega_s, \omega_i)\,|\omega_s, \omega_i\rangle. \tag{1.112}$$

In writing the above expression we have neglected the vacuum contribution and considered photons with the same linear polarization. In Eq. (1.112), the term $f(\omega_s, \omega_i)$ is the joint spectral amplitude (JSA) of the two emitted photons. The JSD is then defined as the squared modulus of the JSA:

$$\Phi_{\omega_s\omega_i} = |f(\omega_s, \omega_i)|^2, \tag{1.113}$$

and allows to recover information about the correlation properties of the generated idler and signal photons [264].

Traditionally, the determination of the JSD follows a statistical approach, based on coincidence measurements. However, in experiment dealing with the spontaneous emission from microring resonators, the determination of the JSD is particularly complicated due to the narrow generation bandwidth of such devices. Thus, determining the JSD would translate in a time-consuming (due to the low generation rate of SFWM) and low-resolution experiment [265, 266]. The solution to the problem is found in the stimulation emission tomography (SET) idea [261]. By performing a stimulated-emission-based measurement, the signal to detect will be much larger than that found in a coincidence measurement. This, in turn, results in an enormous improvement in the speed and signal-to-noise ratio of the experiment. In fact, the number of photon pairs emitted in the stimulated process is proportional to the number that would be emitted in the spontaneous process, and the proportionality constant approximately equal to the average number of photons in the stimulating seed, that can be written as [261]:

$$\frac{\langle n_{\omega_i}\rangle_{A_{\omega_s}}}{\langle n_{\omega_i} n_{\omega_s}\rangle} \approx |A_{\omega_s}|^2, \tag{1.114}$$

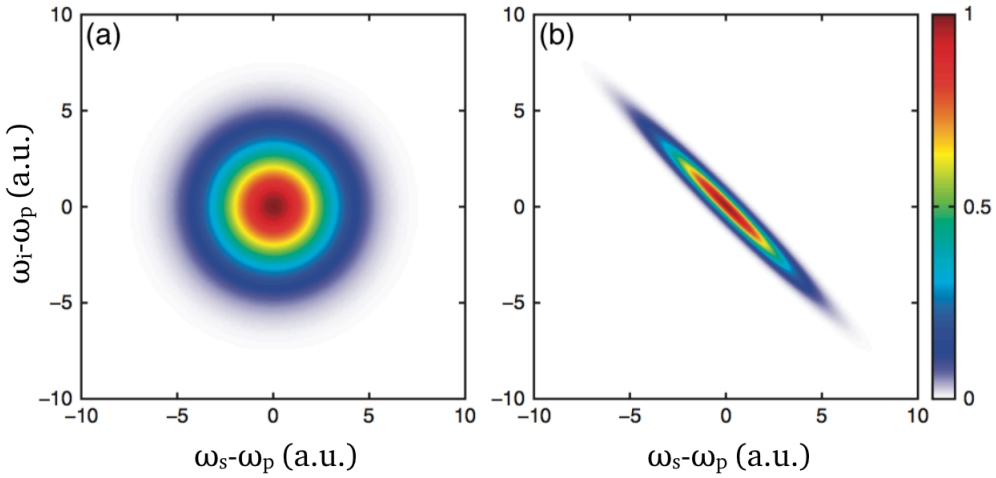

Figure 1.15: Normalized joint spectral density (JSD) of the idler and signal photons in the case of (a) uncorrelated and (b) correlated photons [208]. The JSD basically gives the frequency of the idler (y-axis) as a function of the frequency of the signal (x-axis) and vice versa.

where $\langle n_{\omega_i} \rangle_{A_{\omega_s}}$ is the average number of idler photons at a frequency ω_i stimulated by a signal seed at a frequency ω_s, $\langle n_{\omega_i} n_{\omega_s} \rangle$ is the average number of photon pairs that would be produced through SFWM and $|A_{\omega_s}|^2$ is the average number of photons within the signal coherence time. Many experiments have been carried out exploiting the JSD technique, by using waveguides [262], optical fibers [264], BBO crystals [267] and microring resonators [207].

In particular, in the case of FWM in microring resonators, the assessment made by Helt *et al.* on the possibility of controlling the spectral correlation of the generated photon pairs by tuning properly the spectral properties of the exciting pump [204], has been proved [207]. So, in principle, microring resonators can generate pairs of photons ranging from nearly uncorrelated to highly correlated depending on the laser pump properties, as shown in Fig. 1.15. From the figure, it can be seen that in the case of uncorrelated (a) generated photons, the JSD would have a circular shape and no information on the idler energy can be inferred from the signal energy (and vice versa). On the contrary, in case the photons emitted in the spontaneous process would be energy-entangled (Fig. 1.15 (b)), the JSD would be closely peaked to the antidiagonal and for each signal frequency a single idler frequency can be inferred from the energy-momentum conservation law. Indeed, in the case of a narrow pump laser, which have a long coherence time, the energy-momentum conservation law implies strong energy correlation between the idler and signal photons. Conversely, when a broader laser, with a shorter coherence time, is employed the energy conservation constrain the energies of the emitted photons to be in an interval spanning the pump spectrum. Thus, the generated photons will have low energy correlation.

Chapter 2

FWM in a silicon integrated Bragg waveguide

This thesis is mainly focused on the study of silicon integrated nonlinear optical components, ridge waveguides and microring resonators in particular, with the aim of characterizing their ability to emit pairs of entangled photons. In fact, as explained in Sec. 1.2.2, silicon ridge waveguides and microring resonators are very good sources for nonclassical states of light [46, 27, 268, 224, 22, 208]. In silicon, photons pairs are created by the spontaneous four-wave mixing (SFWM) process (see Sec. 1.2.1), a third-order nonlinear effect in which two pump photons are converted in two other photons at higher (idler) and lower (signal) frequency than the pump light. In the process, energy and momentum are conserved [46], and the emitted pairs can be in a time-energy entangled state [27].

An important aspect we want to study in our work is the efficacy of integrated filters to spectrally clean the generated photon pairs. Besides that, we also want to examine the effect of the filters on the correlations between the emitted photons.

Despite the large field enhancement that can be achieved in silicon ridge waveguides and microring resonators, the efficiency of SFWM is relatively low, with the average number of photon pairs generated being typically 9-10 orders of magnitude smaller than that of the pump photons. Thus, the simultaneous integration of the source with the detection stage on the same chip requires the development of an optical filter capable of 100 dB of pump rejection. This is particularly challenging, for all the frequencies of interest are in the same spectral region, with the signal and idler frequencies symmetrically spaced around the pump. Recent progresses in the integration of such a filter in a silicon chip have been reported exploiting three main strategies: coupled ring resonators [269], Bragg waveguides [37] and cascaded interferometers [270]. However, all these approaches rely on optical elements composed of hundreds of microns of silicon waveguide, which are potential sources of unwanted photon pairs whose spectral and temporal correlations are usually different from those of

the photons emitted by the actual source. For instance, in the case of heralded single-photon sources, these parasitic photons could lower the purity of the heralded single-photon state, thus reducing dramatically the performance of the entire device. However, the purity of the heralded state is of central importance for most quantum information protocols, in which one envisions a large number of multiplexed integrated sources [21, 271, 260] for application in linear optical quantum computation and simulation [83, 125, 272, 91, 92, 93, 273].

In this chapter, we then investigate the generation rate and spectral correlations of parasitic photon pairs generated by SFWM in a Bragg waveguide (BW). Our experimental approach exploits the connection between spontaneous and stimulated four-wave mixing (FWM) [261] and is supported by a theoretical quantum model of pair generation in the integrated structure. First, we will illustrate the fabrication process of our sample, that has been produced in a fab through the standard CMOS procedure. Then, after describing the experimental setup we used, we will report on the characterization of the sample. After that, we will give the details on the performed FWM experiment and the obtained results are then compared to a theoretical model of our device. This work shows the importance of BWs as filters for integrated photonic circuits, in particular for quantum applications when high extinction rates of the optical pump are required. Moreover, this experiment tackle for the first time the problem caused by the emission of photons through FWM in integrated filters. This in fact would pollute the quantum state at the output that should be used for quantum applications.

2.1 Fabrication of the sample

The system used in our experiment was fabricated in the framework of the OpSIS project (Optoelectronic Systems Integration in Silicon [274, 275]), a consortium between the University of Delaware and the institute of microelectronics in Singapore (A*STAR Institute of Microelectronics). The sample is fabricated in a CMOS-compatible industrial process (see Fig. 2.1) applied to a 8-in silicon-on-insulator (SOI) wafer from SOITEC. The SOI wafer is made of different layers: a bulk silicon substrate is covered by a layer of buried oxide (BOX) of 2 μm thickness, on top of which there is a 220-nm-thick epitaxial boron-doped silicon layer [276, 277, 278, 37]. The refractive index contrast between silicon ($n_{Si} = 3.48$ at 1550 nm) and the the silicon oxide ($n_{SiO_2} = 1.44$ at 1550 nm) is quite high, and this brings to strong light confinement in the thin silicon layer because of the total internal reflection (TIR) process. This is the fundamental mechanism that allows to construct all the photonics devices in use.

The fabrication process consists in different steps, based on the fact that silicon dioxide may be grown on the silicon substrate and then selectively removed from designated areas though photolithographic and etching techniques. The process is depicted in Fig. 2.1. First of all, a layer of silicon oxide (SiO_2)

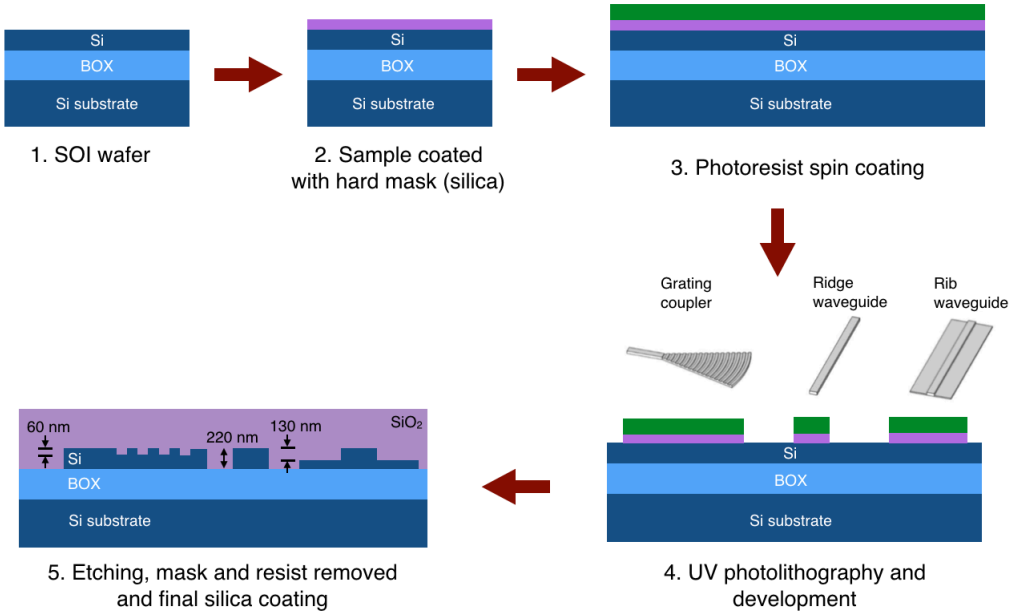

Figure 2.1: Sample fabrication process and components on the chip. The bulk silicon substrate is covered by a 2-μm-thick buried oxide (BOX) layer, on top of which there is a boron-doped silicon layer of 220 nm. The top of the sample is covered with a 2-μm oxide cladding. Three etching steps of different depth define the structures on the sample: 60 nm, 130 nm and 220 nm for grating couplers, rib waveguides and ridge waveguides, respectively. For simplicity, in the figure we depict a single dry-etching step that goes down to three different depths. In the actual process, after the first etching step the photoresist and mask are applied again to impress the desired structures. The same is done after the second etching step. The image is not in scale.

is grown on the SOI wafer. Then, the sample is coated with a photoresist, and exposed to UV radiation at 248 nm through a mask of the designed layout. After these processes, the circuit is drawn on the wafer. The next step is the development, and consists in removing the regions that have been illuminated by the UV photolithography procedure. Finally, the anisotropic dry etching process is used to obtain the structures in the silicon layer. Grating couplers are defined by the first etching step down to 60 nm, whereas rib waveguides are realized through the second etching step to a depth of 130 nm. A final etch step down to the buried oxide is used to pattern the 500-nm-wide by 220-nm-tall ridge waveguides designed to be single mode in the 1500-1600-nm wavelength range. The top of the sample is then covered with a 2-μm oxide cladding in order to protect the photonic structures on the chip. Eventually, in order to activate dopants, a rapid thermal anneal (RTA) of 1030 °C for 5 seconds is performed. Studies on the transmission properties of the sample give measured losses for the ridge and rib waveguides of 0.27 ± 0.06 dB/cm and 1.5 ± 0.6 dB/cm, respectively [277].

Grating couplers

One of the biggest challenges of silicon photonics is coupling light between a single-mode optical fiber and a sub-micron silicon waveguide on a chip. Because the waveguide core layer is only few hundreds-nm-thick and the guided mode is strongly confined in that core, there is a large mismatch between the mode of a waveguide and the one of a single-mode fiber. Among the different strategies studied in order to couple light in and out of the sample, edge coupling and the use of grating couplers seem to be the best solution for many applications.

Through edge coupling, light is coupled in and out of a waveguide by means of a tapered lensed fiber put in correspondence of one side of the waveguide, few microns from the side of the chip. Even if low insertion losses ($< 1\,dB$) have been proved for this kind of coupling [279, 280, 281], the method is very sensitive to alignment and forces to couple light at the edges of the sample only [282].

The other approach used for light coupling, adopted in our sample, is the utilization of grating couplers. They are constructed by expanding the width of the side of the on-chip waveguide and etching a grating that diffracts light out of plane into a fiber placed approximately normal to the surface (see Fig. 2.2). In our case, the etching step down to 60 nm is giving the desired structure. Grating couplers have many advantages over edge coupling. In fact, they can be produced in a CMOS-compatible process (as edge couplers do) and no post-processing is required. They can be placed everywhere across the chip (not only at the edges), not requiring the polishing of the facets and enabling efficient wafer-scale testing. Finally, they facilitate the process of alignment to the chip [282, 283]. However, they have two major drawbacks, that are substrate and mode-mismatch losses. Substrate losses are usually around 35-45 % of the total optical power. They are caused by a power leakage in the

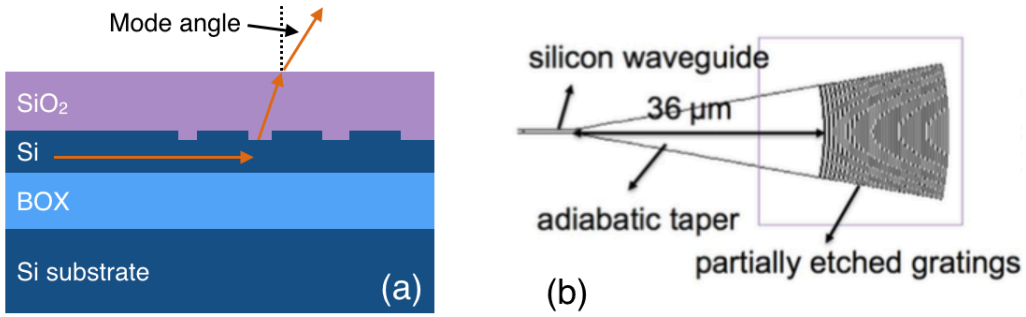

Figure 2.2: Layout (a) and cross-section (b) of the grating coupler (GC) used in our experimet. The device is a 60-nm shallow-etched, nonuniform GC fabricated on a 220-nm layer of silicon on top of a SOI wafer.

silicon substrate instead of an upwards propagation towards the optical fiber, due to gratings being nearly symmetrical in vertical direction. Mode-mismatch losses are, instead, due to the fact that the grating and the fiber have different shape of the mode: exponential and Gaussian respectively. In our sample, mode-mismatch losses are reduced by using nonuniform gratings with spatially varying parameters to adjust the shape of the scattered mode to the mode of the fiber [283]. The grating couplers we use have a mode-field diameter of about 10.5 μm, giving a stable optical coupling. The measured insertion losses for the optimized device are 3.1 dB for a peak wavelength of about 1550 nm abd a 1.5 dB bandwidth of $\approx$50 nm [284]. The layout and cross-section of the grating coupler used in our experiment are shown in Fig. 2.2.

In our chip layout, different grating couplers corresponding to one photonic structure are aligned in the vertical direction and separated by a distance of 127 μm (see Fig. 2.6). This makes possible for us using one single array of fibers, whose cores are separated by 127 μm, to couple light into and out of the sample.

Bragg waveguide

As explained in Sec. 1.2.2, a distributed Bragg reflector (DBR) is a periodic structure formed from alternating two dielectric layers with different refractive index. The DBR can be used to achieve nearly total reflection within a range of frequencies. In integrated photonics, a DBR is obtained by periodically narrowing the width of a waveguide, resulting in an effective change of refractive index. From now on, we call this kind of structure Bragg waveguide (BW).

In our sample (see Fig. 2.6), the BW is made of a channel waveguide and designed to achieve high reflectivity in a 1-2 nm wide stopband centered around $\lambda_0 = 1545$ nm and high transmission outside this range. The layered structure is obtained by periodically shrinking the waveguide width from 500 nm down to 440 nm, with period $\Lambda = \lambda_0/2n_{eff} = 320$ nm and effctive refractive index $n_{eff} \simeq 2.4$, where the value of n_{eff} has been assumed to be compatible with

the BW central wavelength λ_0. The duty cycle of the structure is 50% and the number of periods is $N = 2000$. Measurements of the device obtained from a previous run, exhibited a 20-25 dB extinction ratio for the chosen N. An optical image of the sample is shown in Fig. 2.6, however the BW structure is too small to be observed.

It is important to stress that the actual modulation of the waveguide width is not a sharp-cornered variation but a rounded one. This is due to the fact that the geometric parameters describing the BW are smaller than the diffraction limit of the beam used in the UV photolithography process. Being fabricated well below the resolution limit, the employed BW is far from the ideal case. Moreover, no post-production characterization of the sample has been performed and a SEM image of the device is not available. So, the actual parameters describing the BW could be different from the designed ones for an ideal device. Thus, the simulation described in the following sections gives only approximate information on the used device. Moreover, since the device has been fabricated below the resolution limit of the UV photolithography process, no apodization of the BW has been considered in the simulation.

2.2 Four-wave mixing experiment

In this section we will outline the experimental work needed to complete the measurement. First of all, we will describe the experimental setup we used. Then, we will report on the linear characterization of the sample. Finally, we will explain in detail how we performed the measurement.

2.2.1 Experimental setup

As schematically represented in Fig. 2.3, in order to have a very precise control on the alignment process, the sample is pasted on an aluminum support, which is then fixed on a multiple stage, allowing the translation along the x, y, z directions and the in-plane rotation.

Another important feature for the alignment is to provide a good image of the sample. So, a particular microscope, built in our laboratory for a previous experiment and mounted on a translating stage, is used to have a top-view of the chip. In order to be able to align the fiber array above the sample, we could not bring the objective of the microscope close to the sample surface. The microscope is then built using a Barlow lens in order to satisfy this requirement. The magnified image is then focused on a visible CCD camera and sent to a screen where the sample can be observed. The total magnification of the sample obtained on the screen is of about 200×. Finally, another CCD camera is used to observe the system sample-fiber array from the side. This component is essential for monitoring the distance of the fiber array from the sample during the alignment process.

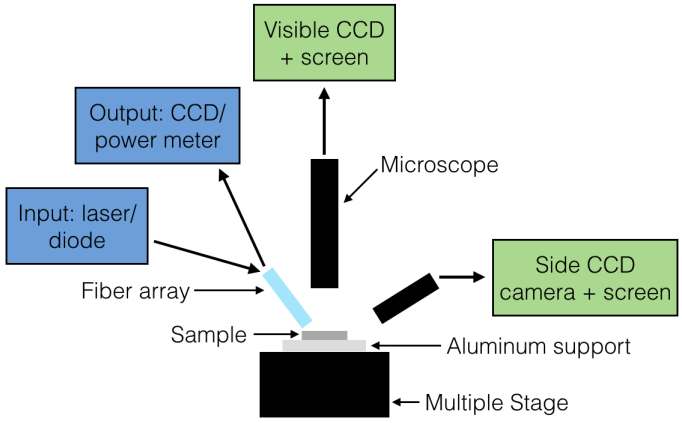

Figure 2.3: Scheme of the experimental setup used for the alignment process. The image is not in scale.

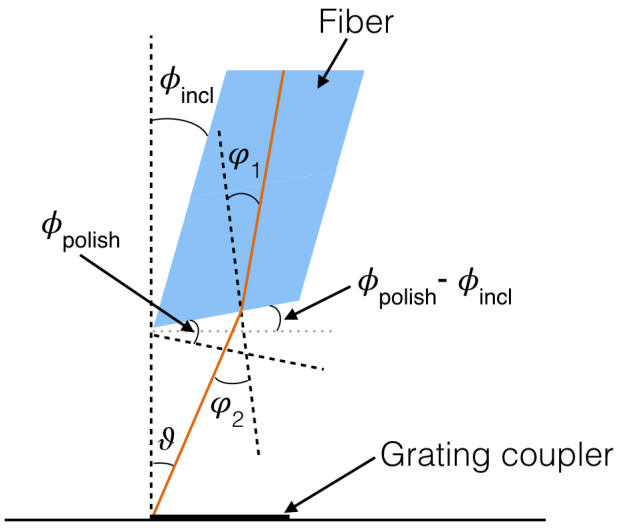

Figure 2.4: Fiber array-grating coupler angle mode matching. ϑ is the mode angle, ϕ_{polish} is the angle at which the fiber array is polished, ϕ_{incl} represents the inclination of the array, and φ_1 and φ_2 are the angles in the Snell's law.

As already mentioned in Section 2.1, the cores of the optical fibers in the fiber array are evenly spaced of 127 μm and this is the same distance of grating couplers on the sample. So, we are able to simultaneously couple up to 8 fibers to the chip. The fiber array, used to couple light in and out of the sample, is mounted on a holder having six degrees of freedom (a three-axis rotating stage and a three-axis piezoelectric translator). This is necessary, in order to fine-tune the position of the fibers over the chip that have to be at a distance of few microns to minimize the coupling to the fiber array of backscattered light due to nearby gratings. In our setup, the mode angle (see Fig. 2.2) is $\vartheta = 17°$ [283] and the angle at which the fiber array is polished is $\phi_{polish} = 14.5°$. If we now want to calculate the correct inclination of the fiber array compared to the vertical direction, we have to consider the Snell's law:

$$n_1 \sin \varphi_1 = n_2 \sin \varphi_2, \tag{2.1}$$

where $n_1 = 1.44$ is the refractive index of silica, $n_2 = 1$ is the refractive index of air and φ_1 and φ_2 are the angles formed by the incident and refracted beam compared to the perpendicular to the air-fiber array interface, respectively, as shown in Fig. 2.4. From the figure it can be seen that:

$$\begin{aligned} \varphi_1 &= \phi_{polish}, \\ \varphi_2 &= \vartheta + \phi_{polish} - \phi_{incl}, \end{aligned} \tag{2.2}$$

and Eq. (2.1) becomes:

$$n_1 \sin \phi_{polish} = \sin \left(\vartheta + \phi_{polish} - \phi_{incl} \right). \tag{2.3}$$

Thus, in order to optimize the coupling at a wavelength of about 1.55 μm, the fiber array has to be tilted compared to the normal to the surface of the chip of an angle ϕ_{incl} of:

$$\phi_{incl} = \vartheta + \phi_{polish} - \arcsin \left(n_1 \sin \phi_{polish} \right) \approx 10°. \tag{2.4}$$

Since the refractive index n_1 depends on the wavelength λ, it is possible to optimize the coupling of the fiber array at a different wavelength by simply varying the inclination angle ϕ_{incl}.

2.2.2 Characterization of the sample

We first obtained a rough alignment to the chip by injecting light from a superluminescent broadband diode (Thorlabs SLD1550P-A1 combined to a Newport Model 6000 controller) and collecting the output light on a spectrometer (Acton Spectra Pro 2500i) equipped with a liquid nitrogen CCD camera (Acton InGaAs OMA V). However, the maximum spectral resolution we had from this measurement is 67 pm. So, in order to have a better scan of the spectrum of the light coming out of the chip, we used a different configuration. In fact, the linear characterization of the BW, is performed by scanning

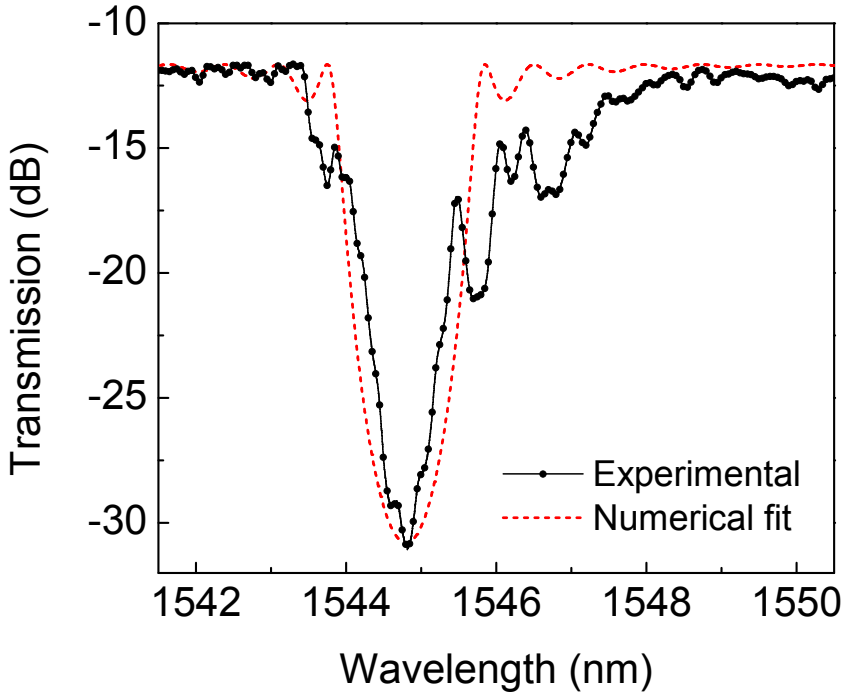

Figure 2.5: Transmission spectrum of the Bragg waveguide around the stopband. The black points are the experimental values, whereas the dashed red line represents the calculation done by using a transfer matrix method.

a monochromatic tunable CW infrared laser (Santec TSL-510) over the desired wavelengths to excite the system and collecting the output light on an InGaAs detector (Newport 918D-IG-OD3) connected to a high dynamic-range power meter (Newport 1936-C). The spectrum was then reconstructed through a Labview software and the resolution is now improved to 2 pm.

The high resolution transmission spectrum of the BW we obtained is shown in Fig. 2.5. The coupling losses at the central wavelength have been estimated to be 5 dB for each grating coupler [37], and the total insertion losses of the sample were measured to be about 11 dB. As shown in the inset of Fig. 2.6, the total length of the waveguide is 1.6 mm, of which the BW takes 640 μm. The spectrum shows a strong reflection around $\lambda = 1544.8$ nm, with a rejection of about 20 dB at the center of the stopband and more than 10 dB rejection over a 1 nm bandwidth.

In Fig. 2.5 we also show a transmission spectrum calculated using a transfer matrix method and assuming an effective refractive index of the 440 nm-wide waveguide $n_{eff} = 2.414$, with an effective refractive index contrast $\Delta n_{eff} = 3.4985 \cdot 10^{-3}$ with respect to the 500 nm-wide waveguide, which can be calculated using the relation [41]:

$$4\left(1 + \frac{\Delta n_{eff}}{n_{eff}}\right)^{-2N} = 10^{-\alpha(dB)/10}, \tag{2.5}$$

where α is the rejection in dB. In Fig. 2.5, an asymmetry in the BW ex-

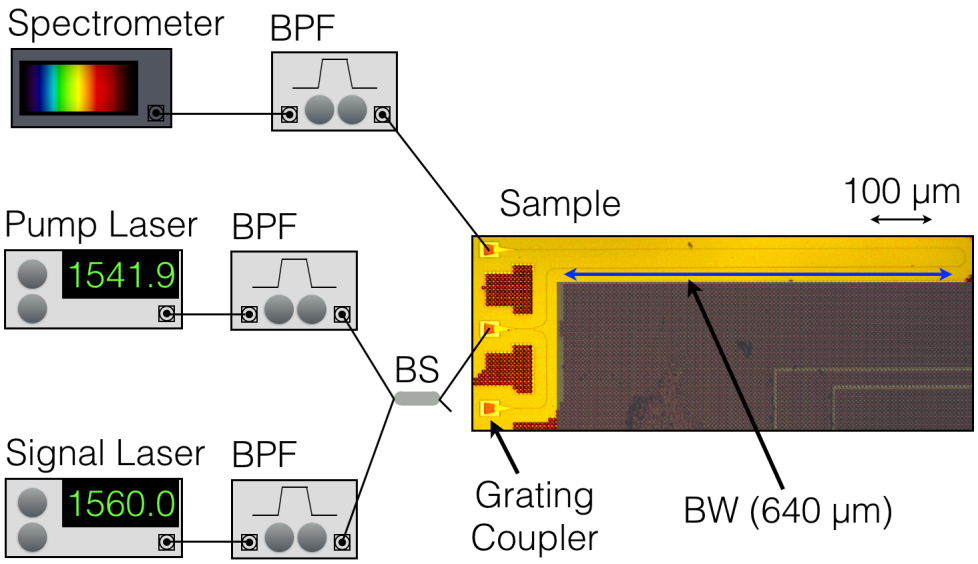

Figure 2.6: Schematic view of the experimental setup used to study four-wave mixing in the Bragg waveguide (BW). BPF stands for band-pass filter and BS for beam splitter. An optical image of the sample used is shown as an inset. The signal wavelength was kept fixed to 1560 nm, whereas the pump wavelength was scanned from 1541.9 nm to 1550 nm in order to probe the FWM process inside the Bragg waveguide stopband.

perimental spectrum can be observed. The main cause for this asymmetry is radiation loss, probably due to the disorder created by the fabrication below the resolution limit in the structure.

2.2.3 Stimulated four-wave mixing

After having characterized the BW on our sample, we proceed with the FWM experiment. As already described in Sec. 1.2.1, FWM is a third-order nonlinear process in which two pump photons are converted in a photon pair (idler and signal photons at a higher and lower frequency than the pump laser, respectively). Energy and momentum are conserved during the process.

The experimental setup we used is represented in Fig. 2.6. Since, in a CW pumping scheme, the SFWM process is too faint to be observed experimentally in a BW, we then studied stimulated FWM. Stimulated FWM has been experimentally investigated by coupling two CW infrared lasers at the pump and the signal frequencies. We fixed the signal laser (Santec TSL-210) at a wavelength of 1560 nm and let the pump laser (Santec TSL-510) scan the wavelength range 1541.9-1550 nm, to probe the FWM process across the BW stopband. Before being injected into the chip, the pump and the signal lasers have been spectrally filtered by means of a 50-dB band-pass filter, to clean out the amplified spontaneous emission (ASE). In fact, the power of the idler

generated through FWM is much weaker than the injected pump and signal powers and the ASE from the two lasers had to be filtered in order to isolate the idler photons. Finally, the pump and signal lasers were combined on a 90:10 polarization maintaining fiber beam splitter (BS) before being injected into the sample through a fiber array, as described in Section 2.2.1. The optical powers coupled to the sample were estimated to be $1.29 \pm 0, .06$ mW and 1.23 ± 0.06 mW for the pump and signal, respectively. Band-pass filters are then used at the output of the sample to suppress the residual pump and signal fields. The idler output was then sent to a spectrometer (Acton Spectra Pro 2500i) and collected by a liquid-nitrogen-cooled CCD camera (Acton InGaAs OMA V).

The band of the used band pass filters is limited to $\sim$5 nm, whereas we scanned the pump through $\Delta\lambda \approx 8$ nm, that translates in an idler bandwidth of $\Delta\lambda \approx 16$ nm. So, we divided the idler generation and pump bandwidths in five steps of about 4 nm and 2 nm, respectively. For each step we collected all the spectra of the generated idler and combined them together in order to obtain one single FWM spectrum, as shown in Fig. 2.7 (a). The results will be discussed in the next section.

Results

The result of the experiment is shown in Fig. 2.7 (a). On the y-axis the measured CCD intensity is plotted against the wavelength range of the pump laser. From the measured CCD intensity we then calculated the idler generation rate inside the BW, obtained after calibrating the CCD response against a high-sensitivity power meter and compensating for the transmission of the output filters. In Fig. 2.7 (b) we report the estimated internal generation rate of idler photons as a function of the pump wavelength, per mW^2 of coupled pump power. The strong suppression of FWM corresponds to the BW stop-band. In Fig. 2.8 we also show one of the FWM spectra obtained during the measurement. In particular, this spectrum corresponds to a pump wavelength of $\lambda_p = 1545.6$ nm, and an acquisition time of the CCD camera of 0.3 seconds. In the figure, the pump and signal positions are indicated by the green and red arrows, respectively. It can be seen that the pump and signal lasers are completely suppressed by the band-pass filters in our setup.

As already mentioned, the SFWM process associated with the stimulated process is too faint to be observed experimentally in a BW. However, the two processes can be related in a simple way. In particular, the spontaneous emission rate $P_{i,spont}$ can be directly connected to the stimulated emission rate $P_{i,stim}$ via the relation [261]:

$$P_{i,spont} = \hbar\omega_i \Delta\omega \frac{P_{i,stim}}{P_s}, \tag{2.6}$$

where P_s is the coupled signal power and $\Delta\omega$ is the emission bandwidth.

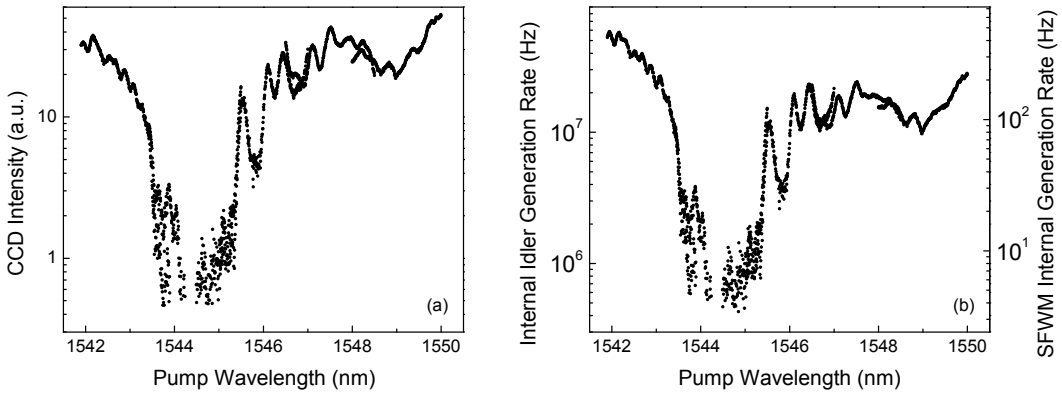

Figure 2.7: (a) CCD intensity measured during the experiment as a function of the pump wavelength. (b) Idler generation rate per mW^2 inside the chip (left y-axis) as a function of the pump wavelength. On the right y-axis we report also the inferred generation rate per mW^2 for the SFWM process.

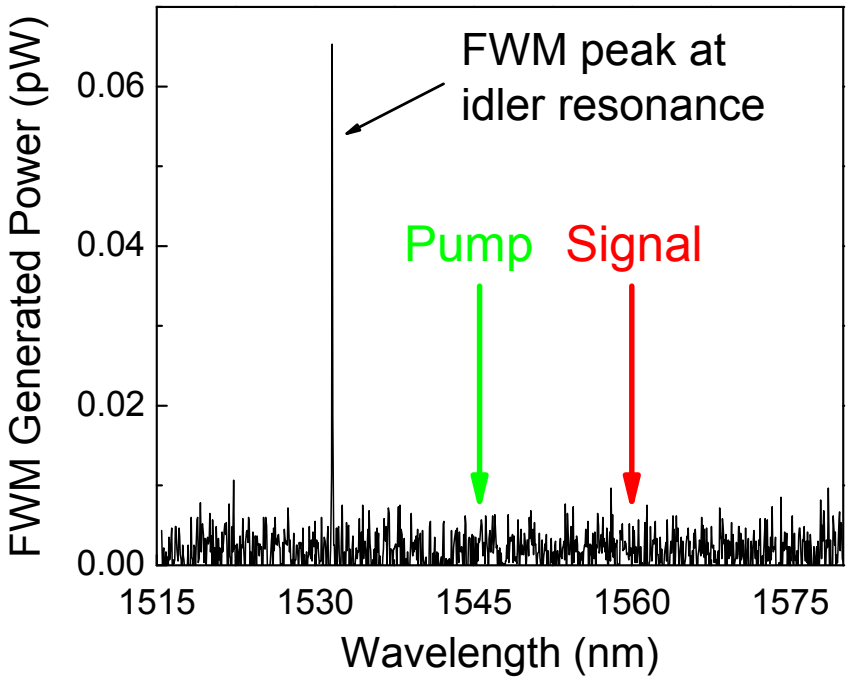

Figure 2.8: One spectrum of the idler photons for $\lambda_p = 1545.6$ nm and $\lambda_s = 1560$ nm (acquisition time of 0.3 seconds).

Since we are interested in filtering photon pairs generated from ring resonators, which usually emit in a narrow bandwidth, we can give an estimation for filtering in actual samples. So, if we consider $\Delta\omega = 2\pi \times 10$ GHz, that is a typical value for integrated sources, resonant or post-filtered, we obtain a quality factor $Q \approx 20000$ at $\lambda \sim 1550$ nm. This is a reasonable quality factor for common light sources, that typically yield generation rates larger than 1 MHz in a 10 GHz bandwidth [208, 207].

We report the expected spontaneous emission rate from the BW on the right y-axis of Fig. 2.7 (b), where we notice that the average rate of photon pairs generated at the bottom of the stopband is 5 Hz (see also the experimental result in Fig. 2.9). Since our BW already provides 20 dB of pump rejection, we expect this figure to be very close to the total generation rate observable in a longer structure as well. This generation rate per mW^2 is at least 5 orders of magnitude smaller than what efficient silicon integrated sources can produce, thus ruling out any hypothesis of spurious contributions introduced by the filter, even for the most demanding schemes where many sources are multiplexed [21, 83, 91, 92, 93, 260, 271].

It is important to stress that, in order to discriminate the generation rate of the BW from the amount of idler generated in the waveguide before the BW in Fig. 2.7 (a), we also measured the stimulated FWM emission from a waveguide on our chip. We then scaled the result to the actual waveguide length before the BW by considering that FWM emission in waveguides goes as $1/L^2$, where L is the length of the waveguide. We found a background of about 20% at the bottom of the BW stopband due to FWM emission from the waveguide before the BW. This value is not enough to change the order of magnitude of the idler generation rate in the BW.

Finally, it is important to notice that when the injected wavelength approaches the BW band edges, the grating reflection reduces and the grating is no more reflecting. So, in *ideal* BWs, when the pump is propagating at the wavelengths corresponding to the band edges, the group delay is maximum and, being in a slow-light regime, an enhancement in the idler generation is expected. However, in our experiment, we dealt with a very long BW (640 μm) with a very small effective index contrast ($\Delta n_{eff} \sim 10^{-3}$). Moreover, the fabrication below the UV photolithography resolution limit produced disorder in the employed structure. For these reasons, the slow-light effect is not present in our device and we do not observe field enhancement at the BW band edges in Fig. 2.7.

2.3 Theoretical model

Our experimental work is then compared to a theoretical model based on a full quantum description of the filter, which also allows to investigate the spectral properties of the generated pairs. In Fig 2.9, we show the theoretical prediction for the pair generation rate as a function of the refractive index

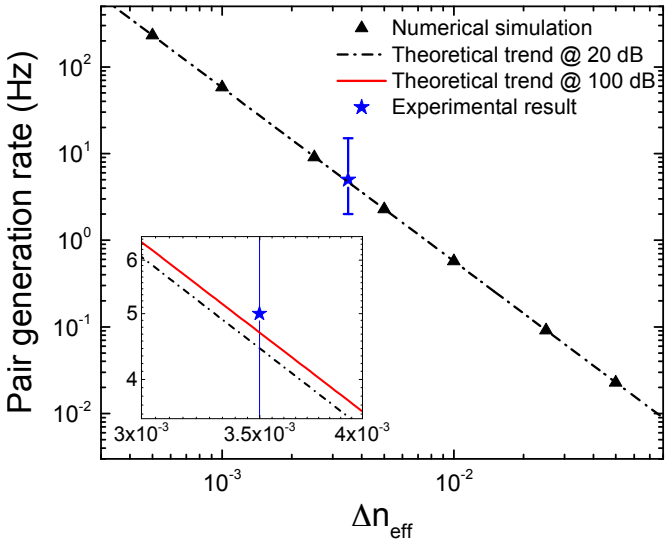

Figure 2.9: Pair generation rate in the Bragg waveguide as a function of the index contrast.

contrast when the BW is modeled using the same parameters adopted for the transmission spectrum, together with the experimental result from our sample.

The results are obtained by means of numerical simulations of the structure based on coupled mode theory [41], the asymptotic-fields method [285] and the backward Heisenberg picture approach [286]. In our computation, we assume a fixed 20 dB extinction rate for the BW and, given a specific effective index contrast, we adjust the number of periods of the BW using Eq. (2.5). Since the probability to generate a photon pair by SFWM in the BW is very low, we are working in the undepleted pump approximation, so that the state of the frequency-converted photons is given by

$$|\psi\rangle = |\text{vac}\rangle + \beta\,|\text{II}\rangle + \cdots, \tag{2.7}$$

where the ellipses refers to higher order terms, which can be neglected in our case, $|\beta|^2$ is the pair generation probability, and $|\text{II}\rangle$ is the normalized two-photon state

$$|\text{II}\rangle = \frac{1}{\sqrt{2}} \int d\omega_1 d\omega_2 \phi(\omega_1, \omega_2) a^\dagger_{\omega 1} a^\dagger_{\omega 2} |\text{vac}\rangle, \tag{2.8}$$

where $\phi(\omega_1, \omega_2)$ is the biphoton wave function (BWF) and $a^\dagger_{\omega i}$ is the creation operator of a photon with frequency ω_i. In our simulation, we assume a waveguide nonlinear parameter $\gamma = 200\ \text{m}^{-1}\text{W}^{-1}$, which is typical of silicon nanowires [46], and modify the effective index of the BW corrugations by Δn_{eff} over the baseline value n_{eff} of the unperturbed waveguide. The pump central wavelength 1544.8 nm corresponds to the center of the stopband. We take a 1 ns top-hat temporal profile [287] to guarantee that the SFWM generation rate converges to its CW limit. The theoretical trend reported in Fig. 2.9 refers to the pair generation rate per 1 mW of coupled pump power when the idler and

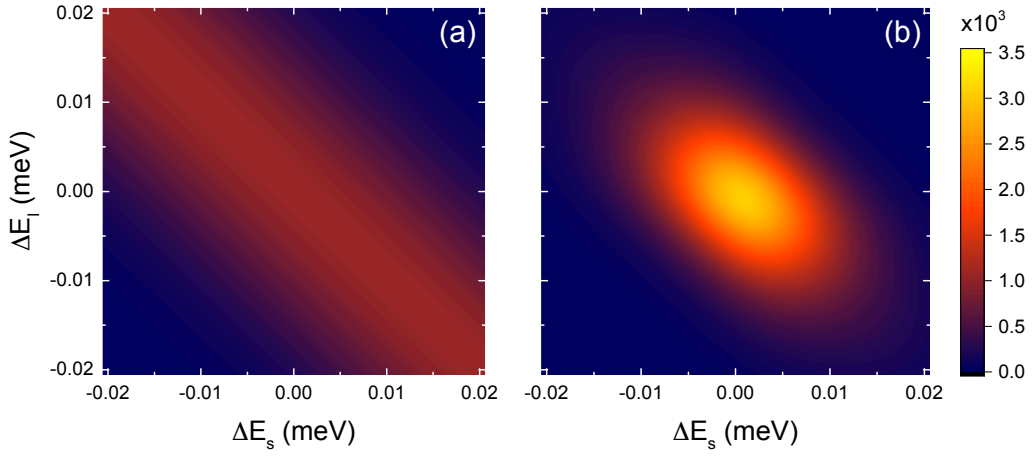

Figure 2.10: Comparison between the JSD of the photon pairs generated by SFWM in (a) a 20 dB Bragg waveguide, and (b) a side-coupled microring resonator.

signal photons are collected in a spectral interval $2\pi \times 10$ GHz wide around 1560.05 nm and 1529.94 nm, respectively. Since the generated idler power is proportional to the square of the waveguide length and the BW length is inversely proportional to the index contrast Δn_{eff} at a target extinction ratio, we expect $P_I \propto (\Delta n_{eff})^{-2}$, which is well verified by our simulations. In Fig. 2.9 we also report the experimental result, which is in good agreement with the theoretical prediction. The figure reports the calculated generation rates for two cases: the measured 20 dB rejection filter, and a 100-dB rejection filter as would be required for a complete pump suppression. Notice that the pair generation rate is almost identical, the difference between the two cases being much smaller than the experimental error bar. Indeed, most of the generation occurs in the first part of the BW, as the pump power decays exponentially within the BW. Therefore, increasing the length would not significantly alter the number of generated pairs.

Another relevant aspect of integrated filters is the characterization of the spectral quantum correlations of the photon pairs generated by SFWM in the filter itself. In Fig. 2.10 we show the joint spectral density (JSD, the square modulus of the BWF) of the frequency-converted photons generated in the BW, along with that of photon pairs that would be generated by a source of heralded single photon states based on SFWM, represented by an integrated microring resonator. In this scheme, when the pump duration is comparable or shorter than the photon dwelling time in the resonator, one can obtain the generation of nearly uncorrelated photon pairs, a key requirement for heralding single photons in a pure quantum state [288].

For our comparison, we consider a 15 μm-radius side-coupled microring resonator, composed of a SOI ridge waveguide. We assume that all the resonances involved in the SFWM process ($\lambda_P = 1534.55$ nm, $\lambda_S = 1544.27$ nm,

and $\lambda_I = 1524.94$ nm) have a quality factor $Q = 40000$, which corresponds to a dwelling time $\tau_d = 33$ ps. Accordingly, we shape the pump pulse with a Gaussian profile with such temporal width. The resulting JSD, reported in Fig. 2.10(b), is approximately circular, which is characteristic of nearly uncorrelated photon pairs. In Fig. 2.10(a) we report the JSD of the photons pairs in our filter. In this case, as expected, we observe the generation of highly anti-correlated photons pairs, a typical feature of straight waveguides. In both cases, the waveguide nonlinear parameter, pump power and waveguide dispersion are assumed identical. In particular, for a 1 mW pump power and a nonlinear waveguide parameter $\gamma = 200$ $\mathrm{W^{-1}m^{-1}}$, we calculate a generation probability per pulse in the microring $|\beta_{Ring}|^2 = 1.0427 \cdot 10^{-3}$, which compares favorably to the same figure in the BW $|\beta_{BW}|^2 = 1.5366 \cdot 10^{-11}$.

2.4 Conclusions

In this chapter we investigated the FWM mechanism in a silicon integrated Bragg waveguide. Since the SFWM process is too faint to be observed in our structure, we first performed a stimulated FWM experiment. We then related the obtained stimulated emission rate to the spontaneous emission rate through Eq. 2.6, that we report here for convenience:

$$P_{i,spont} = \hbar\omega_i \Delta\omega \frac{P_{i,stim}}{P_s}. \tag{2.9}$$

We found that the average rate of photon pairs generated at the bottom of the BW stopband through the SFWM process is about 5 Hz. Our structure provides 20 dB of pump rejection, so we expect that our result can be very close to the total generation rate observable in longer BWs as well. We then compare our result to the theoretical value calculated by means of a full quantum model of the filter, which also allows to investigate the spectral properties of the generated pairs. We find a good agreement between theory and experiment, confirming that stimulated FWM is a valuable approach to characterize the nonlinear response of an integrated filter. Moreover, since efficient silicon integrated sources can produce photon pairs in the MHz range, our result is at least 5 orders of magnitude smaller than that. Thus, filtering through a BW structure will not pollute the quantum state at the output.

We want to stress that BWs are among the most promising for on-chip pump filtering, as they do not require to be actively tuned. Besides, our sample was realized in a silicon photonics fab by using a CMOS compatible process, meaning these filters are widely accessible for general photonics applications. These features, combined with the results of our experiment, show that BW filters are ideal structures to provide large pump extinction while avoiding spurious nonlinear processes that may decrease the fidelity of on-chip generated quantum states. So, BWs can be considered the best candidate for on-chip filtering of the pump in quantum applications.

However, a comment on losses when dealing with long devices is needed. In fact, an 80-dB on-chip rejection of the pump by using a BW has already been proved by N.C. Harris *et al.* in 2014 [37]. In this work, BW losses were estimated to be 3−5 dB. However, longer BWs are needed to achieve the desired 100-dB-rejection filter and losses of about 4−6 dB are then expected. This value has to be decreased for using BWs for actual applications in the field of quantum technology. So, future research is still needed to optimize the filtering of the optical pump on a single chip.

Chapter 3

Photon pairs generation in a self-pumping geometry

In the previous chapter, we have addressed a potential issue met by silicon photonics when dealing with integrated filters, for they could potentially pollute the quantum state produced on a chip.
Now, we want to assess another relevant problem for silicon photonics, that is the integration of the pump laser on a silicon chip. Achieving laser emission in silicon is a long-sought goal, due to the 1.12-eV indirect bandgap of this material, that makes the electron-hole recombination a low-probability phonon-mediated process. Thus, it turns out that silicon is a poor light emitter [289, 290].

In the last years, many different systems have been studied to find a way to achieve laser emission in silicon and that can be compatible with the current microelectronic and optical communication technologies [289, 290, 291]. Some examples are stimulated Raman scattering (SRS) [292], rare-earth doping [293], the use of epitaxial III-V materials [294] and hybrid laser technologies [295, 296]. There are several requirements such a laser source should meet to be used as pump for silicon based sources of photon pairs [291]. For example, the source has to be connected with the fiber-optic network in use, so it should emit around either 1.31 μm or 1.55 μm.

Moreover, due to the need of compact sizes and high integration density, lasing should be achieved through electrical pumping. The potential laser should have sufficient output power with high power efficiency and low energy cost-per-bit in data transmission. Last but not the least, the used technology has to be compatible with the CMOS fabrication process, in order to allow for a mass production of the device.

The first idea of using SRS in silicon waveguides to construct silicon amplifiers and lasers was suggested in 2002 [297]. Spontaneous Raman scattering (RS) occurs when an incident beam is absorbed by the medium and two different radiations are produced at lower (Stokes RS) and higher (anti-Stokes RS) frequencies of the incident light. Conversely, when Stokes photons (signal) are

injected in the material together with the original beam (pump), other Stokes photons are generated and amplification is possible. The process is now called SRS. The first silicon Raman laser was proposed in 2004 [298]. However this technology suffers from a major drawback: the free carrier absorption (FCA) process produces optical losses that prevent a net gain in a silicon waveguide [167]. Another issue is related to the required high pump powers in Raman lasers [299], that produce losses through the two-photon absorption (TPA) mechanism. Even if solutions to these two major problems have been studied and Raman lasers can act as an excellent light sources in a very large of wavelengths, they still cannot be applied to silicon photonics due to their intrinsic optical-pumping mechanism.

Another possible proposed way of solving the light-emission problem in silicon is by using rare-earth doped optical fibers. Usually, the most common dopant in use is erbium, due to its ability to emit light at around 1.55 μm [300]. However, silicon is not suited for hosting erbium and only little emission can be achieved at room temperature. A way of solving the problem has been found in trying to optimize devices geometries and doping distributions, for example as in silicon nanocrystals formed in silicon rich oxide [289, 301]. However, difficulties in the fabrication and integration processes, material gain and energy transfer efficiency are met due to the small sizes and high electrical pumping requirements [290, 291].

Despite its indirect bandgap, even germanium is an attractive choice for making lasers on silicon. This is possible due to the the direct bandgap at 0.8 eV that it exhibits close to the indirect bandgap at 0.66 eV. Due to this particular band structure, germanium can be engineered to emit at the telecom wavelengths around 1.55 μm [302]. The first demonstration of laser emission at around 1.52-1.62 μm in a germanium on silicon CW laser at room temperature was performed at MIT in 2010 [303]. Due to some features of germanium light sources, such as an emission efficiency that increases with temperature and the large gain spectrum, they are competitive candidates for silicon-compatible on-chip lasers. The first electrically pumped germanium laser was successfully demonstrated in 2012 [304], but two major issues of high threshold and low emission efficiency were found. Another big problem to be solved is the narrowing of the bandgap with a consequent redshift of the emitted light to wavelengths far beyond the desired 1.55 μm due to the process used for modifying the germanium band structure [291].

Also III-V compounds, such as GaAs and InP, with direct bandgap and interesting photonic properties can be used to achieve lasing through electrical pumping in the silicon platform. In this technology the major drawback is due to the big mismatch between the lattice constants and the thermal expansion coefficients of silicon and III-V materials. The result is the presence of many defects at the interface that causes large power losses, with the consequent impossibility of growing III-V materials on top of SOI. This is also due to the relatively high temperature needed for the growth that can damage the devices

previously integrated on silicon [290]. Different strategies have been studied to reduce the growth temperature, such as the bottom-up self-organized growth technique used for producing on-chip InGaAs nanopillar lasers [305, 306], that is even CMOS-compatible. However, this technology has to be further developed in order to obtain fully functional devices [291].

Finally, another option for building lasers on top of silicon is the newly developed field of hybrid lasers, which combines different materials instead of one single material grown on silicon. Often, hybrid lasers are made on different substrate (such as germanium or silica) other than silicon, and they are transferred on the silicon substrate at a later stage [307]. The first demonstration of electrically pumped hybrid silicon laser was performed in 2006 [307]. However, improvements on the emission efficiency through the study of the best combination of materials into hybrid lasers and on an easier wafer bonding process are still needed [308]. In this direction, even new structures, such as ring or disk geometries [309], can also be explored. However, the major drawbacks of this technology lie in still low light confinement, high modal losses and high thermal impedance in these devices [290].

Despite all the studied strategies, the difficulty of integrating sources of light in the silicon platform still remains one of the major obstacle in silicon photonics [289, 290, 291]. In particular, one of the biggest issues is to build a fully CMOS-compatible integrated tunable laser. So, in this chapter, we will introduce a method for building a fiber-based silicon integrated source of light, without the need of an external *tunable* laser acting as optical pump. Moreover, in our proposed geometry, the laser frequency is automatically tuned to the pump frequency.

The choice of implementing a fiber-loop laser is that this technology has been widely employed in telecommunication applications since a long time [310]. Deriving from the Raman fiber lasers, where an optical fiber is used as gain medium and the amplification of light is due to the stimulated Raman scattering process, fiber lasers are made of an optical fiber doped with rare-earth elements (such as erbium, ytterbium and so on) that acts as gain medium [310, 311, 312, 313]. The extensive use of the fiber lasers in fiber-optic networks is due to the many advantages this technology can provide [314, 315]. First of all, since no bulk components are present in the cavity, they do not need any kind of alignment. Hence, they are very stable both in wavelength and output power. Moreover, light is already coupled to an optical fiber, thus making the delivery of light out of the laser into the fiber-optic network very simple and the output power can be quite high, for the active region (fiber) can be very long. Second, they are particularly simple to use, for they are usually connected to a user-friendly graphical interface. Third, they have a low cost of ownership, for they have low power consumption, require little maintenance and have long lifetime. Besides, because of the waveguiding properties of the optical fibers, the problems of the optical beam related to the cavity alignment being sensitive to temperature and mechanical vibrations are no longer present.

Thus, fiber lasers have a high optical quality. Finally, they can be very robust and compact in size compared to other lasers (for example gas lasers), due to the fact that the fiber can be coiled in order to reduce the occupied space.

All the listed features make the use of a fiber-based laser the optimal choice for our needs. In fact, our samples are made for being coupled to an optical fiber through grating couplers, thus avoiding unnecessary steps to guide light into the gain medium, that is composed by a doped fiber. Moreover, due to the high losses present in our system, we need a very robust and stable architecture in order to build a lasing cavity.

To address the problem, the photonic structure we used as light source is the microring resonator. In fact, these devices are among the most promising sources of nonclassical states of light for use in quantum technologies [208] and a comprehensive description of this device can be found in Sec 1.2.2. As already explained, silicon microring resonators are microscopic devices integrated on a silicon chip that have been shown to be efficient for on-chip optical nonlinearities. Different effects can be achieved through low-power optical nonlinearities in silicon integrated devices, such as all-optical switching [316], optical bistability [317] and four-wave mixing (FWM) [44]. In particular, we will focus on FWM, that has been shown to be greatly enhanced by the light confinement in microring resonators and can reach high photon pairs production, until the MHz rate [206, 45]. So, microring resonators can act as microscopic, integrated sources of entangled photons [27, 37, 28]. However, as already mentioned above, a big issue still to be solved to facilitate the widespread adoption of microring resonators as quantum optical sources and for the on-chip generation of frequency combs [318, 23] is the need for an external *tunable* optical pump. In fact, as already showed in Sec. 1.2.2, silicon microrings are resonant structures and their spectrum is characterized by discrete sharp spectral resonances. The pump laser is usually tuned to a resonance's frequency. However, the occurrence of thermal or power fluctuations causes spectral changes in the ring resonances, that could even be few hundreds of times the resonance linewidth [319, 320]. Thus, the need of a tunable, or even actively tuned, pump is of pivotal importance in FWM experiments. In particular, the importance of a *tunable* source comes out when dealing with either microring resonators with high quality factors [321] or high pumping powers [46].

The requirement of an expensive and cumbersome external tunable laser acting as optical pump crashes with the need of developing economic devices, that should be quick and easy to operate. So, in this chapter we will show that it is possible to relax the requirement of an external tunable pump by demonstrating that FWM can be achieved in a silicon microring resonator by using a self-pumping geometry [322]. The idea behind this experiment is to insert the microring resonator inside an fiber-loop cavity including an external amplifier. In this geometry gain is spectrally filtered by the microring resonances and lasing can be achieved with enough power to measure FWM emission. Moreover, in the proposed geometry the lasing frequency is automatically tuned to

the pump frequency and follows any shift in the microring's resonances. This effect, in turn, allows to eliminate the saturation effect, usually seen in standard FWM experiments [206], and reach very high FWM generation rates, up to 10^8 Hz.

So, this chapter is focused on the study of the FWM process in a self-pumping regime and is mainly divided in two parts.
The first section is devoted to the study of the stimulated FWM process on a microring resonator with a relatively low quality factor. Here, after illustrating the fabrication process of the sample, we will describe the stimulated FWM measurement. Finally, we will report on the joint spectral density (JSD) experiment carried out in the self-pumping geometry.
The second section is dedicated to the analysis of the spontaneous FWM (SFWM) process on a microring resonator with a high quality factor. We will first give some information on the sample and then we will address the SFWM experiment carried out in our laboratory. Finally, we will report on the coincidence measurement performed in this self-pumping geometry.

3.1 Stimulated four-wave mixing

In this section we will describe how it is possible to perform the stimulated FWM experiment in a silicon microring resonator by using a self-pumping scheme instead of an external laser. First of all, we will illustrate the fabrication process of the used sample. We will then report on the idea behind the experiment, that is to insert a microring resonator in an external-loop cavity with a fibered semiconductor amplifier as a source of gain. The microring resonator will then act as a filter, providing lasing in one of its resonances. The last step of the experiment will be the study of the correlations between signal and idler generated in ths SFWM process. We will do that by using a JSD measurement.

3.1.1 Fabrication of the sample

The sample used for the stimulated FWM experiment is part of a project developed in collaboration with the INtegrated Photonic TEchnologies Center (INPHOTEC) in Pisa. The sample fabrication is CMOS-compatible and is applied to a standard 6-inch silicon-on-insulator (SOI) wafer. The SOI wafer is a layered structure, made of a 3-μm-layer of buried oxide (BOX) on top of a 675-μm silicon substrate, coated with a 220-nm-thick layer of crystalline silicon ($n_{Si} = 3.48$ at 1550 nm). As already explained in Sec. 2.1, the strong light confinement in the silicon layer is due to the high refractive index contrast between silicon and its oxide (TIR).

The fabrication process used for our sample can be summarized in different steps, as depicted in Fig. 3.1. A positive e-beam resist is spin-coated on the top of the SOI wafer. When exposed to an electron-beam (e-beam), the

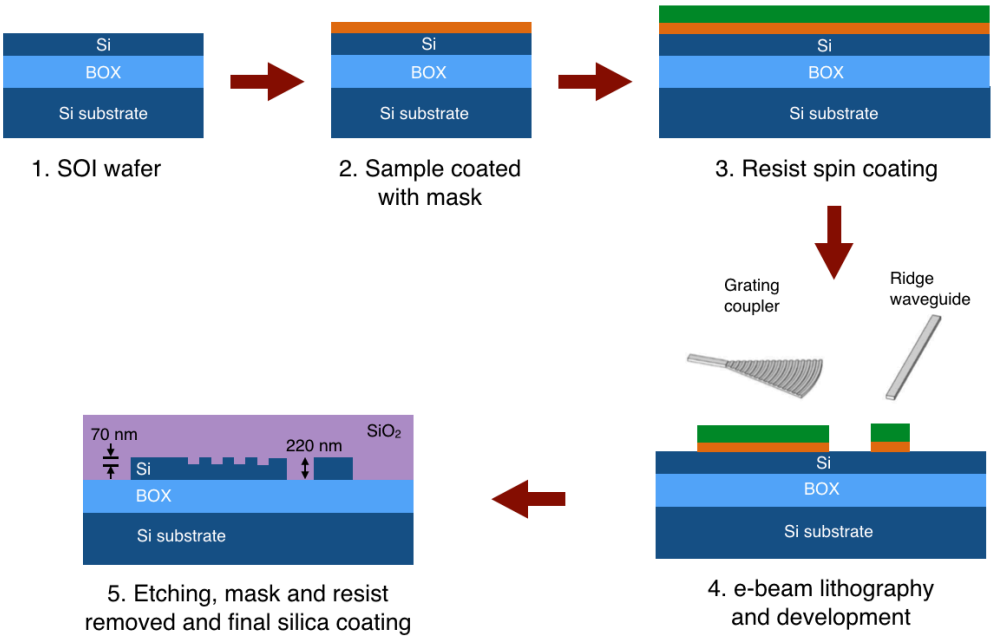

Figure 3.1: Sample fabrication process and components designed on the chip. A 3-μm-layer of buried oxide (BOX) is on top of a 675-μm silicon substrate and then covered with a 220-nm-thick layer of silicon. The top of the sample is coated with silicon dioxide cladding. For simplicity, a single dry-etching step that provides the two structures with different depth (70 nm and 220 nm for grating couplers and ridge waveguides, respectively) is represented. In the actual process, between the two etchings the e-beam resist is deposited again and the chip undergo e-beam lithography another time to impress the waveguide structure. The image is not in scale.

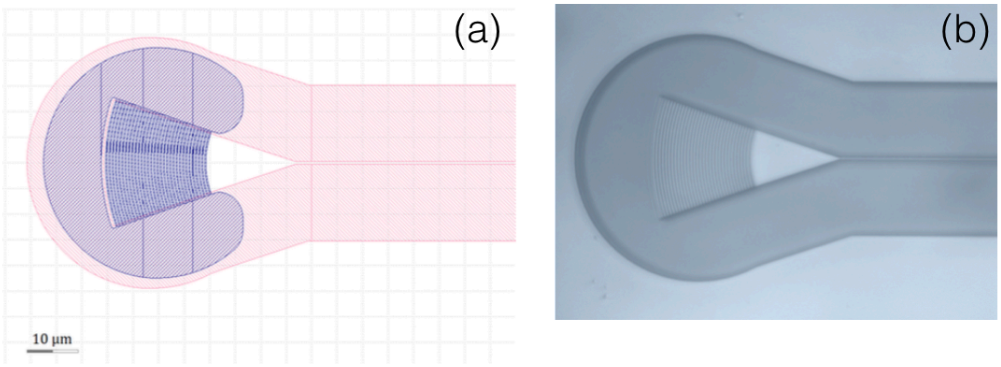

Figure 3.2: (a) Design of the used grating coupler. (b) Optical image of the grating coupler on the chip.

resist solubility will increase. Thus, by using an e-beam lithography process thorough the application of a mask, the designed structures are impressed on the resist. At this point a first shallow-dry-etching step down to 70 nm is performed to obtain grating couplers (GCs) and the remaining non-impressed resist is removed from the surface. The process is then repeated in order to perform a second dry-etching step to get the ridge waveguides. The surface is coated again with the e-beam resist and impressed by e-beam lithography though a mask. The second etching step down to 220 nm is then performed to obtain the desired structures. The non-impressed resist is removed. Finally, a silicon dioxide layer is deposited through a plasma enhanced chemical vapor deposition (PECVD) technique.
The designed chip is completely passive, so no metal deposition nor dopant implantation is required.

Grating couplers

As already extensively explained in the part relative to grating couplers (GCs) in Sec. 2.1, coupling light between a single mode fiber and a sub-micron waveguide on the chip is a challenging task. The main strategies used for coupling light in and out of the sample are either edge coupling or the design of GCs. As in the sample employed in Chapter 2, our choice for light coupling is the adoption of grating couplers. For the advantages of GCs over edge coupling the reader should refer to Sec. 2.1.

The structures on our chip are standard GCs designed and tested at INPHOTEC and they have a similar layout of the GCs used in the FWM experiment on the Bragg Waveguide (see Sec. 2.1). The GCs on our sample are now obtained by expanding the width of the waveguide on one of its sides and etching a grating down 70 nm, as shown in Fig. 3.1. In Fig. 3.2 (a) and (b) the design and optical image of the used GCs are shown, respectively. In Fig. 3.2 (a) the different colors represent the etching steps required to obtain the GC: white surfaces occur where no etching is required (220-nm-thick silicon layer),

pink stands for full-etched zones and blue shows areas where shallow-etching is performed (150-nm-thick silicon layer).

The GCs in this sample are single-polarization focusing (TE mode) optimized for a 0.48-μm-wide waveguide. The diffraction angle is about 10° and the central wavelength is 1550 nm, with a 3-dB bandwidth of 70 nm. Previous measurements indicate insertion losses of 5 dB at 1550 nm.

As in Sec. 2.1, there are different GCs associated to one photonic structure on the chip. These GCs are all aligned in the vertical direction and etched at a distance of 127 μm, that is the gap among the fibers on the fiber array used for light coupling.

Ridge waveguides

As already described in detail in Sec. 1.2.2, the fundamental element used to build photonic circuits is a straight waveguide. The high refractive index contrast between silicon waveguides ($n_{Si} = 3.48$ at 1550 nm) and the material that surrounds it (in our case, silicon dioxide, $n_{SiO_2} = 1.44$ at 1550 nm) makes light confinement possible because of TIR.

The ridge waveguide on the chip used for our experiment is 220-nm tall and 480-nm wide and is designed to be single-mode in the bandwidth 1550-1600 nm. Losses on similar structures fabricated at INPHOTEC have been estimated to be 3 dB/cm.

Microring resonator

As detailed in Sec. 1.2.2, a microring resonator consists in a ridge waveguide looped back onto itself to form a closed path (the so called *all-pass* configuration). Input and output coupling to the microring resonator is obtained through the co-directional evanescent coupling between the ring and a bus waveguide. In microring resonators light confinement is achieved through TIR (as for common waveguides), whereas constructive interference makes them to behave like a resonator. Microring resonators can also be used in a different architecture, that is the *add-drop* configuration. The difference with respect to an all-pass ring resonator is due to the fact that now the microring is coupled to two waveguides. As already explained in Sec. 1.2.2, the term *ring resonator* usually refers to a circular ring, whereas *racetrack resonator* is usually used when the ring shape is elongated and has a straight section in one direction (typically the coupling direction).

For our experiment, we need to use a microring in the add-drop configuration. This because the measurement requires to have one port (the GC labeled as *input* in Fig. 3.3 (a)) for coupling light into the ring, one port (the GC labeled as *drop* in Fig. 3.3 (a)) to close the ring inside a fiber loop and a third port (the GC labeled as *through* in Fig. 3.3 (a)) to observe the FWM emission from the ring resonator. Among the different add-drop ring resonators on the chip, we need to chose a good compromise between a high quality factor (Q)

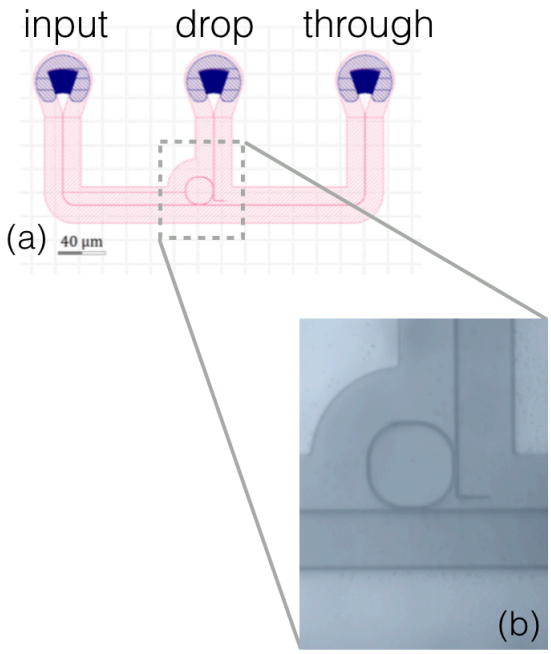

Figure 3.3: (a) Layout of the designed add-drop ring resonator. The ring radius is 10 μm. (b) Optical image of the add-drop ring resonator.

and a relatively big free-spectral range (FSR). In fact, a small separation in the ring's resonances would make the cavity to lase at different wavelengths, instead of one.

So, the resonator we use to perform our experiment is a racetrack in which the radius of the rounded part is 10 μm, that results in a FSR of 7.5 nm. The straight section is 3-μm long and the gap between the bus waveguide and the resonator is of 0.17 μm. The measured quality factor factor is of about 3000. An optical image of the structure is shown in Fig. 3.3. The characterization of the microring resonator is reported in Sec. 3.1.2 (see Fig. 3.13).

3.1.2 Experiment

In this section we will outline the stimulated FWM experiment carried out on our sample. First, we will give the details of the linear characterization of the used sample. We will then report on the design of the built cavity and its characterization. Finally, we will describe the stimulated FWM and JSD measurements we performed and comment on the obtained results.

Characterization of the sample

The building block of the built cavity is made out of the racetrack resonator described in Sec. 3.1.1. So, we first perform the linear characterization of this structure, that consists in measuring the transmission spectra of the resonances and then fitting them by using a Lorentzian function.

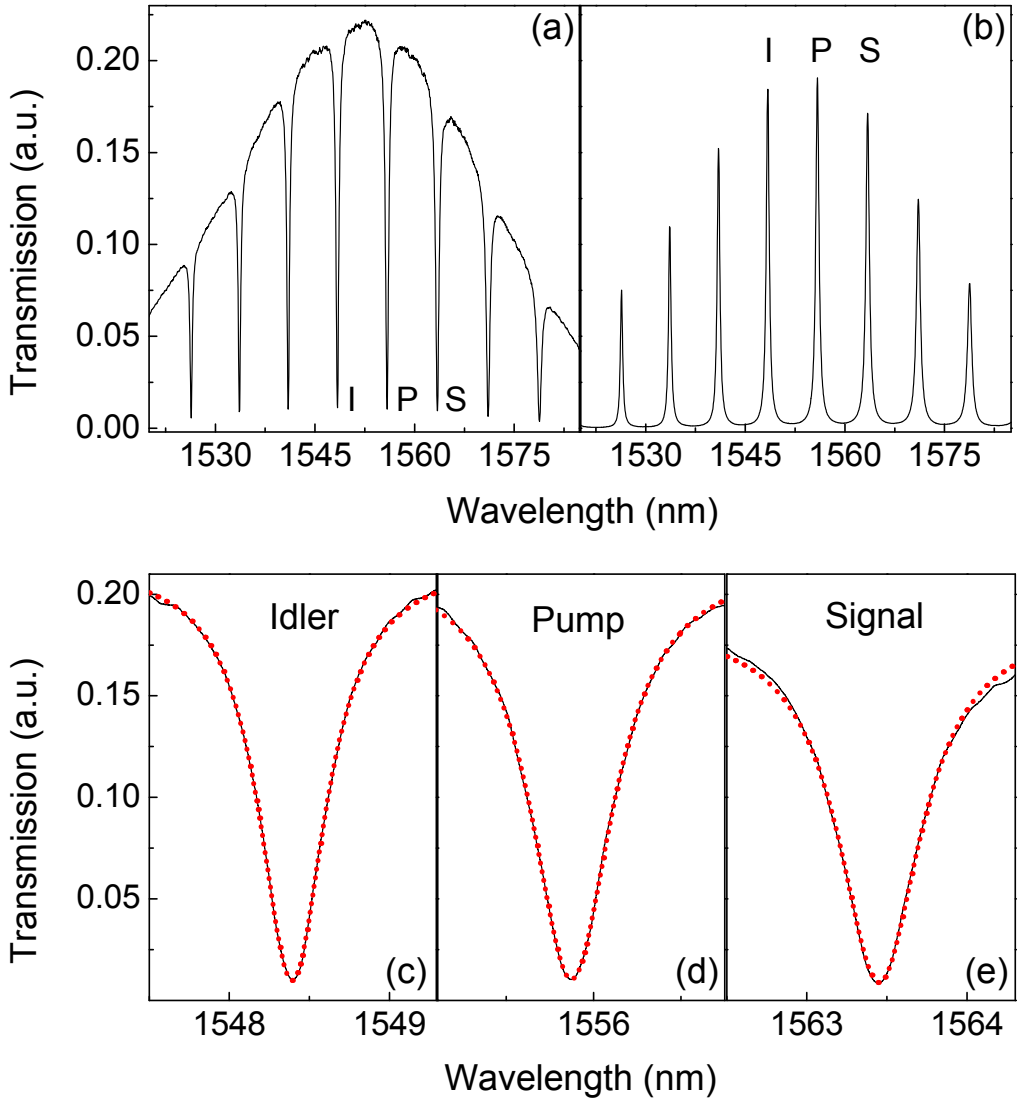

Figure 3.4: Transmission spectra of the (a) through and (b) drop ports of the add-drop ring resonator used in the cavity. The resolution of the spectra is 50 pm. I, P and S stand for the idler, pump and signal resonances used in the stimulated FWM experiment. These resonances are shown in (c)-(e) with a resolution of 2 pm. The black line represents the experimental spectrum, whereas the dotted red line is the Lorentzian fit of the selected resonance. From (a) and (c)-(e), it can be seen that the microring resonances go down to below 5% of transmission. This means that the add-drop ring resonator is close to the critical coupling condition.

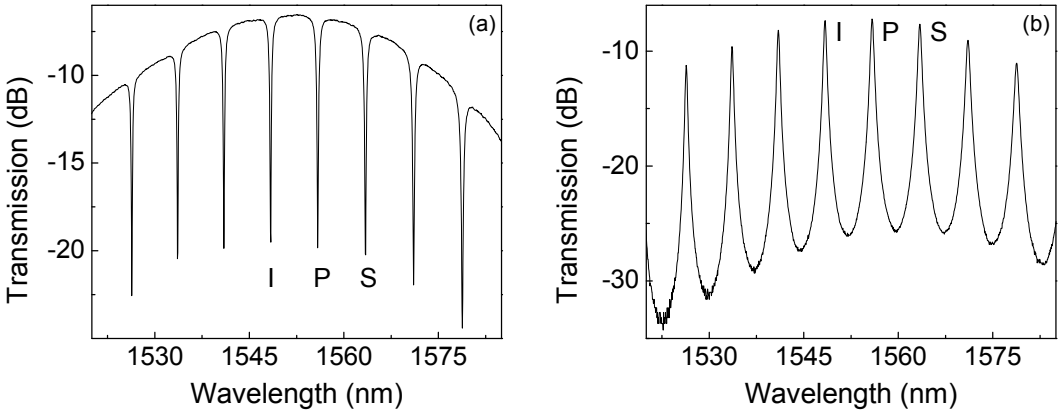

Figure 3.5: Transmission spectra of the (a) through and (b) drop ports of the add-drop ring resonator used in the cavity. The resolution of the spectra is 50 pm. I, P and S stand, respectively, for the idler, pump and signal resonances chosen for the SFWM experiment.

As already descrubed in Sec. 2.2.1, to precisely control the alignment process, the sample is pasted on an aluminum support. This support is fixed on a multiple stage, allowing the translation along the three spatial directions and the in-plane rotation. The image of the sample is provided by the same microscope used in Sec. 2.2.1. This is mounted on a translating stage and gives a top-view of the chip. The magnified image is then focused on a visible CCD camera and sent to a screen where the sample can be observed.
As in Sec. 2.2.1, another CCD camera is employed to have a side view of the sample and monitor the distance of the fiber array from the chip.
As already mentioned, a fiber array in which the fibers' cores are evenly spaced of 127 μm is utilized. This distance is the same separation of grating couplers on the sample. The fiber array is also mounted on a holder having six degrees of freedom: a three-axis rotating stage and a three-axis piezoelectric translator.

A rough alignment to the chip is first obtained by injecting light from a superluminescent broadband diode (Thorlabs SLD1550P-A1 combined to a Newport Model 6000 controller) and collecting the output light on a spectrometer (Acton Spectra Pro 2500i) equipped with a liquid-nitrogen-cooled CCD camera (Acton InGaAs OMA V). The resolution of the output spectrum is of 67 pm.
We then get a more accurate spectrum of the light coming out of the chip by scanning a monochromatic tunable CW infrared laser (Santec TSL-510) over the desired wavelength and collecting the output on a InGaAs detector (Newport 918D-IG-OD3) connected to a high-dynamic-range power meter (Newport 1936-C). A Labview software reconstructs the output spectrum and the resolution can now go down to 2 pm. In Fig. 3.4 the 50-pm-resolution transmission spectra of the through (a) and drop (b) ports are shown. In Fig. 3.5 (a) and (b) the corresponding spectra in dB are also given. I, P and S stand for idler, pump and signal respectively and indicate the resonances chosen for the

FWM experiment. The bell-shape of the spectra is due to the response of the grating couplers, that modulate the intensity transmitted by the sample. We estimated the insertion losses for each grating coupler to be of about 3.6 dB.

In Fig. 3.4 (c)-(e) a high-resolution (2 pm) spectrum (black line) of the single resonances used for the FWM experiment is given along with their Lorentzian fit (dotted red line). The quality factor can be calculated from the fit by using the relation (1.65), that we recall here:

$$Q = \frac{\lambda_0}{\Delta\lambda}, \tag{3.1}$$

where λ_0 is the central wavelength of the resonance and $\Delta\lambda$ is the linewidth of the resonance as obtained from the fit.
The resonances of our racetrack resonator have a linewidth of the order of about 500−600 pm, resulting in a measured quality factor of several thousands (Q=2500−3000), with a free spectral range (FSR) of 7.5 nm. As it can be seen from the figure, the resonances go down to below 5% of transmission, meaning that the ring resonator is close to the critical coupling condition.

Lasing cavity design

As already mentioned, given the persisting difficulty of achieving optical gain in silicon, the idea is to take advantage of an external source of gain and build a closed-loop cavity with the source of entangled photons inside the loop. By using this geometry, we are able to get rid of the external laser used for pumping the system in the FWM experiment.

The scheme of the cavity we built is shown in Fig. 3.6. The add-drop configuration of the resonator is necessary to insert the microring in a loop. So, the source of gain is a Booster Optical Amplifier (Thorlabs BOA1004P) connected to a controller (Thorlabs ITC4005) and with a small signal gain of up to 30 dB. The cavity is closed on the input and drop ports of the racetrack resonator. Input and output coupling with the silicon chip is obtained through the use of grating couplers, as already detailed in Sec. 2.1. The add-drop resonator basically acts, inside the cavity, as a band-pass filter (BPF) for each resonance. In our experiment, a single resonance (λ_p = 1555.87 nm) was selected for lasing by restricting the cavity transmission using an external BPF at the amplifier output. This external filter also serves to reduce amplified spontaneous emission (ASE) from the BOA to a level lower than the generated FWM experiments. In order to obtain the BOA background noise suppression, we cascaded three BPFs for a total rejection of more than 150 dB in the idler generation band. An isolator is also inserted right after the BOA in order to prevent reflected light to go back to the amplifier. A second BPF, identical to the previous one, tuned to the pump resonance was used at the sample output to further improve the rejection of frequencies other than the lasing mode before amplification. The laser power inside the cavity was monitored using a 99:1 polarization maintaining beam splitter (BS_2) before the amplifier.

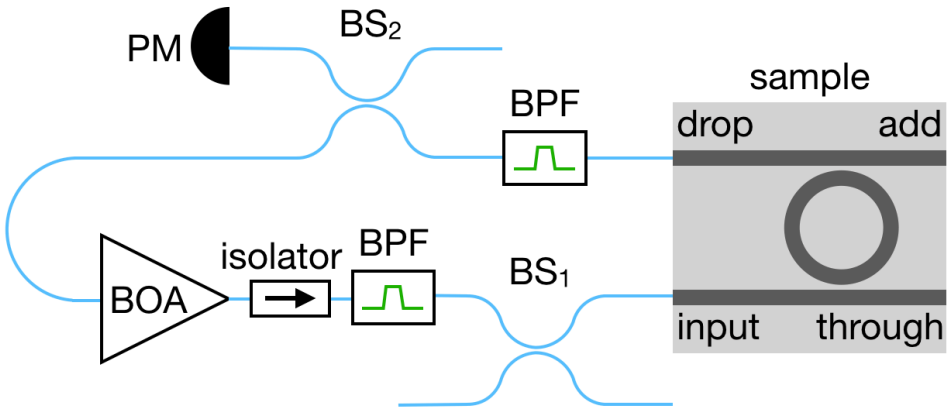

Figure 3.6: Scheme of the cavity. The idea is to insert the microring resonator inside an external fiber-loop cavity including an amplifier in order to provide gain. BPF stands for band-pass filter, BS for beam splitter, PM for power meter and BOA for booster optical amplifier. BS_1 is a 50:50 polarization maintaining beam splitter, whereas BS_2 is a 99:1 polarization maintaining beam splitter, with the 1% port connected to the PM. A schematic view of the add-drop ring resonator used is shown as an inset. The scheme is not in scale.

The 50:50 polarization maintaining beam splitter labeled as BS_1 in Fig. 3.6 is needed to perform the stimulated FWM experiment only.

Lasing cavity characterization

Before characterizing the cavity behavior, we perform some calculations in order to estimate the lasing threshold [323].

A laser cavity reaches the lasing threshold when the sum of all losses experienced by light in one round trip of the cavity is exactly balanced by the optical gain of the laser medium. This can be written as:

$$G_{th}T_{tot}T_{oc} = 1, \tag{3.2}$$

where $G_{th} = e^{g_{th}}$ is the saturated gain of the amplifying medium, T_{tot} is the total transmission of the optical elements in the cavity (except for the transmission of BS_2, from which the output light is collected) and T_{oc} is the transmission of the cavity output coupler. In our setup, this last value is given by the 99:1 beam splitter (BS_2), where 99% of the power, corresponding to T_{oc}, is transmitted inside the cavity and 1% of the radiation, defined by $1-T_{oc}$, is collected at the output on a InGaAs detector (Newport 918D-IG-OD3) connected to a high-dynamic-range power meter (Newport 1936-C). The transmission of the output coupler has been measured to be $T_{oc} = -0.05$ dB $\simeq 98.85\,\%$.

The total losses for one loop, excluding the BOA, are directly measured in the cavity to be $T_{tot} = -18$ dB $\simeq 1.58\%$. This is simply done by opening the cavity and excluding the BOA. We inject light in the isolator from a monochromatic tunable CW infrared laser (Santec TSL-510) and collect the

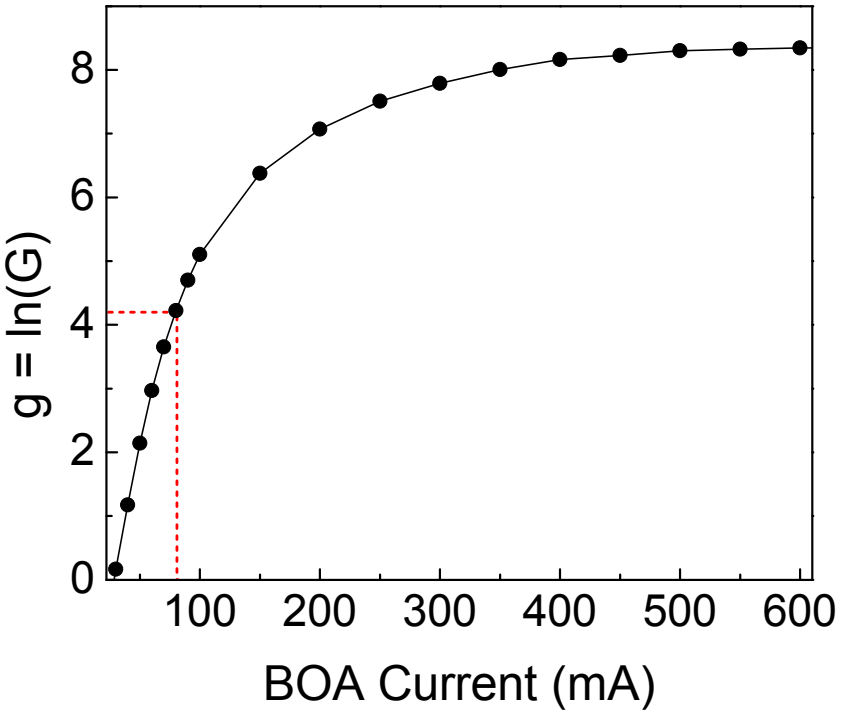

Figure 3.7: Gain characterization of the BOA as a function of the BOA current. The laser power injected in the BOA is $P_{in} = 34\mu$W at a wavelength of 1550 nm. The black points are the experimental data. The expected threshold current corresponding to the threshold gain estimated in Eq. 3.3 is $I_{th} \simeq 83$ mA.

output light at the 99% port of BS_2 on a InGaAs detector (Newport 918D-IG-OD3) connected to a high-dynamic-range power meter (Newport 1936-C). The measured losses are distributed among the components in the cavity in the following way: the coupling losses are 3.6 dB for each grating coupler, the BPFs losses are estimated to be 3.5 dB for each filter, the losses due to BS_1 are 3 dB, whereas the isolator and BS_2 losses are 0.3 dB and 0.5 dB, respectively. The microring round-trip loss is estimated to be $\alpha L \approx 0.02$ dB, where $\alpha = 3$ dB/cm and $L = 2\pi R \approx 74.8$ μm. So, we have:

$$\ln(G_{th}) = g_{th} = -\ln(T_{tot}T_{oc}) \simeq 4.2. \tag{3.3}$$

In Fig. 3.7 we show the measurement done in order to characterize the BOA gain. We inject light from a monochromatic tunable CW infrared laser (Santec TSL-510) into the BOA. The laser power is set to $P_{in} = 0.34$ μW at a wavelength of 1550 nm. We vary the BOA driving current from 30 mA to 600 mA and we collect the output light on a InGaAs detector (Newport 918D-IG-OD3) connected to a high-dynamic-range power meter (Newport 1936-C) right after the isolator. The gain is then calculated by dividing the measured output power by the input power P_{in}. We obtain the estimated threshold gain $g_{th} = 4.2$ for a current $I_{th} \simeq 83$ mA. So, this value is the expected threshold

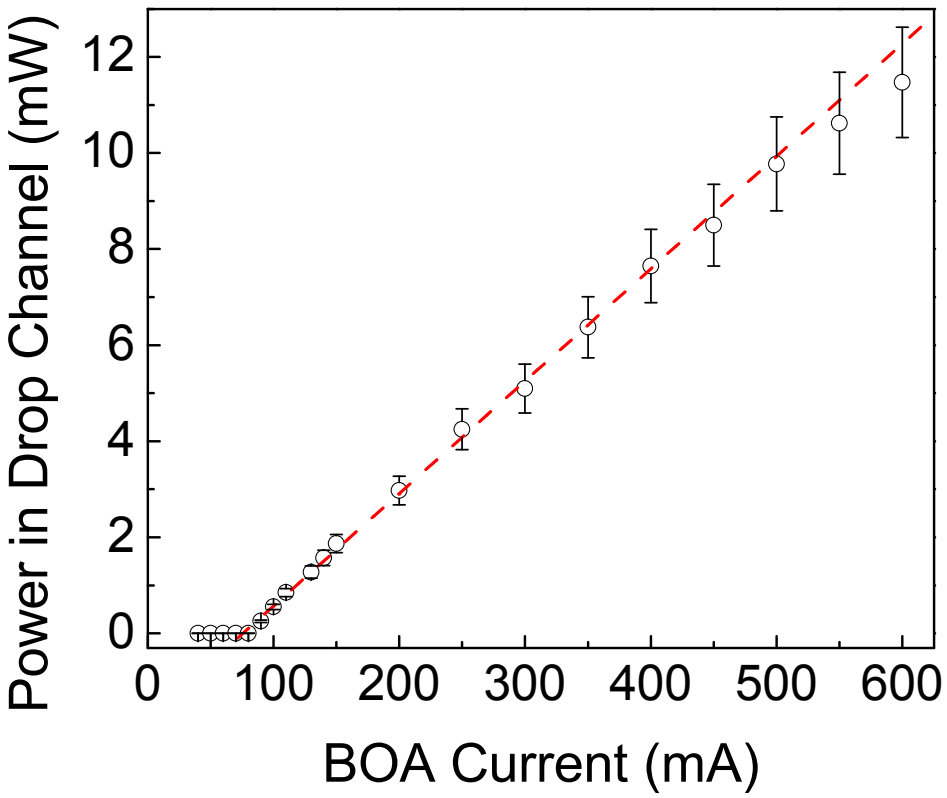

Figure 3.8: Lasing curve of the cavity. The black circles are the experimental values, whereas the dashed red line shows the linear fit corresponding to Eq. (3.4).

current for our laser cavity.

We now characterize the cavity behavior by finding the lasing curve of the built cavity. So, we close the cavity as in Fig. 3.6 and by varying the BOA driving current, we collect the cavity output light from the 1% port of BS_2 on a InGaAs detector (Newport 918D-IG-OD3) connected to a high-dynamic-range power meter (Newport 1936-C). The lasing curve of the cavity is shown in Fig. 3.8 as a function of the BOA current. On the y-axis the optical power estimated at the drop port of the microring resonator is reported. It is calculated from the measured power at the 1% port of BS_2, and compensating for both BPF and coupling losses. This gives an estimated error on the y-axis of 10%, as it can be seen from the figure. A clear threshold behavior is observed around a current $I_{th} = 90$ mA. This value is in agreement with the theoretical value found in Fig. 3.7. Indeed, the lasing threshold corresponds to a current where the BOA small signal gain is 20 dB, close to the inverse of the measured losses.

In Fig. 3.8, it is also reported the linear fit (dashed red line) of the characteristic curve of the cavity according to the following equation:

$$P_{out}(I) = P_{sat}(kI - g_{th}) \frac{G_{th}}{G_{th} - 1} T_{tot}(1 - T_{oc}), \tag{3.4}$$

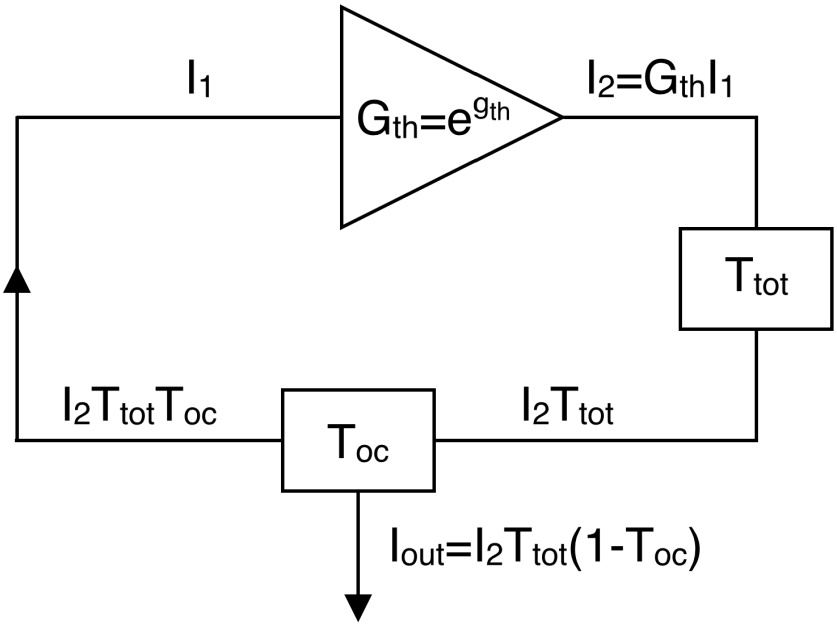

Figure 3.9: Block diagram of the built laser cavity.

where P_{out} is the optical power read at the output of the 1% port of BS_2, I is the BOA current, P_{sat} is saturation power, $G_{th} = e^{g_{th}}$ is the saturated gain of the amplifying medium, $g_0 = kI$ with k constant and g_0 small signal gain (that is the gained obtained when the input signal is so weak that no gain saturation occurs), T_{tot} is the total transmission of the optical elements in the cavity (except for BS_2 transmission) and T_{oc} is the transmission internal to the racetrack resonator, that we call "output coupler".

The output power as a function of the BOA driving current as expressed in Eq. (3.4) can be easily derived following the Rigrod model [324, 325]. Consider the block diagram shown in Fig. 3.9, the gain for unit of length g_l in the active medium depends on the small signal gain for unit of length g_{0l} and from the ratio $\frac{I(z)}{I_{sat}}$, where $I(z)$ is the effective current circulating in the cavity and I_{sat} is the saturation intensity. In particular, we can write:

$$g_l = \frac{g_{0l}}{1 + \frac{I(z)}{I_{sat}}}. \tag{3.5}$$

The amplification intensity follows the equation:

$$\frac{dI(z)}{dz} = g_l I(z) = \frac{g_{0l}}{1 + \frac{I(z)}{I_{sat}}} I(z). \tag{3.6}$$

By separating the variables and integrating, we obtain:

$$\int_{I_1}^{I_2} \left(\frac{1}{I} + \frac{1}{I_{sat}} \right) dI = \int_0^l g_{0l} dz, \tag{3.7}$$

that gives:

$$\ln\left(\frac{I_1}{I_2}\right) + \frac{I_2 - I_1}{I_{sat}} = g_0. \tag{3.8}$$

This equation can be written as:

$$\frac{I_2 - I_1}{I_{sat}} = g_0 + \ln\left(T_{tot}T_{oc}\right), \tag{3.9}$$

that is

$$\frac{I_2 - I_1}{I_{sat}} = g_0 - g_{th}. \tag{3.10}$$

Now, substituting intensities with powers ($P = IA$, where A is the area of the laser mode) and considering that $I_2 = G_{th}I_1$ and $I_{out} = I_2T_{tot}\left(1 - T_{oc}\right)$, we can find the expression for the output power as a function of the small signal gain g_0:

$$P_{out} = P_{sat}\left(g_0 - g_{th}\right)\frac{G_{th}}{G_{th} - 1}T_{tot}\left(1 - T_{oc}\right). \tag{3.11}$$

Since the small signal gain is proportional to the BOA driving current ($g_0 = kI$), from Eq. (3.11) we find Eq. (3.4).

From Fig. 3.8 it can be seen that the experimental points deviate from the linear fit for high BOA current. This might be due to the onset of the two-photon absorption (TPA) process in the microring resonator when high power is stored inside it, but a more accurate study on this effect is needed.

Stimulated FWM

Given the low quality factor of the present racetrack resonator, spontaneous FWM was too weak to be observed. We performed instead the stimulated FWM experiment. As explained in Sec. 1.2.1, FWM is a third-order nonlinear process in which two pump photons interact in the medium, producing a photon pair (idler and signal). In the stimulated FWM process, besides the pump photons, a seed laser (signal) is used to stimulate the system, thus producing an idler photon at a frequency given by the energy-momentum conservation law.

The experimental apparatus is shown in Fig. 3.10. We connected to the cavity the components inside the dashed red rectangles. The experiment consisted in resonantly exciting a resonance (signal) of the microring at a wavelength of 1563.45 nm thus producing a stimulated idler beam at a wavelength of 1548.39 nm. In Fig. 3.4 the resonances used for the FWM experiment are displayed. For the signal photon, we used an external monochromatic tunable CW infrared laser (Santec TSL-510) that is coupled with the ring cavity using a 50:50 BS just before the sample. The signal laser is completely suppressed by the BPF placed before the BOA so that it has no loop gain. Moreover, this laser is spectrally cleaned before being injected into the cavity by means of a tunable band-pass filter (Santec OTF-350) in order to remove spurious

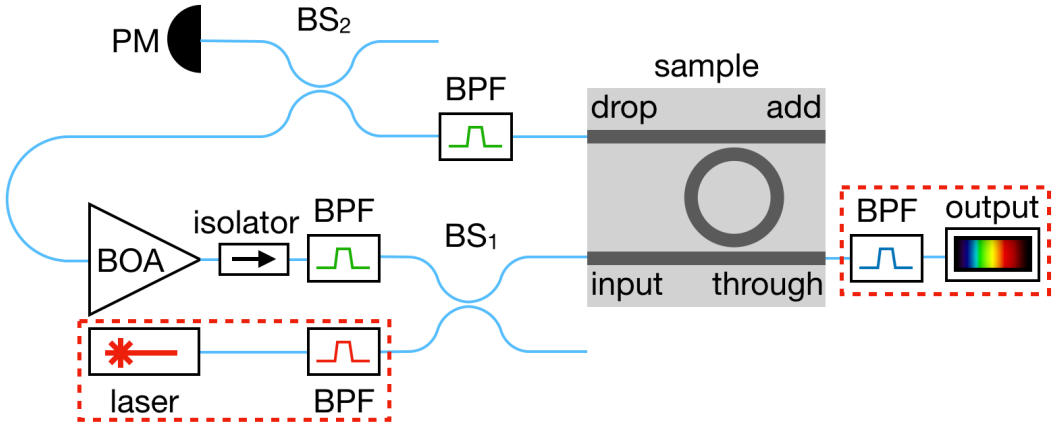

Figure 3.10: Scheme of the experimental apparatus used for the stimulated FWM experiment. The elements inside the dashed red rectangles are connected to the cavity for the experiment only (see Fig. 3.6). An external tunable CW infrared laser is connected to the cavity through a 50:50 polarization maintaining beam splitter (BS_1). The idler photons are finally collected on a spectrometer equipped with a CCD camera. BPF stands for band-pass filter, PM for power meter and BOA for booster optical amplifier. BS_2 is a 99:1 polarization maintaining beam splitter, with the 1% port connected to the PM. The scheme is not in scale.

ASE photons from the amplifier. The idler photons are finally collected on a spectrometer (Acton Spectra pro 2500i) equipped with a liquid-nitrogen cooled CCD camera (Acton InGaAs OMA V).

The conversion efficiencies of the stimulated FWM process are shown in Fig. 3.11 (a) and (b). The idler generation rate is proportional to the square of the lasing power (a) and grows linearly with the signal power (b) inside the microring resonator, proving its parametric origin. In fact, this is what we expect from the theory (see Sec. 1.2.1). In Fig. 3.11 (c) an example of FWM spectrum corresponding to a pump power coupled inside the ring of 1.87 mW and a coupled signal power of 130 μW is also shown.

JSD measurement

As already explained in Sec. 1.3.4, the classical FWM intensity can be used to directly assess the spectral correlations between the signal-idler photons that would be emitted in the spontaneous parametric process [207]. Indeed, the linewidth of the ring resonances is of the order of several tens of GHz and is much larger that the spacing of the modes of the laser-loop cavity, which is several meters in length. This means that the pump laser could encompass many lasing modes and span the whole linewidth. However, the emission of time-entangled photons requires a pump linewidth smaller than that of signal and idler photons [204] and this might not be the case in the used self-pumping geometry. On the other hand, gain narrowing is expected to occur within the

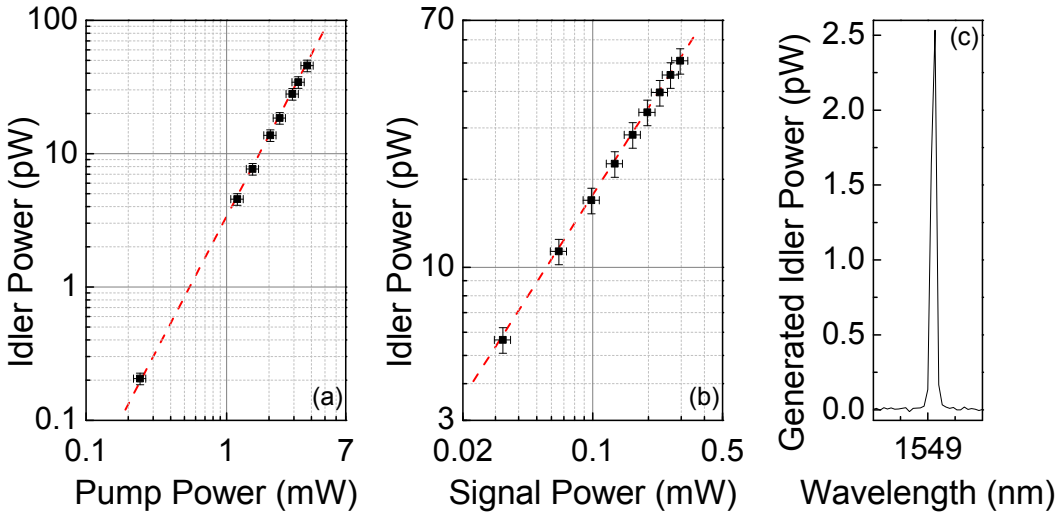

Figure 3.11: (a) and (b) show the stimulated FWM generation rate. The idler generation rate is proportional to the square of the lasing power (a) and grows linearly with the signal power (b) inside the microring resonator. In (a) the signal power coupled to the sample is 130 μW, whereas in (b) the BOA current is fixed at 250 mA. Dashed red lines corresponding to the correct slope required by the stimulated FWM process are added to the graphs. (c) One idler spectrum taken for coupled pump and signal powers of 1.87 mW and 130 μW respectively.

relatively large bandwidth of the microring resonance, solving the problem of having a laser line narrower than the signal and idler resonances.

The idler-signal correlation curve can be directly assessed via a JSD measurement [268, 261, 207, 264, 262, 326], that basically gives the idler wavelength as a function of the signal wavelength and vice versa. As already described in Sec. 1.3.4, the JSD measurement on spontaneously generated photon pairs is done through a coincidence measurement: for each point in the signal resonance, all the wavelengths of the idler resonance have to be recorded. The main issue of this method is that the procedure requires a lot of time. However, the JSD measurement can be more efficiently performed by using the stimulated FWM process [261, 207]. Now, the effect is stimulated by scanning a seed laser over the wavelength range of the signal resonance. The spectral resolution on the signal resonance is given by the scanning step of the seed laser.

The setup used for the JSD measurement is the same of Fig. 3.10. This can be done because of the relatively big resonance width. We still used as seed laser a monochromatic tunable CW infrared laser (Santec TSL-510), and we acquired FWM spectra on a spectrometer (Acton Spectra pro 2500i) equipped with a liquid-nitrogen CCD camera (Acton InGaAs OMA V) by varying the signal wavelength from 1560 nm to 1566 nm in steps of 10 pm. This gives the resolution on the signal resonance. The spectral resolution on the idler resonance is given by the receiving spectrometer and is 67 pm. During the

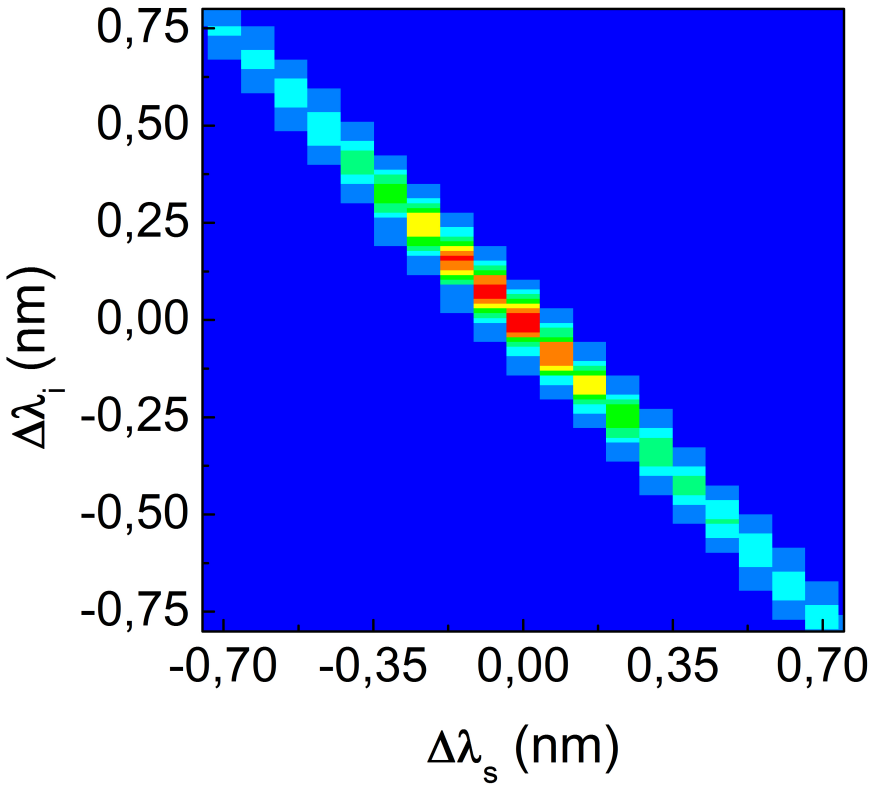

Figure 3.12: Idler-signal correlation measurement as a function of the wavelengths corresponding to the idler and signal resonances. The measured intensity is closely peaked around the antidiagonal, showing clear energy-time correlations. The spectral resolution on the idler resonance is given by the receiving spectrometer and is 67 pm.

measurement, the BOA current was kept fix to 200 mA, whereas the optical power of the signal inside the ring resonator was 250 μW . The correlation measurements are shown in Fig. 3.12 as a function of the signal and idler resonances' relative wavelengths. The measured intensity is closely peaked around the anti-diagonal, showing clear correlations between the signal and idler's energies. This proves that, at least with the current microring quality factor, signal-idler photon pairs emitted in the spontaneous process would be entangled.

3.2 Spontaneous four-wave mixing

In this section we will report on the SFWM experiment carried out on a silicon microring resonator without the need of an external pump laser. First of all, we will give the details on the sample we used, provided by PoliFAB at Politecnico di Milano. We will then describe the components the cavity is made of and show that we are able to achieve lasing in silicon, with the only use of an external amplifier. Finally we will describe the SFWM experiment carried out on the system and the consequent coicidence measurement performed on the generated idler and signal photons.

3.2.1 Sample

The system used for the SFWM experiment has been designed at Politecnico di Milano by the Photonic Devices Group and fabricated through a process very similar to Sec. 2.1.

As usual, the fundamental unit of the photonic circuit is a ridge waveguide, which has a cross-sectional area of 220 $\times$ 500 nm^2. The coupling of light between waveguides on the chip and external optical fibers is obtained through the use of grating couplers, as already detailed in Sec. 2.1 and Sec. 3.1.1. Even in this sample, many grating couplers are associated to one photonic structure on the chip and are aligned along the vertical direction. They are etched at a distance of 127 μm, that is the same gap among the fibers on the used fiber array.

As for the stimulated FWM experiment (Sec 3.1.1), we used a racetrack resonator in the add-drop configuration in order to perform the measurement. The resonator rounded part has a radius of 10 μm and a 2-μm-long straight section, thus giving a measured FSR of 8.6 nm. The gap between the bus waveguide and the recetrack is of 0.2 μm and the measured quality factor is $Q \sim 20000$.

3.2.2 Experiment

In this section we will report on the SFWM experiment performed on a silicon microring resonator without the need of an external laser acting as a

pump. We will first show the linear characterization of the add-drop racetrack resonator. We will then describe how the cavity is built and give its characterization. Finally, we will detail the SFWM and coincidence measurements and comment the results.

Characterization of the sample

As for Sec. 3.1, a racetrack resonator in the add-drop configuration (see Sec. 1.2.2) is the building block of the laser cavity. We first are interested in the characterization of this structure. The procedure we used is the same of Sec. 3.1, so we are not repeating it here.

The results of the characterization are shown in Fig. 3.13 (a)-(e). In 3.13 (a) and (b) a 50-pm-resolution transmission spectra of the through and drop ports is displayed, respectively. In Fig. 3.14 (a) and (b) the transmission spectra in dB corresponding to the through and drop ports are also given. I, P and S represent the resonances chosen for the SFWM experiment and stand for idler, pump and signal, respectively. The grating couplers used to couple light modulate the intensity transmitted by the sample, giving the usual bell-shape for the transmission spectra. We estimated the insertion losses to be about 3.6 dB for each grating coupler.

A high-resolution spectrum (2 pm) of the resonances chosen for the FWM experiment, represented by the black line, is reported in Fig. 3.13 (c)-(e). The dotted red line is the Lorentzian fit to the resonance. We then calculated the quality factor directly from the fit via the relation (1.65). The resonance linewidth is now of the order of $\sim$80 pm, giving a quality factor of Q$\sim$ 20000, with a FSR of 8.6 nm. Moreover, we estimated the photon coherence time from the relation (1.66), that we report here for convenience:

$$Q = 2\pi\Delta t_p \nu_0, \tag{3.12}$$

where ν_0 is the central frequency of the resonance and Δt_p is the photon dwelling time. Then, the estimated quality factor results in a photon lifetime of the order of $\sim$16 ps.

As it can be seen from Fig. 3.13 (c) and (d), the resonances go down to 1% of transmission, meaning that the ring resonator is at the critical coupling condition. The signal resonance in Fig. 3.13 (e) is a bit larger and less deep than the idler and pump resonances because it is actually composed by two distinct deeps and the showed Lorentzian fit is the convolution of the two different fits. The splitting of the resonance is produced by the two different propagation directions (clockwise and counter-clockwise) of light inside the microring resonator due to waveguide roughness. It has been already proved that the splitting of the resonance in a microring resonator does not influence the FWM process [46, 206]. In Fig. 3.15 we show the two Lorentzian fits corresponding to the two different peaks in the idler resonance (dotted blue and green lines, respectively). The dotted red line is the result of the convolution of the two Lorentzian curves and perfectly fits the idler resonance.

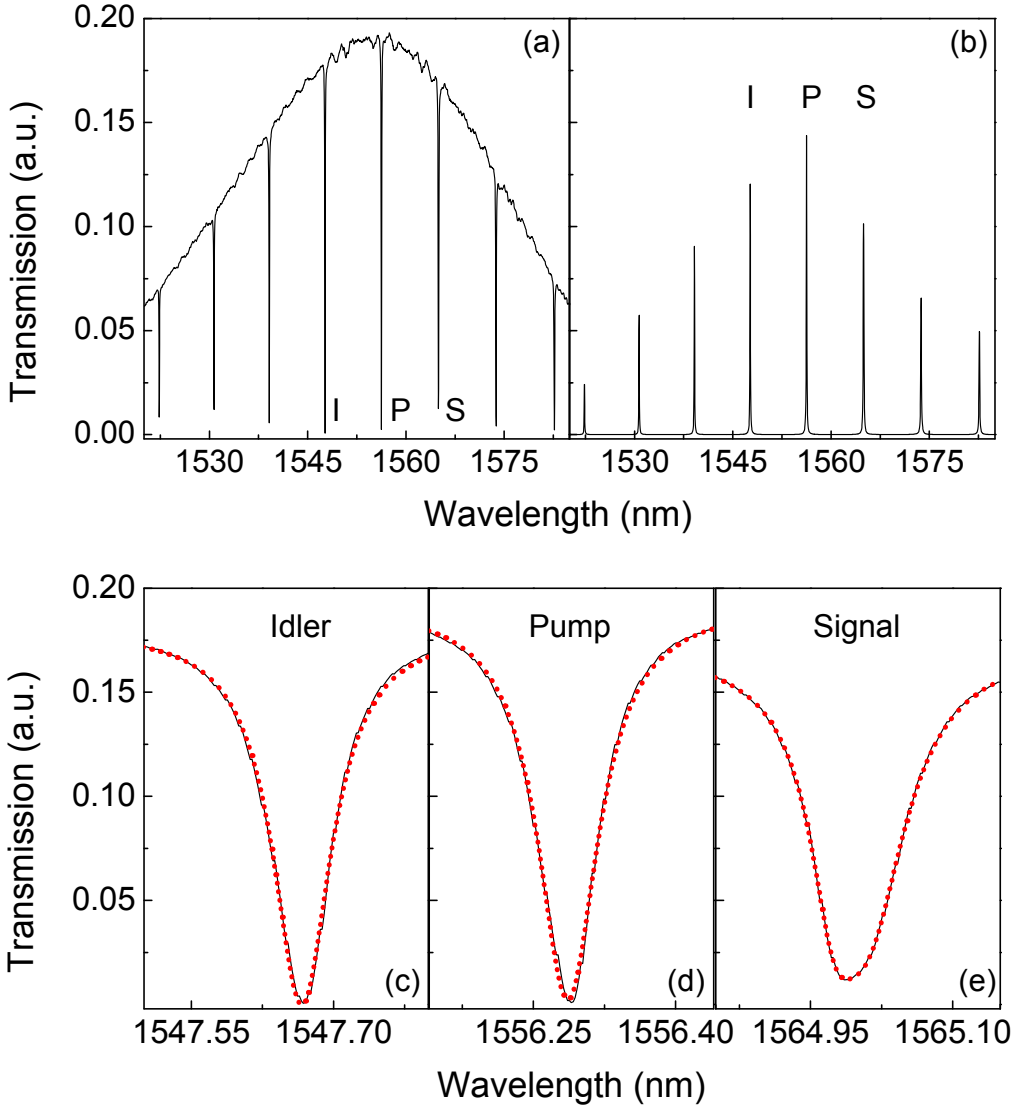

Figure 3.13: Transmission spectra of the (a) through and (b) drop ports of the add-drop ring resonator used in the cavity. The resolution of the spectra is 50 pm. I, P and S stand, respectively, for the idler, pump and signal resonances chosen for the SFWM experiment. These resonances are shown in the spectra (c)-(e) with a resolution of 2 pm. The black line represents the experimental data, whereas the dotted red line is the Lorentzian fit of the resonance. From (a), (c) and (d), it can be seen that the microring resonances go down to below 1% of transmission, meaning that the add-drop ring resonator is at critical coupling condition. (e) The signal resonance goes down to 5% of the transmission because is composed by two deeps, that is it a splitted resonance.

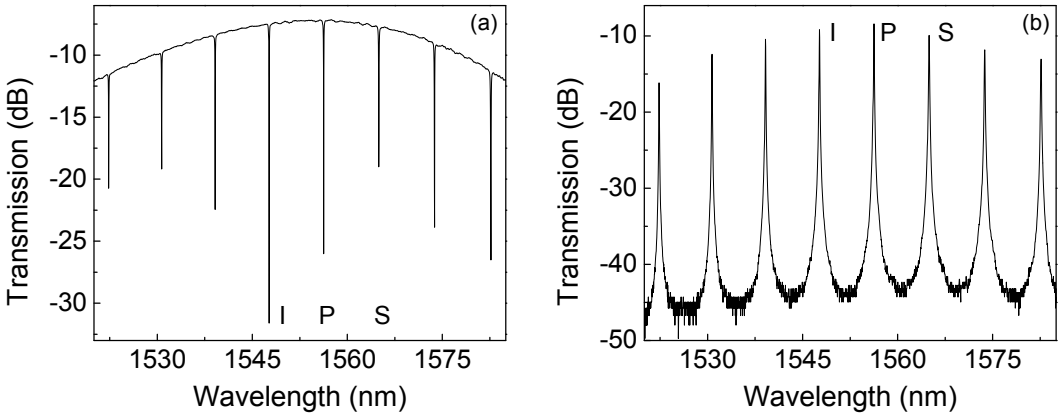

Figure 3.14: Transmission spectra of the (a) through and (b) drop ports of the add-drop ring resonator used in the cavity. The resolution of the spectra is 50 pm. I, P and S stand, respectively, for the idler, pump and signal resonances chosen for the SFWM experiment.

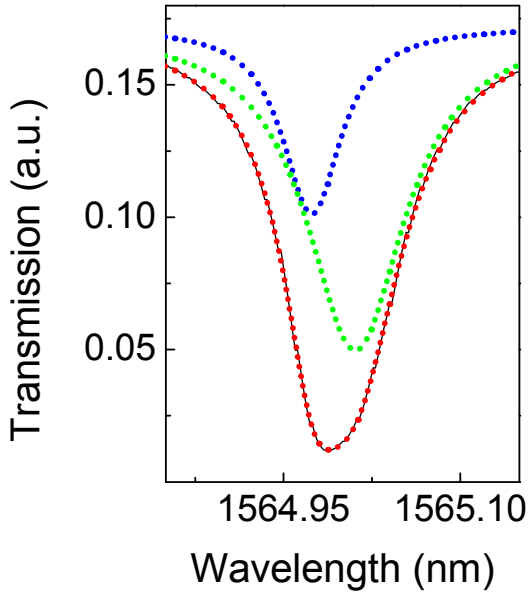

Figure 3.15: Transmission spectrum of the idler resonance (resolution of 2 pm). The dotted blue and green lines represent the Lorentzian fit of the two peaks inside the idler resonance. The dotted red line is the convolution of the two fits.

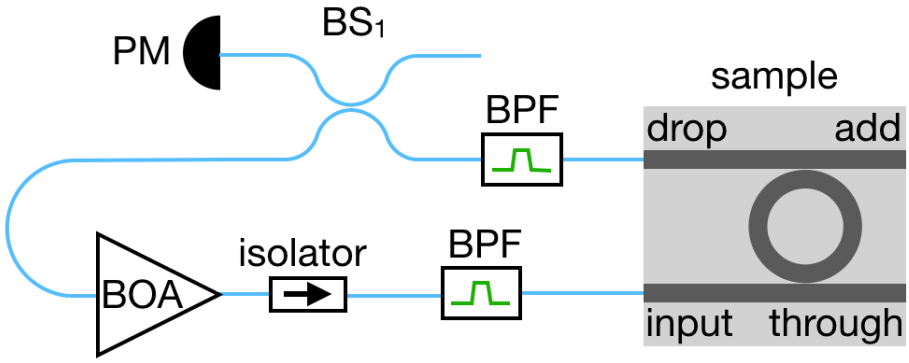

Figure 3.16: Scheme of the cavity built for the SFWM experiment. BPF stands for band-pass filter, PM for power meter and BOA for booster optical amplifier. BS_1 is a 99:1 polarization maintaining beam splitter, with the 1% port connected to the PM. A schematic view of the add-drop ring resonator used is shown as an inset. With respect to the cavity used for the stimulated FWM experiment (Fig. 3.6), we removed the 50:50 beam splitter at the sample input. The scheme is not in scale.

Lasing cavity design

The design of the cavity is shown in Fig. 3.16. The scheme is basically the same of Sec. 3.1. However, we removed the 50:50 polarization maintaining BS, since no more necessary for the SFWM experiment. The source of gain is the same of Sec. 3.1, that is a Booster Optical Amplifier (Thorlabs BOA1004P) connected to a controller (Thorlabs ITC4005) and with a small signal gain of up to 30 dB. The cavity is closed on the input and drop ports of the racetrack resonator and the input/output coupling to the chip is obtained through grating couplers. As in the cavity of Sec. 3.1, the add-drop racetrack resonator acts inside the cavity as a BPF for each resonance.

For the experiment we selected a single resonance at a wavelength $\lambda_p = 1556.29$ nm for lasing. This was done by restricting the transmission of the cavity by using an external BPF at the BOA output. The filter is made of four cascaded BPFs positioned in such a way to have a transmission band of about 4 nm around the lasing wavelength. This filter has a total noise suppression of more than 200 dB in the idler and signal generation bands. So, it also reduces the ASE emission from the amplifier to a level lower than the generated FWM experiments. We always need an isolator at the BOA output in order to prevent reflected light to go back to the amplifier. A tunable band-pass filter (Santec OTF-350), centered at the lasing wavelength and with a transmission band of about 4 nm, was inserted at the sample output to further improve the rejection of frequencies other than the lasing mode before amplification. Finally, as in Sec. 3.1, the cavity laser power was monitored through a 99:1 polarization maintaining BS (BS_1).

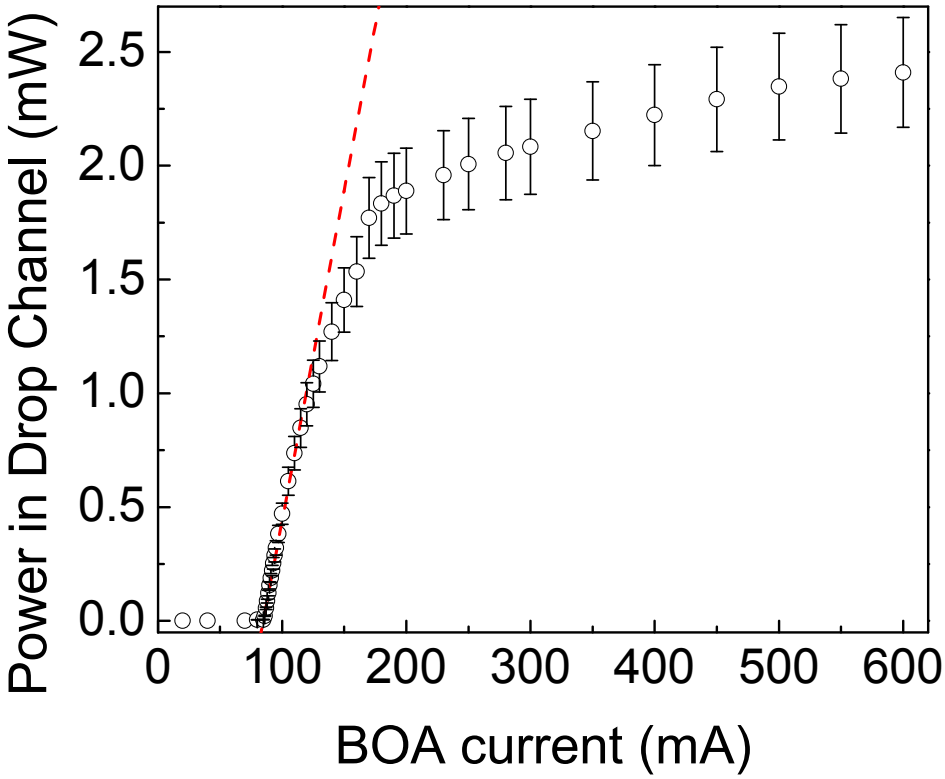

Figure 3.17: Lasing curve of the cavity. The black circles are the experimental values, whereas the dashed red line shows the linear fit corresponding to Eq. (3.4), that it is still valid in the present case.

Lasing cavity characterization

The cavity characterization made in Sec. 3.1 can be easily extended to the cavity of Fig. 3.16. We do not report here all the calculations, for the details the reader is referred to Sec. 3.1. Even if we removed the 50:50 BS in the cavity, the total measured losses for one loop, excluding the BOA, did not change with respect the cavity shown in Fig. 3.6. This happens because of the tunable BPF used to filter the laser wavelength at the output of the sample, that has more losses than the standard BFFs employed. So, $T_{tot} = -18$ dB $\simeq 1.58\%$. The measurement of the losses has been performed as in Sec. 3.1 and, now, they are distributed among the cavity components as follows: coupling losses due to each grating coupler are estimated to be 3.6 dB, the standard BPF losses are 3.5 dB, the tunable BPF is assumed to have 6.5-dB losses, whereas the isolator and 99:1 BS associated losses are 0.3 dB and 0.5 dB, respectively. Since it is assumed $T_{oc} = -0.05$ dB $\simeq 98.85\,\%$, as in Sec. 3.1, we can write Eq. (3.3), which we report here fo convenience:

$$\ln\left(G_{th}\right) = g_{th} = -\ln\left(T_{tot}T_{oc}\right) \simeq 4.2. \tag{3.13}$$

So, Fig. 3.7 is till valid and we obtain an estimated current threshold for $I_{th} \simeq 83$ mA.

As in the cavity characterization in Sec. 3.1, we can now find the cavity lasing curve (the measurement has been performed as in Sec. 3.1): by varying the BOA driving current, we collected the output light from the 1% port of BS_1 (see Fig. 3.16) on a InGaAs detector (Newport 918D-IG-OD3) connected to a high-dynamic-range power meter (Newport 1936-C). Now, the lasing curve of the cavity is shown in Fig. 3.17. On the y-axis we report the optical power estimated at the drop port of the microring resonator, as a function of the amplifier driving current. As in Sec. 3.1, the power in the drop channel is not a direct measurement, but it was inferred from the measured power at the 1% port of BS_1 by compensating for the losses due to coupling and the tunable BPF. Even in this case, a clear threshold behavior is observed around a current $I_{th} = 85$ mA and this value is in agreement with the theoretical value found in Fig. 3.7.

Following the calculations of Sec. 3.1, we can still arrive to Eq. (3.4), that we report here for convenience:

$$P_{out}(I) = P_{sat}(kI - g_{th}) \frac{G_{th}}{G_{th} - 1} T_{tot}(1 - T_{oc}). \tag{3.14}$$

The fit corresponding to this equation is also reported in Fig. 3.17 (dashed red line).

In Fig. 3.8 the experimental points deviate from the linear fit at relatively low powers at the drop port of the racetrack resonator. The divergence from the fit is now clearer than in the cavity built with the low-Q microring resonator (see Fig. 3.8). In fact, the high Q-factor of the present resonator makes the onset of the TPA process possible at lower power injected in the microring. However, an accurate study on the TPA process in this kind of cavities is needed to give quantitative results.

Spontaneous FWM

Given the relatively high quality factor of the available microring resonator, we were able to observe the SFWM process. As detailed in Sec. 1.2.1, SFWM is a third-order nonlinear process in which two pump photons are converted into an idler-signal photons pair. During the process energy and momentum are conserved. Usually, the pump photons are coupled to the nonlinear medium through the use of an external laser. We will now describe a way of obtaining SFWM without the need of an external optical pump.

The experimental apparatus used for the experiment is shown in Fig. 3.18. We basically connected to the cavity depicted in Fig. 3.16 the components inside the dashed red rectangle. At this stage, the separation of the idler and signal photons with their consequent collection is performed. Conversely to standard SFWM experiments, the pump laser is now taken from the built cavity (see Fig. 3.16) and has a wavelength $\lambda_p = 1556.29$ nm. In this way two photons at $\lambda_i = 1547.67$ nm (idler) and $\lambda_s = 1564.97$ nm (signal) are produced. In Fig. 3.13 the resonances chosen for the experiment are shown.

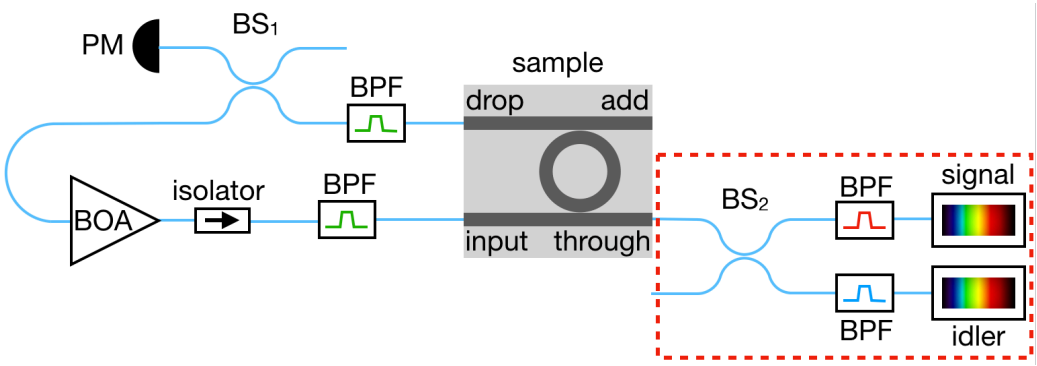

Figure 3.18: Scheme of the experimental apparatus used for the SFWM experiment. The elements inside the dashed red rectangle are connected to the cavity for the experiment only (see Fig. 3.16). The idler and signal photons are separated through a 50:50 polarization maintaining beam splitter (BS_2) and then collected on a spectrometer equipped with a CCD camera. BPF stands for band-pass filter, PM for power meter and BOA for booster optical amplifier. BS_1 is a 99:1 polarization maintaining beam splitter, with the 1% port connected to the PM. The scheme is not in scale.

We connected a 50:50 polarization maintaining BS (BS_2) at the sample output, at the through port of the add-drop microring resonator. At the BS output, we placed two BPFs with more than 150 dB rejection (they are actually three cascaded BPFs) tuned to the idler and signal wavelength, respectively. Finally, the idler and signal photons were collected on a spectrometer (Acton Spectra pro 2500i) equipped with a liquid-nitrogen cooled CCD camera (Acton InGaAs OMA V).

The idler and signal estimated generation rates are shown in Fig. 3.19 (a) as a function of the coupled pump power. The coupled pump power is the estimated power at the drop channel of the racetrack resonator and has been calculated from the measured power at the 1% port of BS_1 (labeled as PM in Fig. 3.18) and compensating for the BPF and coupling losses. The conversion efficiencies are evaluated by calibrating the response of the CCD camera using a power meter with a pW sensitivity and then integrating the emission peaks for the idler and signal resonances. From Fig. 3.19, it can be seen that the generation rates are proportional to the square of the pump power (dashed grey line), a clear sign of the SFWM process (see Sec. 1.2.1). Moreover, in Fig. 3.19 (b) one SFWM spectrum for a coupled pump power of 1.7 mW is given. The position of the pump is represented by the green arrow. The two generated SFWM peaks at the idler (left) and signal (right) resonances, respectively, can be seen.

We want to notice that in standard SFWM experiments on microring resonators with an external laser acting as optical pump, at high pump powers the curve departs from the quadratic dependence and tends to saturate below the quadratic trend. This is due to the thermo-optic effect induced by the TPA

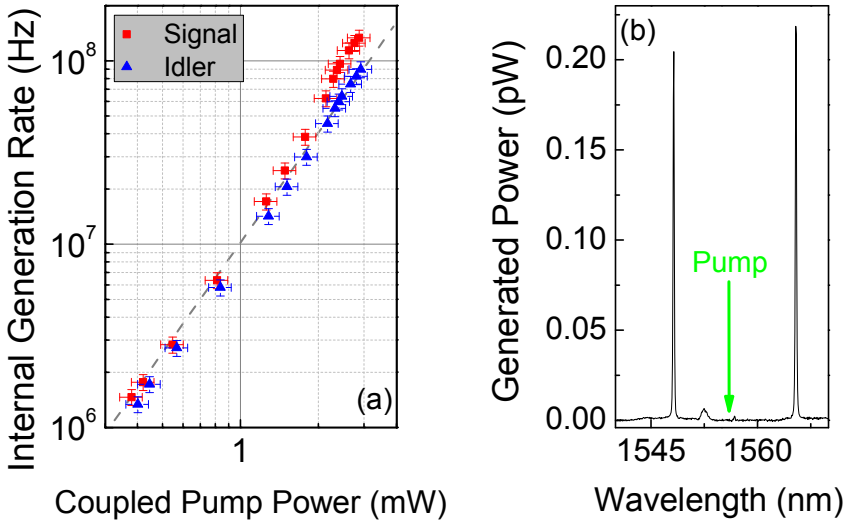

Figure 3.19: (a) SFWM generation rates. Both the idler (blue triangles) and signal (red squares) generation rates are proportional to the square of the lasing power inside the ring resonator. A dashed grey line corresponding to the correct (quadratic) slope required by the SFWM process is added to the graph. (b) SFWM spectrum for a coupled pump power of 1.7 mW. The green arrow indicates the wavelength of the pump. The two peaks are the generated SFWM peaks at the idler (left) and signal (right) resonances, respectively.

process, so the microring's resonances slightly redshift with increasing pump power and take the pump laser "out of resonance" reducing then the intensity of the emitted photons. This effect can be observed above an emission rate of $10^6 - 10^7$ Hz [206]. However, by using the self-pumping geometry and closing the microring resonator in a fiber-loop cavity, we erased this effect, as shown in Fig. 3.19 and the pump laser "follows" the resonances' shift. We want to stress that, in order to eliminate the TPA thermo-optic effect, the BPFs inside and outside the cavity have to be tuned properly, in order to have a sufficiently wide band and thus accommodate the power shift.

Coincidence measurement

Since we have verified the occurrence of SFWM, we can now look at the correlated emission of photon pairs. This can be done through a coincidence measurement, in which the relative arrival times of the idler and signal photons are statistically analyzed.

The setup used for the coincidence measurement is shown in Fig. 3.20. It is basically the same apparatus of Fig. 3.18, but here the output from the two BPFs relative to the idler and signal photons is sent to two superconducting single photon detectors (SSPDs). The SSPDs are mounted in a refrigerating unit inside a liquid-helium dewar at 1.7 K and are biased in order to have dark counts of the order of 100 Hz. The detection efficiencies of the SSPDs are 4%

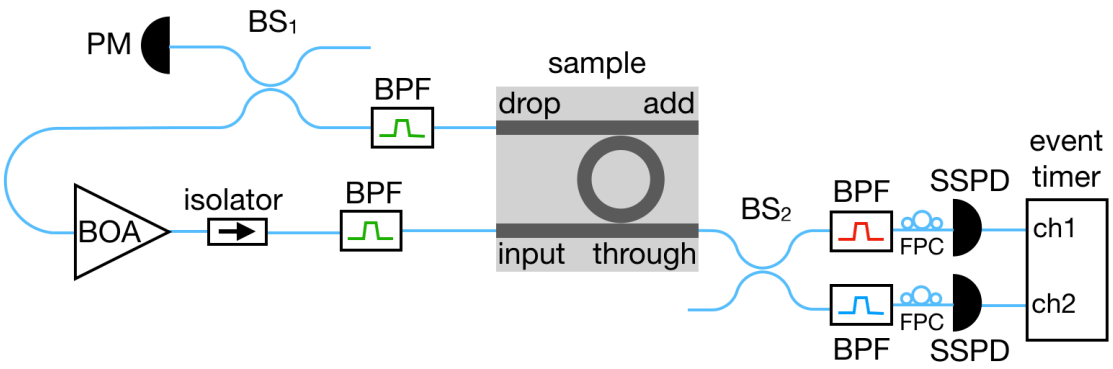

Figure 3.20: Experimental apparatus used for the measurement of the coincidences of the signal and idler photons. PM stands for power meter, BS for beam splitter, BPF for band-pass filter, FPC for fiber polarization controller, SSPD for superconducting single photon detector.

and 1%, respectively, and the time response of each detector is 65 ps. This is a much better time response than usually-employed InGaAs avalanche photodiodes ($\simeq$ few ns). Moreover, InGaAs avalanche photodiodes usually have much higher dark counts rates, of the order of 10^4-10^5 Hz.
We also needed to insert two fiber polarization controllers (FPCs) before each SSPD in order to maximize the single photon detection rate. A Picoquant Hydraharp event timer is used at the output of the SSPDs to correlate the detectors' signals. The event timer records a stream of events on a computer and the data are then analyzed through a C script. In Fig. 3.21 (a) a coincidence histogram for a coupled pump power of 1.5 mW is shown. The curve was taken with an integration time of 5 minutes. The resolution on the x-axis is given by the response time of the SSPDs and is 65 ps. This value also limits the width of the peak. From Fig. 3.21 (a) a clear coincidence peak can be seen over a constant background due to accidental events, proving the concurrent emission of the signal and idler photons produced in the SFWM process.
In Fig. 3.21 (b) the coincidence rate as a function of the coupled pump power is shown. The black dots in the figure are determined by integrating all the points in the coincidence peak and subtracting for the background. As expected, the coincidence rate is proportional to the square of the coupled pump power (dashed red line). In fact, the number of coincidences is proportional to the photon-pairs emission rate and this has a quadratic dependence on the pump power, as already shown in Fig. 3.19.

A very important figure of merit for the evaluation of the performance of a source of correlated photons is the coincidence-to-accidental ratio (CAR) [206, 243, 327]. The CAR, as already explained in Sec 1.3.2, is defined as the ratio between the number of time-correlated photons in the coincidence peak and the average number of accidental photons in the background in the same

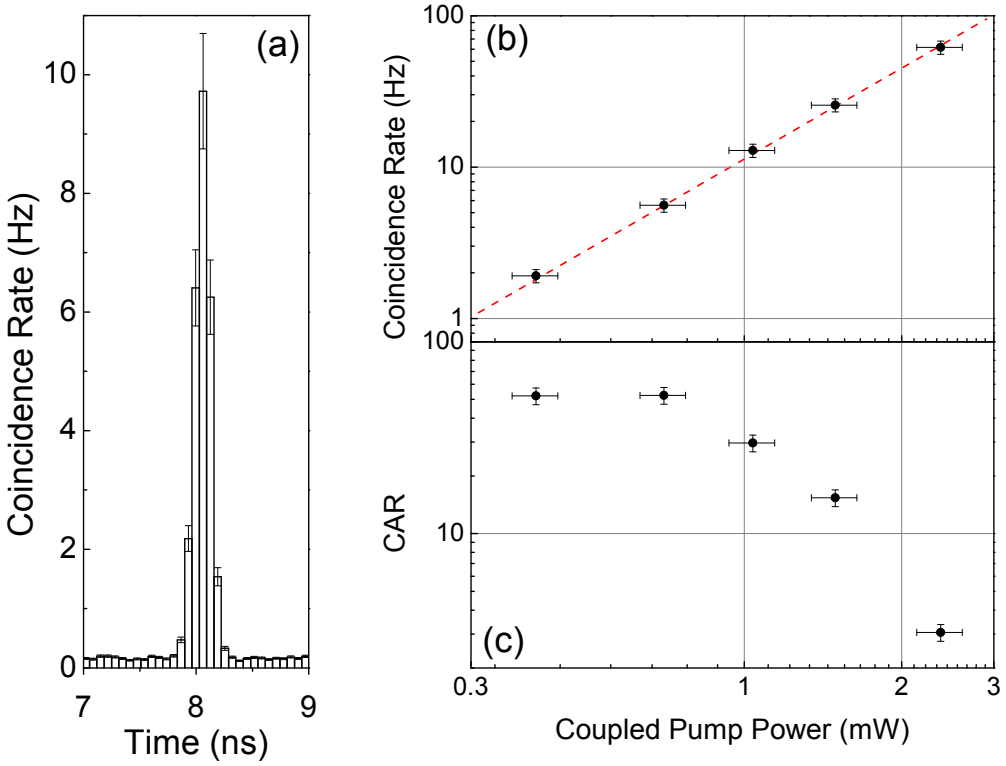

Figure 3.21: (a) Coincidence histogram for a coupled pump power of 1.5 mW. (b) Coincidence rate as a function of the coupled pump power. The dashed red line is a guide to the eye proportional to the square of the pump power, as required by SFWM. (c) Coincidence-to-accidental ratio (CAR) as a function of the coupled pump power.

time window, as expressed by Eq. (1.110) [45, 22]:

$$CAR = \frac{C_C}{C_A} = \frac{1}{\beta \Delta t}, \tag{3.15}$$

where with C_C we indicated the number of correlated photons in the peak, C_A stands for the number of accidentals, β is the generation efficiency and Δt is the detector time-window. The relation (1.110) is valid only in the case of equal losses and detection efficiency for both the idler and the signal photons. Moreover, the expression holds as far as the coherence time of the emitted photons (that depends on the quality factor of the microring resonator) is smaller than the time window, that is given by the time response of the detectors.
In our case we calculated the CAR by integrating the number of coincidences within the peak and dividing by the sum of accidental counts in the background over the same time window. The result is shown in Fig. 3.21 (c) as a function of the coupled pump power. The maximum measured value of the CAR is 52±5 at a coupled pump power of 0.4 mW, allowing a high-fidelity preparation of either entangled photon pairs or heralded single photons. We measured the CAR for high generation rates compared to usual FWM experiments. For example, if we compare the CAR value measured by Azzini *et al.* in 2012 [206] at our generation rate we find agreement between the two measurement. Then, the measured CAR is comparable to the highest CAR measured for cm-long silicon waveguides [328], it is about ten times the value reported the first experiments on microring resonators [45] and it is twenty-five times the one reported for a coupled-resonator optical waveguide [22]. However, the CAR we measured is probably affected by the old SSPDs we used, which have lower efficiency and higher dark counts than expected.
As expected, the CAR decreases as the inverse of the coincidence rate [243] and quadratically with the pump power. Since at low pump powers the generation rate becomes comparable to the dark counts rate, the accidentals are then overestimated, thus decreasing the value of the CAR. This can be seen from the graph, where at low pump pump power the dependence of the CAR on the pump power deviates from the quadratic slope.
Moreover, there are some effects that affect the value of the CAR we measured. First of all, it is important to notice that the CAR could be influenced by the time resolution of the SSPDs (65 pm) which is of the same order of the coherence time of the generated photons, that we calculated to be ≃16 ps. Another effect that could affect the CAR value is the unbalance between the idler and signal detection efficiency.

3.3 Discussion

In this chapter, we have proved that FWM can be achieved in a silicon integrated microring resonator without the need of an external laser acting

as optical pump by closing the microring in a fiber-loop cavity including an amplifier.

As regarding the first section (Sec. 3.1), given the low quality factor of the used microring resonator, we have performed the stimulated FWM experiment in a self-pumping geometry. We have seen that in order to have a potentially usable emission rate ($>$ MHz) for the spontaneous process, a ring resonator with a quality factor exceeding 10000 is needed. We then performed a JSD measurement. The obtained result is a strong indication that the emitted photons would be entangled, even if a definitive proof will consist in a Franson experiment [27, 227] performed under self-pumping conditions.

In the second section (Sec. 3.2), we were able to carry out the SFWM experiment without the need of an external pump laser. This has been possible because the quality factor of the employed microring resonator was of the order of 20000. We then performed a coincidence measurement, proving the concurrent emission of the idler and signal photons in the explored self-pumping geometry. The fact that the pairs are emitted simultaneously can be exploited to achieve time-energy entanglement between the signal and idler beams. As for the result obtained in Sec. 3.1, the verification of the emission of entangled photons rely on a Franson experiment as described in [27, 227].

The results obtained from the stimulated and spontaneous FWM experiments are an important step towards the realization of a silicon-based source of entangled photons that does not require an external *tunable* pump. Moreover, it is important to notice that the described cavity geometry allowed to reach very high generation rates, up to 10^8 Hz. This was possible due to the fact that in our experiment the lasing frequency is *automatically* tuned to the pump frequency and follows any shift in the microring's resonances, eliminating the saturation effect, usually observed at around $10^6 - 10^7$ Hz in standard FWM experiments. Thus, ideally, the more the Q-factor of the microring would be high, the more the spontaneous FWM generation rate would also increase. So, having a Q-factor of the order of 10^5 would theoretically allow to further improve the idler generation rate. However, an experimental study on cavities with high-Q add-drop resonators would be required to give quantitative results on the best Q-factor that could be used. In fact, the more the Q-factor grows, the more the TPA effect appears at low powers injected into the ring. This would result in a further bending of the lasing curve presented in Fig. 3.8 and Fig. 3.17, thus giving, probably, a limit on the employed Q-factor. Moreover, an accurate study on the laser linewidth of the cavity should be made to give an esteem on the best Q-factor. In fact, increasing the Q-factor value would introduce noise in the cavity, thus broadening the laser linewidth till a value at which the emitted photons would no more be entangled.

Another interesting possible output for the system described in this chapter would be to have a separable state, in order to produce single photons via heralding [22]. In order to achieve this, the laser linewidth should be comparable to the linewidth of the ring resonator's mode [261]. This can be obtained

by inserting a modulator inside the cavity to broaden the laser emission. In the case of a ring resonator with a quality factor of 40000, this corresponds to a linewidth of about 5 GHz, a frequency easily achievable with state of the art fiber modulators. In such a scheme one should achieve a state purity comparable to the limit for optical pumping [204].

In addition, a recently very active research direction is the possibility to achieve emission of quantum states of light of more than two photons [202, 329, 330, 331]. Our self-pumping system can reach enough CW power inside the ring resonator to achieve a multiphoton emission regime. Indeed, a power of 5 mW inside a ring resonator of Q$\sim$10000 is sufficient to have an emission rate of multiple pairs exceeding 10^5 Hz inside the ring [206, 243]. Furthermore, multiple photon emission can be obtained by building the laser cavity so to achieve pulsed laser emission. Pulsing in fiber loop cavities has been already accomplished using several different geometries [332, 333], which could be directly ported to our approach.

Finally, we would like to notice that the self-pumping scheme presented in this chapter could be adopted even in the case of an all-pass ring resonator, by closing the cavity on the input port of the microring and using backscattered light. In this configuration, the backscattering at the input port would have the same spectrum found at the drop port of an add-drop resonator and can thus be used to achieve lasing in a fiber-loop cavity. In fact, the backscattering from an all-pass resonator depends on the coupling factor and in it has been showed it can even reach -5 dB [334], being sufficient to produce laser emission.

Chapter 4

Implementation of the Bernstein-Vazirani algorithm using classical waves

In the previous chapters we tackled two major problems in the realization of silicon integrated photonic chips. In the present chapter, we want to show that silicon quantum photonics could also be considered for the on-chip photonic-based emulation of quantum algorithms, even if retaining its classical behavior. This platform could be very useful for educational purposes to learn about quantum algorithms.

In general, quantum computing refers to a large number of different systems and protocols aimed at efficient calculations exploiting quantum mechanical effects [10]. Nowadays, quantum computing protocols are actively investigated in both the academic and industrial environment, as they could be used to solve problems that require exponentially increasing resources when approached using a classical computer. As already discussed in chapter 1, very diverse physical systems have been employed to obtain quantum computation, including superconducting circuits [335], trapped ions [336], and photons [232]. Latterly, systems exceeding ten qubits have been demonstrated [337]. An important complement to quantum computation is the ability to emulate quantum computers, even if inefficiently, on classical platforms, as such systems could be used as convenient testbeds for protocols to be later run on actual quantum computers.

It is important to notice that all quantum computing protocols can be realized by propagating a single particle in a linear network [338]. This has been experimentally demonstrated by using photons propagating in bench-top [339] or fiber-based [340] optical networks. A similar approach, based on distributing a photon between multiple energy resonances, has been recently used to amplify the number of qubits in optical systems [202].

In this chapter, we will experimentally prove that the propagation of a

single particle in a linear network is equivalent to the propagation of a classical wave in the same network, as long as one is interested only in detection probabilities at individual outputs, and no correlations are measured. This means that, at the price of an exponential increase of resources, any quantum information protocol can be realized in a classical wave network. In order to illustrate this point, we will consider the Bernstein-Vazirani (BV) algorithm [341] in a three-qubit configuration and implement it in an analog electronic circuit, which is arguably the most readily available wave system.

So, we will start the chapter with an introduction to the most common quantum computing algorithms, that will be useful for our experiment. We will then describe the experiment carried out to implement the three-qubit BV algorithm. Furthermore, we will discuss the role of entanglement in the exponential scaling of the used resources, and show that the BV protocol can be implemented classically with an efficient (i.e. linear) use of resources, while still retaining its advantage over classical digital computation. Finally, in the last section, we will conclude by giving some considerations on the practical usefulness of this approach.

4.1 An introduction to quantum algorithms

In Sec. 1.1 we introduced the concept of qubit and briefly described the CNOT gate, that is the equivalent of the XOR classical gate. In the present section we would like to extend the previous discussion to the most common quantum gates and algorithms, for some of them will be considered in the proposed BV implementation (Sec. 4.2).

We will start the section by describing single-qubit gates. Then, by considering the classical-quantum parallelism, we will introduce multiple-qubit gates and the most used quantum algorithms. In this section, we will treat just a small part of the vast field of quantum computation. To have a complete picture of the topic, we refer the reader to [10] and [11].

Single-qubit gates

As for classical computers that are made of electrical circuits in which logic gates are implemented, quantum computers are built from quantum circuits that use quantum gates to manipulate the information. As first example, let us consider the NOT gate, that is the only possible non-trivial single-bit gate and interchanges the 0 state in the 1 state, and vice versa. Then, a quantum analogous of this classical gate should bring the state $|0\rangle$ into $|1\rangle$, and vice versa. The quantum NOT is a linear gate, that means that the state

$$\alpha|0\rangle + \beta|1\rangle, \tag{4.1}$$

is changed in

$$\alpha|1\rangle + \beta|0\rangle, \tag{4.2}$$

and can be written in a matrix form as:

$$X \equiv \begin{bmatrix} 0 & 1 \\ 1 & 0 \end{bmatrix}. \tag{4.3}$$

So, in general, single-qubit gates can be represented by 2×2 matrices. Since for any quantum state like Eq. (4.1) it has to be $|\alpha|^2 + |\beta|^2 = 1$, then the matrix U describing the quantum gate has to be unitary, i.e. $U^\dagger U = I$, where $U^\dagger$ is the adjoint of U and I is the identity matrix (2×2). Moreover, conversely to the classical case, many different single-qubit gates are possible. Two of them, which is worth to mention, are the Z gate, which leaves $|0\rangle$ unchanged and brings $|1\rangle$ in $-|1\rangle$, defined as:

$$Z \equiv \begin{bmatrix} 1 & 0 \\ 0 & -1 \end{bmatrix}, \tag{4.4}$$

and the *Hadamard* gate, that is written as:

$$H \equiv \frac{1}{\sqrt{2}} \begin{bmatrix} 1 & 1 \\ 1 & -1 \end{bmatrix}. \tag{4.5}$$

The Hadamard gate takes the state $|0\rangle$ in $\frac{1}{\sqrt{2}}(|0\rangle + |1\rangle)$, whereas $|1\rangle$ is switched to $\frac{1}{\sqrt{2}}(|0\rangle - |1\rangle)$. Moreover, applying two Hadamard gates to a state does not change it, since $H^2 = I$.

The Hadamard gate is one of the most important and used quantum gates. Let us recall the Bloch sphere representation in Fig. 1.1. In general, gates acting on a single qubit are represented by rotations and reflections on the sphere. In particular, the Hadamard gate is obtained by a first rotation of 90° about the y axis, followed by a second rotation of 180° about the x axis.

An interesting property is that an arbitrary single-qubit unitary gate can be decomposed as the product of general rotations, a gate describing the rotation about the z axis and a global phase shift in the following way:

$$V = \begin{bmatrix} \cos\left(\frac{\theta}{2}\right) & -\sin\left(\frac{\theta}{2}\right) \\ \sin\left(\frac{\theta}{2}\right) & \cos\left(\frac{\theta}{2}\right) \end{bmatrix} \begin{bmatrix} e^{-i\varphi/2} & 0 \\ 0 & e^{i\varphi/2} \end{bmatrix} e^{i\gamma}, \tag{4.6}$$

where θ, φ and γ are real numbers. Moreover, it can be proven that any number of qubits can be generated by a finite *universal* set of gates [10].

Multiple-qubit gates

In classical logic, examples of multiple-bit gates are given by the AND, OR, XOR, NAND and NOR gates and a very important property is that any function of bits can be computed by composing NAND gates only. So, the NAND gate is a *universal* gate.

The most important multi-qubit quantum gate is given by the CNOT gate, that has been already introduced in Sec. 1.1. Its circuit representation is given

in Fig. 4.1 (a): there are two input qubits, called the *control* qubit (top line) and *target* qubit (bottom line). The CNOT gate action is the same as the XOR classical gate: when the control qubit is $|0\rangle$, the target qubit remains unchanged; whereas it is flipped when the control qubit is $|1\rangle$. Its matrix representation is given by Eq. (1.9), that we report here for convenience:

$$U_{\mathrm{CNOT}} = \begin{bmatrix} 1 & 0 & 0 & 0 \\ 0 & 1 & 0 & 0 \\ 0 & 0 & 0 & 1 \\ 0 & 0 & 1 & 0 \end{bmatrix}. \tag{4.7}$$

It can easily be shown that U_{CNOT} is a unitary matrix and $U_{\mathrm{CNOT}}^{\dagger} U_{\mathrm{CNOT}} = I$.

A useful generalization of the CNOT gate to a three-qubit configuration is given by the *Toffoli* (or CCNOT) gate. The circuit representation of this gate is presented in Fig. 4.1 (b), where the two control qubits (top and middle line) and the target qubit (bottom line) are shown. The two control qubits are unaffected by the action of the gate, whereas the target qubit is flipped whenever both the control qubits are $|1\rangle$. The Toffoli gate can be represented by an 8×8 unitary matrix with the following form:

$$U_{\mathrm{T}} = \begin{bmatrix} 1 & 0 & 0 & 0 & 0 & 0 & 0 & 0 \\ 0 & 1 & 0 & 0 & 0 & 0 & 0 & 0 \\ 0 & 0 & 1 & 0 & 0 & 0 & 0 & 0 \\ 0 & 0 & 0 & 1 & 0 & 0 & 0 & 0 \\ 0 & 0 & 0 & 0 & 1 & 0 & 0 & 0 \\ 0 & 0 & 0 & 0 & 0 & 1 & 0 & 0 \\ 0 & 0 & 0 & 0 & 0 & 0 & 0 & 1 \\ 0 & 0 & 0 & 0 & 0 & 0 & 1 & 0 \end{bmatrix}. \tag{4.8}$$

There are many other interesting multiple-qubit quantum gates. However, it can be proven that *any* multiple-qubit quantum gate can be decomposed in a CNOT and single-qubit gates [10]. Moreover, the Toffoli gate can be used to simulate the classical NAND gate, thus making the simulation of any function of bits in a classical circuit possible. So, an arbitrary classical circuit can be simulated by an equivalent quantum circuit.

Quantum algorithms

Let us now move to the most important quantum algorithms and start with one of the simplest algorithms that shows that by employing quantum circuits, some advantage can be gained over classical information. So, let us introduce the *Deutsch's algorithm* [342].

Let us consider a binary function of the form:

$$f(x) : \{0,1\} \mapsto \{0,1\}, \tag{4.9}$$

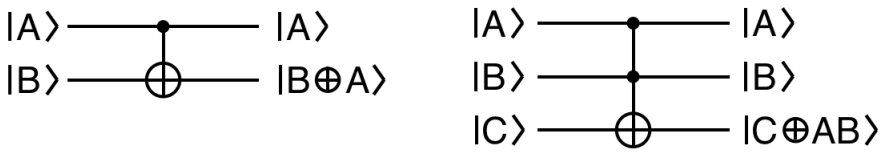

(a) CNOT (b) Toffoli

Figure 4.1: Quantum circuit representation of the (a) CNOT and (b) Toffoli gates.The symbol $\oplus$ is the addition modulo two, that means that the control qubit(s) and the target qubit are XOR-ed and the result is stored in the target qubit.

	f_0	f_1	f_2	f_3
$f(0)$	0	0	1	1
$f(1)$	0	1	0	1

Table 4.1: Possible values for the function $f(x) : \{0,1\} \mapsto \{0,1\}$.

and a unitary transformation U_f associated to $f(x)$, that is called *oracle* and acts as:

$$U_f|x\rangle|y\rangle = |x\rangle|y \oplus f(x)\rangle, \tag{4.10}$$

where $\oplus$ represents the addition modulo two (i.e. y and $f(x)$ are XOR-ed). U_f is a "black box" that we assume we can run without knowing its implementation details. So, the only way to extract information about the function (4.9) computed by the device is to give some input $x \in \{0,1\}$ and look at the output $f(x) \in \{0,1\}$. In Table 4.1 the four possible functions of the type (4.9) are shown. It is clear, two kind of functions are present: f_0 and f_3 are *constant* functions, whereas f_1 and f_2 are *balanced* functions (i.e. 0 and 1 appear the same number of times). In order to solve the problem classically, both $f(0)$ and $f(1)$ have to be determined and compared to check whether $f(0) = f(1)$ or not. This requires two calls to the oracle U_f.

The Deutsch algorithm aims to determine whether the function $f(x)$ is constant or balanced in a single call to U_f (or in a single evaluation of $f(x)$). The idea is to consider as input state (or register) to U_f the quantum state given by:

$$|\psi\rangle = \alpha|0\rangle + \beta|1\rangle, \tag{4.11}$$

and to expect U_f to return a superposition of the two possible outputs $f(0)$ and $f(1)$. The circuit representing the Deutsch's algorithm is shown in Fig. 4.2 (a) and it can be divided in four computation stages, as following. At the beginning of the circuit the state $|\psi_1\rangle = |0\rangle|1\rangle$ is present. Then, two Hadamard gates are applied to both qubits, giving the state:

$$|\psi_2\rangle = H|0\rangle H|1\rangle = |+\rangle|-\rangle, \tag{4.12}$$

where $|+\rangle = \frac{1}{\sqrt{2}}(|0\rangle + |1\rangle)$ and $|-\rangle = \frac{1}{\sqrt{2}}(|0\rangle - |1\rangle)$. After that, the oracle U_f is applied, and the output state is $|\psi_3\rangle = U_f|+\rangle|-\rangle$. Finally, a Hadamard gate

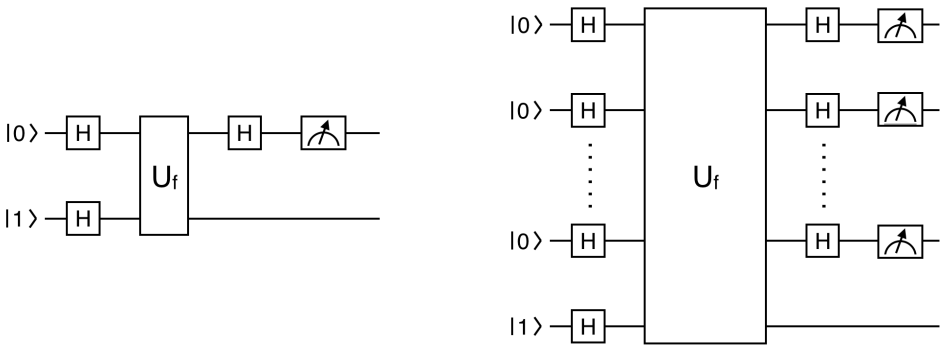

(a) Deutsch (b) Deutsch-Jozsa

Figure 4.2: Quantum circuit representation of the (a) Deutsch and (b) Deutsch-Jozsa algorithms. H represents the Hadamard gate, U_f is the unitary operator associated to the binary function $f(x)$ (see text) and the rectangle with the arrow stands for the measurement on the selected qubit.

is applied to the first qubit giving the state $|\psi_4\rangle$, and a measurement on the first qubit is then performed.

Now, let us consider the case of applying U_f to a input state of the form $|x\rangle|-\rangle$, with $x \in \{0,1\}$. It holds:

$$\begin{aligned} U_f|x\rangle|-\rangle &= \frac{1}{\sqrt{2}}\left(U_f|x\rangle|0\rangle - U_f|x\rangle|1\rangle\right) = \frac{1}{\sqrt{2}}\left(|x\rangle|f(x)\rangle - |x\rangle|1 \oplus f(x)\rangle\right) \\ &= |x\rangle \otimes \frac{1}{\sqrt{2}}\left(|f(x)\rangle - |1 \oplus f(x)\rangle\right). \end{aligned} \tag{4.13}$$

Two cases can now be considered: either $f(x) = 0$ or $f(x) = 1$. In the former case, Eq. (4.13) reduces to the following expression:

$$|\psi\rangle = |x\rangle \otimes \frac{1}{\sqrt{2}}\left(|0\rangle - |1\rangle\right) = |x\rangle|-\rangle. \tag{4.14}$$

On the contrary, when $f(x) = 1$, Eq. (4.13) gives:

$$|\psi\rangle = |x\rangle \otimes \frac{1}{\sqrt{2}}\left(|1\rangle - |0\rangle\right) = -|x\rangle|-\rangle. \tag{4.15}$$

Eq. (4.14) and (4.15) can be summarized as:

$$|\psi\rangle = U_f|x\rangle|-\rangle = (-1)^{f(x)}|x\rangle|-\rangle. \tag{4.16}$$

The above calculation can be easily transferred to the Deutsch's algorithm, since the state after the implementation of U_f is:

$$|\psi_3\rangle = U_f|+\rangle|-\rangle = \frac{1}{\sqrt{2}}\left(U_f|0\rangle|-\rangle + U_f|1\rangle|-\rangle\right). \tag{4.17}$$

By applying Eq. (4.16), $|\psi_3\rangle$ can be written as:

$$|\psi_3\rangle = \frac{1}{\sqrt{2}}\left[(-1)^{f(0)}|0\rangle|-\rangle - (-1)^{f(1)}|1\rangle|-\rangle\right]. \tag{4.18}$$

We can now distinguish between the two cases when $f(x)$ is constant or balanced. If $f(x)$ is *constant*, then $f(0) = f(1)$ and Eq. (4.18) becomes:

$$|\psi_3\rangle = (-1)^{f(0)}|+\rangle|-\rangle. \tag{4.19}$$

Considering that $H|+\rangle = |0\rangle$ and by applying the Hadamard gate to the first qubit, we get:

$$|\psi_4\rangle = (-1)^{f(0)}|0\rangle|-\rangle, \tag{4.20}$$

and the measurement on the first qubit gives as result 0. Conversely, when the function $f(x)$ is *balanced* it is $f(0) \neq f(1)$ and Eq. (4.18) can be written as:

$$|\psi_3\rangle = \pm\frac{1}{\sqrt{2}}(|0\rangle|-\rangle - |1\rangle|-\rangle) = \pm|-\rangle|-\rangle. \tag{4.21}$$

Since $H|-\rangle = |1\rangle$, by applying the Hadamard gate to the first qubit we obtain:

$$|\psi_4\rangle = \pm|1\rangle|-\rangle, \tag{4.22}$$

which gives an outcome of 1 on the measurement on the first qubit.

So, we proved that if the function $f(x)$ is constant, a measurement on the first qubit would output a value of 0, whereas in the case of a balanced function $f(x)$, the result would be a value of 1. Thus, just a *single* query to the oracle U_f is required to determine whether the function $f(x)$ is either constant or balanced.

A generalization of the Deutsch's algorithm to n-bit functions is provided by the *Deutsch-Jozsa algorithm* [343]. Now the function $f(x)$ is:

$$f(\mathbf{x}) : \{0,1\}^n \mapsto \{0,1\}. \tag{4.23}$$

As for in the Deutsch algorithm, the function $f(\mathbf{x})$ is either constant or balanced and the Deutsch-Jozsa algorithm aims to determine which is the case. The oracle U_f is implemented in the same way as Eq. (4.10), where now $\mathbf{x}$ is a n-bit string. The quantum circuit representation of the Deutsch-Jozsa algorithm is shown in Fig. 4.2 (b): each line stands for a qubit and the first n qubits are initialized to $|0\rangle$, whereas the last one is set to $|1\rangle$. Since the Deutsch-Jozsa algorithm is the direct generalization of the Deutsch algorithm, it can be proved that it only needs *one* query to the oracle U_f to determine whether the function $f(\mathbf{x})$ is either constant or balanced.

As already done for the proof of the Deutsch's algorithm, we divide the Deutsch-Jozsa algorithm in four stages. The initial state is:

$$|\psi_1\rangle = |0\rangle^{\otimes n}|1\rangle. \tag{4.24}$$

Then, a Hadamard gate is applied to each qubit of the initial register and the resulting state can be written as [10]:

$$|\psi_2\rangle = |+\rangle^{\otimes n}|1\rangle = \frac{1}{\sqrt{2^n}} \sum_{\mathbf{x}\in\{0,1\}^n} |\mathbf{x}\rangle|-\rangle, \tag{4.25}$$

where, as before, we have considered $|+\rangle = \frac{1}{\sqrt{2}}(|0\rangle + |1\rangle)$ and $|-\rangle = \frac{1}{\sqrt{2}}(|0\rangle - |1\rangle)$. The next step consists in implementing the action of the oracle U_f, that gives:

$$|\psi_3\rangle = \frac{1}{\sqrt{2^n}} \sum_{\mathbf{x}\in\{0,1\}^n} (-1)^{f(\mathbf{x})} |\mathbf{x}\rangle|-\rangle. \tag{4.26}$$

Finally, a Hadamard gate is applied to the first n qubits. By considering that:

$$H^{\otimes n}|\mathbf{x}\rangle = \bigotimes_{i=1}^{n} \frac{|0\rangle + (-1)^{x_i}|1\rangle}{\sqrt{2}} = \frac{1}{\sqrt{2^n}} \sum_{\mathbf{z}\in\{0,1\}^n} (-1)^{\mathbf{x}\cdot\mathbf{z}} |\mathbf{z}\rangle, \tag{4.27}$$

the final state $|\psi_4\rangle$ can be written as [10]:

$$\begin{aligned} |\psi_4\rangle &= \frac{1}{\sqrt{2^n}} \sum_{\mathbf{x}\in\{0,1\}^n} (-1)^{f(\mathbf{x})} H^{\otimes n}|\mathbf{x}\rangle|-\rangle \\ &= \frac{1}{2^n} \sum_{\mathbf{z}\in\{0,1\}^n} \sum_{\mathbf{x}\in\{0,1\}^n} (-1)^{f(\mathbf{x})+\mathbf{x}\cdot\mathbf{z}} |\mathbf{z}\rangle|-\rangle, \end{aligned} \tag{4.28}$$

where $\mathbf{x}\cdot\mathbf{z}$ represent the bitwise inner product of the n-strings $\mathbf{x}$ and $\mathbf{z}$. Then a measurement on the first n qubits is performed and the two cases of $f(\mathbf{x})$ constant and balanced can be separately analyzed.

If $f(\mathbf{x})$ is constant, the term $(-1)^{f(\mathbf{x})}$ can be factorized and Eq. (4.28) can be written as:

$$|\psi_4\rangle = (-1)^{f(\mathbf{x})} \sum_{\mathbf{z}\in\{0,1\}^n} \left(\frac{1}{2^n} \sum_{\mathbf{x}\in\{0,1\}^n} (-1)^{\mathbf{x}\cdot\mathbf{z}} \right) |\mathbf{z}\rangle|-\rangle. \tag{4.29}$$

The amplitude on $|\mathbf{z}\rangle = |0\cdots0\rangle$ is:

$$\frac{1}{2^n} \sum_{\mathbf{x}\in\{0,1\}^n} (-1)^{\mathbf{x}\cdot|0\cdots0\rangle} = 1, \tag{4.30}$$

thus the state $|0\rangle^{\otimes n}|-\rangle$ has amplitude 1 and $|\psi_4\rangle = (-1)^{f(\mathbf{x})}|0\rangle^{\otimes n}|-\rangle$. So, if $f(\mathbf{x})$ *constant*, a measurement on the first n qubits would give $|0\cdots0\rangle$.
In the case of a balanced function $f(\mathbf{x})$, the term $(-1)^{f(\mathbf{x})}$ cannot be factorized. However, by considering the amplitude on the state $|\mathbf{z}\rangle = |0\cdots0\rangle$, it holds:

$$\frac{1}{2^n} \sum_{\mathbf{x}\in\{0,1\}^n} (-1)^{f(\mathbf{x})+\mathbf{x}\cdot|0\cdots0\rangle} = \frac{1}{2^n} \sum_{\mathbf{x}\in\{0,1\}^n} (-1)^{f(\mathbf{x})}. \tag{4.31}$$

In the sum, for half of the terms it is $f(\mathbf{x}) = 0$, whereas for the remaining half it is $f(\mathbf{x}) = 1$ and the sum in Eq. (4.31) becomes zero. Thus, since the amplitude on $|\mathbf{z}\rangle = |0 \cdots 0\rangle$ cancels out, the outcome of the measurement on the first n qubits cannot be $|0 \cdots 0\rangle$.

So, summarizing, if the output of measurement is $|0\rangle^{\otimes n}$, then the function $f(\mathbf{x})$ is a constant function. Conversely, any other n-bit measurement result, would give a balanced function $f(\mathbf{x})$. As for the Deutsch's algorithm only *one* single query to the oracle U_f is needed to discriminate between a constant or balanced function $f(\mathbf{x})$.

Let us now consider a restriction of the Deutsch-Jozsa algorithm, the *Bernstein-Vazirani (BV) algorithm* [341]. This is the test algorithm implemented on an electronic circuit in Sec. 4.2.

As for the Deutsch-Jozsa algorithm, the function to be considered is:

$$f(\mathbf{x}) : \{0,1\}^n \mapsto \{0,1\}, \tag{4.32}$$

where, now,:

$$f(\mathbf{x}) = \mathbf{a} \cdot \mathbf{x} + b, \tag{4.33}$$

with $\mathbf{a} \in \{0,1\}^n$ and $b \in \{0,1\}$. The task of the BV algorithm is to determine $\mathbf{a}$ and b in two calls (one for $\mathbf{a}$ and one for b). Conversely, trying to find $\mathbf{a}$ and b by employing a classical algorithm would require $(n+1)$ queries to the oracle, one to determine b and n to determine $\mathbf{a}$.

The quantum circuit needed for the implementation of the BV algorithm is the same of Fig. 4.2 (b). As the classical case, one query to the oracle is needed to find b and this is done in the same way as in the classical algorithm, that is by determining $f(\mathbf{x})$ for $\mathbf{x} = 0$. Then, in order to find $\mathbf{a}$, the algorithm can still be divided in four stages. The initial state is prepared as in Eq. (4.24), with the first n qubits in the $|0\rangle$ state and the last qubit set as $|1\rangle$. Then a Hadamard gate is applied to each initial qubit, giving a state $|\psi_2\rangle$ as the one described by Eq. (4.25). After that, the oracle U_f is implemented, and the state $|\psi_3\rangle$ of Eq. (4.26) becomes now:

$$|\psi_3\rangle = \frac{(-1)^b}{\sqrt{2^n}} \sum_{\mathbf{x}\in\{0,1\}^n} (-1)^{\mathbf{a}\cdot\mathbf{x}} |\mathbf{x}\rangle|-\rangle. \tag{4.34}$$

Finally, after applying a Hadamard gate on the first n qubits, Eq. (4.28) becomes:

$$\begin{aligned} |\psi_4\rangle &= \frac{(-1)^b}{2^n} \sum_{\mathbf{z}\in\{0,1\}^n} \sum_{\mathbf{x}\in\{0,1\}^n} (-1)^{\mathbf{a}\cdot\mathbf{x}+\mathbf{x}\cdot\mathbf{z}} |\mathbf{z}\rangle|-\rangle \\ &= \frac{(-1)^b}{2^n} \sum_{\mathbf{z}\in\{0,1\}^n} \sum_{\mathbf{x}\in\{0,1\}^n} (-1)^{(\mathbf{a}\oplus\mathbf{z})\cdot\mathbf{x}} |\mathbf{z}\rangle|-\rangle. \end{aligned} \tag{4.35}$$

In the above expression, it can be:

$$\frac{1}{2^n}\sum_{\mathbf{x}\in\{0,1\}^n}(-1)^{(\mathbf{a}\oplus\mathbf{z})\cdot\mathbf{x}}=\begin{cases}1 & \text{if } \mathbf{z}=\mathbf{a}\\ 0 & \text{otherwise}\end{cases} \tag{4.36}$$

and Eq. (4.35) becomes:

$$|\psi_4\rangle=(-1)^b\sum_{\mathbf{a}\in\{0,1\}^n}|\mathbf{a}\rangle|-\rangle, \tag{4.37}$$

and $\mathbf{a}$ is thus determined.

So, the BV algorithm allows to find $\mathbf{a}$ and b in two queries to the oracle U_f, instead of the $(n+1)$ calls required classically. In the BV algorithm, it is always possible to choose $b=0$ without loss of generality. In this case, solving the problem through a classical algorithm would require n queries to the oracle, whereas the BV algorithm would bring to a solution in *one* single call.

In the next section we will introduce the BV algorithm as a test to show that any quantum information protocol can be realized on a simple electronic circuit. While this "classical" implementation would in general suffer from the loss of the exponential advantage provided by quantum mechanics, we will show that the BV algorithm is a *special* case, for it *does not require the qubits to be entangled* [344]. Thus, the BV algorithm can be *efficiently* implemented on a system that employs classical waves and the number of resources would increase *linearly* with the number of emulated qubits.

4.2 Experiment

In this section we will first present the model behind the experiment. We will then describe how the circuit has been built and discuss the results of the experiment.

4.2.1 The model

Let us consider a system like the one depicted in Fig. 4.3, in which lines stand for guides for bosonic particles. Each guide represents one state of a basis for the n-qubit Hilbert space, where an emulated n-qubit state is described by a single boson particle being in a proper superposition in 2^n guides. These are connected in a network of linear components, schematically represented by the white rectangle U, which describes any linear transformation of an initial state. This can be realized by a proper combination of simple units [345], like those shown in Fig. 4.3 (b)-(d): phase shifters (Fig. 4.3 (b)), i.e. elements that change the phase of a wave; mixers (Fig. 4.3 (c)), e.g. devices outputting the coherent sum and the coherent difference of their inputs; and finally crossings (Fig. 4.3 (d)), i.e. points in which guides exchange positions

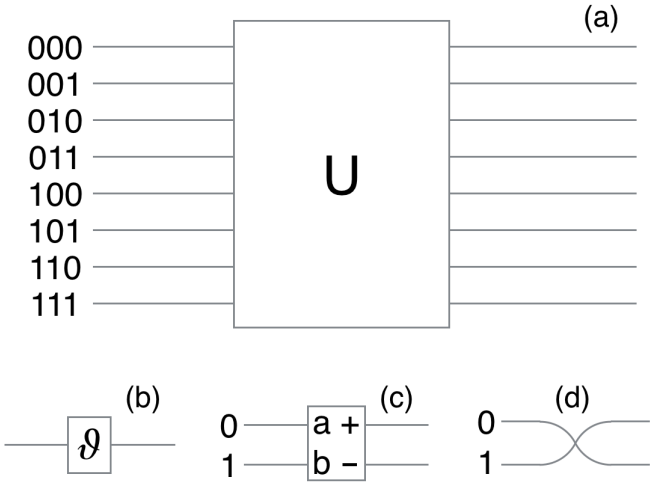

Figure 4.3: (a) Schematic representation of the fundamental components of the considered system. Lines represent guides and the rectangle a linear network mathematically described by the unitary transformation U. (b) A phase shifter, (c) a mixer, (d) two guides swapping place.

(or, if more convenient, are just relabeled). For instance, in the case of an optical implementation, one can take a photon as the boson particle, while the guides could be optical fibers, with mixers obtained by using a combination of phase shifters and beam splitters. It can be shown that this platform would allow the implementation of all the operations needed for quantum information processing.

In general, the input/output relations for a bosonic field propagating in any linear network with m inputs and m outputs can be described by an m-dimensional unitary matrix U so that [345, 346, 347]:

$$\hat{a}_{out,j} = \sum_{i=1}^{m} U_{j,i}\hat{a}_{in,i}, \qquad \hat{a}^{\dagger}_{in,i} = \sum_{j=1}^{m} U_{j,i}\hat{a}^{\dagger}_{out,j}, \tag{4.38}$$

where $\hat{a}^{\dagger}_{in,i}$ and $\hat{a}_{in,i}$ are, respectively, the creation and annihilation operators for a boson at the i-th input of the system, $\hat{a}^{\dagger}_{out,j}$ and $\hat{a}_{out,j}$ are the creation and annihilation operators for a boson at the system j-th output, respectively. Thus, for a single particle input state in the i-th channel, the output state can be written as:

$$|\varphi_{out}\rangle = \sum_{j=1}^{m} U_{j,i}\hat{a}^{\dagger}_{out,j}|\text{vac}\rangle, \tag{4.39}$$

where $|\text{vac}\rangle$ is the vacuum state. Finally, the probability of finding the particle at the j-th output is given by:

$$I_{ij} = \langle\varphi_{out}|\hat{a}^{\dagger}_{out,j}\hat{a}_{out,j}|\varphi_{out}\rangle = |U_{j,i}|^2. \tag{4.40}$$

This is the only relevant quantity in this approach, for I_{ij} is the probability of finding the n-quibt system in the state associated with the j-th guide.

I_{ij} can also be found without the need for a single particle as the network input. So, in particular, let us consider the case of a coherent state as the input in the i-th channel [165]:

$$|\varphi_{in}\rangle = |\alpha_i\rangle = \exp\left[\alpha\hat{a}_i^\dagger - \frac{|\alpha|^2}{2}\right]|\text{vac}\rangle, \tag{4.41}$$

where $|\alpha|^2$ is the average number of particles. Given the input/output relations expressed in Eq. (4.38), the output state becomes:

$$|\varphi_{out}\rangle = \exp\left[\alpha\sum_{j=1}^{m} U_{j,i}\hat{a}_{out,j}^\dagger - \frac{|\alpha|^2}{2}\right]|\text{vac}\rangle, \tag{4.42}$$

which can be written as

$$|\varphi_{out}\rangle = \prod_{j=1}^{m}\exp\left[\beta_j\hat{a}_{out,j}^\dagger - \frac{|\beta_j|^2}{2}\right]|\text{vac}\rangle, \tag{4.43}$$

where $\beta_j \equiv U_{j,i}\alpha$ and $\sum_j U_{j,i} = 1$. The average number of photons at the j-th output is then:

$$\mathcal{I}_{ij} = \langle\varphi_{out}|\hat{a}_{out,j}^\dagger\hat{a}_{out,j}|\varphi_{out}\rangle = |\beta_j|^2 = I_{ji}|\alpha|^2, \tag{4.44}$$

which is proportional to the probability I_{ij} of finding the single particle exiting the j-th guide when entering in the i-th guide. The proportionality factor is simply the average number of particle $|\alpha|^2$ in the input state.

Coherent states with large number of particles, that is when $|\alpha|^2 \gg 1$, are those that best approximate classical waves. In this context, the propagation of a classical wave in a linear network yields equivalent results as the single particle, thus suggesting that the operation of quantum gates might be *emulated* in a fully classical system. However, this approach requires an exponentially increasing amount of resources, for 2^n guides are needed to describe n qubits, voiding any exponential advantage arising from the implementation of a quantum algorithm. Nonetheless, these results are useful in the view of the *emulation* of quantum gates and algorithms. From now on, in this chapter, we can then refer to classical waves propagating in the system, and thus using the word *intensity* instead of *(average) number of particles* or *probability of finding a particle.*

Because of the simplicity and availability of analog electronics, we implemented the BV algorithm by using electronic waves to emulate a quantum circuit. The description of the circuit used will be given in the next section.

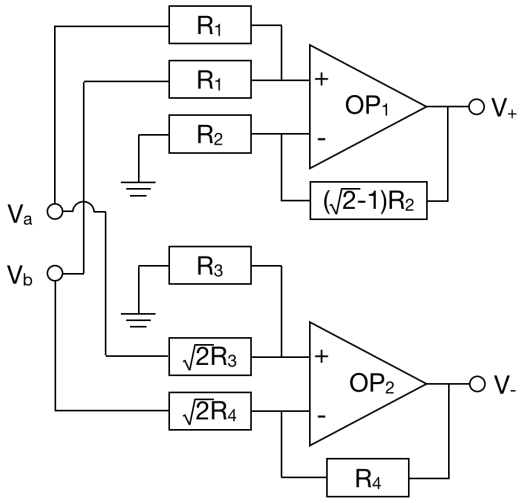

Figure 4.4: Schematic representation of the fundamental unit of the built circuit, the mixer device: the input voltages are fed to two operational amplifiers (OP_1 and OP_2), in the standard non-inverting and inverting configuration. V_a and V_b are the input voltages. OP_1 gives the sum of V_a and V_b, whereas OP_2 their difference. The resistors R_1, R_2, R_3 and R_4 are tuned in order to have $V_+ = \frac{V_a+V_b}{\sqrt{2}}$ and $V_- = \frac{V_a-V_b}{\sqrt{2}}$.

4.2.2 Circuit realization

In the experiment, the BV protocol has been implemented in an electronic circuit built with discrete electronic components, that have to emulate the components of the quantum circuit in Fig. 4.2 (b). The circuit has been designed by using the EAGLE PCB software and the sample has been fabricated by a standard chemical etching process on a printed circuit board (PCB) at the Department of Electronics at the University of Pavia.

The basic element of the circuit is called *mixer* [348] and a schematic is shown in Fig. 4.4. This is a fundamental element, since a combination of different mixers is used to prepare the initial state in a superposition as the one created by the first Hadamard gates in Fig. 4.2 (b). The mixer input voltages V_a and V_b are fed to two operational amplifiers (TL082), OP_1 and OP_2, the first in a non-inverting configuration. The output of the mixer consists in the coherent sum $V_+ = (V_a + V_b)/\sqrt{2}$ and difference $V_- = (V_a - V_b)/\sqrt{2}$ of the input voltages. The operations of sum and difference are due to the operational amplifiers, whereas the factor $\frac{1}{\sqrt{2}}$ at the output is obtained by tuning properly four trimmers of an overall value of $R_T = 3.3\ \mathrm{k}\Omega$. The trimmers are adjusted in order to fix the resistors values to $2R_1 = R_T$, $\sqrt{2}R_2 = R_T$, $\left(\sqrt{2}+1\right) R_3 = R_T$ and $\left(\sqrt{2}+1\right) R_4 = R_T$. In Fig. 4.5 (a) and (b) the designed mixer along with its PCB are given.

The characterization of the mixer device is shown in Fig. 4.5 (c) and (d). In Fig. 4.5 (c), by entering in V_a with a sinusoidal signal of $f = 1$ kHz and

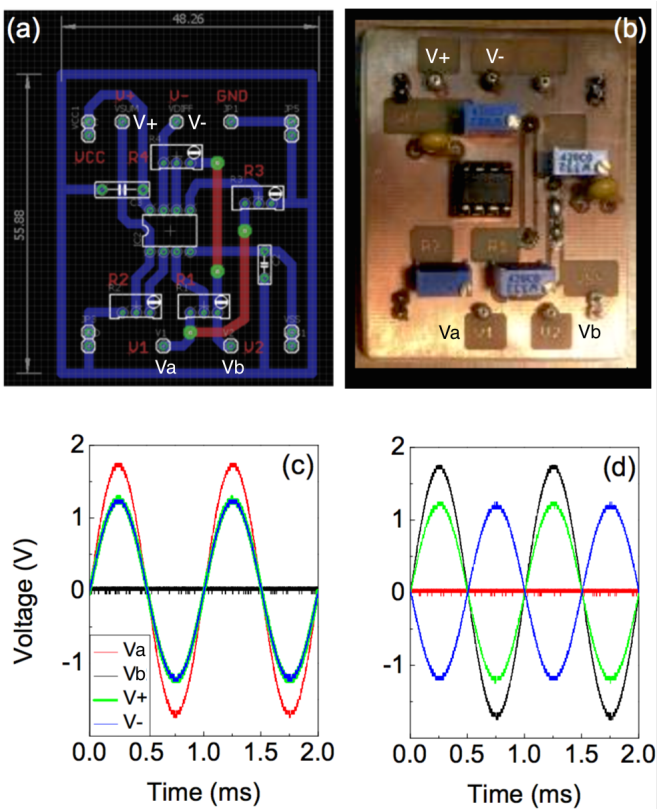

Figure 4.5: (a) Layout of the elementary component of the circuit, the mixer. Given two input signals V_a and V_b, the mixer will give their sum (V_+) and their difference (V_-), divided by a factor $\sqrt{2}$. (b) Image of the elementary unit of the circuit. (c) Result of the measurement of V_+ and V_- when V_a receives a sinusoidal signal of $f = 1$ kHz and $V_{pp} = 4$ V and V_b is connected to ground. (d) Result of the measurement of V_+ and V_- when V_a is connected to ground and V_b receives a sinusoidal signal of $f = 1$ kHz and $V_{pp} = 4$ V.

$V_{pp} = 4$ V and connecting V_b to ground, the output voltages on V_+ and V_- are measured. As expected, the measurement on both V_+ (green) and V_- (blue) gives the result $\frac{V_a}{\sqrt{2}}$. So, in this case, both V_+ and V_- have the same amplitude and the same phase. In Fig. 4.5 (d) the opposite situation is presented. V_a is connected to ground, whereas the sinusoidal signal enters in V_b. The results are now $V_+ = \frac{V_b}{\sqrt{2}}$ (green) and $V_- = \frac{-V_b}{\sqrt{2}}$ (blue) and the two output signals have same amplitude and opposite phase.

The final circuit used to implement the BV algorithm is then built by combining many mixers together, as shown in Fig. 4.6 in the particular configuration of a single CNOT between the first and third qubit. In the figure, starting from left, a first board host three Hadamard gates, H_1, H_2 and H_3 on the first, second and third qubit, respectively. The Hadamard operations are performed by a combination of mixers with the relative crossing of wires at the end of the circuit. A single circuit with two output wires for H_1, two basic elements with four crossing wires for H_2 and four mixers with eight output wires for H_3. In between the two boards, the implementation of the function U is simply given by exchanging the eight available wires exiting from H_3. Finally, on the board on the right two other Hadamard operations are performed on the first (H_1) and second (H_2) qubits, as shown in Fig. 4.2 (b). At the right side of the second board, the output voltages are connected to eight LEDs (one for each qubit) that represent the measurement.
The details of the performed measurements will be presented in the next section.

4.2.3 Measurements

As already mentioned, in our experiment, the BV algorithm [341] has been chosen as a test for the emulation of quantum gates by using electronic waves. As explained in Sec. 4.1, the aim of the BV algorithm is to determine $\mathbf{a}$ when binary functions of the form $f(\mathbf{x}) = \mathbf{a} \cdot \mathbf{x}$ (we chose to be $b = 0$), with both $\mathbf{a}$ and $\mathbf{x}$ binary vectors of length n, are considered. This is achieved in a single call, instead of the n calls required when using classical digital computation, by exploiting superpositions of qubits.

In the first set of measurements, the BV algorithm in a three-qubit configuration (corresponding to 8 independent voltage wires) has been successfully emulated. The algorithm has been validated for all the four possible combinations of the vector $\mathbf{a}$, i.e. $\mathbf{a} = (0,0)\,,\ (0,1)\,,\ (1,0)\,,\ (1,1)$. This can be obtained by appropriately exchanging the wires in between the two boards in the circuit of Fig. 4.6. Here, the initial Hadamard gates prepare the qubits in a superposition of all possible input strings $\mathbf{x}$, and the function is weighted on the superposition.

The measurements are taken by supplying the two boards in Fig. 4.6 with a voltage of ± 15 V. The input signal used is a sine wave of frequency $f = 1$ kHz and amplitude $V_{pp} = 10$ V. The result of the measurement is read as output

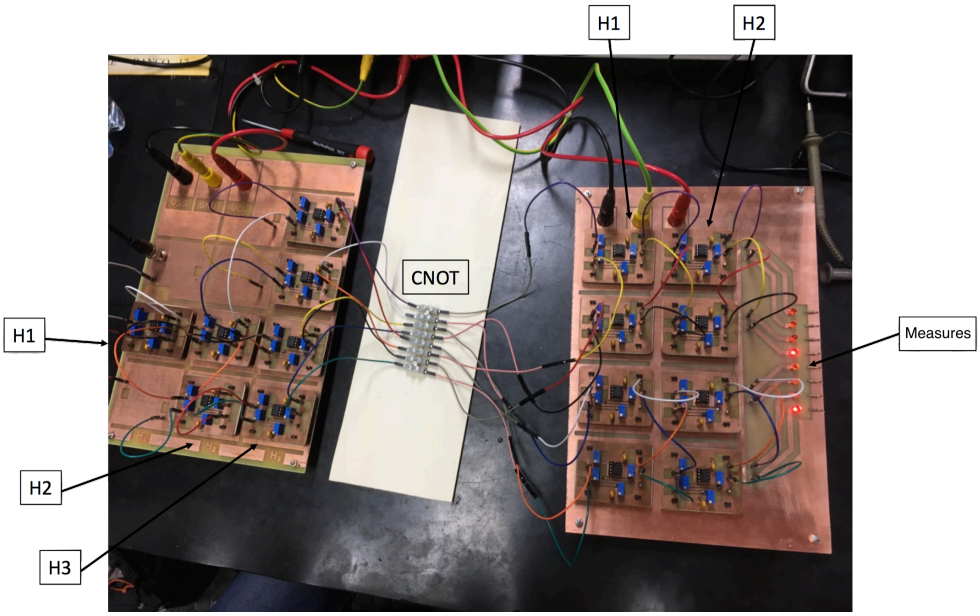

Figure 4.6: Image of the entire circuit (see also Fig. 4.2), in the particular configuration when the function U_f corresponds to a CNOT operation between the first and third qubit. H stands for the Hadamard operation. Before implementing the function U_f, three Hadamard operations are performed on q_1, q_2 and q_3. They are H_1, H_2 and H_3, respectively. After the implementation of the function U_f a Hadamard on q_1 (H_1) and then a Hadamard on q_2 (H_2) are performed. Finally, the LEDs on the right of the circuit represent the output of the measurement.

voltages and can be directly seen through the LEDs that are emitting light. All the possible results of the experiment are shown in Fig. 4.7-4.10. In the figures, (a) gives the schematic view of the quantum circuit and (b) is the sketch of the built electronic circuit corresponding to (a): the mixer is represented by a rectangle, where a and b stand for V_a and V_b, respectively, and + and − represent V_+ and V-, respectively. In (c) the result of the experiment, i. e. the voltages measured across all the eight outputs is presented in a graph. The channels with high output voltage correspond to the two guides for which the first two qubits give the correct answer for the vector **a**. Finally, (d) shows the same result as (c), visualized through the LEDs that are emitting light.

In Fig. 4.7, the function U_f implemented is the identity, so the wires between the two boards are not exchanged. As expected, the voltages are high only for the wires in which the first and second qubit (q_1 and q_2) correspond to the correct value of **a**, that is $\mathbf{a} = (0, 0)$. This can also be verified by eye through the LEDs. Infact, the lights are on for $|q_3q_2q_1\rangle = |000\rangle$, $|100\rangle$.
In Fig. 4.8 the unitary transformation corresponding to the function U_f is implemented using a single CNOT gate between the second (q_2) and the target qubit (q_3). This is achieved in our scheme by exchanging the third wire with the seventh, and the fourth wire with the eighth. In this case, the voltages are high only for the wires in which q_1 and q_2 correspond to $\mathbf{a} = (0, 1)$ and the LEDs' lights are on, as expected, for $|q_3q_2q_1\rangle = |010\rangle$, $|110\rangle$.
In Fig. 4.9 the function U_f is represented by a single CNOT between the first and third qubit, obtained in the circuit by exchanging the second wire with the sixth, and the fourth wire with the eighth. As expected, the wires with high output voltages correspond to $q_1 = 1$ and $q_2 = 0$, that is the correct value of **a**, that is $\mathbf{a} = (1, 0)$. In this case, the LEDs' lights are on for $|q_3q_2q_1\rangle = |001\rangle$, $|101\rangle$.
Finally, in Fig. 4.10 the unitary transformation is implemented through a combination of the two previously described CNOT gates. This time the voltages are high for $q_1 = 1$ and $q_2 = 1$, that give the correct value of **a**, namely $\mathbf{a} = (1, 1)$. As expected, the lights are on for $|q_3q_2q_1\rangle = |011\rangle$, $|111\rangle$.

Linear scaling demonstration

As shown and discussed in the previous section, 2^n waveguides are needed to emulate n qubits as in general the Hilbert space of the system has dimension 2^n. However, the BV algorithm is a special case among quantum algorithms, in which *the qubits are never entangled* [344]. The Hilbert spaces of the qubits remain therefore independent and the BV algorithm can *efficiently* be implemented by exploiting a system that uses classical waves. This is the experiment described in this section. We used two waveguides to implement each qubit and Hadamard transformations are obtained by applying a single mixer to the two waveguides. The unitary transformation representing the function U_f is implemented by "marking" the relevant qubits with a π phase shift on the second waveguide for all the elements of the vector **a** equal to one.

This implementation is carried out using the same circuitry employed for the experiments described in the previous section. The measurements are taken by supplying the two boards in Fig. 4.6 with a voltage of ±15 V. The configuration of the circuit is now given by using only the third raw of mixers in the first board (used to enter the input signal) and the first raw of the second board. The eight wires let us emulate up to four qubits. The input signal used is a sine wave of frequency $f = 1$ kHz and amplitude $V_{pp} = 3.5$ V and enters in each upper waveguide (0). The result of the measurement is read as output voltages at the V_+ and V_- pins of the first raw of mixers in the second board. Each mixer represents a single qubit.
The π phase shift on the desired waveguide is obtained thorugh inverting circuits, as the one shown in Fig. 4.11. They are made of an operational amplifier (LM741) and its four resistors of the same value ($R = 3$ kΩ). They are employed in between the two boards in order to invert the signal, when required. In Fig. 4.12-4.27 the results of the experiment are shown. In the figures, in (a) the schematic view of the quantum circuit is shown, whereas (b) is the sketch of the electronic circuit where the phase shift on the desired waveguide is marked with π. Finally, (c)-(f) represents the results for each qubit. The upper waveguide, labeled as 0 is represented by a black line, whereas the green line stands for the lower waveguide 1. From Fig. 4.12-4.27, as expected, the signal remains high on the upper waveguide when no inversion occurs. On the contrary, when the waveguide is marked with a phase shift, the measured output voltage is high on the lower waveguide.

The experiment can be run for one, two, three, four etc. emulated qubits by using two, four, six and eight and so on wires respectively. This clearly shows that, in the case of the BV algorithm, the relation between emulated qubits and the components used in the classical system can be linear. Furthermore, the advantage of this algorithm with respect to classical *digital* logic is still fulfilled, even in this fully classical implementation. The problem is solved in a single call instead of n calls because the function is still weighted over a superposition of all possible inputs. In contrast to entanglement, such a superposition is achievable with classical waves.

So, the measurement just described proves that the big advantage of quantum information over its classical counterpart lies in the property of *entanglement*, as already mentioned in Sec. 1.1. In fact, as it is clear from our experiment, *any* quantum protocol that does not require the qubits to be entangled (or with limited-entanglement) can be emulated by a classical system, such as electronic waves. In this case, even if dealing with a classical system, a speed-up over classical *digital* logic is still observed and the resources would scale *linearly* with the number of emulated qubits. Obviously, our implementation *would not* give the same result when dealing with protocols that operate with entangled qubits. In this last case, the dominance of quantum computation over classical computation would result.

4.3 Conclusions

In this chapter a way of implementing quantum algorithms by using classical waves has been shown in the special case of the BV algorithm.

We used top-of-the-shelf, analog electronics components due to their availability and ease of implementation, giving an easy reproducibility of the present method. However, a lot more complexity can be gained by using integrated microelectronic circuits. The latest generation of commercial Central Processing Units (CPUs) contain a number of transistor features of the order of 10^{10} and hundreds or thousand of such units can be operated in parallel in existing Graphic Processing Units (GPUs). So, in such systems, general quantum algorithms could be emulated up to at least 30 qubits in a cheap and reliable way. This would in turn constitute an important testbed where quantum algorithms can be developed and tested before being run on actual quantum computers. In the case of quantum algorithms with no or limited [349] entanglement, quantum logic with thousands of qubits can probably be emulated in systems with CPU or GPU level of complexity. This is particularly interesting for quantum search algorithms, that have already been shown can be run, although not efficiently, with limited entanglement [338, 350].

The method described in this chapter could also be interesting for teaching purposes. In fact, the ability of building physical systems capable of running quantum logical protocols using cheap and intuitive components is a key feature for their use in education. This, in turn, could become of primary interest as quantum technologies become more widespread, for a new class of "quantum engineers" will have to be formed in higher education institutions. So, the experiment we carried out can act as an important teaching support in laboratory classes.

Finally, the system we described also sheds light on the importance of entanglement [351] as the discriminating factor for the exponential advantage that quantum information processing systems can have over their classical counterparts.

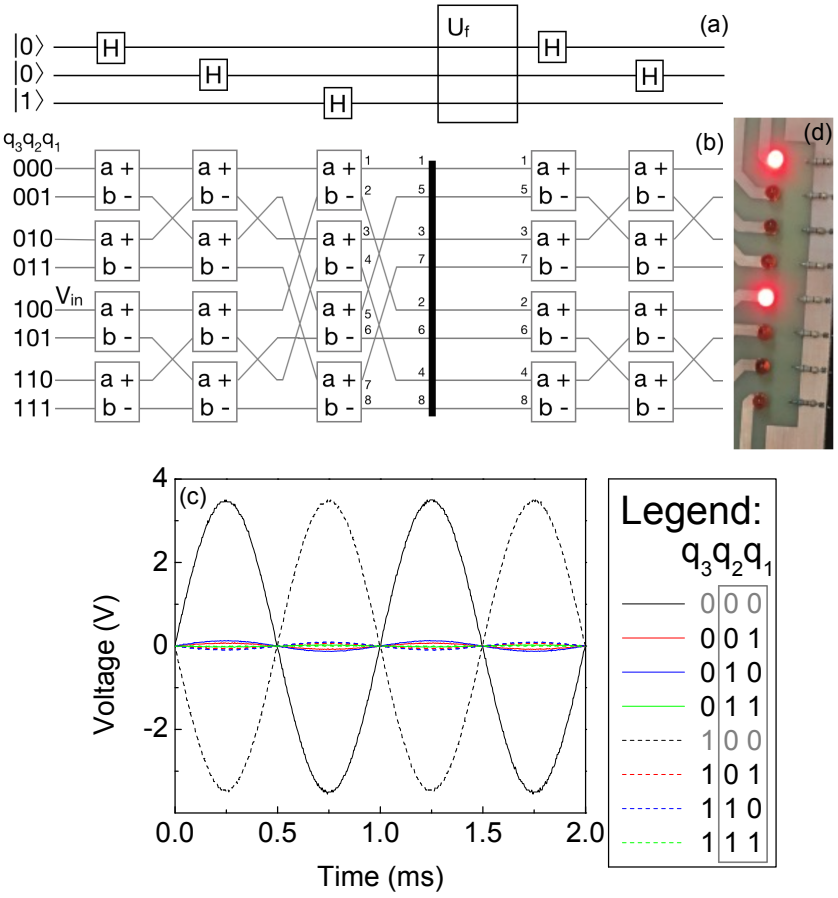

Figure 4.7: (a) Sketch of the quantum circuit when the function U_f is the identity. (b) Scheme of electronic circuit corresponding to (a): a and b stand for the input pins, where we enter in a ($|100\rangle$) with a sinusoidal signal of $f = 1$ kHz and $V_{pp} = 10$ V, whereas b ($|101\rangle$) is connected to ground. All the remaining a and b pins are connected to ground. $+$ and $-$ stand for the outputs (sum and difference of a and b) of the elementary units of the circuit. Since $U_f = \mathbf{a} \cdot \mathbf{x}$ is the identity, then $\mathbf{a} = (0, 0)$. (c) Signals measured at the end of the circuit. The voltage is high only when $|q_3q_2q_1\rangle$ are $|000\rangle$ and $|100\rangle$, that are the correct values for q_1 and q_2 in order to correspond to a. (d) LEDs at the end of circuit of circuit implementing the BV protocol. The lights are on, as expected, when $|q_3q_2q_1\rangle$ are $|000\rangle$ and $|100\rangle$, respectively.

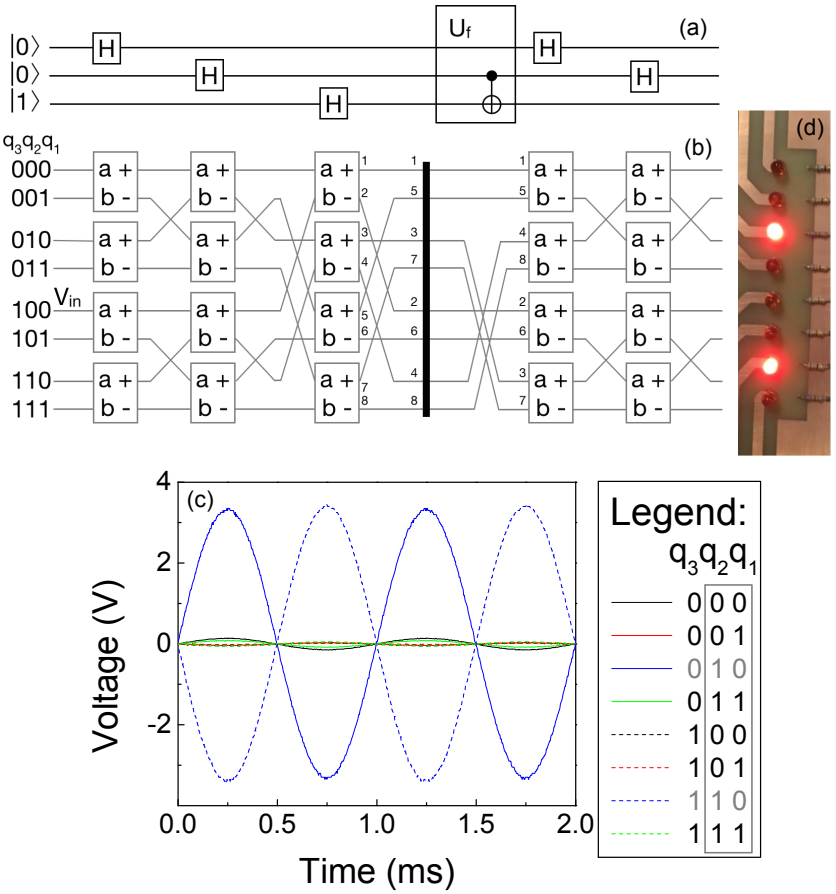

Figure 4.8: (a) Sketch of the quantum circuit when the function U_f is the CNOT operation between the second and third qubit. (b) Scheme of electronic circuit corresponding to (a): a and b stand for the input pins, where we enter in a ($|100\rangle$) with a sinusoidal signal of $f = 1$ kHz and $V_{pp} = 10$ V, whereas b ($|101\rangle$) is connected to ground. All the remaining a and b pins are connected to ground. $+$ and $-$ stand for the outputs (sum and difference of a and b) of the elementary units of the circuit. Since $U_f = \mathbf{a} \cdot \mathbf{x}$ is the CNOT operation between q_2 and q_3, then $\mathbf{a} = (0, 1)$. (c) Signals measured at the end of the circuit. The voltage is high only when $|q_3q_2q_1\rangle$ are $|010\rangle$ and $|110\rangle$, that are the correct values for q_1 and q_2 in order to correspond to a. (d) LEDs at the end of the circuit implementing the BV protocol. The lights are on, as expected, when $|q_3q_2q_1\rangle$ are $|010\rangle$ and $|110\rangle$, respectively.

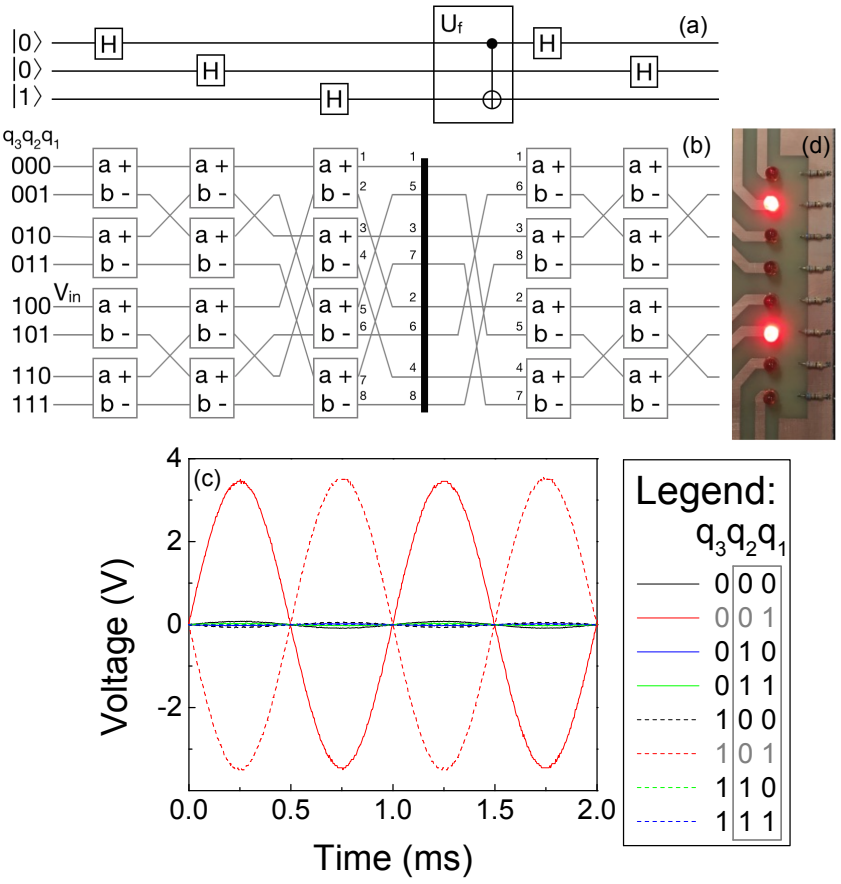

Figure 4.9: (a) Sketch of the quantum circuit when the function U_f is the CNOT operation between the first and third qubit. (b) Scheme of electronic circuit corresponding to (a): a and b stand for the input pins, where we enter in a ($|100\rangle$) with a sinusoidal signal of $f = 1$ kHz and $V_{pp} = 10$ V, whereas b ($|101\rangle$) is connected to ground. All the remaining a and b pins are connected to ground. $+$ and $-$ stand for the outputs (sum and difference of a and b) of the elementary units of the circuit. Since $U_f = \mathbf{a} \cdot \mathbf{x}$ is the CNOT operation between q_1 and q_3, then $\mathbf{a} = (1, 0)$. (b) Signals measured at the end of the circuit. The voltage is high only when $|q_3q_2q_1\rangle$ are $|001\rangle$ and $|101\rangle$, that are the correct values for q_1 and q_2 in order to correspond to a. (c) LEDs at the end of the circuit implementing the BV protocol. The lights are on, as expected, when $|q_3q_2q_1\rangle$ are $|001\rangle$ and $|101\rangle$, respectively.

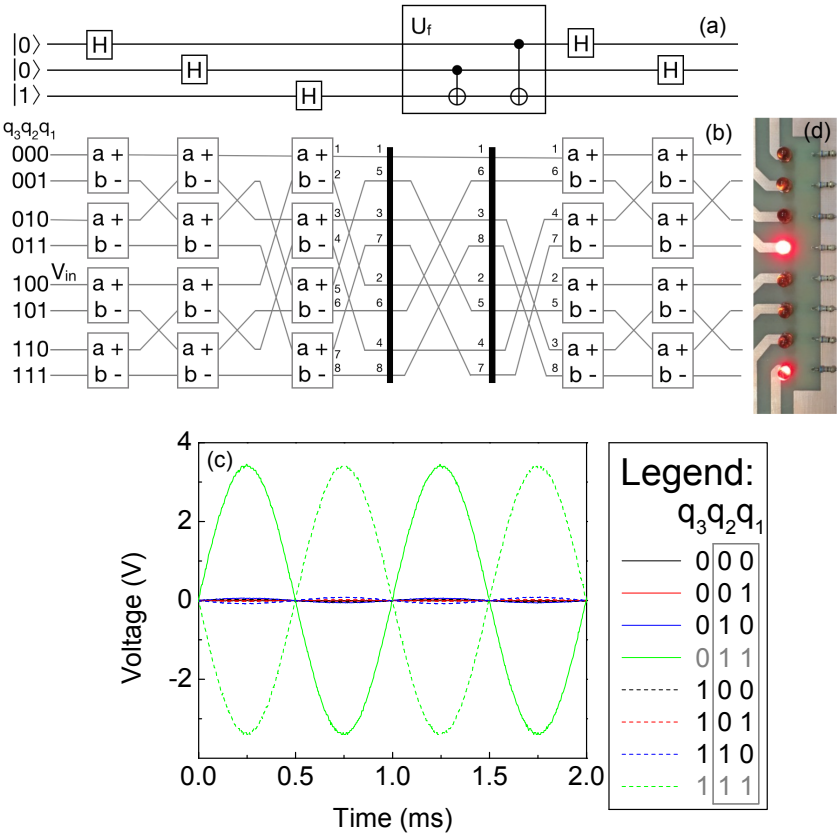

Figure 4.10: (a) Sketch of the quantum circuit when the function U_f is composed by a first CNOT operation between the second and third qubit followed by a second CNOT operation between the first and third qubit. (b) Scheme of electronic circuit corresponding to (a): a and b stand for the input pins, where we enter in a ($|100\rangle$) with a sinusoidal signal of $f = 1$ kHz and $V_{pp} = 10$ V, whereas b ($|101\rangle$) is connected to ground. All the remaining a and b pins are connected to ground. $+$ and $-$ stand for the outputs (sum and difference of a and b) of the elementary units of the circuit. Since $U_f = \mathbf{a} \cdot \mathbf{x}$ is the double CNOT operation between q_2 and q_3 and q_1 and q_3, respectively, then $\mathbf{a} = (1, 1)$. (c) Signals measured at the end of the circuit. The voltage is high only when $|q_3q_2q_1\rangle$ are $|011\rangle$ and $|111\rangle$, that are the correct values for q_1 and q_2 in order to correspond to a. (d) LEDs at the end of the circuit implementing the BV protocol. The lights are on, as expected, when $|q_3q_2q_1\rangle$ are $|011\rangle$ and $|111\rangle$, respectively.

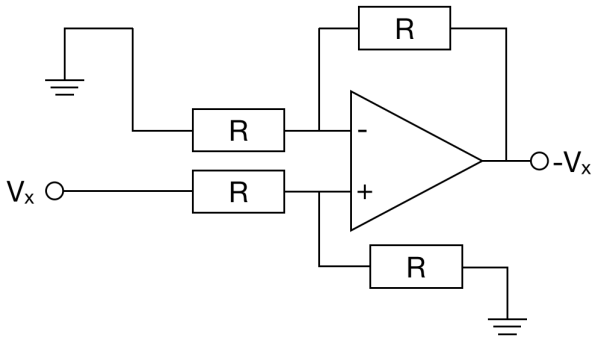

Figure 4.11: Scheme of the inverting circuit used. The operational amplifier gives the difference between the ground and a signal V_x. So, the input signal V_x is inverted. The four resistors are chosen to be of the same value ($R = 3$ kΩ) in order to have a factor 1 multiplying $-V_x$ at the output.

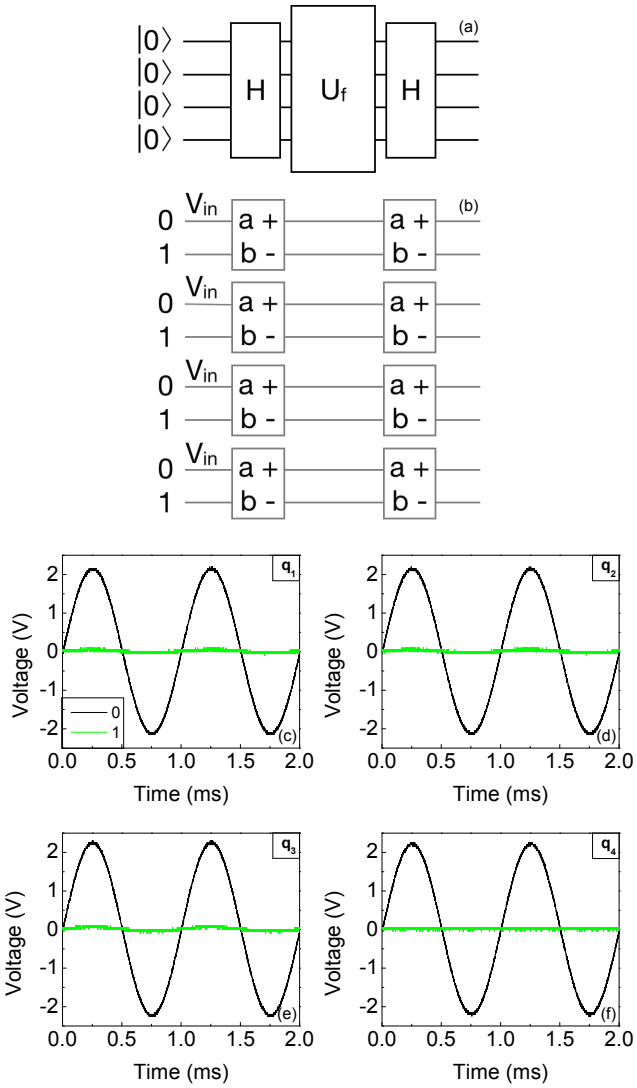

Figure 4.12: (a) Sketch of the general quantum circuit. (b) Scheme of electronic circuit corresponding to (a): a and b stand for the input pins, where we enter in a with a sinusoidal signal of $f = 1$ kHz and $V_{pp} = 3.5$ V, whereas b is connected to ground. $+$ and $-$ stand for the outputs (sum and difference of a and b) of the elementary units of the circuit. In this case, the identity, where no inversion of the signal occurs, is shown. (c)-(f) Measurements done at the $+$ and $-$ ports of the second stage of elementary units of the circuit, corresponding to the second Hadamard operation. The black line represents the upper waveguide (0), whereas the green line stands for the lower waveguide (1). Since in this case $|q_1 q_2 q_3 q_4\rangle = |0000\rangle$, the voltage is high in the upper waveguide for each one of the four qubits, as expected.

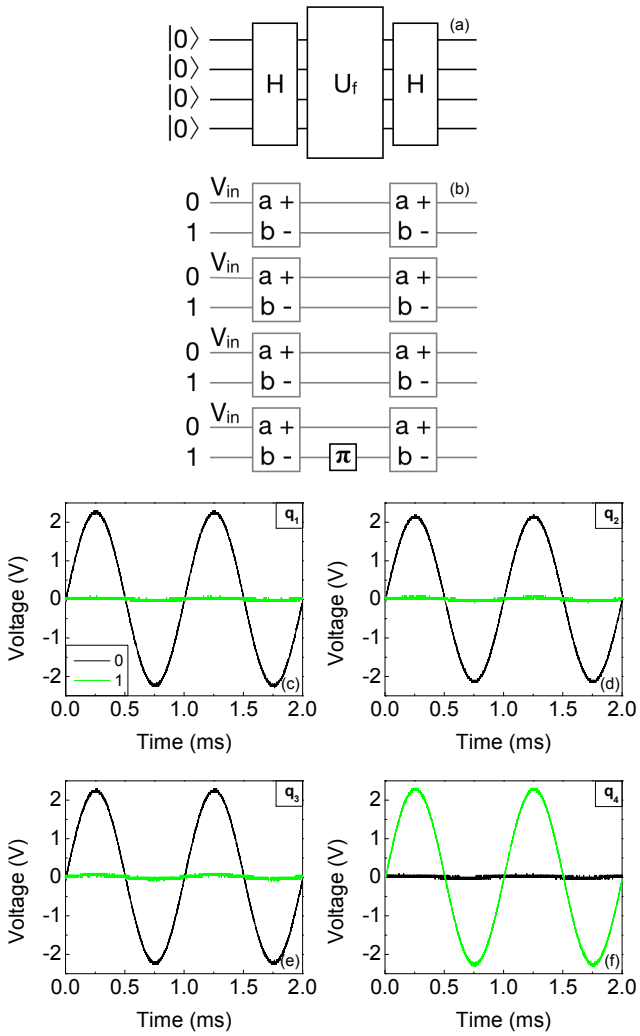

Figure 4.13: (a) Sketch of the general quantum circuit. (b) Scheme of electronic circuit corresponding to (a): a and b stand for the input pins, where we enter in a with a sinusoidal signal of $f = 1$ kHz and $V_{pp} = 3.5$ V, whereas b is connected to ground. + and − stand for the outputs (sum and difference of a and b) of the elementary units of the circuit. In this case, the circuit with only one inversion on q_4 is shown. (c)-(f) Measurements done at the + and − ports of the second stage of elementary units of the circuit, corresponding to the second Hadamard operation. The black line represents the upper waveguide (0), whereas the green line stands for the lower waveguide (1). As expected, the voltage is high in the upper waveguide for the first three qubits, whereas for q_4 the voltage is high for the lower waveguide, for the case $|q_1 q_2 q_3 q_4\rangle = |0001\rangle$ is here considered.

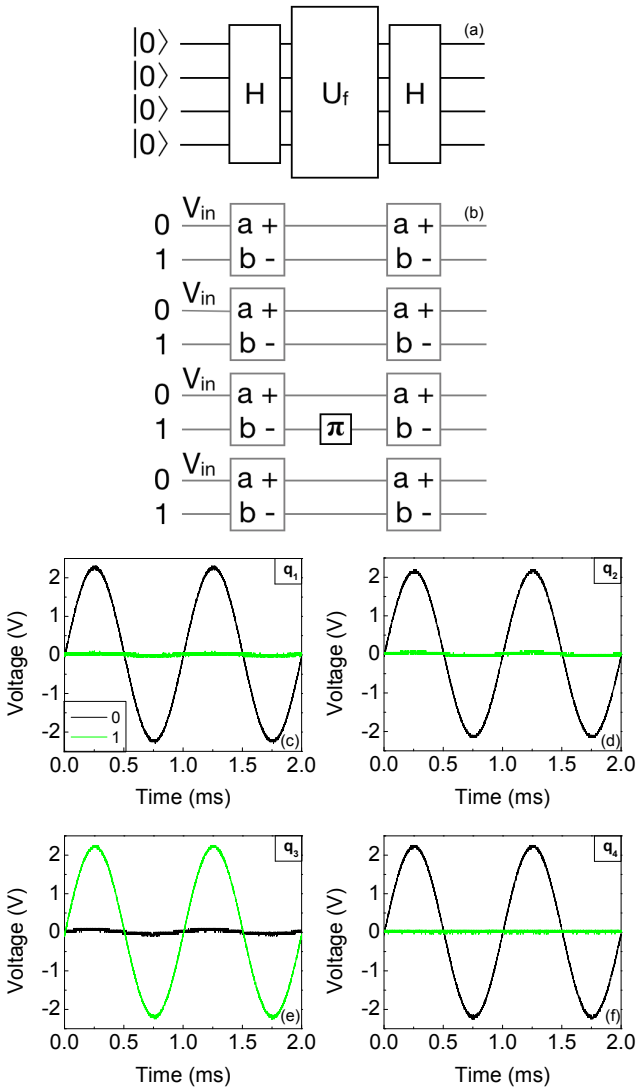

Figure 4.14: (a) Sketch of the general quantum circuit. (b) Scheme of electronic circuit corresponding to (a): a and b stand for the input pins, where we enter in a with a sinusoidal signal of $f = 1$ kHz and $V_{pp} = 3.5$ V, whereas b is connected to ground. $+$ and $-$ stand for the outputs (sum and difference of a and b) of the elementary units of the circuit. In this case, the circuit with only one inversion on q_3 is shown. (c)-(f) Measurements done at the $+$ and $-$ ports of the second stage of elementary units of the circuit, corresponding to the second Hadamard operation. The black line represents the upper waveguide (0), whereas the green line stands for the lower waveguide (1). Since in this case $|q_1 q_2 q_3 q_4\rangle = |0010\rangle$, then the voltage is high in the upper waveguide for q_1, q_2 and q_4, whereas for q_3 the voltage is high for the lower waveguide, as expected.

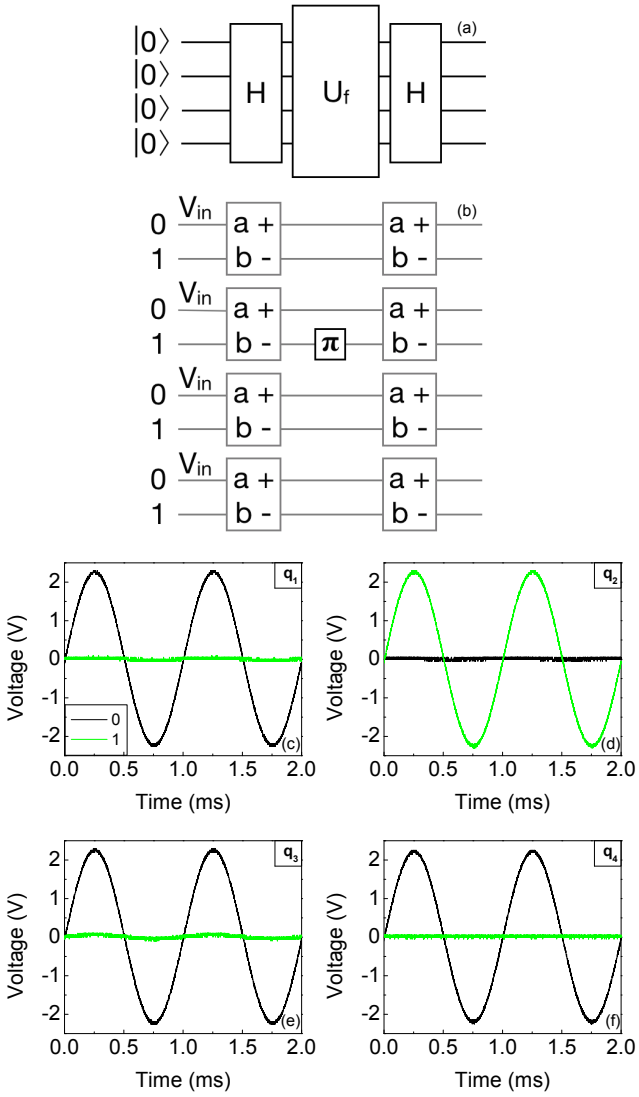

Figure 4.15: (a) Sketch of the general quantum circuit. (b) Scheme of electronic circuit corresponding to (a): a and b stand for the input pins, where we enter in a with a sinusoidal signal of $f = 1$ kHz and $V_{pp} = 3.5$ V, whereas b is connected to ground. $+$ and $-$ stand for the outputs (sum and difference of a and b) of the elementary units of the circuit. In this case, the circuit with only one inversion on q_2 is shown. (c)-(f) Measurements done at the $+$ and $-$ ports of the second stage of elementary units of the circuit, corresponding to the second Hadamard operation. The black line represents the upper waveguide (0), whereas the green line stands for the lower waveguide (1). Since in this case $|q_1 q_2 q_3 q_4\rangle = |0100\rangle$, the voltage is high in the upper waveguide for q_1, q_3 and q_4, whereas for q_2 the voltage is high for the lower waveguide, as expected.

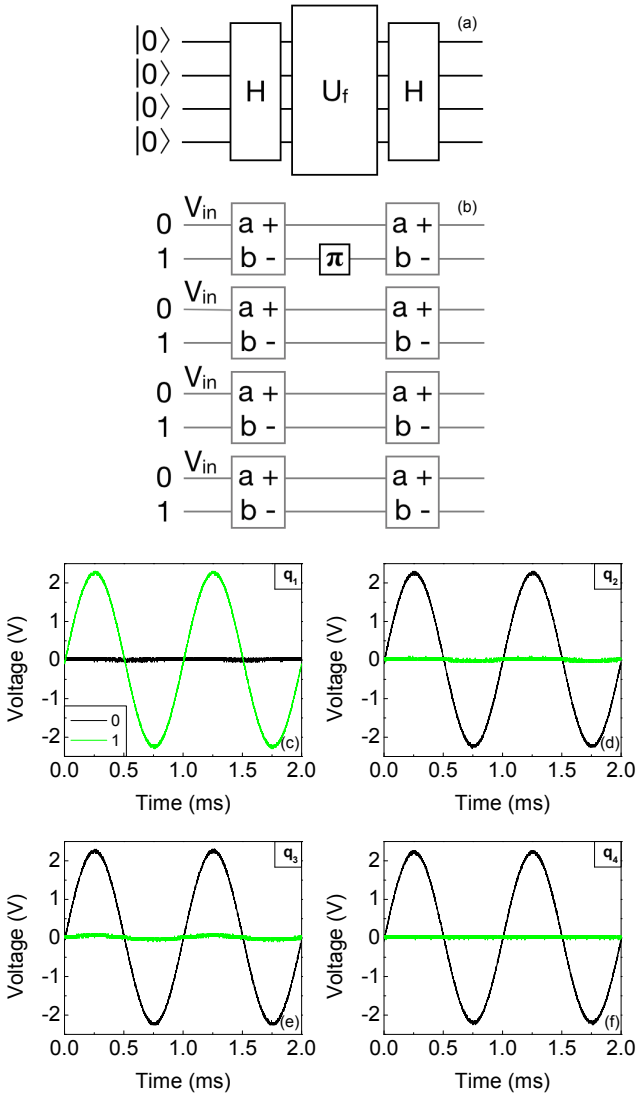

Figure 4.16: (a) Sketch of the general quantum circuit. (b) Scheme of electronic circuit corresponding to (a): a and b stand for the input pins, where we enter in a with a sinusoidal signal of $f = 1$ kHz and $V_{pp} = 3.5$ V, whereas b is connected to ground. $+$ and $-$ stand for the outputs (sum and difference of a and b) of the elementary units of the circuit. In this case, the circuit with only one inversion on q_1 is shown. (c)-(f) Measurements done at the $+$ and $-$ ports of the second stage of elementary units of the circuit, corresponding to the second Hadamard operation. The black line represents the upper waveguide (0), whereas the green line stands for the lower waveguide (1). As expected, the voltage is high in the upper waveguide for q_2, q_3 and q_4, whereas for q_1 the voltage is high for the lower waveguide, for in this case $|q_1q_2q_3q_4\rangle = |1000\rangle$.

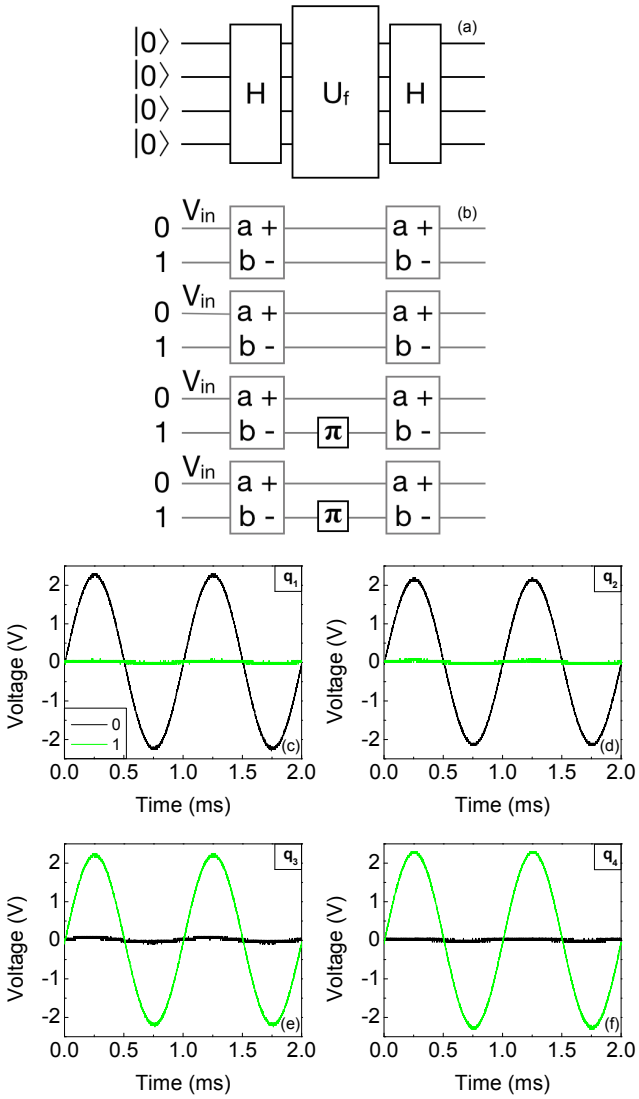

Figure 4.17: (a) Sketch of the general quantum circuit. (b) Scheme of electronic circuit corresponding to (a): a and b stand for the input pins, where we enter in a with a sinusoidal signal of $f = 1$ kHz and $V_{pp} = 3.5$ V, whereas b is connected to ground. $+$ and $-$ stand for the outputs (sum and difference of a and b) of the elementary units of the circuit. In this case, the circuit with two inversions on q_3 and q_4 respectively is shown. (c)-(f) Measurements done at the $+$ and $-$ ports of the second stage of elementary units of the circuit, corresponding to the second Hadamard operation. The black line represents the upper waveguide (0), whereas the green line stands for the lower waveguide (1). Since $|q_1 q_2 q_3 q_4\rangle = |0011\rangle$, as expected, the voltage is high in the upper waveguide for q_1 and q_2, whereas for q_3 and q_4 the voltage is high for the lower waveguide.

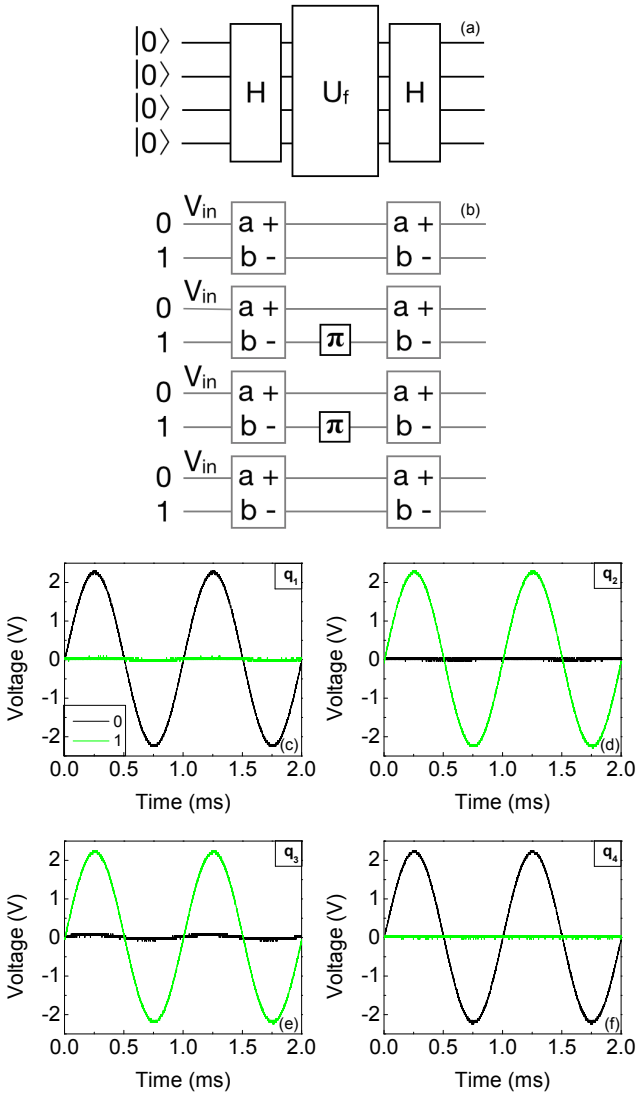

Figure 4.18: (a) Sketch of the general quantum circuit. (b) Scheme of electronic circuit corresponding to (a): a and b stand for the input pins, where we enter in a with a sinusoidal signal of $f = 1$ kHz and $V_{pp} = 3.5$ V, whereas b is connected to ground. $+$ and $-$ stand for the outputs (sum and difference of a and b) of the elementary units of the circuit. In this case, the circuit with two inversions on q_2 and q_3 respectively is shown. (c)-(f) Measurements done at the $+$ and $-$ ports of the second stage of elementary units of the circuit, corresponding to the second Hadamard operation. The black line represents the upper waveguide (0), whereas the green line stands for the lower waveguide (1). Since $|q_1 q_2 q_3 q_4\rangle = |0110\rangle$,as expected, the voltage is high in the upper waveguide for q_1 and q_4, whereas for q_2 and q_3 the voltage is high for the lower waveguide.

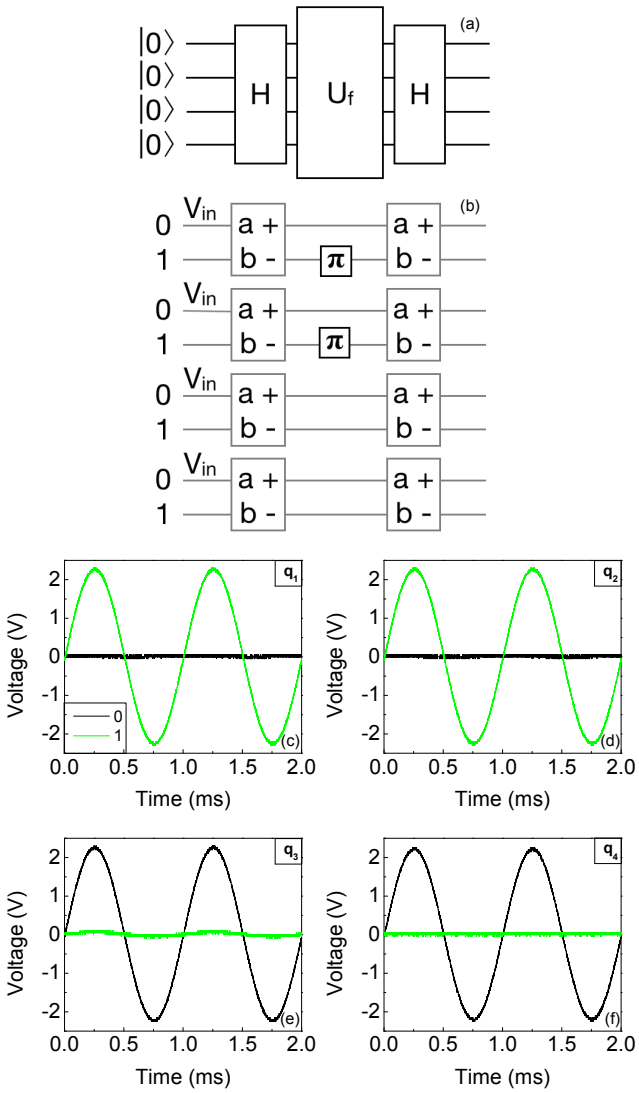

Figure 4.19: (a) Sketch of the general quantum circuit. (b) Scheme of electronic circuit corresponding to (a): a and b stand for the input pins, where we enter in a with a sinusoidal signal of $f = 1$ kHz and $V_{pp} = 3.5$ V, whereas b is connected to ground. $+$ and $-$ stand for the outputs (sum and difference of a and b) of the elementary units of the circuit. In this case, the circuit with two inversions on q_1 and q_2 respectively is shown. (c)-(f) Measurements done at the $+$ and $-$ ports of the second stage of elementary units of the circuit, corresponding to the second Hadamard operation. The black line represents the upper waveguide (0), whereas the green line stands for the lower waveguide (1). In this case $|q_1q_2q_3q_4\rangle = |1100\rangle$, thus, as expected, the voltage is high in the upper waveguide for q_3 and q_4, whereas for q_1 and q_2 the voltage is high for the lower waveguide.

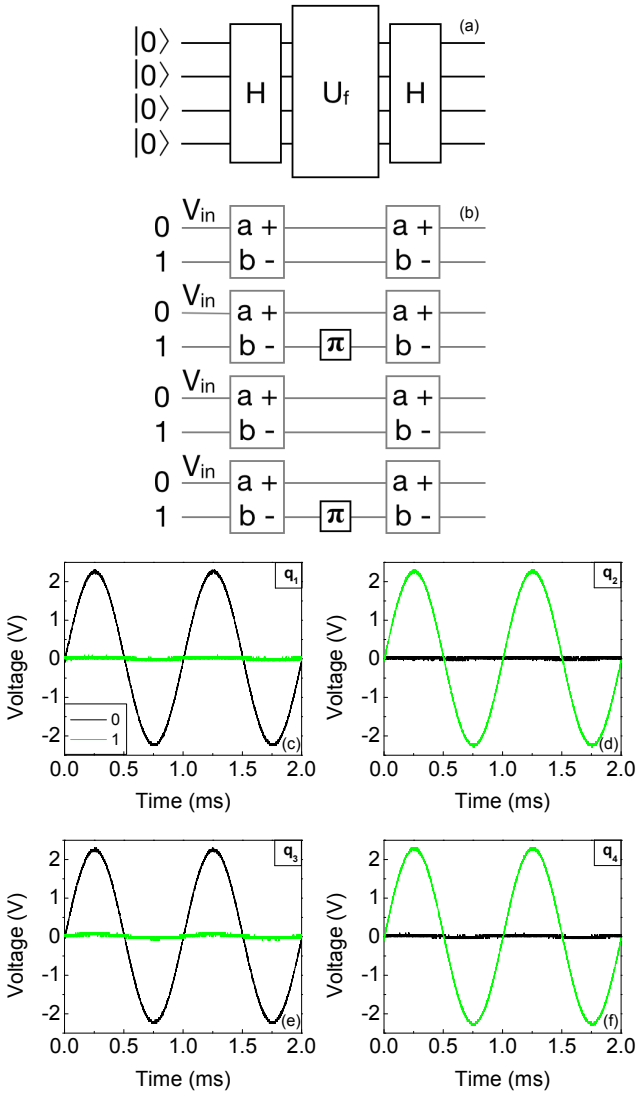

Figure 4.20: (a) Sketch of the general quantum circuit. (b) Scheme of electronic circuit corresponding to (a): a and b stand for the input pins, where we enter in a with a sinusoidal signal of $f = 1$ kHz and $V_{pp} = 3.5$ V, whereas b is connected to ground. $+$ and $-$ stand for the outputs (sum and difference of a and b) of the elementary units of the circuit. In this case, the circuit with two inversions on q_2 and q_4 respectively is shown. (c)-(f) Measurements done at the $+$ and $-$ ports of the second stage of elementary units of the circuit, corresponding to the second Hadamard operation. The black line represents the upper waveguide (0), whereas the green line stands for the lower waveguide (1). In this case, the voltage is high in the upper waveguide for q_1 and q_3, whereas for q_2 and q_4 the voltage is high for the lower waveguide, as it should be for $|q_1 q_2 q_3 q_4\rangle = |0101\rangle$.

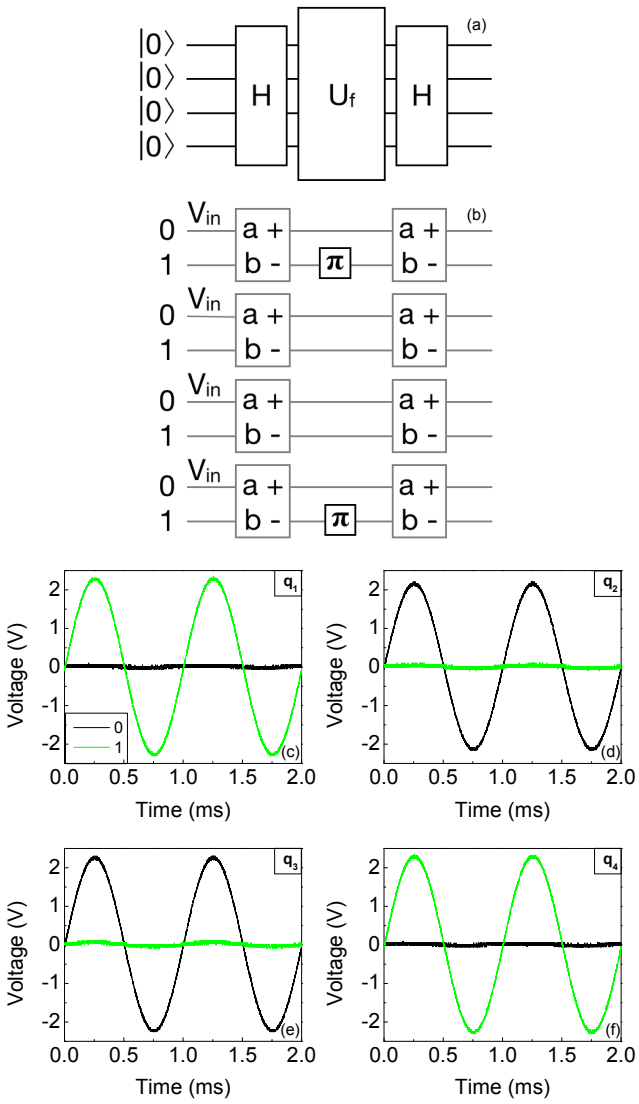

Figure 4.21: (a) Sketch of the general quantum circuit. (b) Scheme of electronic circuit corresponding to (a): a and b stand for the input pins, where we enter in a with a sinusoidal signal of $f = 1$ kHz and $V_{pp} = 3.5$ V, whereas b is connected to ground. $+$ and $-$ stand for the outputs (sum and difference of a and b) of the elementary units of the circuit. In this case, the circuit with two inversions on q_1 and q_4 respectively is shown. (c)-(f) Measurements done at the $+$ and $-$ ports of the second stage of elementary units of the circuit, corresponding to the second Hadamard operation. The black line represents the upper waveguide (0), whereas the green line stands for the lower waveguide (1). Since in this case $|q_1 q_2 q_3 q_4\rangle = |1001\rangle$, as expected, the voltage is high in the upper waveguide for q_2 and q_3, whereas for q_1 and q_4 the voltage is high for the lower waveguide.

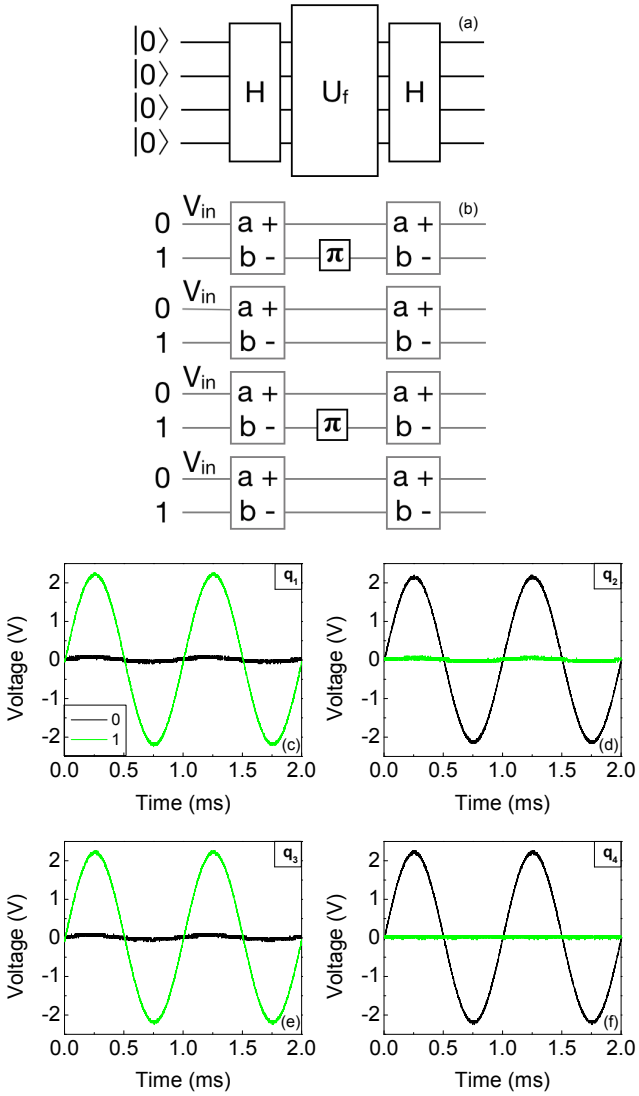

Figure 4.22: (a) Sketch of the general quantum circuit. (b) Scheme of electronic circuit corresponding to (a): a and b stand for the input pins, where we enter in a with a sinusoidal signal of $f = 1$ kHz and $V_{pp} = 3.5$ V, whereas b is connected to ground. $+$ and $-$ stand for the outputs (sum and difference of a and b) of the elementary units of the circuit. In this case, the circuit with two inversions on q_1 and q_3 respectively is shown. (c)-(f) Measurements done at the $+$ and $-$ ports of the second stage of elementary units of the circuit, corresponding to the second Hadamard operation. The black line represents the upper waveguide (0), whereas the green line stands for the lower waveguide (1). As expected, the voltage is high in the upper waveguide for q_2 and q_4, whereas for q_1 and q_3 the voltage is high for the lower waveguide, for the case $|q_1 q_2 q_3 q_4\rangle = |1010\rangle$ is here considered.

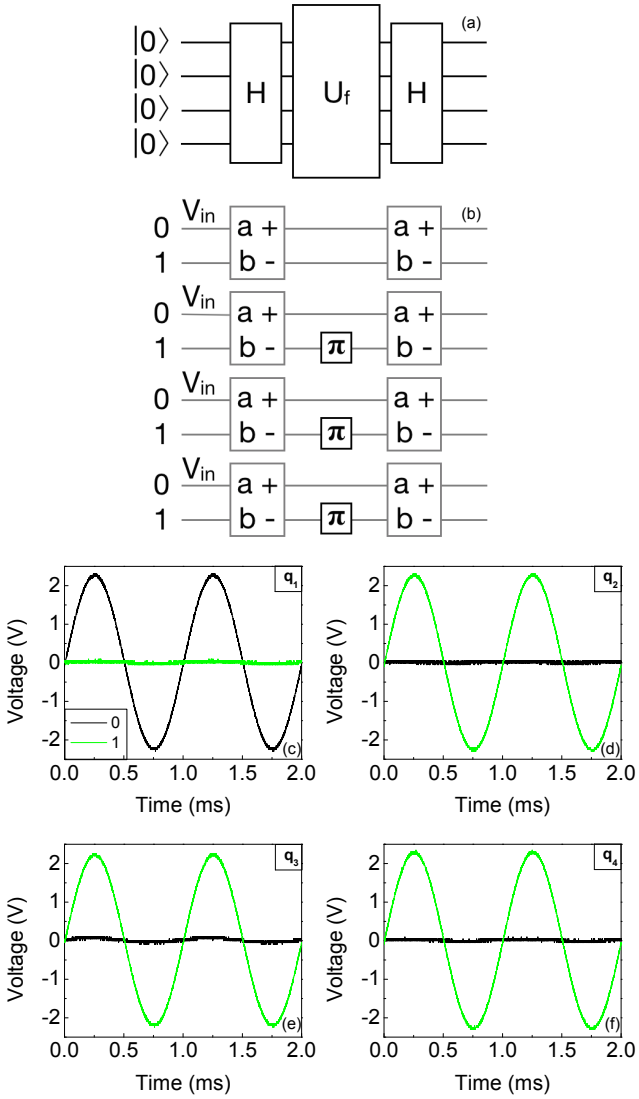

Figure 4.23: (a) Sketch of the general quantum circuit. (b) Scheme of electronic circuit corresponding to (a): a and b stand for the input pins, where we enter in a with a sinusoidal signal of $f = 1$ kHz and $V_{pp} = 3.5$ V, whereas b is connected to ground. + and − stand for the outputs (sum and difference of a and b) of the elementary units of the circuit. In this case, the circuit with three inversions on q_2, q_3 and q_4, respectively, is shown. (c)-(f) Measurements done at the + and − ports of the second stage of elementary units of the circuit, corresponding to the second Hadamard operation. The black line represents the upper waveguide (0), whereas the green line stands for the lower waveguide (1). As expected, the voltage is high in the upper waveguide for q_1, whereas for q_2, q_3 and q_4 the voltage is high for the lower waveguide, giving as result $|q_1q_2q_3q_4\rangle = |0111\rangle$.

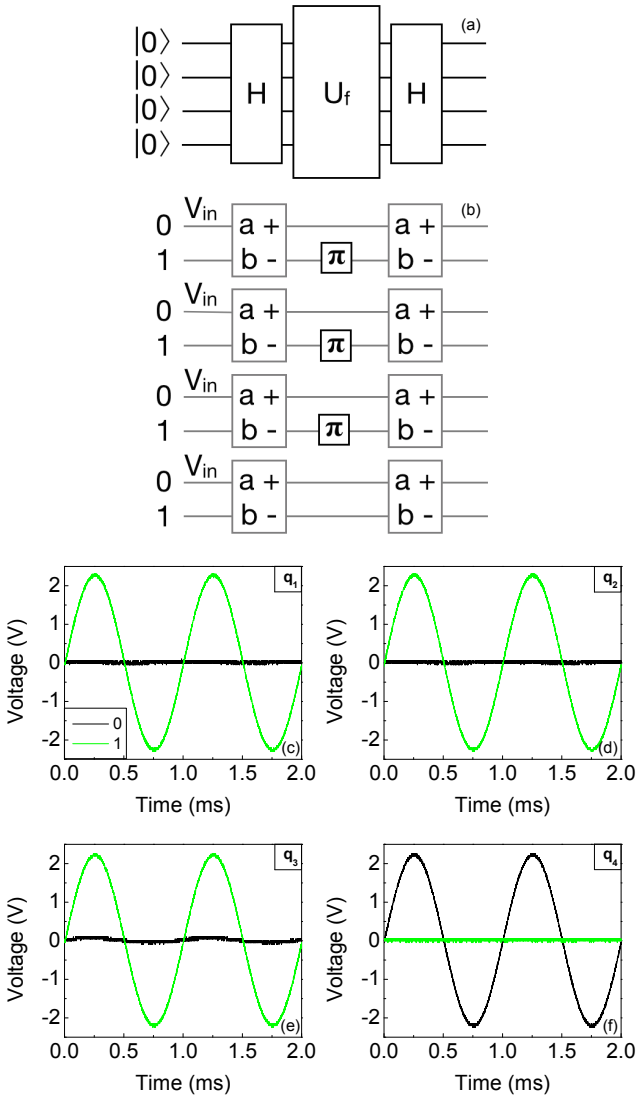

Figure 4.24: (a) Sketch of the general quantum circuit. (b) Scheme of electronic circuit corresponding to (a): a and b stand for the input pins, where we enter in a with a sinusoidal signal of $f = 1$ kHz and $V_{pp} = 3.5$ V, whereas b is connected to ground. $+$ and $-$ stand for the outputs (sum and difference of a and b) of the elementary units of the circuit. In this case, the circuit with three inversions on q_1, q_2 and q_3 respectively is shown. (c)-(f) Measurements done at the $+$ and $-$ ports of the second stage of elementary units of the circuit, corresponding to the second Hadamard operation. The black line represents the upper waveguide (0), whereas the green line stands for the lower waveguide (1). As expected, the voltage is high in the upper waveguide for q_4, whereas for q_1, q_2 and q_3 the voltage is high for the lower waveguide, thus $|q_1 q_2 q_3 q_4\rangle = |1110\rangle$.

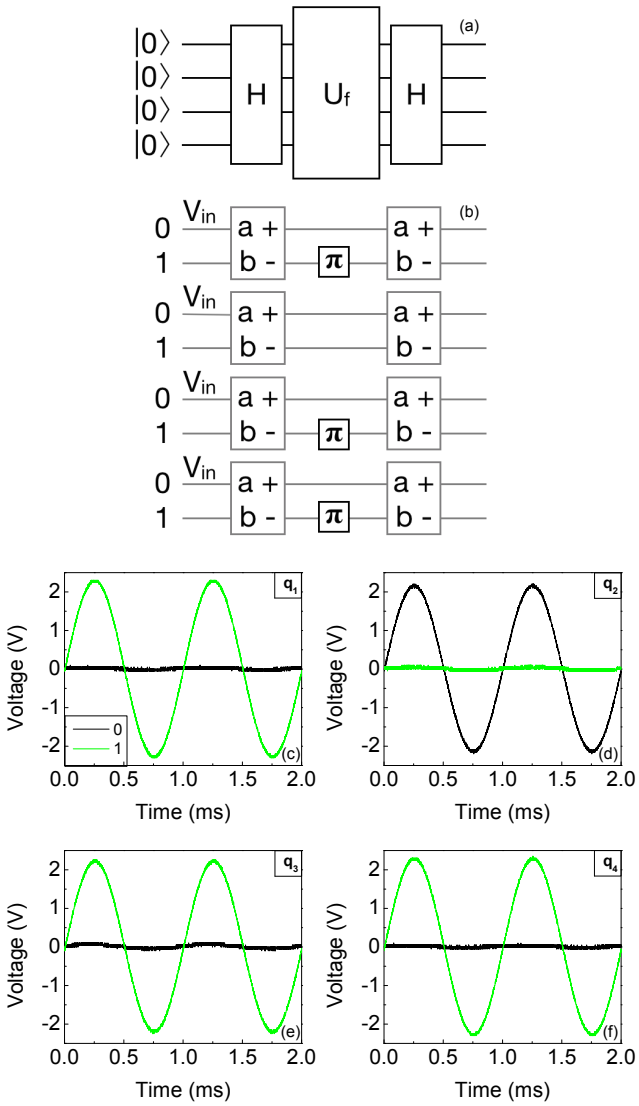

Figure 4.25: (a) Sketch of the general quantum circuit. (b) Scheme of electronic circuit corresponding to (a): a and b stand for the input pins, where we enter in a with a sinusoidal signal of $f = 1$ kHz and $V_{pp} = 3.5$ V, whereas b is connected to ground. $+$ and $-$ stand for the outputs (sum and difference of a and b) of the elementary units of the circuit. In this case, the circuit with three inversions on q_1, q_3 and q_4 respectively is shown. (c)-(f) Measurements done at the $+$ and $-$ ports of the second stage of elementary units of the circuit, corresponding to the second Hadamard operation. The black line represents the upper waveguide (0), whereas the green line stands for the lower waveguide (1). As expected, the voltage is high in the upper waveguide for q_2, whereas for q_1, q_3 and q_4 the voltage is high for the lower waveguide, obtaining $|q_1 q_2 q_3 q_4\rangle = |1011\rangle$.

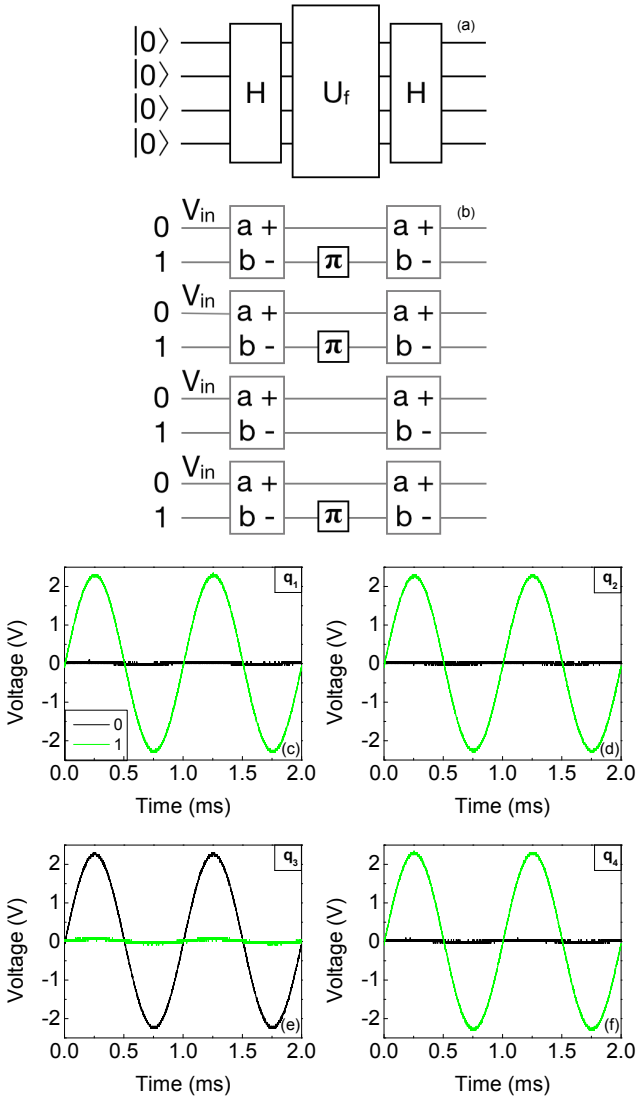

Figure 4.26: (a) Sketch of the general quantum circuit. (b) Scheme of electronic circuit corresponding to (a): a and b stand for the input pins, where we enter in a with a sinusoidal signal of $f = 1$ kHz and $V_{pp} = 3.5$ V, whereas b is connected to ground. $+$ and $-$ stand for the outputs (sum and difference of a and b) of the elementary units of the circuit. In this case, the circuit with three inversions on q_1, q_2 and q_4 respectively is shown. (c)-(f) Measurements done at the $+$ and $-$ ports of the second stage of elementary units of the circuit, corresponding to the second Hadamard operation. The black line represents the upper waveguide (0), whereas the green line stands for the lower waveguide (1). As expected, the voltage is high in the upper waveguide for q_3, whereas for q_1, q_2 and q_4 the voltage is high for the lower waveguide. So, in this case, $|q_1 q_2 q_3 q_4\rangle = |1101\rangle$

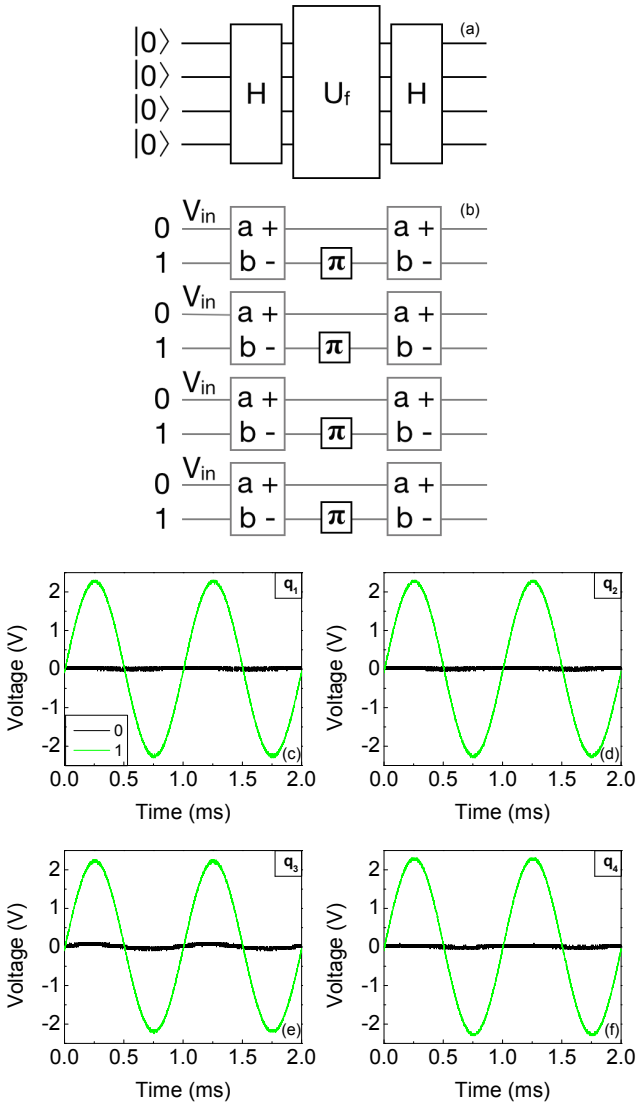

Figure 4.27: (a) Sketch of the general quantum circuit. (b) Scheme of electronic circuit corresponding to (a): a and b stand for the input pins, where we enter in a with a sinusoidal signal of $f = 1$ kHz and $V_{pp} = 3.5$ V, whereas b is connected to ground. $+$ and $-$ stand for the outputs (sum and difference of a and b) of the elementary units of the circuit. In this case, the circuit with the inversion on each one of the four qubits is shown. (c)-(f) Measurements done at the $+$ and $-$ ports of the second stage of elementary units of the circuit, corresponding to the second Hadamard operation. The black line represents the upper waveguide (0), whereas the green line stands for the lower waveguide (1). As expected, the voltage is high in the lower waveguide for each one of the qubits and $|q_1 q_2 q_3 q_4\rangle = |1111\rangle$.

Chapter 5

Conclusions and perspectives

In this thesis we treated two different major topics. Indeed, the first chapters are devoted to the study of two still open problems in the field of integrated photonics. In particular, in the second chapter, we first tackled the issue of the efficacy of integrated filters in spectrally cleaning the generated photon pairs. In the third chapter we then moved to the big issue of the lack of laser emission in silicon, thus complicating the fabrication of a silicon-integrated source of light. All the experiment described in the these two chapters deal with the four-wave mixing (FWM) process. Conversely, the fourth and last chapter is related to the broad field of quantum computation, providing an alternative way of implementing quantum algorithms by using classical waves, although at the price of forfeiting the exponential advantage of true quantum computation.

In the second chapter we studied the issue of spurious photon pairs emission in integrated filters. Indeed, silicon ridge waveguides and microring resonators are very good sources of nonclassical states of light. However, despite the big field enhancement that can be achieved in such devices, the intensity of the spontaneous FWM emission is relatively low, being 9-10 orders of magnitude smaller than that of the pump photons. So, in order to spectrally clean the emitted photon pairs, integrated filters with a rejection capability of 100 dB are required. This is particularly challenging, for in FWM the emitted photons frequencies are symmetrically located around the pump frequency.

Different strategies have been employed to integrate a filter with the desired features, for example by coupling many ring resonators, cascading interferometers and integrating Bragg mirrors onto a silicon waveguide (Bragg waveguides). However, all the listed elements are made of several microns of silicon waveguide, that could potentially generate unwanted photon pairs with different spectral and temporal correlations than the pairs emitted from the actual source. These parasitic photon pairs could be responsible of the pollution of the quantum state at the output, voiding the possibility of implementing quantum information protocols that use spontaneous FWM to generate photons.

So, we performed a stimulated FWM experiment on a Bragg waveguide

and studied the correlation properties of the photons that would be emitted in the spontaneous process. Our experimental work is supported by a theoretical model based on a quantum description of the filter.

The sample used for the measurement was fabricated in a CMOS-compatible fabrication process by periodically shrinking the width of a ridge waveguide, for a total Bragg waveguide length of 640 μm. In order to perform the experiment, we injected two lasers into the sample tuned at the pump and signal frequency, being the pump beam much more intense than the signal beam. We scanned the pump frequency across the Bragg waveguide stopband and observed the resonances due to generation of the idler photon. We then correlated the measured stimulated emission rate to the spontaneous emission rate that would have been obtained through spontaneous FWM and we found that the average rate of photon pairs generated at the bottom of the stopband is of few hertz. This result is also confirmed by the performed simulations. The Bragg waveguide used provides a 20-dB-rejection of the pump frequencies, but we expect to find similar results for longer structures (that provide higher rejection) as well. The found generation rate per mW^2 is at least five order of magnitudes smaller than that of the most efficient silicon sources, thus ruling out the possibility of the introduction of spurious photon pairs due to the presence of the filter.

So, the experiment described in chapter 2 sets Bragg waveguides as the best candidates for on-chip filtering of the optical pump for quantum applications. Moreover, Bragg waveguides are produced through a CMOS-compatible process, a very important feature for the widespread adoption of these devices as filters in silicon integrated chips.

In the third chapter, we wanted to address the major drawback of silicon photonics, that is the lack of lasing in silicon. In fact, silicon has an indirect bandgap of 1.12 eV and the electron-hole recombination is a phonon-mediated process with low probability of occurrence. Turns out that silicon is a poor light emitter.

Even if in the last years many systems, including stimulated Raman scattering, rare-earth doped waveguides, III-V compounds and hybrid laser technologies, have been studied to find a solution to this problem, laser emission in silicon still remains an unsolved problem. In fact, many difficulties are encountered when developing new technologies, for they have to emit at the telecommunication wavelengths in order to be connected to the fiber-optic network, they have to be compact in size and allow for a high level of integration on a chip, they have to be compatible with the CMOS fabrication process, their fabrication process cannot damage the integrated components on the silicon chip, they should have enough output power with high power efficiency and low energy cost-per-bit in data transmission.

However, an interesting way of bypassing the need of an external laser acting as optical pump in silicon, is to engineer a fiber-based cavity with the silicon integrated source of light inside it. The silicon structure we chose for

the experiment is the microring resonator, for its ability of emitting photon pairs through the FWM process. In the experiment one resonance of the ring is selected as pump and lasing frequency. Then the ring is closed in a fiber-loop cavity with an external amplifier in order to provide gain, and laser emission can be achieved with sufficient power in order to observe FWM emission. We chose the add-drop configuration for the microring resonator, so the cavity could be closed on the input and drop ports and FWM emission could be observed in the output port. We performed two distinct experiments.

In the first measurement we employed a silicon microring resonator with a relatively low quality factor ($Q \sim 3000$) and proved that lasing can be achieved in the built cavity. Because of the low quality factor of the microring, we were able to observe only stimulated FWM emission in the self-pumping geometry. Then, we performed a JSD measurement, that showed strong correlations between the emitted photons, thus suggesting that the photons emitted through spontaneous FWM would be time-energy entangled.

In a second experiment, a silicon microring resonator with a higher quality factor has been used ($Q \sim 20000$). The fiber-loop cavity design was the same as in the previous measurement and lasing was still observed. This time we were able to observe spontaneous FWM in the self-pumping scheme and, consequently, perform a coincidence measurement on the emitted photons, that showed a strong coincidence peak. So, even in the self-pumping geometry, the idler and signal photons are emitted at the same time. This is the first step towards the demonstration of time-energy entanglement between the idler and signal photons emitted through spontaneous FWM.

However, for both of the experiments a definitive proof of the emission of the entangled photons will consist in showing the violation of Bell's inequalities through a Franson experiment. Nevertheless, the results obtained are a very important step forward for the photonics field, where the realization of a silicon-based source of entangled photons that does not require an external optical pump is of central importance for industrial applications. Moreover, further applications other than the generation of entangled-photon states, like heralded single photon states and multiple-photon states emission, can be exploited by using the described geometry. Finally, a compelling direction that could be taken would be to extend the presented lasing cavity geometry to an all-pass microring resonator by exploiting the backscattered light at the input port of the resonator.

In the final chapter we explored a different way of employing silicon-based chips that can be applied to the quantum computation field, in particular for educational purposes. Thus, we introduced a way to perform on-chip photonic-based emulation of quantum algorithms, even if loosing the advantage of a real quantum computer. The starting point for our experiment is that all quantum computing protocols can be realized by propagating a single particle in a linear network, and the propagation of a single particle in a linear network is equivalent to the propagation of a classical wave in the same network. This

statement is true as long as one is interested only in detection probabilities at individual outputs, and no correlations are measured. So, any quantum information protocol can be realized in a classical wave network. Obviously, in this case, the number of resources needed increases exponentially with the number of emulated qubits.

In order to prove this point, we considered the Bernstein-Vazirani algorithm in a three-qubit configuration. This algorithm considers functions of the type $f(\mathbf{x}) = \mathbf{a}\cdot\mathbf{x}$, where $\mathbf{a}$ and $\mathbf{x}$ are n-bit strings, and aims to determine $\mathbf{a}$ in a single call instead of the n classical queries needed when using a classical algorithm. In the experiment we implemented the Bernstein-Vazirani algorithm in an analog electronic circuit, which is arguably the most readily available wave system. The electronic circuit used in the experiment has been developed and fabricated in a standard chemical etching process on a printed circuit board at the Department of Electronics at the University of Pavia. We performed two sets of measurements.

First, the Bernstein-Vazirani algorithm in a three-qubit configuration has been successfully emulated by validating all the four possible combinations of the vector $\mathbf{a}$. So, any quantum information protocol can be realized in a classical-wave network, such as an electronic circuit. Obviously, the price to pay is an exponential increase of the employed resources, thus voiding the advantage gained by using a quantum machine.

In a second experiment, we showed that in the *special* case of the Bernstein-Vazirani algorithm, the relation between emulated qubits and the components used in the classical system can be linear, still retaining its advantage over a fully classical implementation. This is possible because in the Bernstein-Vazirani algorithm the qubits are *never* entangled, and the Hilbert spaces of the qubits remain therefore independent. In the measurements we were able to emulate up to four qubits by employing eight wires, but more complex circuits can be built by using microelectronic circuits. Indeed, the number of transistors in the latest-generation commercial Central Processing Units (CPUs) can reach up to 10^{10} units and hundreds, or even thousands, of them can be operated in parallel in existing Graphic Processing Units (GPUs). So, we expect that at least 30 qubits could be emulated in such systems in a cheap and reliable way.

Our implementation could be used as a testbed, where quantum algorithms can be developed and tested before being run on actual quantum computers, lowering thus the costs related to the time spent on a quantum machine. Moreover, quantum algorithms with no or limited entanglement could be emulated in systems with CPU or GPU level of complexity. The described method could also be of potential interest for teaching purposes, for a new class of "quantum engineers" will have to be formed as quantum technologies will become of common use. Finally, the performed experiment also shed light on the importance of entanglement in quantum applications. In fact, we have experimentally proved that entanglement is the responsible factor for the exponen-

tial advantage of quantum information processing systems over their classical counterparts.

A natural continuation of the work we presented in the last chapter would be to extend our results to the quantum search algorithms. At this purpose, some proposals have already been suggested, as, for example, in the case of the Grover's algorithm. This algorithm aims to find an item with a particular property among a database of N elements. By using classical computation, in average $N/2$ items have to checked (N in the worst case). However, doing the same operation on a quantum computer would require $\sqrt{N}$ steps, thus having a quadratic speed-up over classical logic [10, 11]. Even in this case, the algorithm could be implemented by using classical waves in an electronic circuit as we described in our method.

As regarding chapters 2 and 3 dedicated to photonics, our work has the final goal of building a silicon *integrated* source of nonclassical states of light. To this purpose, in this thesis we addressed two major issues met when trying to integrate photon sources on a silicon chip: filtering the generated photons without introducing additional spurious photon pairs and pumping the source without the use of an external laser.

The next needed step would be to connect the performed research and build a source of photons that does not need an external laser acting as a pump, with on-chip-integrated filtering and multiplexing stages. The filtering and multiplexing of generated photons on a silicon chip has already been demonstrated by N.C. Harris *et al.* in 2014 [37]. Moreover, in the self-pumping scheme we presented, we obtained a very high SFWM internal generation rate, up to 100 MHz. This is due to the self pumping geometry that makes the laser emission to remain tuned to the pump resonance even at high pump powers, eliminating the saturation effect encountered when using an external pump [46]. So, being able to pump at high powers, results in higher generation rates. Consequently, another possible line of research to be pursued is trying to reduce as much as possible the chip coupling losses, in order to extract a number of photon pairs close to the internal generation rate.

The achievements obtained in this thesis can be easily included in the framework of the European Flagship in Quantum Technologies, started in 2018. In particular, the research performed in this work, with the next required steps, could be of potential interest for the long-term goal of creating a fast (>100 Mbps) and secure quantum internet connection network in Europe in order to run QKD protocols [8], where integrated photonic solutions will be of crucial importance. At this purpose, extracting the on-chip generated photon pairs with low losses and having high on-chip generation rates are steps of fundamental relevance.

Bibliography

[1] M. Mohseni, P. Read, H. Neven, S. Boixo, V. Denchev, R. Babbush, A. Fowler, V. Smelyanskiy, and J. Martinis, "Commercialize quantum technologies in five years," *Nature*, vol. 543, pp. 171–174, 2017.

[2] `http://research.ibm.com/quantum/`.

[3] `https://newsroom.intel.com/news-releases/intel-invests-us50-million-to-advance-quantum-computing/`.

[4] `https://blogs.microsoft.com/ai/microsoft-doubles-quantum-computing-bet/#sm.00000lqzed0mdof73uxjbeprtqklh`.

[5] `https://www.toshiba.eu/eu/Cambridge-Research-Laboratory/Quantum-Information/`.

[6] J. Yin, Y. Cao, Y.-H. Li, S.-K. Liao, L. Zhang, J.-G. Ren, W.-Q. Cai, W.-Y. Liu, B. Li, H. Dai, G.-B. Li, Q.-M. Lu, Y.-H. Gong, Y. Xu, S.-L. Li, F.-Z. Li, Y.-Y. Yin, Z.-Q. Jiang, M. Li, J.-J. Jia, G. Ren, D. He, Y.-L. Zhou, X.-X. Zhang, N. Wang, X. Chang, Z.-C. Zhu, N.-L. Liu, Y.-A. Chen, C.-Y. Lu, R. Shu, C.-Z. Peng, J.-Y. Wang, and J.-W. Pan, "Satellite-based entanglement distribution over 1200 kilometers," *Science*, vol. 356, no. 6343, pp. 1140–1144, 2017.

[7] M. F. Riedel, D. Binosi, R. Thew, and T. Calarco, "The European quantum technologies flagship programme," *Quantum Science and Technology*, vol. 2, no. 3, p. 030501, 2017.

[8] A. Acín, I. Bloch, H. Buhrman, T. Calarco, C. Eichler, J. Eisert, D. Esteve, N. Gisin, S. J. Glaser, F. Jelezko, S. Kuhr, M. Lewenstein, M. F. Riedel, P. O. Schmidt, R. Thew, A. Wallraff, I. Walmsley, and F. K. Wilhelm, "The quantum technologies roadmap: a European community view," *New Journal of Physics*, vol. 20, no. 8, p. 080201, 2018.

[9] C. E. Shannon, "A mathematical theory of communication," *Bell System Technical Journal*, vol. 27, no. 3, pp. 379–423, 1948.

[10] M. A. Nielsen and I. L. Chuang, *Quantum Computation and Quantum Information: 10th Anniversary Edition*. Cambridge: Cambridge University Press, 2010.

[11] P. Kaye, R. Laflamme, and M. Mosca, *An Introduction to Quantum Computing*. OUP Oxford, 2007.

[12] C. H. Bennett and D. P. DiVincenzo, "Quantum information and computation," *Nature*, vol. 404, pp. 247–255, 2000.

[13] J. P. Home, D. Hanneke, J. D. Jost, J. M. Amini, D. Leibfried, and D. J. Wineland, "Complete methods set for scalable ion trap quantum information processing," *Science*, vol. 325, no. 5945, pp. 1227–1230, 2009.

[14] Y. Nakamura, Y. A. Pashkin, and J. S. Tsai, "Coherent control of macroscopic quantum states in a single-Cooper-pair box," *Nature*, vol. 398, pp. 786–788, 1999.

[15] H. Liu, T. Fujisawa, H. Inokawa, Y. Ono, A. Fujiwara, and Y. Hirayama, "A gate-defined silicon quantum dot molecule," *Applied Physics Letters*, vol. 92, no. 22, p. 222104, 2008.

[16] D. G. Cory, A. F. Fahmy, and T. F. Havel, "Ensemble quantum computing by NMR spectroscopy," *Proc. Natl. Acad. Sci. USA*, vol. 94, no. 5, pp. 1634–1639, 1997.

[17] J. L. O'Brien, "Optical quantum computing," *Science*, vol. 318, no. 5856, pp. 1567–1570, 2007.

[18] N. Gisin and R. Thew, "Quantum communication," *Nature Photonics*, vol. 1, p. 165, 2007.

[19] C. H. Bennett and G. Brassard, "Quantum cryptography: Public key distribution and coin tossing," in *Proceedings of the IEEE International Conference on Computers, Systems and Signal Processing*, pp. 175–179, IEEE, New York, 1984.

[20] O. Alibart, D. B. Ostrowsky, P. Baldi, and S. Tanzilli, "High-performance guided-wave asynchronous heralded single-photon source," *Opt. Lett.*, vol. 30, pp. 1539–1541, 2005.

[21] M. J. Collins, C. Xiong, I. H. Rey, T. D. Vo, J. He, S. Shahnia, C. Reardon, T. F. Krauss, M. J. Steel, A. S. Clark, and B. J. Eggleton, "Integrated spatial multiplexing of heralded single-photon sources," *Nature Communications*, vol. 4, pp. 1–7, 2013.

[22] M. Davanço, J. R. Ong, A. B. Shehata, A. Tosi, I. Agha, S. Assefa, F. Xia, W. M. J. Green, S. Mookherjea, and K. Srinivasan, "Telecommunications-band heralded single photons from a silicon

nanophotonic chip," *Applied Physics Letters*, vol. 100, no. 26, pp. 261104–261106, 2012.

[23] C. Reimer, L. Caspani, M. Clerici, M. Ferrera, M. Kues, M. Peccianti, A. Pasquazi, L. Razzari, B. E. Little, S. T. Chu, D. J. Moss, and R. Morandotti, "Integrated frequency comb source of heralded single photons," *Opt. Express*, vol. 22, no. 6, pp. 6535–6546, 2014.

[24] P. G. Kwiat, K. Mattle, H. Weinfurter, A. Zeilinger, A. V. Sergienko, and Y. Shih, "New high-intensity source of polarization-entangled photon pairs," *Phys. Rev. Lett.*, vol. 75, pp. 4337–4341, 1995.

[25] N. Matsuda, H. Le Jeannic, H. Fukuda, T. Tsuchizawa, W. J. Munro, K. Shimizu, K. Yamada, Y. Tokura, and H. Takesue, "A monolithically integrated polarization entangled photon pair source on a silicon chip," *Scientific Reports*, vol. 2, 2012.

[26] A. S. Solntsev and A. A. Sukhorukov, "Path-entangled photon sources on nonlinear chips," *Reviews in Physics*, vol. 2, pp. 19–31, 2017.

[27] D. Grassani, S. Azzini, M. Liscidini, M. Galli, M. J. Strain, M. Sorel, J. E. Sipe, and D. Bajoni, "Micrometer-scale integrated silicon source of time-energy entangled photons," *Optica*, vol. 2, no. 2, pp. 88–94, 2015.

[28] R. Wakabayashi, M. Fujiwara, K.-i. Yoshino, Y. Nambu, M. Sasaki, and T. Aoki, "Time-bin entangled photon pair generation from Si micro-ring resonator," *Opt. Express*, vol. 23, no. 2, pp. 1103–1113, 2015.

[29] A. Aspect, P. Grangier, and G. Roger, "Experimental realization of Einstein-Podolsky-Rosen-Bohm gedankenexperiment: a new violation of Bell's inequalities," *Phys. Rev. Lett.*, vol. 49, pp. 91–94, 1982.

[30] A. Orieux, A. Eckstein, A. Lemaître, P. Filloux, I. Favero, G. Leo, T. Coudreau, A. Keller, P. Milman, and S. Ducci, "Direct Bell states generation on a III-V semiconductor chip at room temperature," *Phys. Rev. Lett.*, vol. 110, p. 160502, 2013.

[31] H. Takesue, Y. Tokura, H. Fukuda, T. Tsuchizawa, T. Watanabe, K. Yamada, and S.-i. Itabashi, "Entanglement generation using silicon wire waveguide," *Applied Physics Letters*, vol. 91, no. 20, p. 201108, 2007.

[32] L. Olislager, J. Safioui, S. Clemmen, K. P. Huy, W. Bogaerts, R. Baets, P. Emplit, and S. Massar, "Silicon-on-insulator integrated source of polarization-entangled photons," *Opt. Lett.*, vol. 38, no. 11, pp. 1960–1962, 2013.

[33] J. Wang, D. Bonneau, M. Villa, J. W. Silverstone, R. Santagati, S. Miki, T. Yamashita, M. Fujiwara, M. Sasaki, H. Terai, M. G. Tanner, C. M.

Natarajan, R. H. Hadfield, J. L. O'Brien, and M. G. Thompson, "Chip-to-chip quantum photonic interconnect by path-polarization interconversion," *Optica*, vol. 3, pp. 407–413, 2016.

[34] MOSIS service: `http://www.mosis.com`.

[35] M. Streshinsky, R. Ding, Y. Liu, A. Novack, C. Galland, A. E.-J. Lim, P. G.-Q. Lo, T. Baehr-Jones, and M. Hochberg, "The road to affordable, large-scale silicon photonics," *Opt. Photon. News*, vol. 24, no. 9, pp. 32–39, 2013.

[36] K. Yamada, "Silicon photonic wire waveguides: Fundamentals and applications," in *Silicon Photonics II. Topics in Applied Physics* (D. Lockwood and L. Pavesi, eds.), vol. 119, pp. 1–29, Berlin, Heidelberg: Springer, 2011.

[37] N. C. Harris, D. Grassani, A. Simbula, M. Pant, M. Galli, T. Baehr-Jones, M. Hochberg, D. Englund, D. Bajoni, and C. Galland, "Integrated source of spectrally filtered correlated photons for large-scale quantum photonic systems," *Phys. Rev. X*, vol. 4, p. 041047, 2014.

[38] W. Bogaerts, P. De Heyn, T. Van Vaerenbergh, K. De Vos, S. K. Selvaraja, T. Claes, P. Dumon, P. Bienstman, D. Van Thourhout, and R. Baets, "Silicon microring resonators," *Laser and Photonics Reviews*, vol. 6, no. 1, pp. 47–73, 2012.

[39] Y. R. Shen, *The Principles of Nonlinear Optics*. Wiley, 1984.

[40] R. W. Boyd, *Nonlinear Optics*. Elsevier Science, 2003.

[41] A. Yariv and P. Yeh, *Photonics*. Oxford University Press, 2007.

[42] J. Chen, X. Li, and P. Kumar, "Two-photon-state generation via four-wave mixing in optical fibers," *Phys. Rev. A*, vol. 72, p. 033801, 2005.

[43] J. E. Sharping, K. F. Lee, M. A. Foster, A. C. Turner, B. S. Schmidt, M. Lipson, A. L. Gaeta, and P. Kumar, "Generation of correlated photons in nanoscale silicon waveguides," *Opt. Express*, vol. 14, no. 25, pp. 12388–12393, 2006.

[44] A. C. Turner, M. A. Foster, A. L. Gaeta, and M. Lipson, "Ultra-low power parametric frequency conversion in a silicon microring resonator," *Opt. Express*, vol. 16, no. 7, pp. 4881–4887, 2008.

[45] S. Clemmen, K. Phan Huy, W. Bogaerts, R. G. Baets, P. Emplit, and S. Massar, "Continuous wave photon pair generation in silicon-on-insulator waveguides and ring resonators," *Opt. Express*, vol. 17, no. 19, pp. 16558–16570, 2009.

[46] S. Azzini, D. Grassani, M. Galli, L. C. Andreani, M. Sorel, M. J. Strain, L. G. Helt, J. E. Sipe, M. Liscidini, and D. Bajoni, "From classical four-wave mixing to parametric fluorescence in silicon microring resonators," *Opt. Lett.*, vol. 37, no. 18, pp. 3807–3809, 2012.

[47] M. Previde Massara, M. Menotti, N. Bergamasco, N. C. Harris, T. Baehr-Jones, M. Hochberg, C. Galland, M. Liscidini, M. Galli, and D. Bajoni, "Nonlinear characterization of a silicon integrated bragg waveguide filter," *Opt. Lett.*, vol. 43, no. 5, pp. 1171–1174, 2018.

[48] M. Previde Massara, F. A. Sabattoli, F. Pirzio, M. Galli, and D. Bajoni, "Four-wave mixing in a silicon microring resonator using a self-pumping geometry," *Applied Physics Letters*, vol. 113, no. 12, p. 121111, 2018.

[49] C. Monroe, "Quantum information processing with atoms and photons," *Nature*, vol. 416, pp. 238–246, 2002.

[50] B. T. Gard, K. R. Motes, J. P. Olson, P. P. Rohde, and J. P. Dowling, "An introduction to boson-sampling," in *From atomic to mesoscale: the role of quantum coherence in systems of various complexities* (S. Malinovskaya and I. Novikova, eds.), pp. 167–192, New Jersey: World Scientific Publishing, 2015.

[51] A. Einstein, B. Podolsky, and N. Rosen, "Can quantum-mechanical description of physical reality be considered complete?," *Physical Review*, vol. 47, no. 10, pp. 777–780, 1935.

[52] G. Benenti, G. Casati, and G. Strini, *Principles of Quantum Computation and Information, Volume I: Basic Concepts.* World Scientific, Singapore, 2004.

[53] D. P. DiVincenzo, "The physical implementation of quantum computation," *Fortschritte der Physik*, vol. 48, pp. 771–783, 2000.

[54] T. D. Ladd, F. Jelezko, R. Laflamme, Y. Nakamura, C. Monroe, and J. L. O'Brien, "Quantum computers," *Nature*, vol. 464, no. 7285, pp. 45–53, 2010.

[55] D. J. Wineland, C. Monroe, W. M. Itano, D. Leibfried, B. E. King, and D. M. Meekhof, "Experimental issues in coherent quantum-state manipulation of trapped atomic ions," *Journal of Research of the National Institute of Standards and Technology*, vol. 103, pp. 259–328, 1998.

[56] R. Blatt and D. J. Wineland, "Entangled states of trapped atomic ions," *Nature*, vol. 453, pp. 1008–1015, 2008.

[57] D. Leibfried, R. Blatt, C. Monroe, and D. J. Wineland, "Quantum dynamics of single trapped ions," *Rev. Mod. Phys.*, vol. 75, pp. 281–324, 2003.

[58] R. Hanson, L. P. Kouwenhoven, J. R. Petta, S. Tarucha, and L. M. K. Vandersypen, "Spins in few-electron quantum dots," *Rev. Mod. Phys.*, vol. 79, pp. 1217–1265, 2007.

[59] B. E. Kane, "A silicon-based nuclear spin quantum computer," *Nature*, vol. 393, pp. 133–137, 1998.

[60] J. Harrison, M. J. Sellars, and N. B. Manson, "Measurement of the optically induced spin polarisation of N-V centres in diamond," *Diamond and Related Materials*, vol. 15, no. 4, pp. 586–588, 2006.

[61] M. V. G. Dutt, L. Childress, L. Jiang, E. Togan, J. Maze, F. Jelezko, A. S. Zibrov, P. R. Hemmer, and M. D. Lukin, "Quantum register based on individual electronic and nuclear spin qubits in diamond," *Science*, vol. 316, no. 5829, pp. 1312–1316, 2007.

[62] I. Chiorescu, Y. Nakamura, C. J. P. M. Harmans, and J. E. Mooij, "Coherent quantum dynamics of a superconducting flux qubit," *Science*, vol. 299, pp. 1869–1871, 2003.

[63] J. M. Martinis, S. Nam, J. Aumentado, and C. Urbina, "Rabi oscillations in a large Josephson-junction qubit," *Phys. Rev. Lett.*, vol. 89, p. 117901, 2002.

[64] D. Vion, A. Aassime, A. Cottet, P. Joyez, H. Pothier, C. Urbina, D. Esteve, and M. H. Devoret, "Manipulating the quantum state of an electrical circuit," *Science*, vol. 296, no. 5569, pp. 886–889, 2002.

[65] N. A. Gershenfeld and I. L. Chuang, "Bulk spin-resonance quantum computation," *Science*, vol. 275, no. 5298, pp. 350–356, 1997.

[66] L. M. K. Vandersypen, M. Steffen, G. Breyta, C. S. Yannoni, M. H. Sherwood, and I. L. Chuang, "Experimental realization of Shor's quantum factoring algorithm using nuclear magnetic resonance," *Nature*, vol. 414, pp. 883–887, 2001.

[67] C. Negrevergne, T. S. Mahesh, C. A. Ryan, M. Ditty, F. Cyr-Racine, W. Power, N. Boulant, T. Havel, D. G. Cory, and R. Laflamme, "Benchmarking quantum control methods on a 12-qubit system," *Phys. Rev. Lett.*, vol. 96, p. 170501, 2006.

[68] A. Micheli, G. K. Brennen, and P. Zoller, "A toolbox for lattice-spin models with polar molecules," *Nature Physics*, vol. 2, pp. 341–347, 2006.

[69] J. J. L. Morton, A. M. Tyryshkin, A. Ardavan, S. C. Benjamin, K. Porfyrakis, S. A. Lyon, and G. A. D. Briggs, "Bang-bang control of fullerene qubits using ultrafast phase gates," *Nature Physics*, vol. 2, pp. 40–43, 2006.

[70] N. Mason, M. J. Biercuk, and C. M. Marcus, "Local gate control of a carbon nanotube double quantum dot," *Science*, vol. 303, no. 5658, pp. 655–658, 2004.

[71] B. Trauzettel, D. V. Bulaev, D. Loss, and G. Burkard, "Spin qubits in graphene quantum dots," *Nature Physics*, vol. 3, pp. 192–196, 2007.

[72] P. M. Platzman and M. I. Dykman, "Quantum computing with electrons floating on liquid helium," *Science*, vol. 284, no. 5422, pp. 1967–1969, 1999.

[73] M. N. Leuenberger and D. Loss, "Quantum computing in molecular magnets," *Nature*, vol. 410, pp. 789–793, 2001.

[74] `https://quantumcomputingreport.com/news/intel-fabricates-49-qubit-superconducting-chip/`.

[75] `https://www-03.ibm.com/press/us/en/pressrelease/53374.wss`.

[76] `https://quantumcomputingreport.com/news/google-announces-a-72-qubit-superconducting-quantum-chip/`.

[77] I. M. Georgescu, S. Ashhab, and F. Nori, "Quantum simulation," *Rev. Mod. Phys.*, vol. 86, pp. 153–185, 2014.

[78] M. Neeley, M. Ansmann, R. C. Bialczak, M. Hofheinz, E. Lucero, A. D. O'Connell, D. Sank, H. Wang, J. Wenner, A. N. Cleland, M. R. Geller, and J. M. Martinis, "Emulation of a quantum spin with a superconducting phase qudit," *Science*, vol. 325, no. 5941, pp. 722–725, 2009.

[79] J. T. Barreiro, M. Müller, P. Schindler, D. Nigg, T. Monz, M. Chwalla, M. Hennrich, C. F. Roos, P. Zoller, and R. Blatt, "An open-system quantum simulator with trapped ions," *Nature*, vol. 470, pp. 486–491, 2011.

[80] B. P. Lanyon, C. Hempel, D. Nigg, M. Müller, R. Gerritsma, F. Zähringer, P. Schindler, J. T. Barreiro, M. Rambach, G. Kirchmair, M. Hennrich, P. Zoller, R. Blatt, and C. F. Roos, "Universal digital quantum simulation with trapped ions," *Science*, vol. 334, no. 6052, pp. 57–61, 2011.

[81] J. Du, N. Xu, X. Peng, P. Wang, S. Wu, and D. Lu, "NMR implementation of a molecular hydrogen quantum simulation with adiabatic state preparation," *Phys. Rev. Lett.*, vol. 104, p. 030502, 2010.

[82] M. A. Broome, A. Fedrizzi, B. P. Lanyon, I. Kassal, A. Aspuru-Guzik, and A. G. White, "Discrete single-photon quantum walks with tunable decoherence," *Phys. Rev. Lett.*, vol. 104, p. 153602, 2010.

[83] A. Peruzzo, M. Lobino, J. C. F. Matthews, N. Matsuda, A. Politi, K. Poulios, X.-Q. Zhou, Y. Lahini, N. Ismail, K. Wörhoff, Y. Bromberg, Y. Silberberg, M. G. Thompson, and J. L. O'Brien, "Quantum Walks of Correlated Photons," *Science*, vol. 329, no. 5998, pp. 1500–1503, 2010.

[84] J. C. F. Matthews, K. Poulios, J. D. A. Meinecke, A. Politi, A. Peruzzo, N. Ismail, K. Wörhoff, M. G. Thompson, and J. L. O'Brien, "Observing fermionic statistics with photons in arbitrary processes," *Scientific Reports*, vol. 3, no. 1539, 2013.

[85] A. Aspuru-Guzik and P. Walther, "Photonic quantum simulators," *Nature Physics*, vol. 8, pp. 285–291, 2012.

[86] B. P. Lanyon, J. D. Whitfield, G. G. Gillett, M. E. Goggin, M. P. Almeida, I. Kassal, J. D. Biamonte, M. Mohseni, B. J. Powell, M. Barbieri, A. Aspuru-Guzik, and A. G. White, "Towards quantum chemistry on a quantum computer," *Nature Chemistry*, vol. 2, pp. 106–111, 2010.

[87] X.-s. Ma, B. Dakic, W. Naylor, A. Zeilinger, and P. Walther, "Quantum simulation of the wavefunction to probe frustrated Heisenberg spin systems," *Nature Physics*, vol. 7, pp. 399–405, 2011.

[88] S. Aaronson and A. Arkhipov, "The computational complexity of linear optics," in *Research in Optical Sciences*, p. QTh1A.2, Optical Society of America, 2014.

[89] B. T. Gard, K. R. Motes, J. P. Olson, P. P. Rohde, and J. P. Dowling, *An Introduction to Boson-Sampling*, ch. Chapter 8, pp. 167–192. 2015.

[90] M. A. Broome, A. Fedrizzi, S. Rahimi-Keshari, J. Dove, S. Aaronson, T. C. Ralph, and A. G. White, "Photonic Boson Sampling in a Tunable Circuit," *Science*, vol. 339, no. 6121, pp. 794–798, 2013.

[91] A. Crespi, R. Osellame, R. Ramponi, D. J. Brod, E. F. Galvao, N. Spagnolo, C. Vitelli, E. Maiorino, P. Mataloni, and F. Sciarrino, "Integrated multimode interferometers with arbitrary designs for photonic boson sampling," *Nature Photonics*, vol. 7, no. 7, pp. 545–549, 2013.

[92] J. B. Spring, B. J. Metcalf, P. C. Humphreys, W. S. Kolthammer, X.-M. Jin, M. Barbieri, A. Datta, N. Thomas-Peter, N. K. Langford, D. Kundys, J. C. Gates, B. J. Smith, P. G. R. Smith, and I. A. Walmsley, "Boson sampling on a photonic chip," *Science*, vol. 339, no. 6121, pp. 798–801, 2013.

[93] M. Tillmann, B. Dakic, R. Heilmann, S. Nolte, A. Szameit, and P. Walther, "Experimental boson sampling," *Nature Photonics*, vol. 7, no. 7, pp. 540–544, 2013.

[94] D. González Olivares, B. Peropadre, A. Aspuru-Guzik, and J. J. García-Ripoll, "Quantum simulation with a boson sampling circuit," *Phys. Rev. A*, vol. 94, p. 022319, 2016.

[95] A. E. Moylett and P. S. Turner, "Quantum simulation of partially distinguishable boson sampling," *Phys. Rev. A*, vol. 97, p. 062329, 2018.

[96] V. Giovannetti, S. Lloyd, and L. Maccone, "Advances in quantum metrology," *Nature Photonics*, vol. 5, pp. 222–229, 2011.

[97] G.-Y. Xiang and G.-C. Guo, "Quantum metrology," *Chinese Physics B*, vol. 22, no. 11, p. 110601, 2013.

[98] V. Giovannetti, S. Lloyd, and L. Maccone, "Quantum-enhanced measurements: beating the standard quantum limit," *Science*, vol. 306, pp. 1330–1336, 2004.

[99] B. Bell, S. Kannan, A. R. McMillan, A. S. Clark, W. J. Wadsworth, and J. G. Rarity, "Multicolor quantum metrology with entangled photons," *Phys. Rev. Lett.*, vol. 111, p. 093603, 2013.

[100] D. F. V. James, P. G. Kwiat, W. J. Munro, and A. G. White, "Measurement of qubits," *Phys. Rev. A*, vol. 64, p. 052312, 2001.

[101] I. Chuang and M. A. Nielsen, "Prescription for experimental determination of the dynamics of a quantum black box," *Journal of Modern Optics*, vol. 44, no. 11–12, pp. 2455–2467, 1997.

[102] J. F. Poyatos, J. I. Cirac, and P. Zoller, "Complete characterization of a quantum process: the two-bit quantum gate," *Phys. Rev. Lett.*, vol. 78, pp. 390–393, 1997.

[103] J. B. Altepeter, D. Branning, E. Jeffrey, T. C. Wei, P. G. Kwiat, R. T. Thew, J. L. O'Brien, M. A. Nielsen, and A. G. White, "Ancilla-assisted quantum process tomography," *Phys. Rev. Lett.*, vol. 90, p. 193601, 2003.

[104] M. Cramer, M. B. Plenio, S. T. Flammia, R. Somma, D. Gross, S. D. Bartlett, O. Landon-Cardinal, D. Poulin, and Y.-K. Liu, "Efficient quantum state tomography," *Nature Communications*, vol. 1, p. 149, 2010.

[105] J. A. Smolin, J. M. Gambetta, and G. Smith, "Efficient method for computing the maximum-likelihood quantum state from measurements with additive gaussian noise," *Phys. Rev. Lett.*, vol. 108, p. 070502, 2012.

[106] T. B. Pittman, Y. H. Shih, D. V. Strekalov, and A. V. Sergienko, "Optical imaging by means of two-photon quantum entanglement," *Phys. Rev. A*, vol. 52, pp. R3429–R3432, 1995.

[107] M. Malik and R. W. Boyd, "Quantum imaging technologies," *Riv. Nuovo Cim.*, vol. 37, no. 5, pp. 273–332, 2014.

[108] D. V. Strekalov, A. V. Sergienko, D. N. Klyshko, and Y. H. Shih, "Observation of two-photon "ghost" interference and diffraction," *Phys. Rev. Lett.*, vol. 74, pp. 3600–3603, 1995.

[109] R. S. Bennink, S. J. Bentley, and R. W. Boyd, ""two-photon" coincidence imaging with a classical source," *Phys. Rev. Lett.*, vol. 89, p. 113601, 2002.

[110] A. Gatti, E. Brambilla, M. Bache, and L. A. Lugiato, "Correlated imaging, quantum and classical," *Phys. Rev. A*, vol. 70, p. 013802, 2004.

[111] A. Gatti, E. Brambilla, M. Bache, and L. A. Lugiato, "Ghost imaging with thermal light: comparing entanglement and classical correlation," *Phys. Rev. Lett.*, vol. 93, p. 093602, 2004.

[112] E. Brambilla, A. Gatti, L. Lugiato, and M. Kolobov, "Quantum structures in traveling-wave spontaneous parametric down-conversion," *Eur. Phys. J. D*, vol. 15, pp. 127–135, 2001.

[113] E. Brambilla, L. Caspani, O. Jedrkiewicz, L. A. Lugiato, and A. Gatti, "High-sensitivity imaging with multi-mode twin beams," *Phys. Rev. A*, vol. 77, p. 053807, 2008.

[114] G. Brida, M. Genovese, and I. Ruo Berchera, "Experimental realization of sub-shot-noise quantum imaging," *Nature Photonics*, vol. 4, pp. 227–230, 2010.

[115] G. Barreto Lemos, V. Borish, G. D. Cole, S. Ramelow, R. Lapkiewicz, and A. Zeilinger, "Quantum imaging with undetected photons," *Nature*, vol. 512, pp. 409–412, 2014.

[116] A. N. Boto, P. Kok, D. S. Abrams, S. L. Braunstein, C. P. Williams, and J. P. Dowling, "Quantum interferometric optical lithography: exploiting entanglement to beat the diffraction limit," *Phys. Rev. Lett.*, vol. 85, pp. 2733–2736, 2000.

[117] M. D'Angelo, M. V. Chekhova, and Y. Shih, "Two-photon diffraction and quantum lithography," *Phys. Rev. Lett.*, vol. 87, p. 013602, 2001.

[118] J. Kitching, S. Knappe, and E. A. Donley, "Atomic sensors - a review," *IEEE Sensors Journal*, vol. 11, no. 9, pp. 1749–1758, 2011.

[119] M. Brownnutt, M. Kumph, P. Rabl, and R. Blatt, "Ion-trap measurements of electric-field noise near surfaces," *Rev. Mod. Phys.*, vol. 87, pp. 1419–1482, 2015.

[120] C. L. Degen, F. Reinhard, and P. Cappellaro, "Quantum sensing," *Rev. Mod. Phys.*, vol. 89, p. 035002, 2017.

[121] W. K. Wootters and W. H. Zurek, "A single quantum cannot be cloned," *Nature*, vol. 299, pp. 802–803, 1982.

[122] A. K. Ekert, "Quantum cryptography based on Bell's theorem," *Phys. Rev. Lett.*, vol. 67, pp. 661–663, 1991.

[123] N. Gisin, G. Ribordy, W. Tittel, and H. Zbinden, "Quantum cryptography," *Rev. Mod. Phys.*, vol. 74, pp. 145–195, 2002.

[124] L.-M. Duan and H. J. Kimble, "Scalable photonic quantum computation through cavity-assisted interactions," *Phys. Rev. Lett.*, vol. 92, p. 127902, 2004.

[125] E. Knill, R. Laflamme, and G. J. Milburn, "A scheme for efficient quantum computation with linear optics," *Nature*, vol. 409, no. 6816, pp. 46–52, 2001.

[126] G. Della Valle, R. Osellame, and P. Laporta, "Micromachining of photonic devices by femtosecond laser pulses," *Journal of Optics A: Pure and Applied Optics*, vol. 11, no. 1, p. 013001, 2009.

[127] J. L. O'Brien, B. Patton, M. Sasaki, and J. Vučković, "Focus on integrated quantum optics," *New Journal of Physics*, vol. 15, no. 3, p. 035016, 2013.

[128] N. Thomas-Peter, N. K. Langford, A. Datta, L. Zhang, B. J. Smith, J. B. Spring, B. J. Metcalf, H. B. Coldenstrodt-Ronge, M. Hu, J. Nunn, and I. A. Walmsley, "Integrated photonic sensing," *New Journal of Physics*, vol. 13, no. 5, p. 055024, 2011.

[129] A. Politi, J. C. F. Matthews, and J. L. O'Brien, "Shor's quantum factoring algorithm on a photonic chip," *Science*, vol. 325, no. 5945, p. 1221, 2009.

[130] J. C. F. Matthews, A. Politi, A. Stefanov, and J. L. O'Brien, "Manipulation of multiphoton entanglement in waveguide quantum circuits," *Nature Photonics*, vol. 3, no. 6, pp. 346–350, 2009.

[131] C. H. Bennett, G. Brassard, C. Crépeau, R. Jozsa, A. Peres, and W. K. Wootters, "Teleporting an unknown quantum state via dual classical and Einstein-Podolsky-Rosen channels," *Phys. Rev. Lett.*, vol. 70, no. 13, pp. 1895–1899, 1993.

[132] D. Bouwmeester, J.-W. Pan, K. Mattle, M. Eibl, H. Weinfurter, and A. Zeilinger, "Experimental quantum teleportation," *Nature*, vol. 390, pp. 575–579, 1997.

[133] H. J. Kimble, "The quantum internet," *Nature*, vol. 453, pp. 1023–1030, 2008.

[134] D. Stucki, N. Gisin, O. Guinnard, G. Ribordy, and H. Zbinden, "Quantum key distribution over 67 km with a plug & play system," *New Journal of Physics*, vol. 4, no. 1, p. 41, 2002.

[135] Z.-S. Yuan, Y.-A. Chen, B. Zhao, S. Chen, J. Schmiedmayer, and J.-W. Pan, "Experimental demonstration of a BDCZ quantum repeater node," *Nature*, vol. 454, pp. 1098–1101, 2008.

[136] S.-J. Yang, X. J. Wang, X.-H. Bao, and J.-W. Pan, "An efficient quantum light-matter interface with sub-second lifetime," *Nature Photonics*, vol. 10, pp. 381–384, 2016.

[137] C. Kurtsiefer, P. Zarda, M. Halder, H. Weinfurter, P. M. Gorman, P. R. Tapster, and J. G. Rarity, "A step towards global key distribution," *Nature*, vol. 419, p. 450, 2002.

[138] R. Ursin, F. Tiefenbacher, T. Schmitt-Manderbach, H. Weier, T. Scheidl, M. Lindenthal, B. Blauensteiner, T. Jennewein, J. Perdigues, P. Trojek, B. Ömer, Fürst, M. Meyenburg, J. G. Rarity, Z. Sodnik, C. Barbieri, H. Weinfurter, and A. Zeilinger, "Entanglement-based quantum communication over 144 km," *Nature Physics*, vol. 3, pp. 481–486, 2007.

[139] T. Schmitt-Manderbach, H. Weier, M. Fürst, R. Ursin, F. Tiefenbacher, T. Scheidl, J. Perdigues, Z. Sodnik, C. Kurtsiefer, J. G. Rarity, A. Zeilinger, and H. Weinfurter, "Experimental demonstration of free-space decoy-state quantum key distribution over 144 km," *Phys. Rev. Lett.*, vol. 98, p. 010504, 2007.

[140] M. Aspelmeyer, H. R. Böhm, T. Gyatso, T. Jennewein, R. Kaltenbaek, M. Lindenthal, G. Molina-Terriza, A. Poppe, K. Resch, M. Taraba, R. Ursin, P. Walther, and A. Zeilinger, "Long-distance free-space distribution of quantum entanglement," *Science*, vol. 301, no. 5633, pp. 621–623, 2003.

[141] C.-Z. Peng, T. Yang, X.-H. Bao, J. Zhang, X.-M. Jin, F.-Y. Feng, B. Yang, J. Yang, J. Yin, Q. Zhang, N. Li, B.-L. Tian, and J.-W. Pan, "Experimental free-space distribution of entangled photon pairs over 13 km: towards satellite-based global quantum communication," *Phys. Rev. Lett.*, vol. 94, p. 150501, 2005.

[142] A. Fedrizzi, R. Ursin, T. Herbst, M. Nespoli, R. Prevedel, T. Scheidl, F. Tiefenbacher, T. Jennewein, and A. Zeilinger, "High-fidelity transmission of entanglement over a high-loss free-space channel," *Nature Physics*, vol. 5, pp. 389–392, 2009.

[143] X.-M. Jin, J.-G. Ren, B. Yang, Z.-H. Yi, F. Zhou, X.-F. Xu, S.-K. Wang, D. Yang, Y.-F. Hu, S. Jiang, T. Yang, H. Yin, K. Chen, C.-Z. Peng, and J.-W. Pan, "Experimental free-space quantum teleportation," *Nature Photonics*, vol. 4, pp. 376–381, 2010.

[144] J. Yin, J.-G. Ren, H. Lu, Y. Cao, H.-L. Yong, Y.-P. Wu, C. Liu, S.-K. Liao, F. Zhou, Y. Jiang, X.-D. Cai, P. Xu, G.-S. Pan, J.-J. ia, Y.-M. Huang, H. Yin, J.-Y. Wang, Y.-A. Chen, C.-Z. Peng, and J.-W. Pan, "Quantum teleportation and entanglement distribution over 100-kilometre free-space channels," *Nature*, vol. 488, pp. 185–188, 2012.

[145] X.-S. Ma, T. Herbst, T. Scheidl, D. Wang, S. Kropatschek, W. Naylor, B. Wittmann, A. Mech, J. Kofler, E. Anisimova, V. Makarov, T. Jennewein, R. Ursin, and A. Zeilinger, "Quantum teleportation over 143 kilometres using active feed-forward," *Nature*, vol. 489, pp. 269–273, 2012.

[146] G. Leo, V. Berger, C. Ow Yang, and J. Nagle, "Parametric fluorescence in oxidized algaas waveguides," *J. Opt. Soc.Am. B*, vol. 16, no. 9, pp. 1597–1602, 1999.

[147] G. Reithmaier, M. Kaniber, F. Flassig, S. Lichtmannecker, K. Müller, A. Andrejew, J. Vučković, R. Gross, and J. J. Finley, "On-chip generation, routing, and detection of resonance fluorescence," *Nano Letters*, vol. 15, no. 8, pp. 5208–5213, 2015.

[148] M. Schwartz, E. Schmidt, U. Rengstl, F. Hornung, S. Hepp, S. L. Portalupi, K. Ilin, M. Jetter, M. Siegel, and P. Michler, "Fully on-chip single-photon hanbury-brown and twiss experiment on a monolithic semiconductor-superconductor platform," *Nano Letters*, vol. 18, no. 11, pp. 6892–6897, 2018.

[149] J. P. Sprengers, A. Gaggero, D. Sahin, S. Jahanmirinejad, G. Frucci, F. Mattioli, R. Leoni, J. Beetz, M. Lermer, M. Kamp, S. Höfling, R. Sanjines, and A. Fiore, "Waveguide superconducting single-photon detectors for integrated quantum photonic circuits," *Applied Physics Letters*, vol. 99, no. 18, p. 181110, 2011.

[150] C. P. Dietrich, A. Fiore, M. G. Thompson, M. Kamp, and S. Höfling, "Gaas integrated quantum photonics: Towards compact and multi-functional quantum photonic integrated circuits," *Laser & Photonics Reviews*, vol. 10, no. 6, pp. 870–894, 2016.

[151] M. Davanço, J. Liu, L. Sapienza, C.-Z. Zhang, J. V. De Miranda Cardoso, V. Verma, R. Mirin, S. W. Nam, L. Liu, and K. Srinivasan, "Heterogeneous integration for on-chip quantum photonic circuits with single quantum dot devices," *Nature Communications*, vol. 8, p. 889, 2017.

[152] Q. Li, M. Davanço, and K. Srinivasan, "Efficient and low-noise single-photon-level frequency conversion interfaces using silicon nanophotonics," *Nature Photonics*, vol. 10, pp. 406–414, 2016.

[153] A. M. Zaitsev, *Optical properties of diamond: A data handbook*. Springer-Verlag Berlin Heidelberg, 2001.

[154] B. J. M. Hausmann, B. J. Shields, Q. Quan, Y. Chu, N. P. de Leon, R. Evans, M. J. Burek, A. S. Zibrov, M. Markham, D. J. Twitchen, H. Park, M. D. Lukin, and M. Loncăr, "Coupling of nv centers to photonic crystal nanobeams in diamond," *Nano Letters*, vol. 13, no. 12, pp. 5791–5796, 2013.

[155] `http://www.aimphotonics.com/`.

[156] B. Jalali, V. Raghunathan, R. Shori, S. Fathpour, D. Dimitropoulos, and O. Stafsudd, "Prospects for silicon mid-IR Raman lasers," *IEEE Journal of Selected Topics in Quantum Electronics*, vol. 12, no. 6, pp. 1618–1627, 2006.

[157] M. Dinu, F. Quochi, and H. Garcia, "Third-order nonlinearities in silicon at telecom wavelengths," *Appl. Phys. Lett.*, vol. 82, p. 2954, 2003.

[158] G. P. Agrawal, *Nonlinear fiber optics*. Academic Press, 2001.

[159] M. Galli, D. Gerace, K. Welna, T. F. Krauss, L. O'Faolain, G. Guizzetti, and L. C. Andreani, "Low-power continuous-wave generation of visible harmonics in silicon photonic crystal nanocavities," *Opt. Express*, vol. 18, no. 25, pp. 26613–26624, 2010.

[160] J. S. Levy, M. A. Foster, A. L. Gaeta, and M. Lipson, "Harmonic generation in silicon nitride ring resonators," *Opt. Express*, vol. 19, no. 12, pp. 11415–11421, 2011.

[161] M. A. Foster, A. C. Turner, J. E. Sharping, B. S. Schmidt, M. Lipson, and A. L. Gaeta, "Broad-band optical parametric gain on a silicon photonic chip," *Nature*, vol. 441, no. 7096, pp. 960–963, 2006.

[162] R. Salem, M. A. Foster, D. F. Geraghty, M. Lipson, and A. L. Gaeta, "Signal regeneration using low-power four-wave mixing on silicon chip," *Nature Photonics*, vol. 2, pp. 35–38, 2007.

[163] M. Dinu, "Dispersion of phonon-assisted nonresonant thord-order nonlinearities," *IEE J. Quantum Electron.*, vol. 39, pp. 1498–1503, 2003.

[164] v. Lin, O. J. Painter, and G. P. Agrawal, "Nonlinear optical phenomena in silicon waveguides: Modeling and applications," *Opt. Express*, vol. 15, no. 25, pp. 16604–16644, 2007.

[165] R. Loudon, *The quantum theory of light*. Oxford University Press, 2000.

[166] A. G. Rickman, G. T. Reed, and F. Namavar, "Silicon-on-insulator optical rib waveguide loss and mode characteristics," *J. Lightwave Technol.*, vol. 12, pp. 1771–1776, 1994.

[167] H. Rong, A. Liu, R. Jones, O. Cohen, D. Hak, R. Nicolaescu, A. Fang, and M. Paniccia, "An all-silicon Raman laser," *Nature*, vol. 433, pp. 292–294, 2005.

[168] P. Dumon, W. Bogaerts, V. Wiaux, J. Wouters, S. Beckx, J. Van Campenhout, D. Taillaert, B. Luyssaert, P. Bienstman, D. Van Thourhout, and R. Baets, "Low-loss SOI photonic wires and ring resonators fabricated with deep UV lithography," *Photon. Technol. Lett.*, vol. 16, pp. 1328–1330, 2004.

[169] Y. A. Vlasov and S. J. McNab, "Losses in single-mode silicon-on-insulator strip waveguides and bends," *Opt. Express*, vol. 12, pp. 1622–1631, 2004.

[170] T. Tsuchizawa, H. Yamada, K. an Fukuda, T. Watanabe, J. Takahashi, M. Takahashi, T. Shoji, E. Tamechika, S. Itabashi, and H. Morita, "Microphotonics devices based on silicon microfabrication technology," *IEEE J. Sel. Top. Quantum. Electron.*, vol. 11, pp. 232–240, 2005.

[171] T. Horikawa, D. Shimura, and T. Mogami, "Low-loss silicon wire waveguides for optical integrated circuits," *MRS Communications*, vol. 6, no. 1, pp. 9–15, 2016.

[172] M. Notomi, A. Shinya, S. Mitsugi, E. Kuramochi, and H. Ryu, "Waveguides, resonators and their coupled elements in photonic crystal slabs," *Opt. Express*, vol. 12, no. 8, pp. 1551–1561, 2004.

[173] W. Bogaerts, R. Baets, P. Dumon, V. Wiaux, S. Beckx, D. Taillaert, B. Luyssaert, J. Van Campenhout, P. Bienstman, and D. Van Thourhout, "Nanophotonic waveguides in silicon-on-insulator fabricated with CMOS technology," *J. Lightwave Technol.*, vol. 23, no. 1, pp. 401–412, 2005.

[174] W. Bogaerts, P. Dumon, D. Van Thourhout, D. Taillaert, P. Jaenen, J. Wouters, S. Beckx, V. Wiaux, and R. Baets, "Compact wavelength-selective functions in silicon-on-insulator photonic wires," *IEEE J. Sel. Top. Quantum. Electron.*, vol. 12, no. 6, pp. 1394–1401, 2006.

[175] P. Lusse, P. Stuwe, J. Schule, and H.-G. Unger, "Analysis of vectorial mode fields in optical waveguides by new finite difference method," *J. Lightwave Technol.*, vol. LT-12, pp. 487–493, 1994.

[176] M. Koshiba, S. Maruyama, and K. Hirayama, "A vector finite element method with the high-order mixed-interpolation-type triangular elements for optical waveguiding problems," *J. Lightwave Technol.*, vol. LT-12, pp. 495–502, 1994.

[177] A. S. Sudbo, "Film mode matching: a versatile numerical method for vector mode field calculations in dielectric waveguides," *Pure Appl. Opt.*, vol. 2, pp. 211–233, 1993.

[178] A. C. Turner, C. Manolatou, B. S. Schmidt, M. Lipson, M. A. Foster, J. E. Sharping, and A. L. Gaeta, "Tailored anomalous group-velocity dispersion in silicon channel waveguides," *Opt. Express*, vol. 14, pp. 4357–4362, 2006.

[179] F. P. Payne and J. P. R. Lacey, "A theoretical analysis of scattering loss from planar optical waveguides," *Optical and Quantum Electronics*, vol. 26, pp. 977–986, 1994.

[180] S. K. Selvaraja, P. Jaenen, W. Bogaerts, D. Van Thourhout, P. Dumon, and R. Baets, "Fabrication of photonic wire and crystal circuits in silicon-on-insulator using 193-nm optical lithography," *J. Lightwave Technol.*, vol. 27, pp. 4076–4083, 2009.

[181] C. Kopp, S. Bernabe, B. Ben Bakir, J.-M. Fedeli, R. Orobtchouk, F. Schrank, H. Porte, L. Zimmermann, and T. Tekin, "Silicon photonic circuits: on-CMOS integration, fiber optical coupling, and packaging," *IEEE Journal of Selected Topics in Quantum Electronics*, vol. 17, pp. 498–509, 2011.

[182] W. Bogaerts, D. Taillaert, B. Luyssaert, P. Dumon, J. Van Campenhou, P. Bienstman, D. Van Thourhout, R. Baets, V. Wiaux, and S. Beckx, "Basic structures for photonic integrated circuits in silicon-on-insulator," *Opt. Express*, vol. 12, pp. 1583–1591, 2004.

[183] D. Taillaert, P. Bienstman, and R. Baets, "Compact efficient broadband grating coupler for silicon-on-insulator waveguides," *Opt. Lett.*, vol. 29, pp. 2749–2751, 2004.

[184] H. Fukuda, K. Yamada, T. Shoji, M. Takahashi, T. Tsuchizawa, T. Watanabe, J.-i. Takahashi, and S.-i. Itabashi, "Four-wave mixing in silicon wire waveguides," *Opt. Express*, vol. 13, no. 12, pp. 4629–4637, 2005.

[185] Ø. S. Heavens, *Optical Properties of Thin Solid Films*. Dover Publications, Inc., New York, 1965.

[186] Ø. S. Heavens, *Thin Film Physics*. Methuen and Company, Ltd., London, 1970.

[187] J. Heebner, R. Grover, and T. Ibrahim, *Optical microresonators: theory, fabrication and applications*. Springer series in Optical Science (Springer, London), 2008.

[188] B. E. Little, S. Chu, H. A. Haus, J. Foresi, and J.-P. Laine, "Microring resonator channel dropping filters," *Journal of Lightwave Technology*, vol. 15, pp. 998–1005, 1997.

[189] W. Bogaerts, S. Selvaraja, P. Dumon, J. Brouckaert, K. De Vos, D. Van Thourhout, and R. Baets, "Silicon-on-insulator spectral filters fabricated with CMOS technology," *IEEE Journal of Selected Topics in Quantum Electronics*, vol. 16, no. 1, pp. 33–44, 2010.

[190] J. Brouckaert, W. Bogaerts, P. Dumon, D. Van Thourhout, and R. Baets, "Planar concave grating demultiplexer fabricated on a nanophotonic silicon-on-insulator platform," *Journal of Lightwave Technology*, vol. 25, no. 5, pp. 1269–1275, 2007.

[191] J. Brouckaert, W. Bogaerts, S. Selvaraja, P. Dumon, R. Baets, and D. Van Thourhout, "Planar concave grating demultiplexer with high reflective Bragg reflector facets," *IEEE Photon. Technol. Lett.*, vol. 20, no. 4, pp. 309–311, 2008.

[192] M. Watts, T. Barwicz, M. Popovic, L. Socci, P. Rakich, E. Ippen, H. Smith, and F. Kaertner, "Design, fabrication, and characterization of a free spectral range doubled ring-resonator filter," in *Proceedings of the Conference on Lasers and Electro-Optics (CLEO, Baltimore, MD)*, vol. 1–3, pp. 269–272, 2005.

[193] A. Simbula, G. A. Rodriguez, M. Menotti, S. De Pace, S. M. Weiss, M. Galli, M. Liscidini, and D. Bajoni, "Low-power four-wave mixing in porous silicon microring resonators," *Applied Physics Letters*, vol. 109, p. 021106, 2016.

[194] F. Xia, L. Sekaric, and Y. A. Vlasov, "Ultracompact optical buffers on a silicon chip," *Nature Photonics*, vol. 1, pp. 65–71, 2007.

[195] J. K. S. Poon, J. Scheuer, Y. Xu, and A. Yariv, "Designing coupled-resonator optical waveguide delay lines," *J. Opt. Soc. Am. B, Opt. Phys.*, vol. 21, no. 9, pp. 1665–1673, 2004.

[196] A. Melloni, A. Cianciamilla, C. Ferrari, F. Morichetti, L. O'Faolain, T. Krauss, R. M. De La Rue, A. Samarelli, and M. Sorel, "Tunable delay lines in silicon photonics: coupled resonators and photonic crystals, a comparison," *IEEE Photonics J.*, vol. 2, no. 2, pp. 181–194, 2010.

[197] J. K. S. Poon, L. Zhu, G. A. DeRose, and A. Yariv, "Transmission and group delay of microring coupled-resonator optical waveguides," *Optics Letters*, vol. 31, no. 4, pp. 456–458, 2006.

[198] G. Calò and V. Petruzzelli, "Compact design of photonic crystal ring resonator 2×2 routers as building blocks for photonic networks on chip," *J. Opt. Soc. Am. B*, vol. 31, pp. 517–525, 2014.

[199] T. J. Kippenberg, R. Holzwarth, and S. A. Diddams, "Microresonator-based optical frequency combs," *Science*, vol. 332, no. 6029, pp. 555–559, 2011.

[200] T. Udem, R. Holzwarth, and T. W. Hänsch, "Optical frequency metrology," *Nature*, vol. 416, pp. 233–237, 2002.

[201] S. T. Cundiff and J. Ye, "Colloquium: Femtosecond optical frequency combs," *Rev. Mod. Phys.*, vol. 75, pp. 325–342, 2003.

[202] C. Reimer, M. Kues, P. Roztocki, B. Wetzel, F. Grazioso, B. E. Little, S. T. Chu, T. Johnston, Y. Bromberg, L. Caspani, D. J. Moss, and R. Morandotti, "Generation of multiphoton entangled quantum states by means of integrated frequency combs," *Science*, vol. 351, no. 6278, pp. 1176–1180, 2016.

[203] P. P. Absil, J. V. Hryniewicz, B. E. Little, P. S. Cho, R. A. Wilson, L. G. Joneckis, and P.-T. Ho, "Wavelength conversion in GaAs micro-ring resonators," *Opt. Lett.*, vol. 25, no. 8, pp. 554–556, 2000.

[204] L. G. Helt, Z. Yang, M. Liscidini, and J. E. Sipe, "Spontaneous four-wave mixing in microring resonators," *Opt. Lett.*, vol. 35, no. 18, pp. 3006–3008, 2010.

[205] L. G. Helt, M. Liscidini, and J. E. Sipe, "How does it scale? comparing quantum and classical nonlinear optical processes in integrated devices," *J. Opt. Soc. Am. B*, vol. 29, no. 8, pp. 2199–2212, 2012.

[206] S. Azzini, D. Grassani, M. J. Strain, M. Sorel, L. G. Helt, J. E. Sipe, M. Liscidini, M. Galli, and D. Bajoni, "Ultra-low power generation of twin photons in a compact silicon ring resonator," *Opt. Express*, vol. 20, no. 21, pp. 23100–23107, 2012.

[207] D. Grassani, A. Simbula, S. Pirotta, M. Galli, M. Menotti, N. C. Harris, T. Baehr-Jones, M. Hochberg, C. Galland, M. Liscidini, and D. Bajoni, "Energy correlations of photon pairs generated by a silicon microring resonator probed by stimulated four wave mixing," *Scientific Reports*, vol. 6, p. 23564, 2016.

[208] L. Caspani, C. Xiong, B. J. Eggleton, D. Bajoni, M. Liscidini, M. Galli, R. Morandotti, and D. J. Moss, "Integrated sources of photon quantum states based on nonlinear optics," *Light: Science & Applications*, vol. 6, p. e17100, 2017.

[209] J. S. Bell, "On the Einstein-Podolsky-Rosen paradox," *Physics*, vol. 1, pp. 195–200, 1964.

[210] R. Horodecki, "Informationally coherent quantum systems," *Phys. Lett. A*, vol. 187, pp. 145–150, 1994.

[211] A. Peres, "Separability criterion for density matrices," *Phys. Rev. Lett.*, vol. 77, pp. 1413–1415, 1996.

[212] L. M. Duan, G. Giedke, J. I. Cirac, and P. Zoller, "Inseparability criterion for continuous variable systems," *Phys. Rev. Lett.*, vol. 84, pp. 2722–2725, 2000.

[213] R. Simon, "Peres-Horodecki separability criterion for continuous variable systems," *Phys. Rev. Lett.*, vol. 84, pp. 2726–2729, 2000.

[214] W. J. Munro, K. Nemoto, and A. G. White, "The Bell inequality: a measure of entanglement?," *J. Mod. Opt.*, vol. 48, pp. 1239–1246, 2001.

[215] J. F. Clauser, M. A. Horne, A. Shimony, and R. A. Holt, "Proposed experiment to test local hidden-variable theories," *Phys. Rev. Lett.*, vol. 23, pp. 880–884, 1969.

[216] A. Shimony, "Bell's theorem," in *Zalta EN editor. The Stanford Encyclopedia of Philosophy. Palo Alto: Stanford University*, 2016.

[217] J. D. Franson, "Bell inequality for position and time," *Phys. Rev. Lett.*, vol. 62, pp. 2205–2208, 1989.

[218] H. Takesue, K. Inoue, O. Tadanaga, Y. Nishida, and M. Asobe, "Generation of pulsed polarization-entangled photon pairs in a 1,55-μm band with a periodically poled lithium niobate waveguide and an orthogonal polarization delay circuit," *Optics Letters*, vol. 30, no. 3, pp. 293–295, 2005.

[219] G. Fujii, N. Namekata, M. Motoya, S. Kurimura, and S. Inoue, "Bright narrowband source of photon pairs at optical telecommunication wavelengths using a type-II periodically poled lithium niobate waveguide," *Opt. Express*, vol. 15, no. 20, pp. 12769–12776, 2007.

[220] X. Li, P. L. Voss, J. E. Sharping, and P. Kumar, "Optical-fiber source of polarization-entangled photons in the 1550 nm telecom band," *Phys. Rev. Lett.*, vol. 94, no. 5, p. 053601, 2005.

[221] R. Kaltenbaek, B. Blauensteiner, M. Żukowski, M. Aspelmeyer, and A. Zeilinger, "Experimental interference of independent photons," *Phys. Rev. Lett.*, vol. 96, p. 240502, 2006.

[222] H. Takesue and Y. Noguchi, "Implementation of quantum state tomography for time-bin entangled photon pairs," *Opt. Express*, vol. 17, p. 10976, 2009.

[223] K.-i. Harada, H. Takesue, H. Fukuda, T. Tsuchizawa, T. Watanabe, K. Yamada, Y. Tokura, and S.-i. Itabashi, "Generation of high-purity entangled photon pairs using silicon wire waveguide," *Opt. Express*, vol. 16, no. 25, pp. 20368–20373, 2008.

[224] E. Engin, D. Bonneau, C. M. Natarajan, A. S. Clark, M. G. Tanner, R. H. Hadfield, S. N. Dorenbos, V. Zwiller, K. Ohira, N. Suzuki, H. Yoshida, N. Iizuka, M. Ezaki, J. L. O'Brien, and M. G. Thompson, "Photon pair generation in a silicon micro-ring resonator with reverse bias enhancement," *Opt. Express*, vol. 21, no. 23, pp. 27826–27834, 2013.

[225] S. Ramelow, A. Farsi, S. Clemmen, D. Orquiza, K. Luke, M. Lipson, and A. L. Gaeta, "Silicon-Nitride Platform for Narrowband Entangled Photon Generation," *arXiv preprint arXiv:1508.04358*, 2015.

[226] J. Brendel, N. Gisin, W. Tittel, and H. Zbinden, "Pulsed energy-time entangled twin-photon source for quantum communication," *Phys. Rev. Lett.*, vol. 82, pp. 2594–2597, 1999.

[227] J. D. Franson, "Two-photon interferometry over large distances," *Phys. Rev. A*, vol. 44, pp. 4552–4555, 1991.

[228] Z. Y. Ou, X. Y. Zou, L. J. Wang, and L. Mandel, "Observation of nonlocal interference in separated photon channels," *Phys. Rev. Lett.*, vol. 65, pp. 321–324, 1990.

[229] P. G. Kwiat, W. A. Vareka, C. K. Hong, H. Nathel, and R. Y. Chiao, "Correlated two-photon interference in a dual-beam Michelson interferometer," *Phys. Rev. A*, vol. 41, pp. 2910–2913, 1990.

[230] M. J. Werner and A. Imamoğlu, "Photon-photon interactions in cavity electromagnetically induced transparency," *Phys. Rev. A*, vol. 61, p. 011801, 1999.

[231] I. Marcikic, H. de Riedmatten, W. Tittel, V. Scarani, H. Zbinden, and N. Gisin, "Time-bin entangled qubits for quantum communication created by femtosecond pulses," *Phys. Rev. A*, vol. 66, p. 062308, 2002.

[232] A. Politi, M. J. Cryan, J. G. Rarity, S. Yu, and J. L. O'Brien, "Silica-on-silicon waveguide quantum circuits," *Science*, vol. 320, no. 5876, pp. 646–649, 2008.

[233] D. A. Antonosyan, A. S. Solntsev, and A. A. Sukhorukov, "Effect of loss on photon-pair generation in nonlinear waveguide arrays," *Phys. Rev. A*, vol. 90, p. 043845, 2014.

[234] J. L. O'Brien, G. J. Pryde, A. G. White, T. C. Ralph, and D. Branning, "Demonstration of an all-optical quantum controlled-NOT gate," *Nature*, vol. 426, p. 264, 2003.

[235] R. Hanbury Brown and R. Q. Twiss, "Correlation between photons in two coherent beams of light," *Nature*, vol. 177, pp. 27–32, 1956.

[236] L. Mandel and E. Wolf, *Optical Coherence and Quantum Optics*. Cambridge: Cambridge University Press, 1995.

[237] A. K. Ekert and P. L. Knight, "Entangled quantum systems and the Schmidt decomposition," *American Journal of Physics*, vol. 63, no. 5, pp. 415–423, 1995.

[238] U. Leonhardt, *Measuring the quantum state of light*. Cambridge: Cambridge University Press, 1997.

[239] H. A. Bachor and T. C. Ralph, *A guide to experiments in quantum optics*. Wiley-VCH: Berlin, 2004.

[240] A. R. McMillan, v. Fulconis, M. Halder, C. Xiong, J. G. Rarity, and W. J. Wadsworth, "Narrowband high-fidelity all-fibre source of heralded single photons at 1570 nm," *Opt. Express*, vol. 17, pp. 6156–6165, 2009.

[241] E. Pomarico, B. Sanguinetti, T. Guerreiro, R. Thew, and H. Zbinden, "MHz rate and efficient synchronous heralding of single photons at telecom wavelengths," *Opt. Express*, vol. 20, pp. 23846–23855, 2012.

[242] Z. Vernon, M. Liscidini, and J. E. Sipe, "No free lunch: the trade-off between heralding rate and efficiency in microresonator-based heralded single photon sources," *Opt. Lett.*, vol. 41, no. 4, pp. 788–791, 2016.

[243] H. Takesue and K. Shimizu, "Effects of multiple pairs on visibility measurements of entangled photons generated by spontaneous parametric processes," *Optics Communications*, vol. 283, no. 2, pp. 276 – 287, 2010.

[244] M. D. Eisaman, J. Fan, A. Migdall, and S. V. Polyakov, "Invited review article: single-photon sources and detectors," *Review of Scientific Instruments*, vol. 82, p. 071101, 2011.

[245] J. McKeever, A. Boca, A. D. Boozer, R. Miller, J. R. Buck, A. Kuzmich, and H. J. Kimble, "Deterministic generation of single photons from one atom trapped in a cavity," *Science*, vol. 303, no. 5666, pp. 1992–1994, 2004.

[246] D. B. Higginbottom, L. Slodička, G. Araneda, L. Lachman, R. Filip, M. Hennrich, and R. Blatt, "Pure single photons from a trapped atom source," *New Journal of Physics*, vol. 18, no. 9, p. 093038, 2016.

[247] P. Michler, A. Kiraz, C. Becher, W. V. Schoenfeld, P. M. Petroff, L. Zhang, E. Hu, and A. Imamoglu, "A quantum dot single-photon turnstile device," *Science*, vol. 290, no. 5500, pp. 2282–2285, 2000.

[248] C. Santori, M. Pelton, G. Solomon, Y. Dale, and Y. Yamamoto, "Triggered single photons from a quantum dot," *Phys. Rev. Lett.*, vol. 86, pp. 1502–1505, 2001.

[249] E. Togan, Y. Chu, A. S. Trifonov, L. Jiang, J. Maze, L. Childress, M. V. G. Dutt, A. S. Sørensen, P. R. Hemmer, A. S. Zibrov, and M. D. Lukin, "Quantum entanglement between an optical photon and a solid-state spin qubit," *Nature*, vol. 466, pp. 730–734, 2010.

[250] I. Aharonovich and E. Neu, "Diamond nanophotonics," *Advanced Optical Materials*, vol. 2, no. 10, pp. 911–928, 2014.

[251] A. Sipahigil, K. D. Jahnke, L. J. Rogers, T. Teraji, J. Isoya, A. S. Zibrov, F. Jelezko, and M. D. Lukin, "Indistinguishable photons from separated silicon-vacancy centers in diamond," *Phys. Rev. Lett.*, vol. 113, p. 113602, 2014.

[252] N. Somaschi, V. Giesz, L. De Santis, J. C. Loredo, M. P. Almeida, G. Hornecker, S. L. Portalupi, T. Grange, C. Antón, J. Demory, C. Gómez, I. Sagnes, N. D. Lanzillotti-Kimura, A. Lemaítre, A. Auffeves, A. G. White, L. Lanco, and P. Senellart, "Near-optimal single-photon sources in the solid state," *Nature Photonics*, vol. 10, pp. 340–345, 2016.

[253] M. Reindl, K. D. Jöns, D. Huber, C. Schimpf, Y. Huo, V. Zwiller, A. Rastelli, and R. Trotta, "Phonon-assisted two-photon interference from remote quantum emitters," *Nano Letters*, vol. 17, no. 7, pp. 4090–4095, 2017.

[254] J. Martín-Sánchez, R. Trotta, A. Mariscal, R. Serna, G. Piredda, S. Stroj, J. Edlinger, C. Schimpf, J. Aberl, T. Lettner, J. Wildmann, H. Huang, X. Yuan, D. Ziss, J. Stangl, and A. Rastelli, "Strain-tuning of the optical properties of semiconductor nanomaterials by integration onto piezoelectric actuators," *Semiconductor Science and Technology*, vol. 33, no. 1, p. 013001, 2018.

[255] J. H. Weber, J. Kettler, H. Vural, M. Müller, J. Maisch, M. Jetter, S. L. Portalupi, and P. Michler, "Overcoming correlation fluctuations in two-photon interference experiments with differently bright and independently blinking remote quantum emitters," *Phys. Rev. B*, vol. 97, p. 195414, 2018.

[256] A. Christ and C. Silberhorn, "Limits on the deterministic creation of pure single-photon states using parametric down-conversion," *Phys. Rev. A*, vol. 85, p. 023829, 2012.

[257] A. L. Migdall, D. Branning, and S. Castelletto, "Tailoring single-photon and multiphoton probabilities of a single-photon on-demand source," *Phys. Rev. A*, vol. 66, no. 5, p. 053805, 2002.

[258] X.-S. Ma, S. Zotter, J. Kofler, T. Jennewein, and A. Zeilinger, "Experimental generation of single photons via active multiplexing," *Phys. Rev. A*, vol. 83, p. 043814, 2011.

[259] G. J. Mendoza, R. Santagati, J. Munns, E. Hemsley, M. Piekarek, E. Martín-López, G. D. Marshall, D. Bonneau, M. G. Thompson, and J. L. O'Brien, "Active temporal and spatial multiplexing of photons," *Optica*, vol. 3, pp. 127–132, 2016.

[260] C. Xiong, X. Zhang, Z. Liu, M. J. Collins, A. Mahendra, L. G. Helt, M. J. Steel, D.-Y. Choi, C. J. Chae, P. H. W. Leong, and B. J. Eggleton, "Active temporal multiplexing of indistinguishable heralded single photons," *Nature Communications*, vol. 7, p. 10853, 2016.

[261] M. Liscidini and J. E. Sipe, "Stimulated emission tomography," *Phys. Rev. Lett.*, vol. 111, p. 193602, 2013.

[262] A. Eckstein, G. Boucher, A. Lemaître, P. Filloux, I. Favero, G. Leo, J. E. Sipe, M. Liscidini, and S. Ducci, "High-resolution spectral characterization of two photon states via classical measurements," *Laser and Photonics Reviews*, vol. 8, no. 5, pp. L76–L80, 2014.

[263] K. Garay-Palmett, H. J. McGuinness, O. Cohen, J. S. Lundeen, R. Rangel-Rojo, A. B. U'Ren, M. G. Raymer, C. J. McKinstrie, S. Radic, and I. A. Walmsley, "Photon pair-state preparation with tailored spectral properties by spontaneous four-wave mixing in photonic-crystal fiber," *Opt. Express*, vol. 15, no. 22, pp. 14870–14886, 2007.

[264] B. Fang, O. Cohen, M. Liscidini, J. E. Sipe, and V. O. Lorenz, "Fast and highly resolved capture of the joint spectral density of photon pairs," *Optica*, vol. 1, no. 5, pp. 281–284, 2014.

[265] B. J. Smith, P. Mahou, O. Cohen, J. S. Lundeen, and I. A. Walmsley, "Photon pair generation in birefringent optical fibers," *Opt. Express*, vol. 17, no. 26, pp. 23589–23602, 2009.

[266] M. Avenhaus, A. Eckstein, P. J. Mosley, and C. Silberhorn, "Fiber-assisted single-photon spectrograph," *Opt. Lett.*, vol. 34, no. 18, pp. 2873–2875, 2009.

[267] L. Rozema, C. Wang, D. H. Mahler, A. Hayat, A. M. Steinberg, J. E. Sipe, and M. Liscidini, "Characterizing an entangled-photon source with classical detectors and measurements," *Optica*, vol. 2, no. 5, pp. 430–433, 2015.

[268] J. W. Silverstone, R. Santagati, D. Bonneau, M. J. Strain, M. Sorel, J. L. O'Brien, and M. G. Thompson, "Qubit entanglement between ring-resonator photon-pair sources on a silicon chip," *Nature Communications*, vol. 6, p. 7948, 2015.

[269] J. R. Ong, R. Kumar, and S. Mookherjea, "Silicon microring-based wavelength converter with integrated pump and signal suppression," *Opt. Lett.*, vol. 39, no. 15, pp. 4439–4441, 2014.

[270] M. Piekarek, D. Bonneau, S. Miki, T. Yamashita, M. Fujiwara, M. Sasaki, H. Terai, M. G. Tanner, C. M. Natarajan, R. H. Hadfield, J. L. O'Brien, and M. G. Thompson, "High-extinction ratio integrated photonic filters for silicon quantum photonics," *Opt. Lett.*, vol. 42, no. 4, pp. 815–818, 2017.

[271] C. Xiong, T. D. Vo, M. J. Collins, J. Li, T. F. Krauss, M. J. Steel, A. S. Clark, and B. J. Eggleton, "Bidirectional multiplexing of heralded single photons from a silicon chip," *Opt. Lett.*, vol. 38, no. 23, pp. 5176–5179, 2013.

[272] A. Crespi, R. Ramponi, R. Osellame, L. Sansoni, I. Bongioanni, F. Sciarrino, G. Vallone, and P. Mataloni, "Integrated photonic quantum gates for polarization qubits," *Nature Communications*, vol. 2, no. 1, 2011.

[273] N. C. Harris, G. R. Steinbrecher, M. Prabhu, Y. Lahini, J. Mower, D. Bunandar, C. Chen, F. N. C. Wong, T. Baehr-Jones, M. Hochberg, S. Lloyd, and D. Englund, "Quantum transport simulations in a programmable nanophotonic processor," *Nature Photonics*, vol. 11, pp. 447–452, 2017.

[274] K. Bourzac, "Photonic chips made easier," *Nature*, vol. 483, p. 388, 2012.

[275] Y. Zhang, T. Baehr-Jones, R. Ding, T. Pinguet, Z. Xuan, and M. Hochberg, "Silicon multi-project wafer platforms for optoelectronic system integration," in *The 9th International Conference on Group IV Photonics (GFP)*, pp. 63–65, 2012.

[276] T. Baehr-Jones, R. Ding, A. Ayazi, T. Pinguet, M. Streshinsky, N. C. Harris, J. Li, L. He, M. Gould, Y. Zhang, A. E.-J. Lim, T.-Y. Liow, S. Hwee-Gee Teo, G.-Q. Lo, and M. Hochberg, "A 25 Gb/s silicon photonics platform," *arXiv preprint arXiv:1203.0767*, 2012.

[277] C. Galland, A. Novack, Y. Liu, R. Ding, M. Gould, T. Baehr-Jones, Q. Li, Y. Yang, Y. M. Ma, Y. Zhang, K. Padmaraju, K. Bergmen, A. E.-J. Lim, G.-Q. Lo, and M. Hochberg, "A CMOS-compatible silicon photonic platform for high-speed integrated opto-electronics," *Proceedings of SPIE*, vol. 8767, 2013.

[278] A. Novack, Y. Liu, R. Ding, M. Gould, T. Baehr-Jones, Q. Li, Y. Yang, Y. Ma, Y. Zhang, K. Padmaraju, K. Bergmen, A. E.-J. Lim, G.-Q. Lo, and M. Hochberg, "A 30 GHz silicon photonic platform," 2013.

[279] T. Shoji, T. Tsuchizawa, T. Watanabe, K. Yamada, and H. Morita, "Low loss mode size converter from 0.3 /spl mu/m square Si wire waveguides to singlemode fibres," *Electronics Letters*, vol. 38, no. 25, pp. 1669–1670, 2002.

[280] S. J. McNab, N. Moll, and Y. A. Vlasov, "Ultra-low loss photonic integrated circuit with membrane-type photonic crystal waveguides," *Opt. Express*, vol. 11, no. 22, pp. 2927–2939, 2003.

[281] M. Pu, L. Liu, H. Ou, K. Yvind, and J. M. Hvam, "Ultra-low-loss inverted taper coupler for silicon-on-insulator ridge waveguide," *Optics Communications*, vol. 283, no. 19, pp. 3678–3682, 2010.

[282] D. Taillaert, F. Van Laere, M. Ayre, W. Bogaerts, D. Van Thourhout, P. Bienstman, and R. Baets, "Grating couplers for coupling between optical fibers and nanophotonic waveguides," *Japanese Journal of Applied Physics*, vol. 45, no. 8R, p. 6071, 2006.

[283] L. He, Y. Liu, C. Galland, A. E. J. Lim, G.-Q. Lo, T. Baehr-Jones, and M. Hochberg, "A High-Efficiency Nonuniform Grating Coupler Realized With 248-nm Optical Lithography," *Photonics Technology Letters, IEEE*, vol. 25, no. 14, pp. 1358–1361, 2013.

[284] Y. Liu, R. Ding, M. Gould, T. Baehr-Jones, Y. Yang, Y. Ma, Y. Zhang, A. E.-J. Lim, T.-Y. Liow, S. H.-G. Teo, G.-Q. Lo, and M. Hochberg, "30GHz silicon platform for photonics system," *Optical Interconnects Conference, OI 2013*, vol. 1, pp. 27–28, 2013.

[285] M. Liscidini, L. G. Helt, and J. E. Sipe, "Asymptotic fields for a hamiltonian treatment of nonlinear electromagnetic phenomena," *Physical Review A*, vol. 85, no. 1, p. 013833, 2012.

[286] Z. Yang, M. Liscidini, and J. E. Sipe, "Spontaneous parametric down-conversion in waveguides: a backward Heisenberg picture approach," *Physical Review A*, vol. 77, no. 3, p. 033808, 2008.

[287] T. Onodera, M. Liscidini, J. E. Sipe, and L. G. Helt, "Parametric fluorescence in a sequence of resonators: An analogy with Dicke superradiance," *Physical Review A*, vol. 93, no. 4, p. 043837, 2016.

[288] Z. Vernon, M. Menotti, C. C. Tison, J. A. Steidle, M. L. Fanto, P. M. Thomas, S. F. Preble, A. M. Smith, P. M. Alsing, M. Liscidini, and J. E. Sipe, "Truly unentangled photon pairs without spectral filtering," *Opt. Lett.*, vol. 42, no. 18, pp. 3638–3641, 2017.

[289] L. Pavesi, "A review of the various efforts to a silicon laser," 2003.

[290] Z. Fang, Q. Y. Chen, and C. Z. Zhao, "A review of recent progress in lasers on silicon," *Optics & Laser Technology*, vol. 46, pp. 103–110, 2013.

[291] Z. Zhou, B. Yin, and J. Michel, "On-chip light sources for silicon photonics," *Light: Science & Applications*, vol. 4, p. e358, 2015.

[292] O. Boyraz and B. Jalali, "Demonstration of a silicon Raman laser," *Opt. Express*, vol. 12, no. 21, pp. 5269–5273, 2004.

[293] A. J. Kenyon, "Erbium in silicon," *Semiconductor Science and Technology*, vol. 20, no. 12, p. R65, 2005.

[294] M. Bulsara, "Optical interconnects promised by III-V on-silicon integration," *Solid State Technology*, vol. 47, pp. 22–25, 2004.

[295] G. Roelkens, D. Van Thourhout, R. Baets, R. Nötzel, and M. Smit, "Laser emission and photodetection in an InP/InGaAsP layer integrated on and coupled to a silicon-on-insulator waveguide circuit," *Opt. Express*, vol. 14, no. 18, pp. 8154–8159, 2006.

[296] A. W. Fang, H. Park, O. Cohen, R. Jones, M. J. Paniccia, and J. E. Bowers, "Electrically pumped hybrid AlGaInAs-silicon evanescent laser," *Opt. Express*, vol. 14, no. 20, pp. 9203–9210, 2006.

[297] R. Claps, D. Dimitropoulos, Y. Han, and B. Jalali, "Observation of Raman emission in silicon waveguides at 1.54 μm," *Opt. Express*, vol. 10, no. 22, pp. 1305–1313, 2002.

[298] S. Ashley, "Making light of silicon," *Scientific American*, vol. 293, no. 20, 2005.

[299] S. M. Spillane, T. J. Kippenberg, and K. J. Vahala, "Ultralow-threshold Raman laser using a spherical dielectric microcavity," *Nature*, vol. 415, pp. 621–623, 2002.

[300] M. E. Castagna, S. Coffa, L. Caristia, A. Messina, and C. Bongiorno, "Quantum dot materials and devices for light emission in silicon," in *32nd European Solid-State Device Research Conference*, pp. 439–442, 2002.

[301] M. Q. Huda and S. Subrina, "Multiple excitation of silicon nanoclusters during erbium sensitization process in silicon rich oxide host," *Applied Physics Letters*, vol. 98, no. 11, p. 111905, 2011.

[302] J. Liu, X. Sun, D. Pan, X. Wang, L. C. Kimerling, T. L. Koch, and J. Michel, "Tensile-strained, n-type Ge as a gain medium for monolithic laser integration on Si," *Opt. Express*, vol. 15, no. 18, pp. 11272–11277, 2007.

[303] J. Liu, X. Sun, R. E. Camacho-Aguilera, L. C. Kimerling, and J. Michel, "Ge-on-Si laser operating at room temperature," *Optics Letters*, vol. 35, no. 5, pp. 679–681, 2010.

[304] R. E. Camacho-Aguilera, Y. Cai, N. Patel, J. T. Bessette, M. Romagnoli, L. C. Kimerling, and J. Michel, "An electrically pumped germanium laser," *Opt. Express*, vol. 20, no. 10, pp. 11316–11320, 2012.

[305] R. Chen, T.-T. Tran, K. Ng, W. Ko, L. Chuang, F. Sedgwick, and C. Chang-Hasnain, "Nanolasers grown on silicon," *Nature Photonics*, vol. 5, pp. 170–175, 2011.

[306] M. T. Hill, "Nanolasers with a twist," *Nature Photonics*, vol. 5, pp. 130–131, 2011.

[307] J. E. Bowers, D. Liang, A. W. Fang, H. Park, R. Jones, and M. J. Paniccia, "Hybrid silicon lasers: the final frontier to integrated computing," *Opt. Photon. News*, vol. 21, no. 5, pp. 28–33, 2010.

[308] G. Roelkens, Y. De Koninck, S. Keyvaninia, S. Stankovic, M. Tassaert, M. Lamponi, G. Duan, D. Van Thourhout, and R. Baets, "Hybrid silicon lasers," in *Optoelectronic Integrated Circuits XIII*, vol. 7942, p. 79420D, 2011.

[309] D. Lian, M. Fiorentino, T. Okumura, H.-H. Chang, D. T. Spencer, Y.-H. Kuo, A. W. Fang, D. Dai, R. G. Beausoleil, and J. E. Bowers, "Electrically-pumped compact hybrid silicon microring lasers for optical interconnects," *Optics Express*, vol. 17, no. 22, pp. 20355–20364, 2009.

[310] I. P. Kaminow and L. Tingye, *Optical fiber telecommunications IV A. Components*. Academic Press, 2002.

[311] Commercial fiber lasers can be found at: `https://www.thorlabs.com/navigation.cfm?guide_id=2215`.

[312] J. K. Sahu, Y. Jeong, D. J. Richardson, and J. Nilsson, "A 103 W erbium-ytterbium co-doped large-core fiber laser," *Optics Communications*, vol. 227, no. 1, pp. 159–163, 2003.

[313] V. V. Dvoyrin, M. Tan, A. S. Zlenko, V. M. Mashinsky, M. A. Melkumov, E. M. Dianov, P. Harper, and S. K. Turitsyn, "Bi-doped fiber laser for telecom applications," in *Conference on Lasers and Electro-Optics*, p. STu1F.4, Optical Society of America, 2016.

[314] M. Kimura, *Fiber lasers: research, technology and applications*. Lasers and electro-optics research and technology series, Nova Science, 2009.

[315] R. Mary, D. Choudhury, and A. K. Kar, "Applications of fiber lasers for the development of compact photonic devices," *IEEE Journal of Selected Topics in Quantum Electronics*, vol. 20, no. 5, pp. 72–84, 2014.

[316] V. R. Almeida, C. A. Barrios, R. R. Panepucci, and M. Lipson, "All-optical control of light on a silicon chip," *Nature*, vol. 431, no. 7012, pp. 1081–1084, 2004.

[317] V. R. Almeida and M. Lipson, "Optical bistability on a silicon chip.," *Opt. Lett.*, vol. 29, no. 20, pp. 2387–2389, 2004.

[318] A. Pasquazi, L. Caspani, M. Peccianti, M. Clerici, M. Ferrera, L. Razzari, D. Duchesne, B. E. Little, S. T. Chu, D. J. Moss, and R. Morandotti, "Self-locked optical parametric oscillation in a cmos compatible microring resonator: a route to robust optical frequency comb generation on a chip," *Opt. Express*, vol. 21, no. 11, pp. 13333–13341, 2013.

[319] T. Carmon, L. Yang, and K. J. Vahala, "Dynamical thermal behavior and thermal self-stability of microcavities," *Opt. Express*, vol. 12, no. 20, pp. 4742–4750, 2004.

[320] M. Peccianti, A. Pasquazi, Y. Park, B. E. Little, S. T. Chu, D. J. Moss, and R. Morandotti, "Demonstration of a stable ultrafast laser based on a nonlinear microcavity," *Nature Communications*, vol. 3, p. 765, 2012.

[321] W. C. Jiang, X. Lu, J. Zhang, O. Painter, and Q. Lin, "Silicon-chip source of bright photon pairs," *Opt. Express*, vol. 23, no. 16, pp. 20884–20904, 2015.

[322] C. Reimer, M. Kues, L. Caspani, B. Wetzel, P. Roztocki, M. Clerici, Y. Jestin, M. Ferrera, M. Peccianti, A. Pasquazi, B. E. Little, S. T. Chu, D. J. Moss, and R. Morandotti, "Cross-polarized photon-pair generation and bi-chromatically pumped optical parametric oscillation on a chip," *Nature Communications*, vol. 6, p. 8236, 2015.

[323] A. E. Siegman, *Lasers*. University Science Books, 1986.

[324] W. W. Rigrod, "Saturation effects in high-gain lasers," *J. Appl. Phys.*, vol. 36, no. 8, pp. 2487–2490, 1965.

[325] A. C. Eckbreth, "Coupling considerations for ring resonators," *IEEE J. Quantum Electron.*, vol. 11, no. 9, pp. 796–798, 1975.

[326] I. Jizan, B. Bell, L. G. Helt, A. Casas Bedoya, C. Xiong, and B. J. Eggleton, "Phase-sensitive tomography of the joint spectral amplitude of photon pair sources," *Opt. Lett.*, vol. 41, no. 20, pp. 4803–4806, 2016.

[327] C. A. Husko, A. S. Clark, M. J. Collins, A. De Rossi, S. Combrié, G. Lehoucq, I. H. Rey, T. F. Krauss, C. Xiong, and B. J. Eggleton, "Multi-photon absorption limits to heralded single photon sources," *Scientific Reports*, vol. 3, 2013.

[328] K. Harada, H. Takesue, H. Fukuda, T. Tsuchizawa, T. Watanabe, K. Yamada, Y. Tokura, and S. Itabashi, "Frequency and polarization characteristics of correlated photon-pair generation using a silicon wire waveguide," *IEEE Journal of Selected Topics in Quantum Electronics*, vol. 16, no. 1, pp. 325–331, 2010.

[329] D. Llewellyn, Y. Ding, I. Faruque, S. Paesani, R. Santagati, J. Kennard, D. Bacco, K. Rottwitt, L. K. Oxenløwe, J. L. O'Brien, J. Wang, and M. G. Thompson, "Generation and manipulation of multi-photon entangled states on a silicon photonic device," in *Conference on Lasers and Electro-Optics*, p. FTh1G.7, Optical Society of America, 2018.

[330] M. Zhang, L.-T. Feng, Z.-Y. Zhou, Y. Chen, H. Wu, M. Li, G.-P. Guo, G.-C. Guo, D.-X. Dai, and X.-F. Ren, "Generation of multiphoton entangled quantum states with a single silicon nanowire," 2018.

[331] N. Bergamasco, M. Menotti, J. E. Sipe, and M. Liscidini, "Generation of path-encoded Greenberger-Horne-Zeilinger states," *Phys. Rev. Applied*, vol. 8, p. 054014, 2017.

[332] A. F. J. Runge, C. Aguergaray, R. Provo, M. Erkintalo, and N. G. R. Broderick, "All-normal dispersion fiber lasers mode-locked with a nonlinear amplifying loop mirror," *Optical Fiber Technology*, vol. 20, no. 6, pp. 657 – 665, 2014.

[333] X. Yang, Z. Li, E. Tangdiongga, D. Lenstra, D. Khoe, and H. J. S. Dorren, "Sub-picosecond pulse generation employing an SOA-based nonlinear polarization switch in a ring cavity," *Opt. Express*, vol. 12, no. 11, pp. 2448–2453, 2004.

[334] F. Morichetti, A. Canciamilla, M. Martinelli, A. Samarelli, R. M. De La Rue, M. Sorel, and A. Melloni, "Coherent backscattering in optical microring resonators," *Applied Physics Letters*, vol. 96, no. 8, p. 081112, 2010.

[335] J. Clarke and F. K. Wilhelm, "Superconducting quantum bits," *Nature*, vol. 453, no. 7198, pp. 1031–1042, 2008.

[336] T. P. Harty, D. T. C. Allcock, C. J. Ballance, L. Guidoni, H. A. Janacek, N. M. Linke, D. N. Stacey, and D. M. Lucas, "High-fidelity preparation, gates, memory, and readout of a trapped-ion quantum bit," *Phys. Rev. Lett.*, vol. 113, p. 220501, 2014.

[337] Y. Wang, Y. Li, Z.-q. Yin, and B. Zeng, "16-qubit IBM universal quantum computer can be fully entangled," *ArXiv e-prints*, 2018.

[338] S. Lloyd, "Quantum search without entanglement," *Phys. Rev. A*, vol. 61, p. 010301, 1999.

[339] N. J. Cerf, C. Adami, and P. G. Kwiat, "Optical simulation of quantum logic," *Phys. Rev. A*, vol. 57, pp. R1477–R1480, 1998.

[340] E. Brainis, L.-P. Lamoureux, N. J. Cerf, P. Emplit, M. Haelterman, and S. Massar, "Fiber-optics implementation of the Deutsch-Jozsa and Bernstein-Vazirani quantum algorithms with three qubits," *Phys. Rev. Lett.*, vol. 90, p. 157902, 2003.

[341] E. Bernstein and U. Vazirani, "Quantum complexity theory," in *Proceedings of the Twenty-fifth Annual ACM Symposium on Theory of Computing*, STOC '93, (New York, NY, USA), pp. 11–20, ACM, 1993.

[342] D. Deutsch, "Quantum theory, the church-turing principle and the universal quantum computer," *Proceedings of the Royal Society of London A: Mathematical, Physical and Engineering Sciences*, vol. 400, no. 1818, pp. 97–117, 1985.

[343] D. Deutsch and R. Jozsa, "Rapid solution of problems by quantum computation," *Proceedings of the Royal Society of London A: Mathematical, Physical and Engineering Sciences*, vol. 439, no. 1907, pp. 553–558, 1992.

[344] D. Bruß and C. Macchiavello, "Multipartite entanglement in quantum algorithms," *Phys. Rev. A*, vol. 83, p. 052313, 2011.

[345] M. Reck, A. Zeilinger, H. J. Bernstein, and P. Bertani, "Experimental realization of any discrete unitary operator," *Phys. Rev. Lett.*, vol. 73, pp. 58–61, 1994.

[346] J. Skaar, J. C. García Escartín, and H. Landro, "Quantum mechanical description of linear optics," *American Journal of Physics*, vol. 72, no. 11, pp. 1385–1391, 2004.

[347] K. P. Seshadreesan, J. P. Olson, K. R. Motes, P. P. Rohde, and J. P. Dowling, "Boson sampling with displaced single-photon fock states versus single-photon-added coherent states: The quantum-classical divide and computational-complexity transitions in linear optics," *Phys. Rev. A*, vol. 91, p. 022334, 2015.

[348] P. Horowitz and W. Hill, *The Art of Electronics*. Cambridge University Press, 2015.

[349] R. Jozsa and N. Linden, "On the role of entanglement in quantum-computational speed-up," *Proceedings of the Royal Society of London A: Mathematical, Physical and Engineering Sciences*, vol. 459, no. 2036, pp. 2011–2032, 2003.

[350] D. A. Meyer, "Sophisticated quantum search without entanglement," *Phys. Rev. Lett.*, vol. 85, pp. 2014–2017, 2000.

[351] E. Karimi and R. W. Boyd, "Classical entanglement?," *Science*, vol. 350, no. 6265, pp. 1172–1173, 2015.